Universidade do Minho
Escola de Engenharia

José Luís Duarte Granja

Continuous characterization of stiffness of cement-based materials: experimental analysis and micro-mechanics modelling

January, 2016

Continuous characterization of stiffness of cement-based materials: experimental analysis and micro-mechanics modelling
José Luís Duarte Granja
UMinho | 2016

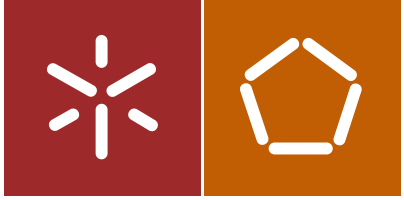

Universidade do Minho
Escola de Engenharia

José Luís Duarte Granja

Continuous characterization of stiffness of cement-based materials: experimental analysis and micro-mechanics modelling

Philosophy Doctorate Thesis
Civil Engineering

Work conducted under supervision of:
Professor Doctor Miguel Ângelo Dias Azenha

January, 2016

STATEMENT OF INTEGRITY

I hereby declare having conducted my thesis with integrity. I confirm that I have not used plagiarism or any form of falsification of results in the process of the thesis elaboration.

I further declare that I have fully acknowledged the Code of Ethical Conduct of the University of Minho.

University of Minho, 28 de janeiro de 2016

Full name: José Luís Duarte Granja

Signature: _____

“Logic will get you from A to B
Imagination will take you everywhere”
Albert Einstein

This page intentionally left blank

Abstract

The structural performance and durability of reinforced concrete structures are strongly influenced by the material properties of concrete. Concrete's characteristics endure strong evolution since casting, passing from a solid suspension to a structural material. Therefore, it is extremely important to understand and predict the structural behaviour of concrete since the beginning of the hardening process for a good structural design, particularly in regard to the development of self-induced stresses (due to heat of hydration and shrinkage). Apart from these issues related to structural design, relevant urges are brought about by the necessity of shortening construction schedules, both due to pressures by society, as well as due to economic and sustainability concerns. In view of these motivations, there are enough reasons to justify the importance of having experimental methods that allow continuous monitoring of the evolution of mechanical properties of concrete since very early ages, both in laboratory environment and "*in-situ*". In such concern, several methods experimental have been proposed throughout the years, particularly in regard to the evaluation of the E-modulus of concrete. However, the most widespread methods still present limitations/complexities which make them inadequate for the wider intents mentioned above. Thus a new experimental method called EMM-ARM (Elasticity Modulus Measurement through Ambient Response Method) was proposed in 2009, which is based on the modal identification of a composite beam (acrylic and concrete) during the curing period of concrete, allowing the continuous measurement of

concrete E-modulus since casting. Despite the good results obtained during the first implementation prior to this thesis, the EMM-ARM is still lacked extensive validation and presented several laminations that needed to be overcome.

Following the encouraging results obtained in the first application of EMM-ARM, the work reported in this thesis intended to achieve an improved robust tool based on EMM-ARM to provide early information of the cementitious materials stiffness, readily available for application on behalf of both scientists and practitioners. In pursuit of that goal, relevant changes were introduced in EMM-ARM, particularly in concern to the geometry and materials involved in the EMM-ARM mould, as well as to the modal identification of technique. These changes allowed overcoming the identified constraints and to significantly improve the usability and robustness of the method. This thesis also presents a systematic study of the application of EMM-ARM compared to competing methods that mechanical characterization of cementitious materials at early ages with mutual validation objectives. This systematic study allowed proving that the results of EMM-ARM are metrologically robust and also to clearly identify the strengths and limitations of EMM-ARM.

After the optimization and validation of EMM-ARM the method was applied in different conditions such as: (*i*) different isothermal curing temperatures in the range 10-40ºC; (*ii*) the implementation in a construction site; and (*iii*) non-isothermal conditions.

This research also permitted demonstrating that EMM-ARM can be used to characterize a wide range of materials that undergoes chemical hardening such as structural epoxy adhesives. In addition, a new version of EMM-ARM for monitoring the concrete viscoelasticity during the fresh state was suggested.

The thesis ends with a foray into the microstructural simulation of the stiffness evolution of cementitious materials by taking advantage of the unprecedented quantitative experimental information obtained with EMM-ARM. The stiffness evolution of cement pastes, simulated by μic/AMIE, developed at EPFL (*École polytechnique fédérale de Lausanne*) was validated through comparison with EMM-ARM results.

Resumo

A performance estrutural e a durabilidade de estruturas de betão armado são fortemente influenciadas pelas propriedades do betão. As características do betão sofrem uma grande evolução desde a betonagem, passando de uma suspensão de sólidos para um material estrutural. Desta forma torna-se extremamente importante compreender e prever o comportamento estrutural do betão desde o inicio do processo de endurecimento para se conseguir efetuar um correto dimensionamento estrutural, especialmente no que diz respeito ao desenvolvimento de tensões autoinduzidas (devido ao calor de hidratação e à retração). Adicionalmente a estas questões relacionadas com o dimensionamento estrutural, o desempenho estrutural do betão é também relevante do ponto de vista da redução dos períodos de construção devido a pressões da sociedade assim como devido a questões económicas e de sustentabilidade. Tendo em conta estas motivações, há razões suficientes para justificar a importância a existência de métodos experimentais que permitam a monitorização continua da evolução das propriedades mecânicas do betão desde as primeiras idades, tanto para a aplicação em laboratório assim como "*in-situ*". Nesse sentido vários métodos experimentais têm vindo a ser propostos ao longo dos anos, particularmente no que diz respeito à avaliação do módulo de elasticidade de betão. No entanto, os métodos mais disseminados ainda apresentam limitações e/ou complexidades que os tornam inadequados para os propósitos mais amplos acima mencionados. Desta forma um novo método experimental foi proposto em 2009 chamado

EMM-ARM (*Elasticity Modulus Measurement through Ambient Response Method*) que é baseado na identificação modal de uma viga composta (acrílico e betão) durante o processo de cura, permitindo a monitorização continua do modulo de elasticidade do betão desde a betonagem. Apesar dos bons resultados obtidos durante a primeira aplicação do método antes desta tese, o EMM-ARM ainda requer uma extensa validação e apresenta algumas limitações que necessitam de ser eliminadas.

Na sequência dos resultados encorajadores obtidos na primeira aplicação do EMM-ARM, o trabalho reportado nesta tese pretende alcançar uma ferramenta melhorada e robusta baseada no EMM-ARM para fornecer informação antecipada sobre a rigidez materiais cimentícios e fornece-la em tempo real ao utilizador. Na busca deste objetivo foram introduzidas alterações relevantes no EMM-ARM, particularmente no que diz respeito à geometria e materiais envolvidos no molde, assim como na técnica de identificação modal. Estas adaptações permitiram superar as limitações identificadas e melhorar significativamente a usabilidade e a robustez do método. Esta tese apresenta também um estudo sistemático da aplicação do EMM-ARM comparado aos métodos concorrentes capazes de caracterizar as propriedades mecânicas dos materiais cimentícios nas primeiras idades com o objetivo de fazer a validação mútua dos métodos. Este estudo sistemático permitiu provar que os resultados obtidos pelo EMM-ARM são metrologicamente robustos e ainda identificar claramente os pontos fortes e limitações do método.

Após a otimização e validação do EMM-ARM, o método foi aplicado sob diferentes condições, tais como: (*i*) diferentes temperaturas isotérmicas de cura na gama entre 10-40ºC; (*ii*) a implementação num estaleiro de obra; e (*iii*) condições não-isotérmicas.

Este trabalho permitiu também demonstrar que o EMM-ARM pode ser utilizado para caracterizar uma vasta gama de materiais que sofre endurecimento químico, tais como adesivos epoxídicos. Adicionalmente, foi ainda sugerida uma nova versão do EMM-ARM para monitorizar a viscoelasticidade do betão durante o estado fresco.

A tese termina com uma incursão na simulação microestrutural da evolução da rigidez de materiais cimentícios, tirando partido da informação experimental quantitativa sem precedentes obtida com o EMM-ARM. A evolução rigidez de pastas de cimento, simulada pelo modelo μic/AMIE, desenvolvido na EPFL (*École polytechnique fédérale de Lausanne*) foi validada através de comparação com os resultados obtidos pelo EMM-ARM.

Acknowledgments

Many people have contributed with insight and encouragement throughout the whole process that culminated in this PhD thesis.

I am in great debt to my first supervisor, Prof. Miguel Azenha. His enthusiasm, knowledge, confidence, and guidance were absolutely critical to complete this work. I would like also to acknowledge his availability and willingness to discuss each idea and their enthusiastic help in filtering the best ones.

I wish also to acknowledge Dr. Cyrille Dunant and Prof. Karen Scrivener for hosting me at *École polytechnique fédérale de Lausanne* (EPFL), Switzerland, where their guidance and discussions where an important contribute to the present work. Within that research activity, my gratitude goes also to Prof. Violeta Bosiljkov for making possible my presence in a short scientific mission on the scope of research activity COST Action TU1404 entitled: characterization of cement-based materials: experimental analysis and micro-mechanics modelling.

I would like to express my gratitude also to the constructions companies Casais, S.A. and Teixeira Duarte, S.A. for their openness to perform tests during the execution of construction works.

To the PhD student Miram Lizancos and MSc students Nuno Carvalho and Carlos Araújo I express my gratitude for their contribution to the work presented in this thesis.

To all the PhD students and colleagues in the Civil Engineering Department of University of Minho, I would like to thank for the hours spent together discussing each other works, even within so different fields of research. Their different perspectives allowed me to see outside the box and were a fruitful contribution to the present work.

My gratitude goes also to the to all the staff of the Civil Engineering Department of University of Minho for the positive and productive atmosphere, to the Structural Lab from University of Minho and its staff who offered me their assistance, experience and advices.

My acknowledgements extend also to the *Fundação para a Ciência e Tecnologia* (FCT) for the grant funding. This study would not have existed without the financial support of this institution.

Finally, I want to express my gratitude to my family and all my friends for the unconditional support given during the long journey of my PhD thesis.

Content

This page intentionally left blank

List of Figures

This page intentionally left blank

List of Tables

This page intentionally left blank

List of Abbreviations

µic	New platform for modelling the hydration of cements
ACC	Automated Classical Cyclic Compression test
ASTM	American Society for Testing and Materials
BE	Bender-extender Elements
BTJASPE	BéTon au Jeune Age, Suivi de la Prise et du module d'Élasticité
C_2S	Dicalcium silicate (Belite)
C_3A	Tricalcium aluminate (Aluminate)
C_3S	Tricalcium silicate (Alite)
C_4AF	Tetracalcium alumino ferrite (Ferrite)
CC	Classical Cyclic Compression test
CEMHYD3D	Three-dimensional cement hydration and microstructure development model
CEN	European Committee for Standardization
CH	Calcium Hydroxide
CSH	Calcium Silicate Hydrate
CV	Computational Volume
DFT	Discrete Fourier Transform

DOFs	Degrees Of Freedom
DuCOM	Durability Models of COncrete
EMA	Experimental modal analysis
EMI	Electromechanical Impedance method
EMM-ARM	Elasticity Modulus Measurement through Ambient Response Method
EMPA	Swiss Federal Laboratories for Materials Science and Technology
EN	European Norm
EPFL	École Polytechnique Fédérale de Lausanne
ERA	Eigensystem Realization Algorithm
ERA-FD	Eigensystem Realization Algorithm in Frequency Domain
EVD	Eigenvalue Decomposition
FEM	Finite Element Model
FFT	Fast Fourier Transform
FRF	Frequency Response Function
HD CSH	High Density Calcium Silicate Hydrate
HydratiCA	Hydration by Cellular Automata
HYMOSTRUC	HYdration, MOrphology and STRUCtural development
IDFT	Inverse Discrete Fourier Transform
IFFT	Inverse Fast Fourier Transform
IFT	Inverse Fourier Transform
IRF	Impulse Response Function
ISO	International Organization for Standardization
LD CSH	Low Density Calcium Silicate Hydrate
LMC	Laboratory of Construction Materials at EPFL
LMFD	Left Matrix-Fraction Description
LNEC	Portuguese Nacional Civil Engineering Laboratory
LS	Least Squares algorithm
LVDT	Linear Variable Differential Transformers
MDOF	Multiple Degree Of Freedom
NPSD	Normalized Power Spectrum Density
OMA	Operational Modal Analysis
PP	Peak-Picking
PUCP	Pontificia Universidad Católica del Perú

PZT	Piezoelectric Lead Zirconate Titanate
QR	Orthogonal decomposition
RILEM	International Union of Laboratories and Experts in Construction Materials, Systems and Structures
SDOF	Single Degree Of Freedom
SMAG	SMart AGgregates
SSI	Subspace System Identification
SVD	Singular Value Decomposition
TF	Transfer Function
TSTM	Temperature Stress Testing Machine
UWR	Ultrasound Wave Reflection
UWT	Ultrasound Wave Transmission
w/c	Water to Cement ratio
WTM	Wave Transmission Method
XFEM	Extended Finite Element Model

This page intentionally left blank

List of Symbols

The list of symbols presented here is valid for the entire thesis with exception to the Chapter 4.

$\varnothing_e$	External diameter
$\varnothing_i$	Internal diameter
A_1	Constant
A_2	Constant
A_3	Constant
A_4	Constant
A_f, B_f and C_f	Fitting parameters of the relation between f_{cm} and E
A_t	Proportionality constant
b	Non-linear parameter in the stress-strain relationship
B	Cross-section width of the EMM-ARM 'U-shape' beam
d, e and f	Fitting parameters of the resonance frequency of SMEA tests
$d\alpha/dt$	Rate of the degree of hydration
E	Elastic modulus
$\bar{E}$	Homogenized elasticity modulus
E_0	Initial elastic modulus

E_{act}	Apparent activation energy
E_c	Concrete elastic modulus
E_{dyn}	Dynamic elastic modulus
E_m	Mould elastic modulus
E_{stat}	Static elastic modulus
E_{ult}	Asymptotic ultimate elastic modulus
f	Fraction of material reacted in Avrami equation
$f(\alpha)$	Function that describes the hydration reaction mechanism
f_{cm}	Uniaxial compressive strength in cylinders
fr	Linear resonance frequency
H	Cross-section height of the EMM-ARM 'U-shape' beam
$\bar{I}$	Homogenized second area moment of inertia
k	Support stiffness
$k(T)$	Hydration rate constant
$k \cdot T/W_a$	404 MPa at the temperature of test $T = 293°K$
k_1	Avrami rate constant
K_{BT}	BTJASPE experimental stiffness
k_p	Structural parameter
L	Specimen length
l_1 and l_2	Spacing between the effective point where the rods touch the supports and the EMM-ARM concrete beams
L_{hs}	Half of the span of the beam
$\bar{m}$	Uniformly distributed mass along the beam
m_p	Concentrated mass located at the mid span
n	Avrami exponent
p	Volume fraction of the solid phase in a cement paste
p_c	Volume fraction of the solid phase at which the solid starts to become interconnected in a cement paste
R	Universal gas constant (8.314 J/mol·K)
SD	Standard deviation
T	Temperature
t	Time
t_{eq}	Equivalent age

th	Specimen thickness
V	Wave velocity
V_P	Compressional (P) wave velocity
V_S	Shear (S) wave velocity
$\dot{y}$	Peak velocity
$Y(t)$	Amplitude of the vertical displacement
α	Degree of hydration
α_1, α_2, τ_1, τ_2, β_1 and β_2	f_{cm}, E and V_p fitting parameters
Δl	Distance between probes
Δt	Time interval
Δt_w	Wave propagation time
$\dot{\varepsilon}$	Strain rate
$\dot{\varepsilon_0}$	Quasi-static strain rate
ε_a	Longitudinal strain correspondent to the maximum stress
ε_b	Longitudinal strain correspondent to the initial stress
ε_c	Strain of breaking the interatomic bonds
η	Normalized resonance frequency of SMEA tests
H	Constant (4.73 for the first mode of vibration)
θ	Phase angle
λ	Radius of gyration
ν_{dyn}	Dynamic Poisson's ratio
ρ	Density
σ_a	Maximum longitudinal stress
σ_b	Initial longitudinal stress
$\phi(x)$	Deflection mode
ω	Angular resonance frequency

This page intentionally left blank

Chapter 1

Introduction

1.1. Scope and overview

Concrete is one of the most used materials for the construction of infrastructures, such as bridges, buildings and containment structures. It is a multiphase material that undergoes significant changes in the microstructural level during the hydration of cement. The hydration process begins when the cement powder is mixed with water. The hydrated cement paste creates a matrix that fills the space between the aggregated and keeps them together. In fact, the development of concrete properties is closely linked with the properties evolution of the cement paste contained therein. Although hydration is a lengthy process that normally progresses during the entire lifetime of concrete, is in the early ages after mixing that the development is stronger, in correspondence to a period that is normally addressed as the curing time. During this period, the mechanical properties such as modulus of elasticity and compressive strength, increase rapidly.

Understanding the development of these mechanical properties at early ages is of utmost importance to the science of materials, making it possible to obtain forecasts of early age cracking which is a phenomenon that controls half the paradigm load/resistance (Lura, 2003). The importance of making a correct characterization of the evolution of concrete properties from the earliest age is also understandable from an operational point of view of the construction processes of reinforced concrete structures. Indeed, this knowledge can provide the bases to support decision making both in stripping operations or prestressing applications, among others.

To attempt to solve the issues raised in the previous paragraphs, several destructive and non-destructive testing methods have been proposed over the years for characterizing the mechanical properties of concrete from the earliest ages. In this thesis, the author intends to make an approach to non-destructive methods to characterize the evolution of the concrete hardening process, focusing especially attention in the modulus of elasticity and the structural setting.

Given the importance of knowing the evolution of the elastic modulus of concrete since casting, many methods have been developed over the years for such purpose: mechanical methods (Maia *et al.*, 2012b, Boulay *et al.*, 2010, Staquet *et al.*, 2012, Boulay *et al.*, 2013b); equivalent age method (Chanvillard and D'aloia, 1997, D'Aloia and Chanvillard, 2002); wave propagation methods (Voigt, 2005, Reinhardt and Grosse, 2004, Carette and Staquet, 2015); resonance methods (Kim *et al.*, 2009, Wang *et al.*, 2010a); and methods based on dielectric properties (Beek, 2000). However, all the mentioned methods still carry one or more of the following limitations: specimens need to be demoulded for the test to begin, thus hindering the possibility of obtaining results in the very early ages of curing; need for complex test setups and data-processing to obtain estimates of strength/stiffness, which frequently rely in the need for pre-calibrated relationships between the intended mechanical property and the actually measured property (e.g. an electric property); limitations in concern to high sensitivity to local effects caused by aggregates, which are normally felt in acoustic methods (Neville, 1995).

Based on the intent to overcome limitations associated to existing techniques for E-modulus assessment of cement-based materials, the scientific advisor of this thesis has recently proposed a method called EMM-ARM (Elastic Modulus Measurement through Ambient Response

Method) (Azenha, 2009) which allows continuous measurement of the elastic modulus of cement-based materials since casting. The method is based on modal identification of a composite beam under ambient vibration. However, despite the successful results obtained in the first application of EMM-ARM (Azenha, 2009, Azenha *et al.*, 2010a), the method could be considered at a very early stage of development when the work reported in this thesis began. In fact, at such state of development, the method still required a skilled and experienced operator to ensure that the experiment was adequately carried out, and particularly to do it in such conditions that would not negatively affect the quality of the E-modulus estimation. In fact the user needed to be aware of all the techniques used during the whole experimental procedure to be able to perform the experiment correctly, as opposed to several commercial systems that frequently almost allow a 'one-button' operation framework (Brouwers *et al.*, 2011). Furthermore, the EMM-ARM test beams for concrete were still relatively large and consumed relevant quantities of concrete, thus limiting the ease of handling and even disposal after testing. Another challenging issue was related to the high sensitivity of EMM-ARM to potentially disturbing ambient noises that posed significant difficulties to the process of modal identification. Additionally, the EMM-ARM still lacked systematic validation programs through careful metrological analysis and by comparing the results with other methods. In fact, prior to this thesis the method had only been properly validated in its version for concrete testing through comparison with the results obtained by cyclic compression tests. These limitations were hindering a widespread systematic application of EMM-ARM among researchers and practitioners within the field of cement-based materials, particularly that of concrete.

It is also important to remark the great importance of using simulation models to estimate the mechanical properties of cement-based materials, for both structural and materials science points of view. Throughout the history of cement/concrete science, simulation models have played an important role. Since the emergence of the first simple models, there has been a continuing effort to improve and increase in sophistication. However, although there are several models to simulate the cement hydration, few of them extend the field of mechanical properties in order to simulate the setting time and the evolution of the stiffness of cement paste/concrete. Nevertheless, to estimate the mechanical properties of cement-based materials throughout the cement hydration process, some authors have recently suggested different simulation models/strategies (Do, 2013, Sanahuja *et al.*, 2007b, Pichler *et al.*, 2007, Chamrová, 2010, Kamali-Bernard and Bernard, 2009). The most advance methods are based on the

microstructural simulation of the cement paste microstructure evolution along the cement hydration (Bishnoi and Scrivener, 2009, Thomas *et al.*, 2011). Based on the cement paste microstructure the mechanical properties can be estimated through the use of homogenization theories (Sanahuja *et al.*, 2007a) or through finite element modelling (Do, 2013). Despite the encouraging results obtained in the more recent studies the existing simulation strategies still lack experimental validation of the simplifications and assumptions made.

1.1.1. Research questions

From the above described research opportunity, the following research questions can be raised:

- *Is EMM-ARM metrologically robust?*
- *What are the limitations of EMM-ARM?*
- *Can the quality of EMM-ARM results be improved by the application of new geometries/mould materials, as well as different modal identification techniques?*
- *Can EMM-ARM be implemented and applied in the construction industry as a quality control and decision support tool (with specific standards)?*
- *How can EMM-ARM be used to validate/improve the microstructural simulation models of the cement-based materials mechanical properties?*

1.2. Research objectives, methods and Chapter outline

The previous section highlighted a research gap on a recent proposed experimental technique for early age monitoring of cement-based materials stiffness. The main purpose of the research conducted during this thesis is to provide to the technical and scientific communities with a framework based on EMM-ARM that is capable of providing real-time information s about the elastic modulus of cement-based materials along the whole cement hydration process.

The conducted research reported in this thesis is organized in 8 Chapters (including the present introduction). The overall research strategy is summarised in Figure 1.1 and briefly addressed in the next paragraphs.

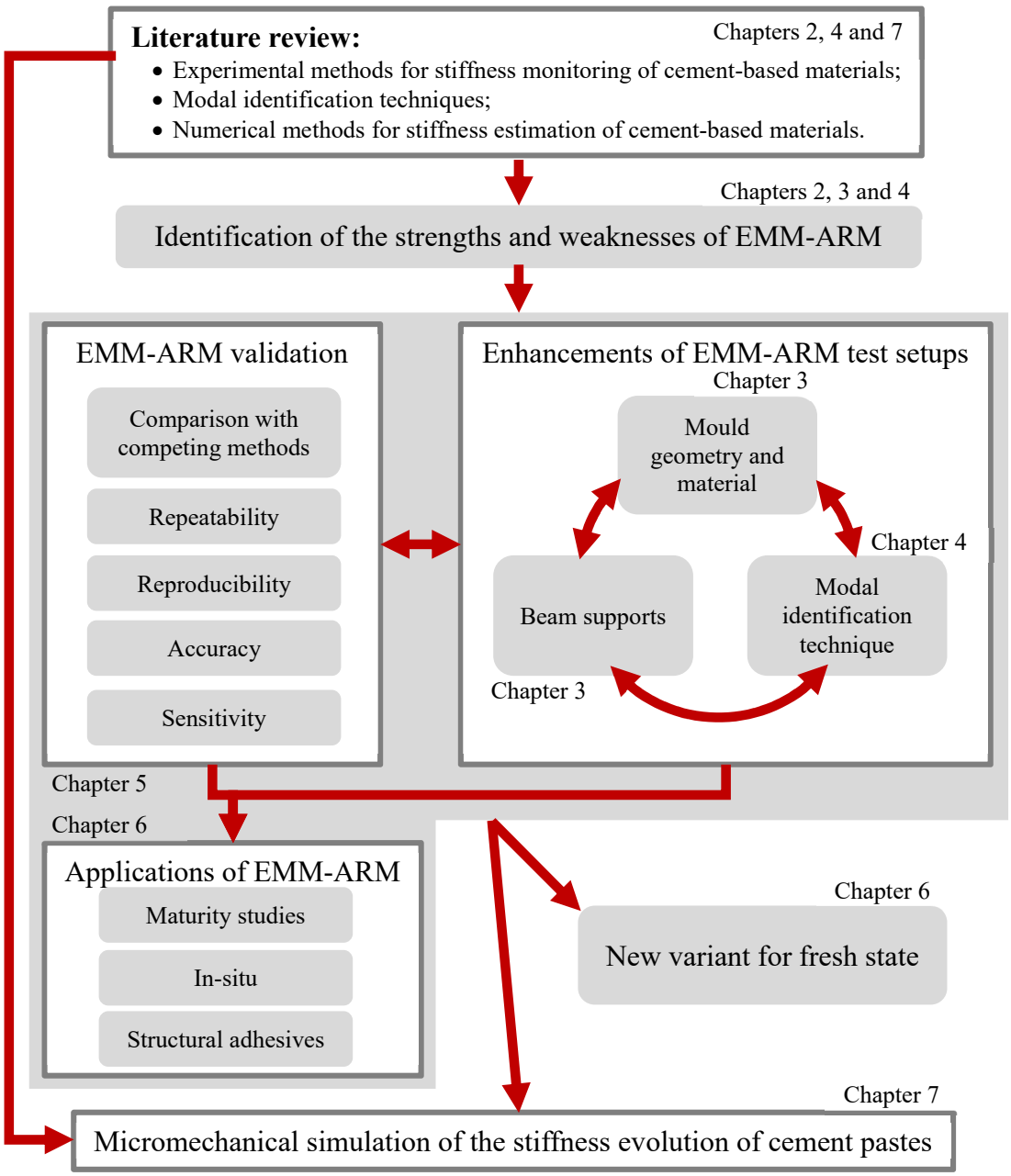

Figure 1.1. Research strategy.

Firstly, an extensive literature review on experimental methods for monitoring the elastic modulus of the cement-based materials is presented in Chapter 2. Along such Chapter, the strengths and weaknesses of the different existing methods are highlighted as well as their application scopes. Still within this Chapter, the state of development of the EMM-ARM prior to this thesis is presented, and some of the limitations of the original implementation are raised. The Chapter ends with a critical review on existing comparative studies regarding the presented experimental methods.

Despite the results obtained in the original EMM-ARM method being quite consistent, the method still has aspects that need to be addressed in order to improve its usability and robustness. Therefore, after identifying the limitations and weaknesses of EMM-ARM, Chapter 3 focuses on a detailed study of enhancements the test setup of EMM-ARM. This study aims to improve the robustness of the method and to reduce the user dependency. In fact, the original testing beam has a very high slenderness, to enable the use of very simple modal identification techniques, and the mould is made of a rather brittle material (acrylic) that poses some problems when a systematic application is considered. One of the most relevant improvements is related to the adaptation of the testing mould, by changing the geometry and supports in regard to the original implementation. However, this study will have impact in the modal identification of the resonance frequency of the beams.

Therefore, the enhancements of EMM-ARM test setup will be accompanied by a simultaneous study of adaptations to the modal analysis technique used to identify the resonance frequency of the composite beams. This parallel study, presented in Chapter 4, aims to improve the accuracy and reduce the user dependency in the process of identification of the first resonance frequency of the tested beam. The Chapter will begin with a short literature review on structural dynamics models, followed by a survey on existing modal identification techniques. After the identification of the most promising techniques to use in the EMM-ARM experiments, the Chapter will follow with a comparison study of the accuracy of different modal identification techniques applied to EMM-ARM tests.

In spite of the improvements introduced and the consistency of the results obtained by EMM-ARM, the method still lacked an extensive validation and an evaluation of its complementarity EMM-ARM with the currently existing techniques for the same purpose. This research has attempted to fill such gap with a systematic study of the application of different methods for mechanical characterization of cementitious materials. Therefore, Chapter 5 is initially dedicated to the comparison of various existing methods that have been described in the literature review, namely: EMM-ARM, cyclic compression, ultrasonic wave transmission and bender-extender elements. Another feature of this Chapter is the description of an inter-laboratory comparison focused specially on comparing the EMM-ARM results with BTJASPE and TSTM methods recently developed at IFSTTAR and ULB, respectively. This inter-compassion of experimental results allowed to further validate the EMM-ARM elastic modulus

estimations and to promote the method among the scientific community as a valid method for continuous E-modulus estimations of cement-based materials. After the inter-comparison of methods for mechanical characterization of cementitious materials, the second part of Chapter 5 deals with the EMM-ARM validation study. This part of the Chapter addresses the accuracy, repeatability, reproducibility and sensitivity issues of EMM-ARM experiments.

After the validation of EMM-ARM, the method was applied in various different scenarios. Chapter 6 starts with the application of EMM-ARM to study the kinetics of elastic modulus evolution of cement-based materials as function of temperature. This study aims to prove the versatility of the method in view of its capacity for evaluating the E-modulus evolution under different temperature histories. The second part this Chapter pertains to an applied investigation about the possibility of using the EMM-ARM as tool to support decision making during the construction of a segmental bridge in Portugal. The proof-of-concept associated to this in-situ application of EMM-ARM can be a relevant asset in the dissemination the method over the industrial community. In addition, due to a construction company request a new variant to EMM-ARM for monitoring concrete viscoelasticity during the fresh state was developed and discussed in the thesis. The Chapter ends with the application of EMM-ARM to the study of structural epoxy adhesives, highlighting the versatility of the principles of the technique for application outside the scope of cement-based materials.

In this work, it was also intended to provide a contribution to existing microstructural simulation models of cement-based materials through the application of a currently existing model together with EMM-ARM data. In fact, the availability of an unprecedented quantitative experimental information from the innovative method EMM-ARM provides advantages in terms of experimental information for the improvement/validation of micromechanical simulation models. Therefore, Chapter 7 starts with a brief literature review on mechanical properties simulations strategies and cement hydration simulation models. From the survey, a simulation strategy based on microstructural cement hydration simulation model μic together with the finite element modelling software AMIE, developed at EPFL (*École polytechnique fédérale de Lausanne*), was chosen to be implemented and validated in comparison with EMM-ARM results. This study was made within a STSM (short term scientific mission) at EPFL in collaboration with Cyrille Dunant.

The main conclusions of this thesis are summarized in Chapter 8, together with some suggestions for possible extensions to the performed research.

Chapter 2

Stiffness monitoring of cement-based materials

2.1. Introduction

The measurement of stiffness in cementitious materials is for several years a big challenge to the scientific and technical communities especially with regard to the early ages monitoring in the last decades (Powers, 1938, Jones, 1949, RILEM, 1975, Boulay and Colson, 1979, Chengju, 1989, Boumiz *et al.*, 1996, Jin and Li, 2001, Bentz, 2008, Boulay *et al.*, 2013b). Several distinct methodologies have been proposed throughout the years that allow more or less direct assessment of stiffness or stiffness-related properties. This Chapter provides a literature review on the various experimental methodologies that enable to estimate the stiffness of cement-based materials. The following methods will be described: (*i*) cyclic loading methods; (*ii*) wave propagation methods; (*iii*) dielectric methods; (*iv*) resonance based methods and (*v*) other methods. The Chapter ends with a critical review of all the methods found in the literature for this purpose, with particular focus on the distinction between fields of application, measured properties and the direct comparisons that have already been made between existing methods.

2.2. Cyclic loading methods

The cyclic loading methods are the most accepted and commonly used to obtain the elastic properties of cement-based materials within the industry and scientific community.

2.2.1. Classical uniaxial cyclic compression method

The basis of this method consists in applying a unidirectional stress to a specimen and recording the corresponding deformations in the same direction. In the variant for concrete, this methodology has already been standardized by various entities, such as: EN 12390-13 (2013), ISO 1920-10 (2010), LNEC E397 (1993), RILEM CPC8 (1975) and ASTM C469 (2006). To obtain the elastic modulus of concrete according to the standard ISO 1920-10 (2010), a series of at least four uniaxial loading/unloading cycles need to be applied to cylindrical concrete specimen with a height/diameter ratio of 2:1, as shown in Figure 2.1. The loading/unloading cycles are performed between an initial stress of 0.5 MPa and one third of the average concrete compressive strength in similar cylinders ($f_{cm}/3$) at the age of testing. The strains induced in the specimen are obtained by measuring the variation of longitudinal distance between two metallic rings attached to the specimen. The measurement is made through at least three displacement sensors, as shown in Figure 2.1.

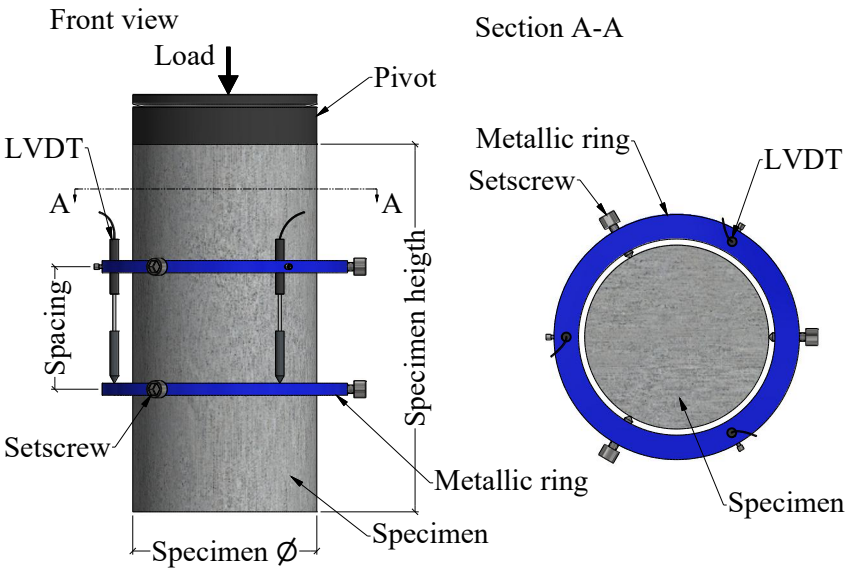

Figure 2.1. Scheme of the uniaxial cycle compression method.

The first cycle of loading/unloading is normally disregarded and the E-modulus is obtained through the analysis of the remaining cycles, by dividing the stress variations by strain variations within each cycle, as shown in equation (2.1):

$$E_c = \frac{\Delta\sigma}{\Delta\varepsilon} = \frac{\sigma_a - \sigma_b}{\varepsilon_a - \varepsilon_b} \tag{2.1}$$

where E_c is the material E-modulus (Pa), σ_a is the maximum stress (Pa), σ_b is the initial stress (Pa), ε_a is the longitudinal strain corresponding to the maximum stress (m/m) and ε_a is the longitudinal strain corresponding to the initial stress (m/m).

Even though this methodology has been originally developed for concrete testing, it has been demonstrated in the works of Chamrová (2010) and Maia *et al.* (2011b) that it can also be applied to other cementitious materials, by using specimens with adapted dimensions. The two cited works have used this methodology applied to cement pastes, reporting good results. However, although widely accepted, according to Bischoff and Perry (1991) this method is sensitive to the loading rate, with different values are obtained for the same material by applying the load in a different loading rates. According to the authors one quasi-static test must have a strain-rate between approximately 10^{-2} and 10^{-7} m/m·s.

2.2.2. Other methods

The classical uniaxial cyclic compression method described in the previous subsection requires the use of a demoulded specimen, thus preventing such tests from being performed at very early ages of curing, i.e., ages at which the materials do not yet have sufficient strength in order to be demoulded and tested without significant damage risks. To overcome this limitation of the classical method, Boulay *et al.* (2010) developed a method called BTJASPE (acronym for *BéTon au Jeune Age, Suivi de la Prise et du module d'Élasticité*), which allows the application of compression cycles without demoulding the specimen (Boulay *et al.*, 2010, Boulay *et al.*, 2013a, Boulay *et al.*, 2013b, Delsaute *et al.*, 2016, Boulay *et al.*, 2012).

A special cylindrical chamber was designed to hold a sample with 100 mm in diameter and 200 mm in length (see Figure 2.2). As the test is conducted with the specimen inside the mould, the interpretation of test results becomes harder than classical testing because of the necessary corrections related to the lateral confinement created by the mould. The physical measurements (load and longitudinal displacement) measured during the test allow the calculation of an experimental stiffness of the sample (named here as K_{BT}). This stiffness represents the combination between the material stiffness and the lateral confinement provided by the mould. The separation of these two parts is based on a relationship between the E-modulus of the material inside the mould and the experimental stiffness K_{BT} obtained through a finite element calculation performed during the design of the device (Boulay *et al.*, 2010):

$$E_c = 1.03\times10^{-8} \cdot K_{BT}^2 + 22.7 \cdot K_{BT} \text{ with } K_{BT} \text{ in N/m} \quad (2.2)$$

Wherer E_c is the E-modulus of the material inside the mould (Pa). Despite this additional complexity, this apparatus and procedure allow obtaining stiffness values right after the structural setting of the material. This chamber also allows to perform the control of the specimen temperature and the measurement of other physical characteristics such as creep and the thermal expansion coefficient.

a) b) c) d)

Figure 2.2. Model of BTJASPE test method: a) Mould; b) +float and 3 LVDT's; c) +upper bearing; d) +lower bearing and fixtures (adapted from Boulay *et al.* (2010)).

Another method that also allows evaluation of the elastic modulus by cyclic mechanical tests is the Temperature Stress Testing Machine (TSTM) (Boulay *et al.*, 2013a, Boulay *et al.*, 2013b, Darquennes *et al.*, 2011, Delsaute *et al.*, 2016, Staquet *et al.*, 2012, Kishi *et al.*, 2008, Schoppel *et al.*, 1994, Klausen *et al.*, 2015). Originally, this method was developed for monitoring the tensile creep of concrete, but also allows the implementation of short loading cycles during the curing process, without the need to demould the sample. It is conceptually quite similar to BTJASPE method, however being different geometry of the mould and the ability to apply both compressive stresses and tensile (Delsaute *et al.*, 2012). A general scheme of a TSTM is shown in Figure 2.3. Typically, these type of machines are composed of a dog-bone shaped specimen fixed on one end by a steel grip and the other extremity is connected to a movable steel grip, controlled by an actuator. Additionally, the machine is capable of controlling the temperature of the specimen through a cryostatic bath connected to the framework of the specimen. During the experiments the distance between two points in the specimen is measured and the applied load is recorder by a load cell placed between the actuator and the moving cross-head. All the data is recorder in a computer that control autonomously the entire experiment.

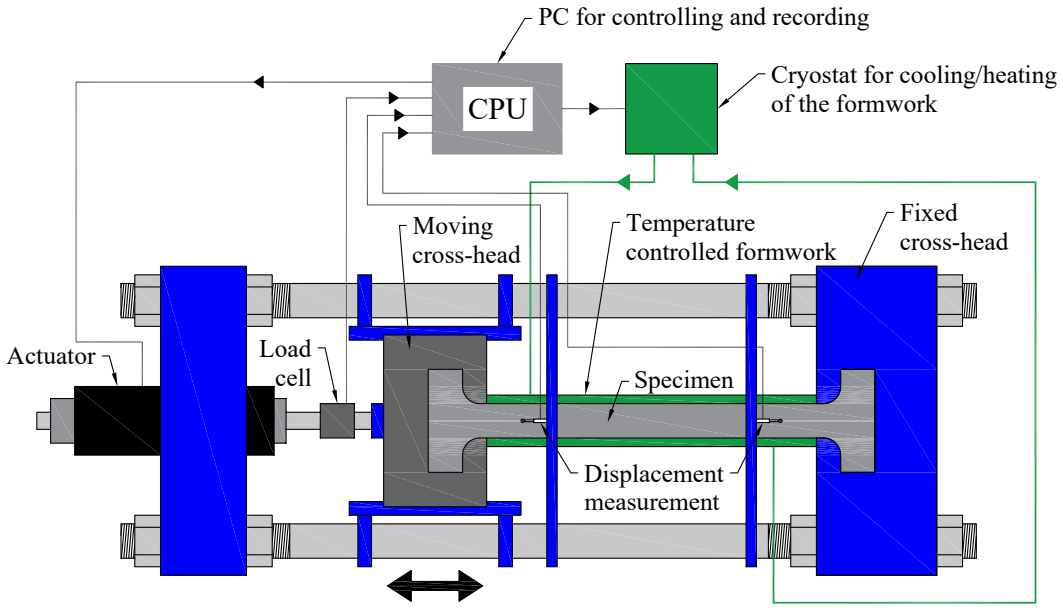

Figure 2.3. General scheme of a TSTM. Adapted from Schoppel *et al.* (1994).

2.3. Wave propagation methods

The methods based on the wave propagation are often called acoustic methods. Two major groups of methods based on this principle are normally applied in the context of stiffness-related measurements: the wave transmission and the wave reflection methods.

2.3.1. Wave transmission methods (WTM)

The idea of using the measurement of the wave propagation velocity to determine the start and end of the setting period in cement-based materials was first described in the 1940s (Jones, 1949). The basic principle on which the wave transmission method is based is that the velocity of a propagating wave through a medium is dependent on its elastic properties and density (Meyers and Chawla, 2008). In the majority of the studies where these experimental techniques were implemented and the velocity variations of longitudinal waves over time were compared with the physicochemical characteristics of cementitious materials, it was found that the changes in the velocity of the propagated waves are related to the formation of connections between the cement particles during cement hydration (Lee *et al.*, 2004). According to Chotard *et al.* (2001) and Smith *et al.* (2002) the velocity of propagated waves is sensitive to solid hydrate formation and the variation of velocity observed over time correspond to the cement hydration and hardening process.

The general scheme of application of this type of experimental methodologies is shown in Figure 2.4. In this method, an ultrasonic wave is generated on one side of the sample, which is transmitted through the material and is ultimately received on the opposite side of the specimen. Both generated and transmitted signals are measured to be able to obtain the propagation time of the waves through the material. These methods can be applied using compressional waves (P-waves) or shear waves (S-waves) (Van Den Abeele *et al.*, 2009).

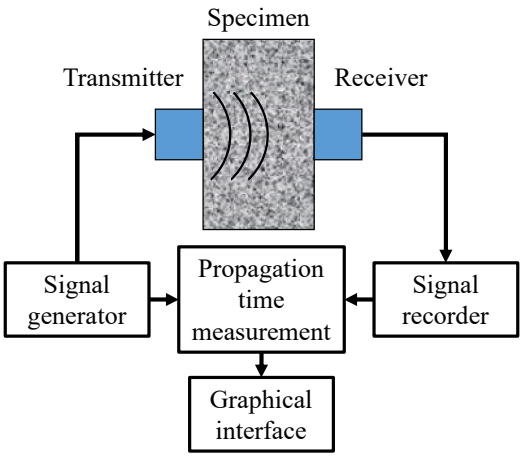

Figure 2.4. Application scheme of ultrasound transmission methodology. Adapted from ASTM (1991).

The accurate determination of the wave propagation time is crucial for the accuracy of this method. However, this determination is a difficult issue to solve, and can be time-consuming and often inaccurate. In the determination of the propagation time there is always an uncertainty about the instant when the ultrasonic wave reaches the receiver probe, as can be seen in Figure 2.5, where an emitted wave and the correspondent received waves during an experiment performed with P-waves are shown (Granja, 2011). Indeed, in Figure 2.5, it is possible to imagine three different estimates for the instant of arrival of the wave (1, 2 and 3), which is a typical pattern on measurements taken in cement-based materials. Thus, depending on subjective interpretations of the operator, the arrival time of the propagated wave may differ, since it is unclear where the received waveform actually begins. In fact, no clear indications were found in the literature regarding which of these three possible points is really the point of arrival of the wave (Lee and Santamarina, 2005).

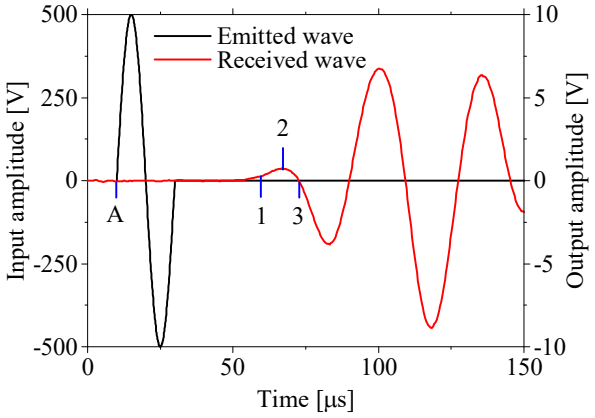

Figure 2.5. Determination of the ultrasonic wave propagation time.

Finally, after the determination of the wave propagation time is possible to obtain the velocity of wave propagation (V), given by:

$$V = \frac{\Delta l}{\Delta t_w} \tag{2.3}$$

Where Δl is the distance between probes and Δt_w is wave propagation time. After obtaining the velocity of the wave, a correlation can be made with the elastic properties of the medium, through the following equations of wave propagation theory, which are applicable for homogeneous and isotropic media (e.g. Meyers and Chawla, 2008):

$$V_P = \sqrt{\frac{(1-\nu_{dyn})\cdot E_{dyn}}{(1+\nu_{dyn})(1-2\cdot\nu_{dyn})\cdot\rho}} \qquad V_S = \sqrt{\frac{E_{dyn}}{(1+\nu_{dyn})\cdot 2\cdot\rho}} \tag{2.4}$$

where V_P is the compressional (P) wave velocity (m/s), V_S the shear (S) wave velocity (m/s), ν_{dyn} the dynamic Poisson's ratio, E_{dyn} the dynamic elastic modulus (Pa) and ρ the density (kg/m^3). However it must be noted here that concrete may not always be considered as a homogeneous and isotropic medium, particularly at early ages (Tuleubekov, 2012). In fact the presence of large aggregates in the mixture introduces heterogeneity that can transmit the waves even before the structural setting, leading to higher velocities than expected.

In addition to these problems, these correlations also add another problem to these methods: obtaining dynamic Poisson's ratio. This property can be obtained by the following equation (Meyers and Chawla, 2008):

$$\nu_{dyn} = \frac{\left(\frac{V_P}{V_S}\right)^2 - 2}{2 \cdot \left(\frac{V_P}{V_S}\right)^2 - 2} \tag{2.5}$$

Therefore, in order to convert the measured ultrasonic wave velocity in to the dynamic E-modulus, both the velocities of compressional waves and the shear waves need to be assessed (Boumiz *et al.*, 1996). This causes an increase in the complexity of these methods, since the sensors typically used only record and/or transmit one type of wave, thus making it necessary to duplicate the entire experimental apparatus.

In wave transmission methods, the ultrasonic signals can be generated in several ways: by an ultrasonic contact probe, a smart aggregate, a bender-extender element (BE) or an impact. These signal generating techniques are discussed in the next sub-sections.

2.3.1.1. Contact probes

In various applications made by several authors with this methodology (Boumiz *et al.*, 1996, Lee *et al.*, 2004, Naik *et al.*, 2004, Reinhardt and Grosse, 2004, Van Den Abeele *et al.*, 2009, Voigt *et al.*, 2005, Voigt *et al.*, 2006, Carette and Staquet, 2015, Boulay *et al.*, 2012, Deniz and Erdoğan, 2015, Larcher *et al.*, 2015), the adopted experimental setup was similar to that shown in Figure 2.6. In this experimental setup one ultrasonic wave transmitter probe is positioned in one side of a sample and the transmitted wave is received on the opposite side by a similar probe. The wave is generated in a function generator and transmitted to the sample by the transmitter, passing directly through the sample to the receiver. Due to the characteristics of the commonly used transmission and receiver devices in experiments with this method usually only P-waves are measured due to the limited efficiency in the shear wave emission.

For application of this method for continuous monitoring of cement pastes hardening from the fresh state, Reinhardt and Grosse (2004) resorted to filling a container with the mixture of cement paste, in which was previously embedded two ultrasonic probes (Figure 2.6). To avoid the possibility of transmission waves through the acrylic mould that supports the probe, it consists of two separate parts that are connected to each other by an insulating material that also acts as a form. Even though this mould has proved effective in cement paste and mortar, its applicability to concrete is quite limited due to the limitations in the sample size.

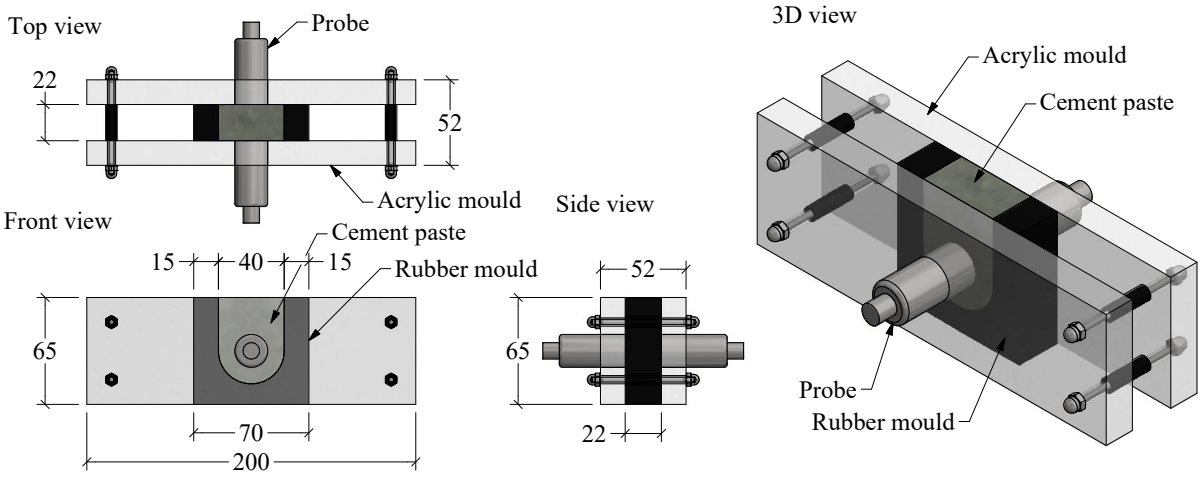

Figure 2.6. Mould used by several authors for cement pastes. Adapted from Reinhardt and Grosse (2004).

It is additionally noted that several authors mention that the air content in mortars and cement pastes can have drastic effects on the reduction of the velocity of longitudinal ultrasonic waves, as the reflection of the waves in the air bubbles causes a severe attenuation (Lee *et al.*, 2004, Boumiz *et al.*, 1996, Sant *et al.*, 2009). Zhu *et al.* (2011a) state that this velocity reduction caused by the air bubbles is especially relevant at very early ages and can limit the ability of this method to identify stiffness variations at instants nearby the setting time. Therefore, this method becomes potentially inadequate (or at least somehow limited) to monitor the mechanical characteristics of a cement paste, mortar or concrete as these materials typically contain air bubbles.

Since the geometrical scale in which these tests with contact probes are usually conducted (small samples, such as cubes, with small distances between probes), this technique is very

sensitive to local effects caused by the aggregates and, therefore, several authors reject their ability to effectively measure the elastic modulus in concrete, which renders the results of the method to be more adequately considered qualitative, rather than quantitative (Azenha, 2009, Abo-Qudais, 2005, Karaiskos *et al.*, 2015). For all these reasons and because a large number of variables affect the relationship between the concrete strength and the velocity of ultrasonic waves, the use of this method to estimate the compressive strength and other mechanical characteristics of concrete is not recommended unless calibration tests have been made beforehand (Naik *et al.*, 2004). However, the validity of the calibration tests may be limited in the case of in-situ applications due to the naturally occurring variations that may occur in the mixture with respect to the mixture previously used to define the correlation between the wave velocity and the mechanical properties.

Despite these limitations, this method was successfully applied in laboratory (Reinhardt and Grosse, 2004, Trtnik and Gams, 2015, Zhang *et al.*, 2015) and in construction sites (Boumiz *et al.*, 1996, Staquet *et al.*, 2009) with very reproducible results. This fact, combined with the knowledge that ultrasound techniques provide an effective means for detecting surface and internal cracks in concrete structures, increases the usefulness of this method (Naik *et al.*, 2004). The procedures for such tests have been standardized by ASTM (ASTM, 1991), CEN (CEN, 2004) and other organizations (RILEM, 1972, BSI, 1997, ISO, 2014), exist for this purpose several commercial equipment available (Proceq, 2014, Controls, 2015, Qualitest, 2015).

2.3.1.2. Smart aggregates (SMAG)

The SMAGs consist of piezoelectric sensors that can be embedded within a concrete element to continuously monitor the evolution of the velocity of P-waves during the curing process. To allow embedment in the concrete the piezoelectric sensor (which is very sensitive) is enclosed by an impermeable coating and incorporated into a small cube or cylinder made of mortar (see Figure 2.7). The first smart aggregates (SMAG) were developed at Houston University by Gu *et al.* (2006).

This experimental technique follows quite similar principles to the ultrasonic wave transmission method with contact probes presented before (Qin and Li, 2008, Dumoulin *et al.*, 2012). Two SMAGs are embedded in concrete at a known distance, one working as a transmitter and the

other as receiver. As the probes are embedded into concrete, the potentially de-coupling problems that are felt when contact probes are used, become eliminated (Song *et al.*, 2008). The SMAGs still allow the sensor to operate at different frequencies, depending on the stiffness of the material in which they are embedded, improving the quality of the transmitted signal.

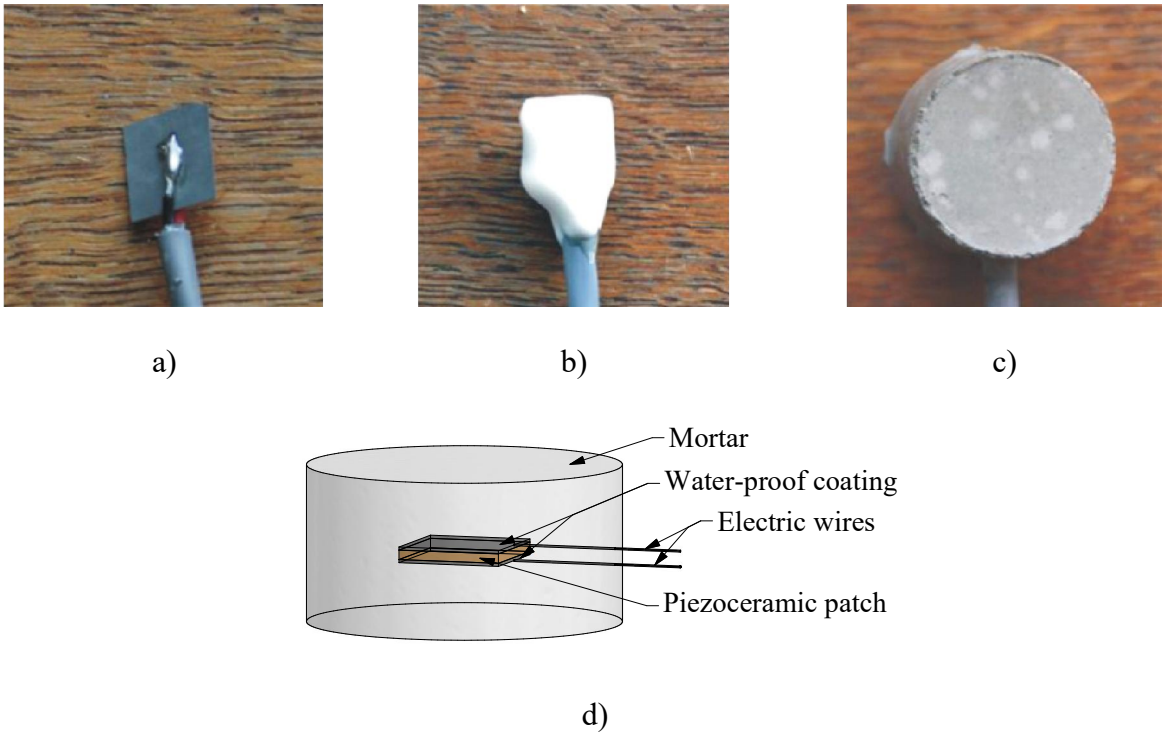

Figure 2.7. Assemble of a SMAG probe: a) Piezoelectric sensor; b) Waterproof coating; c) Final SMAG; d) Scheme of a SMAG. Adapted from Dumoulin *et al.* (2012) and Song *et al.* (2008).

2.3.1.3. Bender-extender elements (BE)

The bender-extender elements (BE) were initially used to measure the shear wave velocity in marine sediments by Shirley and Hampton (1978). A BE is a dual transducer composed of two thin piezoceramic plates, rigidly connected to a metal core sheet with electrodes on its outer surfaces (Figure 2.8). The metal plate serves as a mechanical support, since the piezoceramic plates are extremely fragile. This set is protected by a rigid epoxy resin coating in for electrical isolation and prevention from direct contact with the material and water. The typical thickness of these range between 0.5 and 1.0 mm. The electrical connection of the plates is made with respect to the polarization directions of the two plates in order to ensure a proper flexion

(Ferreira, 2008, Lee and Santamarina, 2005). The controlled excitation of the two piezoelectric elements causes flexion of the BE at a certain frequency, thus generating an ultrasonic wave in the material in which it is embedded. Then the wave travels through the material and when reaches the receiver the wave bends the BE generating an electric signal. Both emitted and received signals are acquired by data acquisition system and the wave velocity is computed.

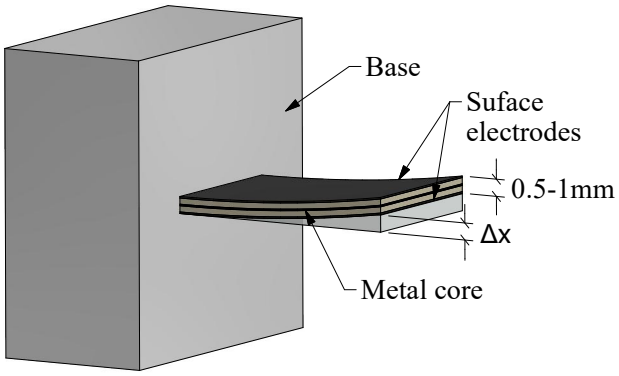

Figure 2.8. Scheme of a BE sensor. Adapted from Ferreira (2009).

The small thickness of the BE probes allows the application of a large displacement and relatively small force generated in low acoustic impedance materials such as soils and sediments (Zhu *et al.*, 2011b). This technique has been widely adopted to evaluate the shear modulus in laboratory soil samples (Thomann and Hryciw, 1991). Applications of BE in soils or stabilized soils with lime or cement are numerous, involving aspects such as: monitoring of stiffness parameters, comparing the dynamic and static stiffness moduli, assessing the anisotropy of the material, etc. (Ferreira, 2008). The bender-extender elements have satisfactory results in the study of soils, which are materials with great heterogeneity and great presence of air voids (Ferreira, 2008), due to the fact that it is possible to adjust the frequency to which these sensors operate within a wide frequency range, to match the optimum resonance frequency of the set probe-material.

Despite these good results, currently there are few studies reporting the application of this method to cementitious materials, only emphasizing the works of Zhu *et al.* (2011b) and Liu *et al.* (2014). In the first application of this method to cementitious materials, made by Zhu *et al.* (2011b), a scheme similar to the Figure 2.9 was used. This pioneer experience intended to monitor two types of waves between the emission source and the two distinct receivers:

compressional waves (P) recorded in receiver 1 and shear waves (S) recorded in receiver 2. According to the conclusions reported in the study the signals from the receiver 2 were similar to the signal receiver 1, i.e, the receiver 2 was also more effective in measuring the S-wave rather than P-waves.

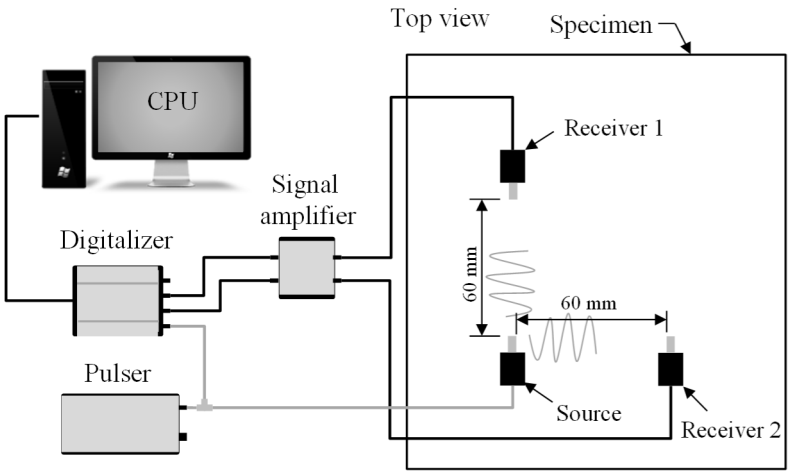

Figure 2.9. Application diagram of the BE method. Adapted from Zhu and Kee (2010).

To eliminate the uncertainty in the estimation of the wave transmission velocity several alternatives are proposed in the literature. According to Fonseca *et al.* (2008) it is possible to use a frequency sweep as an input signal and a spectrum analyser of the input and output signals with significant advantages in the sense that the process becomes fully automatable. In spite of that, this methodology also has problems related to the uncertainty in regard to the estimation of wave propagation velocity. Figure 2.10 shows an example of the results of the method applied to a sand. In this case, the input signal consisted of a frequency sweep between 1 kHz and 50 kHz within a short period of 20 seconds. The first to estimate the wave transmission velocity consists in transforming the two recorded signals (input and output) from the time domain (Figure 2.10a) to the frequency domain. This transformation allows the estimation of the coherence (Figure 2.10c) and the phase angle (θ) between the output and input signals (Figure 2.10b). However the phase angle obtained is limited to the interval [π, -π], thus making it necessary to carry out an operation named *unwrap* (Greening *et al.*, 2003). From the unwrapped phase angle between the two signals, shown in Figure 2.10d, a calculation is made in regard to the slope of a line tangent to the unwrapped phase angle, in a region of frequencies for which the coherence between the signals is close to unity. This is the point where the method also presents some uncertainty, since the choice of points to be used to obtain the slope of the

line depends on the user options. The slope of this line ($d\theta/df$) allows obtaining the transmission time wave (Δt_w) through the material under study by the application of equation (2.5) (Greening and Nash, 2004).

$$\Delta t_w = \frac{1}{2\pi} \cdot \frac{d\theta}{df} \tag{2.6}$$

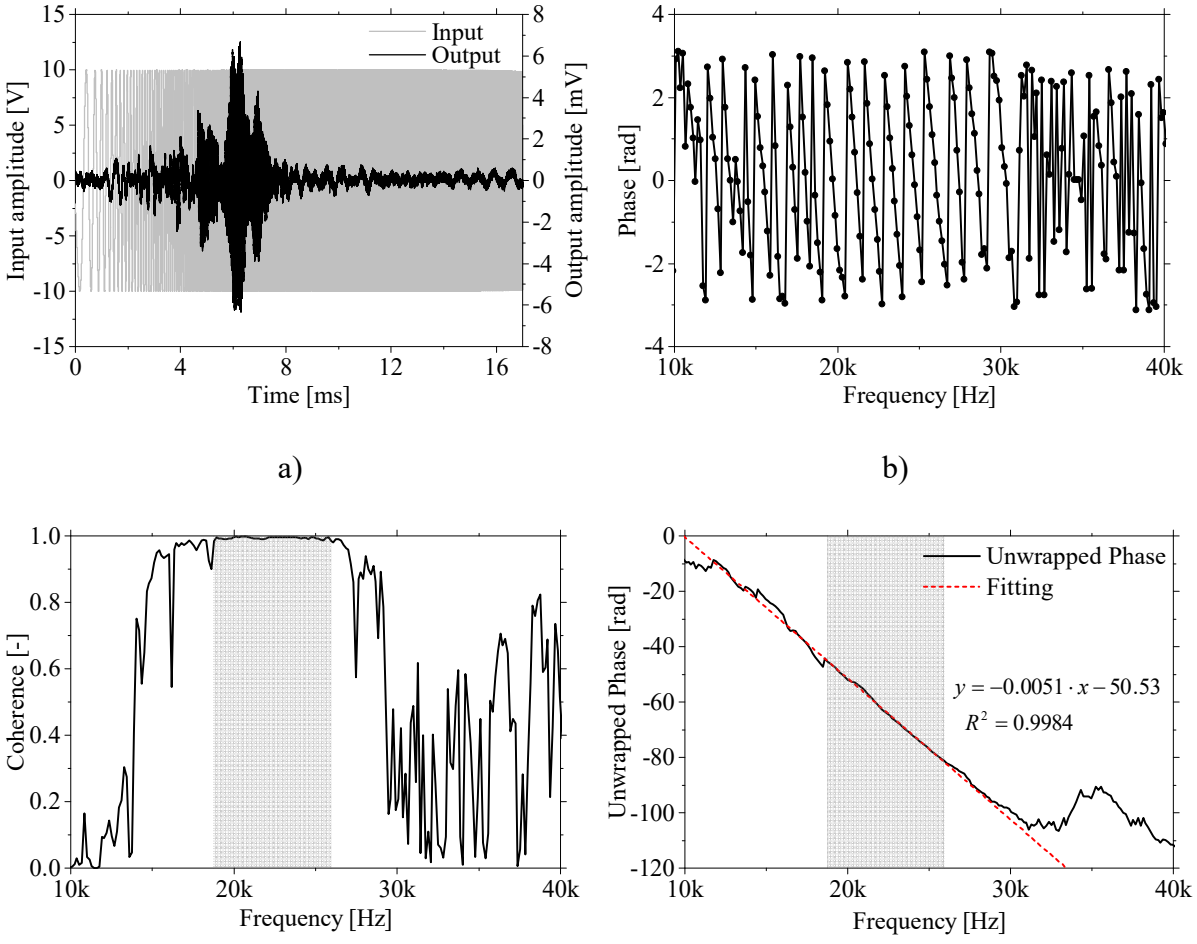

Figure 2.10. Results for a sand.

2.3.1.4. Impact echo

In addition to the methodologies presented for measuring ultrasonic wave velocity, there is a variant where the excitation/wave transmission is performed using an impact on the material's surface. This variant is designated by impact echo method and was already applied successfully

by several authors (Carino, 2004b, Voigt, 2005, Pessik and Carino, 1988, Lee *et al.*, 2004, Jin and Li, 2001, Hassan and Jones, 2012, Lu *et al.*, 2013) and the American Society for Testing and Materials already have a standard for these method (ASTM, 2015b). However, the application of this variant of the method to cementitious materials is not feasible at early ages in which the material does not have stiffness/strength sufficient to sustain the impact without damage.

2.3.2. Wave reflexion methods

The ultrasonic wave reflection method (UWR) is based on the knowledge that a wave propagating an interface between two different mediums is partly transmitted and partly reflected (Reinhardt and Grosse, 2004). The decrease in amplitude of the reflected wave depends on the reflection coefficient, which in turn is a function of the acoustic properties of the materials at the interface. This technique was used to monitor concrete properties was introduced by Ozturk *et al.* (1999) and Rapoport *et al.* (2000).

The operation scheme of this experimental method applied to the study of cement-based materials is shown in Figure 2.11. This method has been successfully implemented by several authors (Voigt *et al.*, 2006, Kim *et al.*, 2009, Popovics and Subramaniam, 2014, Chung *et al.*, 2012, Suraneni *et al.*, 2015, Chung *et al.*, 2013). A plate of a buffer material (usually steel) is placed in contact with fresh cement-based material. Then, a UWR probe is attached to the plate and a S-wave pulse is emitted at the buffer material surface. When the tested material is in the liquid state, the pulse is almost completely reflected in the interface between the buffer-material and the tested material, since S-waves do not propagate in fluids (t_0). Thus, the reflection coefficient is close to one. As cement hydration progresses and begins forming a rigid skeleton, shear waves start being able to propagate through the cementitious material. This causes a portion of the shear wave to be transmitted through cementitious material, resulting in loss during the reflection process (t_1). Consequently, the reflection coefficient starts to decrease. This process evolves until the end of the hardening process (t_2).

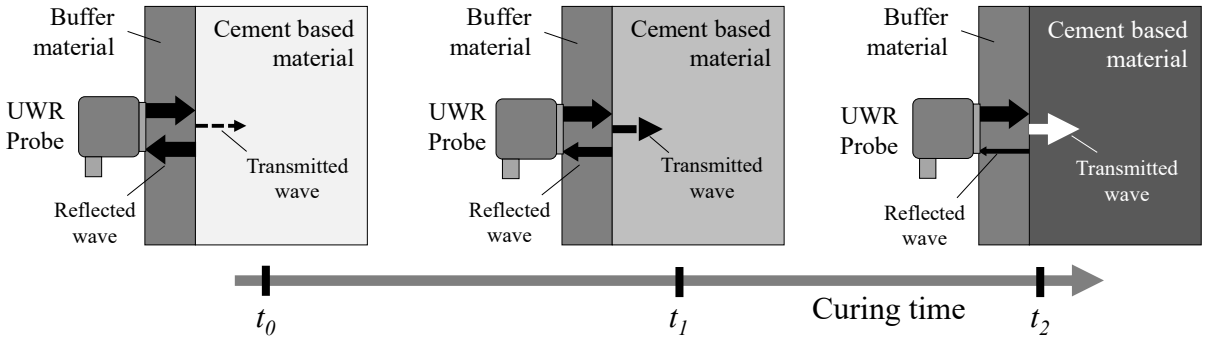

Figure 2.11. Operating scheme of the ultrasonic wave reflection method. Adapted from Voigt *et al.* (2006).

According to Wang *et al.* (2010b) the accuracy of reflection technique depends on the ability to detect changes in characteristics of the reflected ultrasonic wave, which varies with the acoustic impedance[1] of the cementitious material. Immediately after mixing, and the initial stage of hydration, cementitious materials have very low levels of distortion and acoustic impedance modulus. Therefore, UWR measurements sensitive to change of the shear modulus in the first hours of hydration has remained a challenge. Over time, increased shear modulus produces an increase of the acoustic impedance of the material, thus improving the applicability of the method.

The UWR can be very useful especially in construction sites where usually it is only practical to access the concrete surface (Lee *et al.*, 2004, Reinhardt and Grosse, 2004). Although it is fairly easy to apply and just need to the availability of one single surface of the material for testing, this method has some drawbacks. The method consists on the measurement of wave reflection on a surface of concrete, and not on its internal properties which are quite relevant form an engineering point of view. Furthermore, the harvested results actually correspond to the cement paste/mortar in the vicinity of the interface, thus being highly influenced by the presence of large aggregates in the vicinity of the interface. It is therefore arguable the applicability of this method to measure the properties of concrete itself (Voigt, 2005).

[1] Impedance can be characterized as a sound propagating from a medium, with certain specific characteristics, to another with different characteristics. This difference is directly related to the energy that will be reflected in the media interface in question.

2.4. Dielectric methods

The dielectric properties of a material (permittivity and conductivity) determine the response of the material when subjected to an electric field (Beek and Hilhorst, 1999). The permittivity is the electrical polarization of a material, while the electrical conductivity is the amount of electrical current that travels through it. The dielectric properties of concrete can be represented by a parallel combination of a resistance, that corresponds to the electrical conductivity, and a capacitor, which stands for the electrical permittivity (Figure 2.12) (Beek and Hilhorst, 1999, Beek, 2000, Beek *et al.*, 1999).

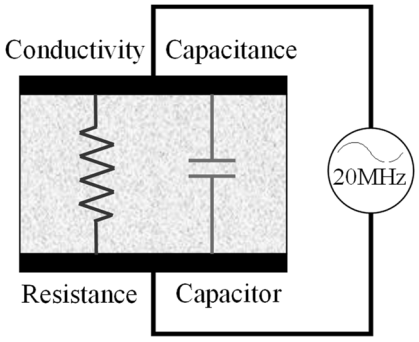

Figure 2.12. Dielectric properties of the concrete represented as a resistor and a capacitor. Adapted from Beek and Hilhorst (1999)

The concept behind the application of this method to concrete is based on the changes in dielectric properties of the different phases present in this material during its early ages. Young concretes have a high quantities of present free water in the pores, which will be consumed during hydration (Beek, 2000, Beek and Hilhorst, 1999). In fact, the dielectric properties of concrete are highly conditioned by ionic water that fills almost all the pores of the cement paste on concrete. The pore water has a high permittivity and a high conductivity, which does not occur with the cement particles, whether or not hydrated (Beek *et al.*, 1999). In this way, changes in dielectric properties can be considered to mostly occur due to change of free water available in the pore network in the cement paste.

A wide variety of applications of electrical methods on cementitious materials are reported, ranging from monitoring changes in pore solution and pore connectivity with time (Christensen *et al.*, 1994) , effects of mineral and chemical admixtures (Christensen *et al.*, 1992), diffusion,

permeability and chloride conductivity (Neithalath *et al.*, 2006), determination of setting time (Xian-yu *et al.*, 2002, Sanish *et al.*, 2013, Wei and Li, 2006) and assessment of mechanical properties (Neithalath *et al.*, 2010). Additionally, there are already available commercial equipments to perform this tests (Brouwers *et al.*, 2011, Gigatec, 2015).

Indeed, this approach has some advantages in the sense that it allows measurements to begin effectively immediately after mixing, it provides continuous measurements, and it does not disturb the samples. However, it has the relevant drawback of requiring the experimental establishment of correlations between the dielectric and mechanical properties for each mix, as to be able to infer mechanical properties based the measurement of dielectric properties.

2.5. Resonance based methods

This subchapter provides a literature review on existing methods for assessing elastic properties of cement-based materials with basis on resonance principles. Existing resonance based methods can be classified in three main categories: (*i*) the classical resonance method; (*ii*) the electromechanical impedance (EMI) method (*iii*) the EMM-ARM method.

2.5.1. Classical resonance method

This method was first developed by Powers (1938) who has determined the resonant frequency a concrete prism (51×51×241 mm) by matching the musical tone created, when hit by a hammer, to the sound created by one of a set of orchestral bells calibrated according to the frequency of the generated sound. The shortcomings of this approach are obvious, such as the subjective nature of the test, and limitation to a discrete and relatively small range of frequencies. However, this method laid the foundation for the later development of more sophisticated approaches.

An important dynamic property of any elastic system is its natural frequency of vibration. As an example, if a vibrating beam with known dimensions is considered, its natural frequency of vibration is mostly related to its geometry, support conditions, density and elastic modulus of the material. Thus, the elastic modulus of a material can be determined from the measurement

of the natural vibration frequency of prismatic beams using existing mathematical relationships between the two parameters, provided that all other parameters are known. These relationships were derived for homogeneous solid media, isotropic and perfectly elastic. They may however be also applied to heterogeneous systems, such as concrete, when the sample sizes are large relative to the size of the heterogeneities. Therefore, according to Malhotra and Sivasundaram (2003) for the longitudinal test configuration shown in Figure 2.13, the elastic modulus of a cementitious material can be obtained by equation (2.6).

$$E_{dyn} = \frac{4 \cdot \pi^2 \cdot L^4 \cdot fr^2 \cdot \rho}{\mathrm{H}^4 \cdot \lambda^2} \tag{2.7}$$

where E_{dyn} is dynamic E-modulus of the tested material's (Pa), ρ is the density (kg/m^3), L is the length of the specimen (m), fr is the resonance frequency of the fist mode of vibration, λ is the radius of gyration of the section around an axis perpendicular to the bending plane ($\lambda = th/12$ for rectangular sections), th is the thickness (m) and H is a constant (4.73 for the first mode of vibration).

This method is already standardized by ASTM (2002). To measure the longitudinal first natural frequency of the sample, the sample is excited with an impact at one end and the accelerations are recorded at the opposite end. According to the ASTM C215 (2002) the test can be performed in several alternative configurations, as shown in Figure 2.13, for the collection of other vibration modes (eg transverse or torsional). However, the most common test setup consists in the configuration for assessment of the longitudinal mode of vibration (Giner *et al.*, 2011, Hassan and Jones, 2012, Zhao *et al.*, 2014, Lee *et al.*, 1997, Kolluru *et al.*, 2000, Wang and Subramaniam, 2011).

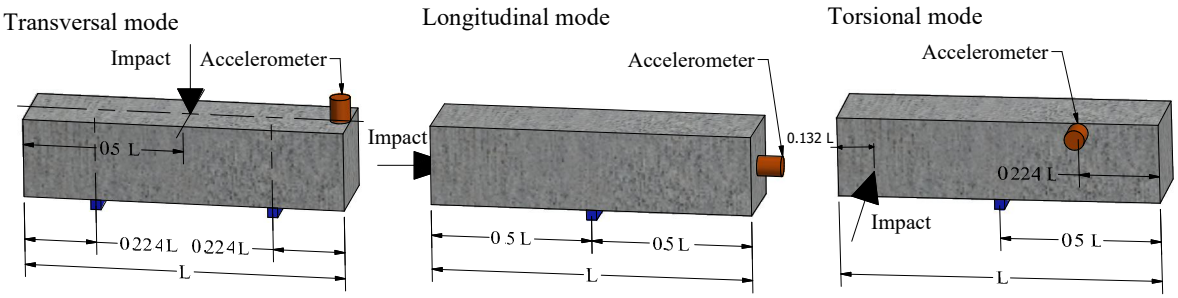

Figure 2.13. Position and direction of the impact (black arrow) and accelerometer for the various vibration configurations of the sample. Adapted from ASTM (2002).

In order to allow free vibration of the sample, the mould needs to be removed prior to the beginning of the test. Due to this fact, and the need to apply an impact on the sample, this method does not allow the continuous measurement from the fresh state. Despite these disadvantages this methodology allows the measurement of global properties of a sample, while the vast majority of the methods only obtain local values of properties (Kim *et al.*, 2009).

2.5.2. Electromechanical impedance (EMI) method

This technique was originally developed by Liang *et al.* (1994) for the assessment of damage in structures. To better understand this method it is necessary to introduce the concept of mechanical impedance. The mechanical impedance of a point on a structure is the relationship between force applied at such point and the resulting velocity in that same point. It is a mechanical property and has a direct relationship with the physical parameters such as elastic modulus and density (Shin *et al.*, 2008, Wang *et al.*, 2010a, Wang and Zhu, 2011). Thus, the concrete mechanical properties can be estimated by measuring the mechanical impedance.

Piezoelectric materials such as PZT (piezoelectric lead zirconate titanate) exhibit the piezoelectric effect, i.e they are able to generate an electric charge in response to an applied mechanical stress (direct effect) and, conversely, a mechanical stress is produced in response to an applied electric field (inverse effect) (Shin *et al.*, 2008, Park *et al.*, 2003). The process used in EMI simultaneously uses both direct and inverse piezoelectric effects to assess the mechanical impedance. When a PZT attached to a sample is triggered by a fixed alternating electric field, a small deformation is produced in the PZT as well as in the sample area where

the PZT is attached. This excitation is then reflected as a mechanical vibration and is transferred back to the PZT which transforms in an electrical response (Park and Inman, 2005). Thus any change in the mechanical properties of the material where the PZT is coupled causes a change in the measured response of PZT.

An electromechanical model describing the process is displayed in Figure 2.14. The PZT is usually connected directly to the surface of the sample under study by a high-strength adhesive to ensure adequate mechanical coupling.

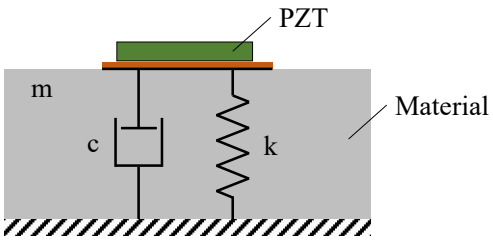

Figure 2.14. Mechanical model of an assembly of a PZT. Adapted from Liang *et al.* (1996).

This method then enables continuous monitoring of the mechanical impedance of cementitious materials properties by measuring the electrical admittance of PZT sensor attached to the tested sample, as illustrated in Figure 2.15. However, to estimate the mechanical properties of the material pre-calibrated correlations between the property and the electrical admittance are needed.

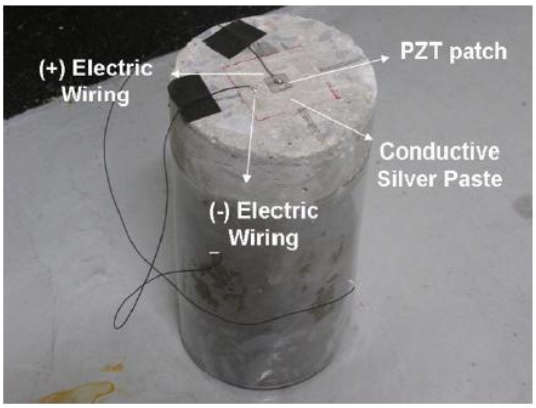

Figure 2.15. Photo of the specimen used in an experiment with PZT made by Shin *et al.* (2008).

Due to the ease implementation of the EMI method and the possibility of making measurements right after the structural setting, this method has been used by numerous different authors (Wang *et al.*, 2014, Lim and Soh, 2014, Song *et al.*, 2013, Guo and Sun, 2012, Yang *et al.*, 2010, Wang *et al.*, 2015, Wang and Zhu, 2011, Shin *et al.*, 2008, Park *et al.*, 2003). Furthermore, the small size of the sensors and the possibility of attaching a sensor directly in the test material makes this method very interesting for in-situ applications. In fact some authors have applied this methodology successfully in construction environment (Yang *et al.*, 2010, Song *et al.*, 2013, Wang *et al.*, 2015).

2.5.3. Ambient vibration method

The EMM-ARM testing technique is a variant of the classical resonance method and has been initially proposed by Azenha *et al.* (2010a). Through a continuous non-parametric modal identification of a composite beam (composed by the mould filled inside with the material to be tested) with known geometry and support conditions, it is possible to obtain the evolution of the flexural resonant frequency of the first mode of vibration. From this evolution, it is then possible to directly and quantitatively estimate the evolution of E-modulus of the tested material, without any kind of ambiguity of user dependency in the data processing. The original setup of the method for concrete testing includes a 2 meters long cylindrical acrylic tube with external/internal diameters of 100/92 mm. The mould is horizontally placed over four concrete cubes through two horizontal threaded rods (with 5 mm in diameter) that laterally trespass the composite beam through its cross-sectional centre as shown schematically in Figure 2.16. This configuration allows the structure to behave as simply supported with a free span of 1.8 meters. To avoid debonding between the mould and the material inside, potentially caused by concrete shrinkage associated to the relatively large length of the beam, 5 vertical connectors are placed at even spacing along the total length of the composite beam.

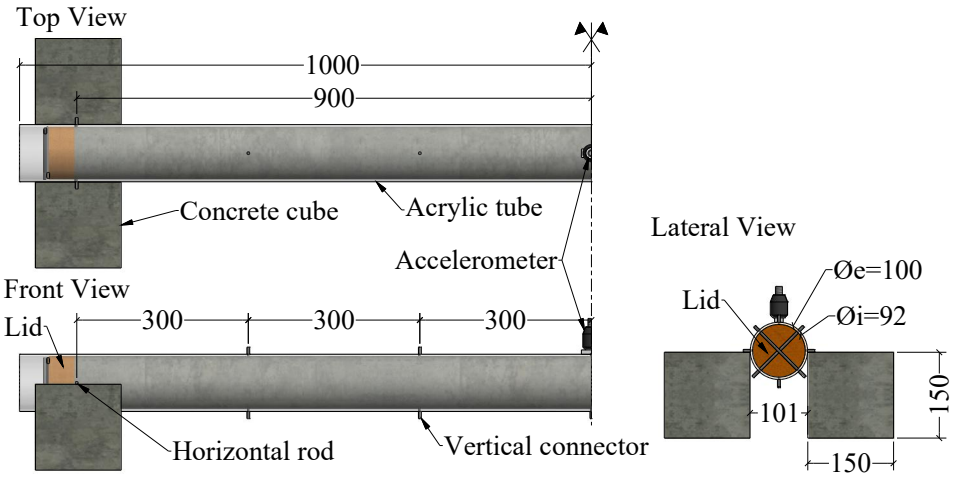

a)

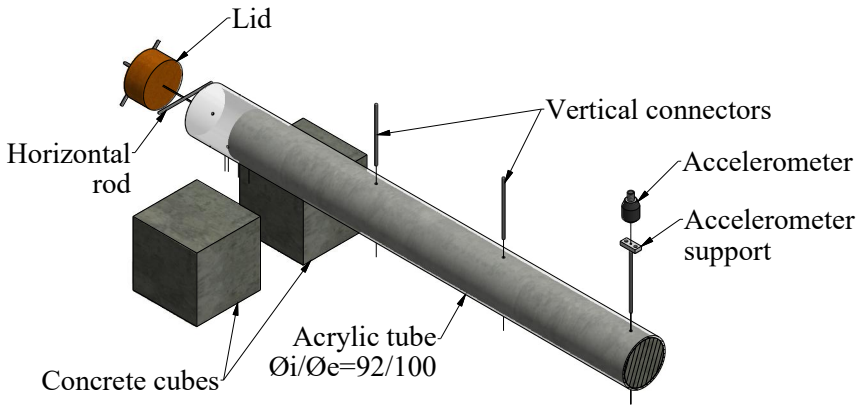

b)

Figure 2.16. EMM-ARM original test apparatus: a) Scheme; b) 3D exploded view [units: mm].

The beam is then excited by the environmental noise (e.g.: wind, people walking, noises from construction site, etc.) which can conceptually be assumed to have an average behaviour of white noise, i.e. a stochastic process with constant spectral intensity in all frequencies. The resulting vibrations are then acquired in the vertical direction through an accelerometer attached at mid span to the composite beam. It should be noted that due to high slenderness of the composite beam, it is highly excitable and the input provided by the environmental noise is enough to induce vibrations that can be detected by the accelerometer, allowing the test to be carried out without the need for explicitly exciting the composite beam. Nonetheless, in order to increase the amplitude of vibration of the beam and facilitate the resonance frequency detection, a fan is placed in the vicinity of the experiment and blowing air towards the beam.

In regard to data processing, Figure 2.17 shows a flowchart with a brief overall description of the framework adopted to estimate the stiffness of the tested concrete along the curing process. First the vibrations at the mid span of the beam are acquired in packages of 900 seconds (Figure 2.17 (a)). From the recorded accelerograms (Figure 2.17(b)), the collected data is converted from the time domain to the frequency domain through the Welch procedure (Welch, 1967), thus resulting in the normalized power spectrum density (NPSD) of each measured package of data (Figure 2.17 (c)) – see further details in Azenha *et al.* (2012b). The NPSDs can then be included side-by-side in a coloured frequency *vs* time surface, with colouring that is proportional to the intensity of the power spectra (Figure 2.17 (d)). Then, the resonance frequencies of the first vibration mode are identified through the highest peak in each amplitude spectrum (Figure 2.17 (e)). In order to obtain a continuous evolution of the resonance frequency of the composite beam, this whole process is repeated every 60 minutes.

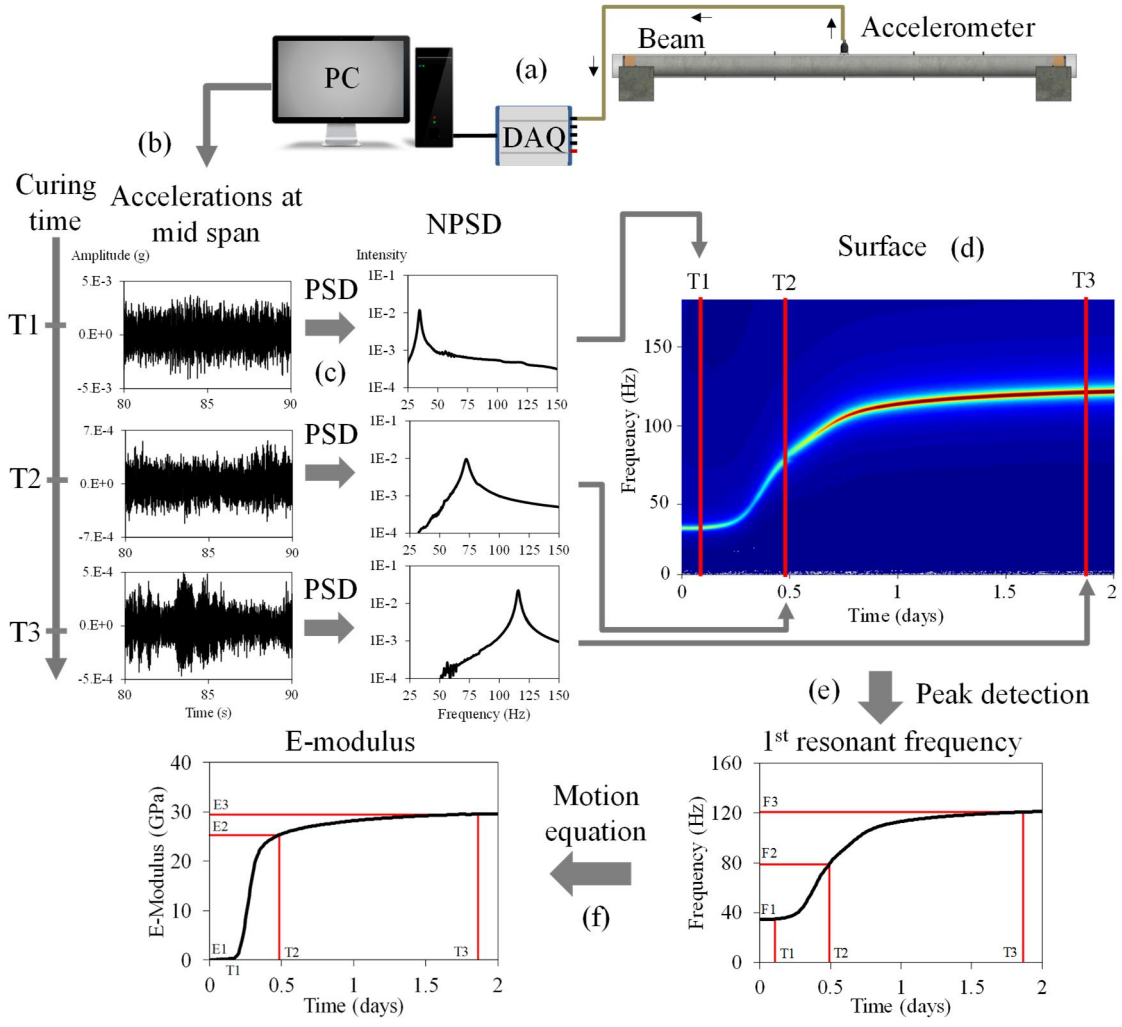

Figure 2.17. Non-parametric data processing and stiffness estimation flow chart.

Finally, the stiffness evolution of the material can be inferred based on the resonance frequency evolution of the composite beam using the motion equation of a simple supported beam with a mass at mid span:

$$\overline{EI}\frac{\partial^4[\phi(x)\cdot Y(t)]}{\partial x^4}+\overline{m}\frac{\partial^2[\phi(x)\cdot Y(t)]}{\partial t^2}=0 \tag{2.8}$$

where *Y(t)* represents the amplitude of the vertical displacement along the acquisition time, *t* (in seconds), expressed in relation to the deflection mode $\phi(x)$, x is the coordinate along the span of the beam (m), $\overline{E}$ and $\overline{I}$ are the homogenized elasticity modulus (Pa) and second area moment of inertia (m^4) of the composite cross-section, respectively and $\overline{m}$ is the uniformly distributed mass along the beam (kg/m). Form the equation (2.7) it is possible to express $\phi(x)$ as a function of A_1, A_2, A_3 and A_4, as shown below:

$$\phi(x)=A_1\cdot\cos(a\cdot x)+A_2\cdot\sin(a\cdot x)+A_3\cdot\cosh(a\cdot x)+A_4\cdot\sinh(a\cdot x) \tag{2.9}$$

With $a=\sqrt[4]{\frac{\omega^2\cdot\overline{m}}{\overline{EI}}}$

where $\omega=2\pi f$ is the first angular resonance frequency of the beam (rad^{-1}) and f is the linear frequency (Hz). At this stage boundary conditions need to be applied to equation (2.8) for the present beam, with a double support in one end and a vertical sliding support on the other, one has:

$$\text{At}\quad x=0:\qquad \overline{EI}\cdot\phi'''(0)=-k\cdot\phi(0)\ ,\qquad \overline{EI}\cdot\phi''(0)=0 \tag{2.10}$$

$$\text{At}\quad x=L:\qquad \overline{EI}\cdot\phi'''(L)=-\omega^2\cdot\phi(L)\cdot m_p\ ,\qquad \phi'(L)=0$$

Where m_p is the concentrated mass located at the mid span (kg), L is half of the span of the beam (m) and k is the vertical stiffness of the supports (N/m). Introducing these boundary conditions in equation (2.8) a set of equations is obtained, whose eigenvalues ω may be computed according to:

$$\frac{1}{2\cdot k}\begin{bmatrix} \overline{EI}\cdot a^3\cdot\omega^2\cdot m_p\cdot\left[1+\cosh(a\cdot L)^2-\sinh(a\cdot L)^2+2\cdot\cos(a\cdot L)\cdot\cosh(a\cdot L)\right] \\ +2\cdot\overline{EI}\cdot a^6\cdot\left[\sin(a\cdot L)\cdot\cosh(a\cdot L)+\cos(a\cdot L)\cdot\sinh(a\cdot L)\right] \\ +4\cdot\overline{EI}\cdot a^3\cdot k\cdot\cos(a\cdot L)\cdot\cosh(a\cdot L) \\ +2\cdot k\cdot\omega^2\cdot m_p\cdot\left[\cos(a\cdot L)\cdot\sinh(a\cdot L)+\cosh(a\cdot L)\cdot\sin(a\cdot L)\right] \end{bmatrix}=0 \qquad (2.11)$$

With the results of modal identification, all variables in equation (2.10) are known except for $\overline{EI}$, thus allowing to mathematically obtain this unknown. Bearing in mind the composite tubular section of known internal/external diameters ($\varnothing_i$, $\varnothing_e$), and the known E-modulus of the mould E_m, it is possible to compute the E-modulus of the tested material (concrete) E_c through equation (2.11):

$$\overline{EI}=E_m\frac{\pi\left(\phi_e^4-\phi_i^4\right)}{64}+E_c\frac{\phi_i^4}{64} \qquad (2.12)$$

By performing the above procedure for all data packages (corresponding to one age of testing at every 60 minutes after casting), the E-modulus *versus* time evolution curve can be obtained (Figure 2.17(f)).

Since the original proposed method for concrete testing (Azenha *et al.*, 2010a), the technique has been adapted to test other materials like cement pastes (Azenha *et al.*, 2012a, Maia *et al.*, 2011a, Maia *et al.*, 2011b, Maia *et al.*, 2012b, Maia *et al.*, 2012c) and stabilized soils (Azenha *et al.*, 2011, Silva, 2010, Silva *et al.*, 2013a, Silva *et al.*, 2014). The variant for cement paste testing differs from the concrete version in two main aspects: (*i*) the cross section of the tube used is greatly reduced and (*ii*) the structural system of the beam now consists of a cantilever. The Figure 2.18 depict the experimental setup for this variant of the method.

Although this variant uses a distinct structural system, the test procedure to obtain the resonance frequency of the composite beam is quite similar to the variant for concrete described before. However after determining the first flexural resonant frequency of the composite beam, equation (2.10) is no longer valid due to the different structural system.

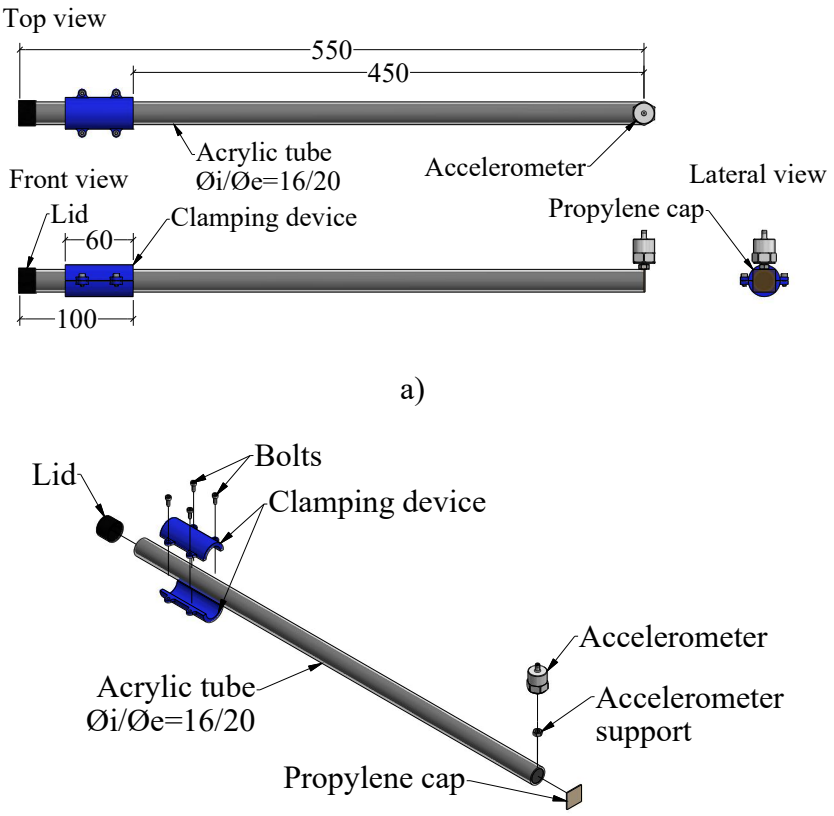

Figure 2.18: Experimental setup for EMM-ARM testing of cement paste: a) Scheme; b) 3D exploded view [units: mm].

Therefore, in order to infer the stiffness of the tested material, it becomes necessary to derive a new formulation of the cantilever structural system (Figure 2.18). In this case the boundary conditions to introduce in equation (2.8), in correspondence to the fixed support in one end, are:

$$\text{At} \quad x=0: \qquad \overline{EI}\cdot\phi''(0)=k_\theta\cdot\phi'(0) \;, \qquad \phi(0)=0 \tag{2.13}$$

$$\text{At} \quad x=L: \qquad \overline{EI}\cdot\phi'''(L)=-\omega^2\cdot\phi(L)\cdot m_p \;, \qquad \phi''(L)=0$$

where k_θ is the rotational stiffness of the support (N/m). Therefore, the relation between the frequency of the first mode of vibration and the stiffness of the composite beam can be computed according to equation (2.13):

$$a^3\left[\cosh(a\cdot L)\cdot\cos(a\cdot L)+1\right]+\frac{\omega^2\cdot m_p}{\overline{E}\overline{I}}\left[\cos(a\cdot L)\cdot\sinh(a\cdot L)-\cosh(a\cdot L)\cdot\sin(a\cdot L)\right]$$
$$+\frac{\overline{E}\overline{I}\cdot a^4}{k_\theta}\left[\cos(a\cdot L)\cdot\sinh(a\cdot L)-\cosh(a\cdot L)\cdot\sin(a\cdot L)\right] \quad (2.14)$$
$$-2\cdot\frac{a\cdot m_p\cdot\omega^2}{k}\cdot\sin(a\cdot L)\cdot\sinh(a\cdot L)=0$$

Then the E-modulus of the material inside the mould can be estimated based on the geometry and stiffness of the acrylic tube through the equation (2.11).

2.6. Other experimental methods

In addition to the experimental methods presented in previous subchapters there are some methods not mentioned because of the fact that they do not provide estimations the stiffness (or stiffness related parameters) of the tested cementitious materials. However, they allow the assessment of mechanical properties along the cement hydration reaction that may be related to the stiffness of cementitious materials. The following methods can be included in such group: general impact method (Gaede, 1941, Voigt, 2005), indentation method (Voigt, 2005), rebound hammer method (Basu and Aydin, 2004, Cano-Barrita *et al.*, 2015, Rojas-Henao *et al.*, 2012), direct pull-out method (Voigt, 2005, Carino, 2004a), break-off method (Voigt, 2005, Naik, 2004), acoustic emission method (Mindess, 2004, Pazdera *et al.*, 2014), rheometer method (Voigt, 2005, De Larrard *et al.*, 1997, Jau and Yang, 2010, Hu and Wang, 2011, Sun *et al.*, 2006).

In addition there are methods based on penetration resistance in near-fresh states which have special interest due their capacity to define the structural setting. There are several methods for the assessment of the evolution of penetration resistance of cementitious materials since the early ages. The Table 2.1 summarizes the various methods found in the literature within this thesis: (*i*) Vicat needle (Bentz *et al.*, 2012, Wang *et al.*, 2013, Liao and Wei, 2014); (*ii*) Penetrometer (Malhotra and Carette, 2004); (*iii*) Proctor needle (Malhotra and Carette, 2004) and (*iv*) Hilti needle (Malhotra and Carette, 2004, Lootens *et al.*, 2009, CEN, 2005b). This table shows the type of measurement of each method, some observations on the nature of the method of execution as well as the applicable standards.

Table 2.1. Penetration resistance methods. Adapted from Lootens et al. (2009).

Test	*Measurement type*	*Observations*	*Standards*
Vicat	Measurement of the penetration depth for an applied load	Discrete but possibility of multiple measurements at various points (can be automated)	ISO 9597 ASTM C191-04 AASHTO T131 EN 196-3
Penetrometer	Measurement of the force required to maintain a given penetration rate	Continuous at the same point (can be automated)	D 3441-79 D 1558-84
Proctor needle	Measurement of the force required for the needle penetrate a depth of 25 mm	Discrete but possibility of multiple measurements at various points (manual)	ASTM C403
Hilti needle	Measuring the depth reached by a shot from a nail	Discrete but possibility of multiple measurements at various points (manual)	EN 14488-2

Despite the ability to monitor the setting of cementitious materials, these methods are destructive and consequently continuous measurements can not be performed in the same point. On the other hand, the accuracy of these methods depends largely on the operator skills and experience (Lee *et al.*, 2004). Consequently, the significance of the results can be considered questionable (Sleiman *et al.*, 2010).

According to Voigt (2005) there are also radioactive methods for monitoring the evolution of the cementitious materials properties. Within this group, the following methods can be listed: gamma radiometry (Mitchell, 2004, Hönig, 1991, Voigt, 2005, Kovler, 2006), x-ray microscopy (Mitchell, 2004, Voigt, 2005, Sun *et al.*, 2014) and x-ray microtomography (Voigt, 2005, Provis *et al.*, 2012, Ma *et al.*, 2015). All these methods have the great disadvantage that they issue quite harmful radiation to health, which is why its practical implementation is extremely limited.

It is also possible to analyse the characteristics of cementitious materials through the analysis of images obtained by scanning optical microscopy (Poon and Groves, 1988, Diamond, 2004, Segre and Joekes, 2000, Igarashi *et al.*, 2004, Li *et al.*, 2004, Bentz and Stutzman, 2006, Sanchez and Sobolev, 2010, Scrivener, 2004, Muller *et al.*, 2013). With this type of analysis, it is possible to evaluate the development of the microstructure of the cement paste and to obtain qualitative information on the state of the hydration reaction (as shown in the example in Figure

2.19). However, these methods are very difficult to implement, requiring very expensive equipment and complex procedures for sample preparation.

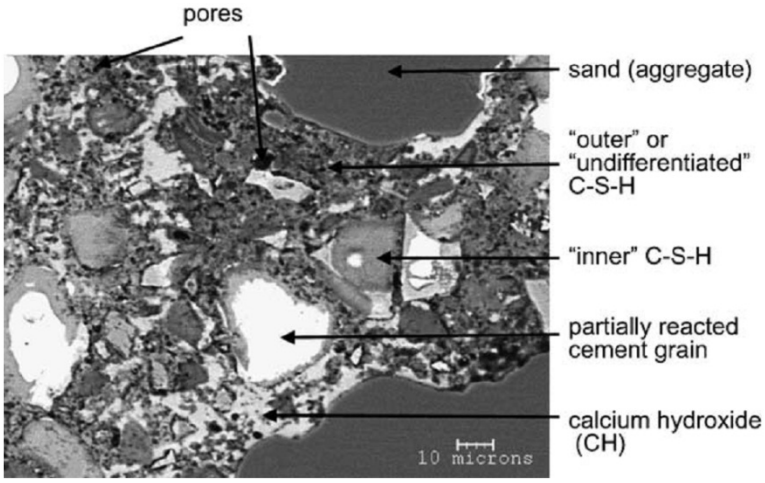

Figure 2.19. Typical mortar image (with 200 days of curing) obtained by an surface electronic microscope (Scrivener, 2004).

2.7. Summary

Table 2.2 provides a summary of all experimental methods to evaluate changes in the stiffness or strength related properties since early ages of cementitious materials found in the literature review conducted in the scope of this thesis. As can be observed in Table 2.2, there is a large variety of experimental methods for such purposes. Nevertheless, the results that can be obtained are not necessarily always quantitative and the measured property is not always of the same nature thus not all can be directly compared. Since the rise of the different experimental techniques that some authors have discussed this issue. It was Powers (1938) who launched the discussion in the scientific community on the applicability of the experimental methods for determining the stiffness of cementitious materials, with the discussion of the results obtained from the classical cyclic compression method and dynamic tests (classical resonance). Later Philleo (1955) added a new technique to the discussion: the ultrasonic wave transmission method (UWT). In these studies, the authors concluded that dynamic tests (classical resonance and UWT) deal only with purely elastic effects, while the static tests deal with nonlinear deformation (such as instant creep), leading the estimations of the dynamic tests to conduct to higher values than those obtained through static tests.

Table 2.2. Summary of the existent experimental methods to evaluate changes in the properties of cementitious materials.

Method	*Excitation*	*Measured response*	*Destructive (Yes/No)*	*Application (Lab/in-situ)*	*Relationship with stiffness*
Cyclic loading	Application of a given compressional / tensile stress at a given stress rate	Strain variation	No	Lab	Direct (E_{stat})
US wave transmission	Application of an ultrasonic excitation	Wave propagation velocity	No	Lab/*in-situ*	Direct (E_{dyn})
BE	Application of an ultrasonic excitation	Wave propagation velocity	No	Lab/*in-situ*	Direct (E_{dyn})
US wave reflection	Reflection of an ultrasonic pulse	Wave reflection loss	No	Lab/*in-situ*	Direct (E_{dyn})
Classic resonance	Application of an external impact	Resonance frequency of the specimen	No	Lab	Direct (E_{stat}/E_{dyn})
PZT	Application of an ultrasonic excitation	Resonance frequency of the sensor	No	Lab	Direct (E_{dyn})
EMM-ARM	Passive	Resonance frequency of the specimen	No	Lab	Direct (E_{stat})
Chemical shrinkage	Passive	Water-embedded volume	No	Lab	Indirect
Autogenous shrinkage	Passive	Exterior volume	No	Lab	Indirect
Conductivity	Application of an electrical voltage	Variation in the conductivity	No	Lab	Indirect
Acoustic emission	Passive	Cavitation of the air bubbles	No	Lab/*in-situ*	Indirect
Vicat / penetrometer	Penetration by a needle/metal rod	Penetration resistance	Yes	Lab/*in-situ*	Indirect
Rheometer	Application of a shear stress at a given rate	Increase in shear stress	Yes	Lab	Indirect
Isothermal calorimeter	Passive	Heat release	No	Lab	Indirect
Semi-adiabatic calorimeter	Passive	Temperature profile	No	Lab	Indirect
Restrained shrinkage	Passive	Change in stress	Yes	Lab	Indirect
Maturity	Passive	Temperature history	No	Lab/*in-situ*	Indirect

Voigt *et al.* (2005) present a set of comparisons between experimental methods to estimate the mechanical properties of cementitious materials, namely: UWT, UWR, penetration resistance, adiabatic calorimetry and temperature. In such paper, the authors concluded that both the transmission and reflection ultrasonic methods have the ability to make quantitative and qualitative monitoring of cement hydration reaction. A good consistency was observed between the results of ultrasonic reflection and penetration resistance indicating that both methods evaluate the same mechanism: the development of rigid connections between the cement particles. However, the results of the ultrasonic transmission methods begin to evolve earlier than those obtained through penetrometer readings, indicating that it is affected by the formation of hydrated products, such as ettringite, which have little influence on the stiffness of the material.

One of the most extensive work for comparison of experimental methods to evaluate changes in the properties of cementitious materials was performed by Sant *et al.* (2009) where several methodologies capable to detect the transition from fluid to solid of cementitious materials were compared during the hydration process: monitoring of chemical shrinkage, autogenous shrinkage, acoustic emission, electrical conductivity, Vicat needle, UWT, rheological measurements, isothermal and semi-adiabatic calorimeter and restrained ring shrinkage test. However, in this paper the authors only intended to verify the ability of each method in detecting the transition from liquid to solid, not being addressed the ability of experimental methods to quantify the stiffness of the material.

Concerning the EMM-ARM methodology, it was only compared to some of the more classical methods such as the classic cyclic compression and calorimetry (Maia *et al.*, 2012b, Maia *et al.*, 2012c, Azenha *et al.*, 2010a). These studies have shown that the method is capable of obtaining similar results to cyclic compression. Yet it still was not made a deep study to examine the phenomenon that leads a method which at first sight could be classified as ‘dynamic’, to be able capable of producing the same results (or very similar) to the ‘static’ results that can be obtained with classical uniaxial cyclic testing.

In the context of the comparison between experimental methods of interest to evaluate the evolution of physical/mechanical properties of cement-based materials since early ages, several

other studies exist, which were not enumerated above. Table 2.4 shows a summary of the literature concerning comparative studies involving two or more techniques.

By analysing Table 2.4, it appears that although there are already several studies in which it was discussed the relevance of the results for each experimental methodology, few are those that focus directly on the issue of getting the elastic modulus.

Table 2.3. Comparisons between different experimental methodologies present in the bibliography.

Authors	*Experimental methods compared*	*Properties under study*
Popovics *et al.* (2008)	Classical cycle compression; Ultrasonic wave transmission; Classical resonance	E-modulus
Philleo (1955)	Classical cycle compression; Ultrasonic wave transmission; Classical resonance	E-modulus
Voigt *et al.* (2005)	Ultrasonic wave transmission; Ultrasonic wave reflexion; Penetration resistance; Adiabatic calorimetry; Temperature evolution	Microstructure evolution
Sant *et al.* (2009)	Chemical and autogenous shrinkage; Acoustic emission; Electric conductivity; Vicat needle; Ultrasonic wave transmission; Rheometer; Isothermal calorimetry; Semi-adiabatic calorimetry; Restrained shrinkage	Setting
Maia *et al.* (2012b), Maia *et al.* (2012c), Azenha *et al.* (2010a)	EMM-ARM; Classical cycle compression; Calorimetry; Chemical shrinkage	Microstructure evolution
Boumiz *et al.* (1996)	Ultrasonic wave transmission; Electric conductivity; Isothermal calorimetry; Compressive strength	E-modulus
Kamada *et al.* (2005)	Ultrasonic wave transmission; Rheometer; Penetration resistance	Physical and chemical and properties
Sun *et al.* (2006)	Rheometer; Ultrasonic wave reflexion	Viscoelastic properties
Voigt *et al.* (2006)	Ultrasonic wave reflexion; Maturity	Compressive strength
Amziane (2006)	Measurements of total and hydraulic pressures; Vicat needle.	Setting
Malhotra and Carette (2004)	Penetration resistance; Esclerometer	Compressive strength

2.7.1. Applicability range

In addition to the comparison of results, it is also important to define the applicability range in terms of curing stage of the cementitious materials of each experimental method. Figure 2.20 shows a qualitative representation of the relevant methodologies to characterize the evolution of the properties of cementitious materials, at several stages of hydration, including the evolution from the solid suspension to the hardened solid.

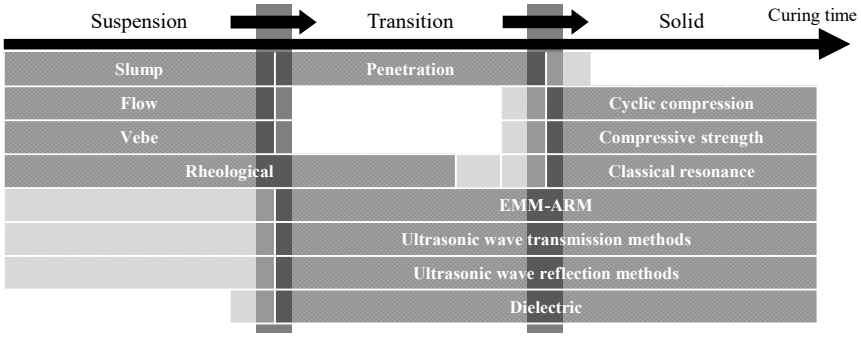

Figure 2.20. Range of application of the experimental methods to evaluate changes in the properties of cementitious materials (partly based on the work of Kamada et al. (2005))

Immediately after mixing, concrete behaves like a fluid with suspended particles. Hence, at this stage it is only feasible to apply methods suited to measure fluid properties, such as the slump, flow and Vebe tests. After some reactions between cement and free water, which create hydrated compounds, there is an increase in viscosity of the fluid. In this period, rheological methods can be applied, making it possible to determine the viscoelastic properties of the material. After some time, the material enters a period of transition between the liquid and solid state, beginning to develop some stiffness, although residual. It becomes thus possible to use methods capable of determining the stiffness of the material that do not require the test specimen to be removed from the mould, such as: EMM-ARM, UWT, UWR and dielectric properties. It is also possible at this stage to determine the beginning and end of setting of the material through methods based on penetration resistance. With the increased stiffness of the material, it begins to behave as a solid. The rheological and methods based on penetration resistance are no longer be able to study the material in this phase and is, however, possible to use the traditional methods for the determination of the mechanical characteristics of the

concrete: the method of the cyclic compression of the classic resonance and compressive strength.

2.7.2. Stress/strain rate effect on mechanical properties estimation

It is well known that strength and stiffness of cementitious materials depends on the rate of loading (Shkolnik, 2008, Bischoff and Perry, 1991, Popovics *et al.*, 2008, Fischer *et al.*, 2014, Pichler *et al.*, 2014a). As the stress or strain rate increases the values of strength or stiffness increases as well. This phenomenon is due to the reduction of the test duration and that provides less time for non-linear creep-related mechanisms to reduce the initial strength/stiffness of the material. Thus several authors separate the properties in quasi-static or dynamic depending on the test method used. However, the definitions of quasi-static and dynamic modulus is dubious. For concrete cylinders in uniaxial unconfined compression, ISO 1920-10 (2010) recommends a quasi-static loading rate of 0.20 to 0.60 MPa/second. For typical concretes the modulus of elasticity is 30 GPa, hence for the linear part of the stress-strain curve, this translates into a test strain rate between 6.7×10^{-6} and 2×10^{-5} s^{-1}. This is in agreement with the MC2010 (CEB-FIP, 2010) quasi-static strain rate of 3×10^{-5} s^{-1} for compression. Despite the agreement about the strain rate for quasi-static testing of concrete, the range for dynamic stress or strain rate is not so well defined. Bischoff and Perry (1991) define in its work three different ranges of dynamic strain rates: earthquake between 10^{-3} and 10^{-2} s^{-1}, hard impact between 10^{0} and 20 s^{-1} and blast between 10^{2} and 10^{3} s^{-1}. However more recent research works (Pichler *et al.*, 2014b, Fischer *et al.*, 2014) found that only above a stain rate of 10^{0} s^{-1} the cement-based materials strength start to increase.

Several authors have suggested relationships between the dynamic and quasi-static modulus (E_{dyn} and E_{stat}, respectively) as can be seen in Table 2.3.

Table 2.4. Relations between dynamic modulus E_{dyn} (GPa) and static modulus E_{stat} (GPa).

Author	*Model*
Neville (1995)	$E_{stat} = 0.83 \cdot E_{dyn}$
Swamy and Bandyopadhyay (1975)	$E_{stat} = 1.25 \cdot E_{dyn} - 19$
Yuan *et al.* (2004)	$E_{stat} = 1.033 \cdot E_{dyn} - 7.245$

However, these expressions are purely empirical and do not take into account the stress/strain rate of the dynamic test. According to MC2010 (CEB-FIP, 2010) the effect of high strain rate on the E-modulus in compression can be estimated from equation (2.15). A similar correlation (equation (2.16)) was also suggested by Shkolnik (2008) based on experimental data fitting.

$$\frac{E}{E_0} = \left(\frac{\dot{\varepsilon}}{\dot{\varepsilon}_0}\right)^{0.026} \tag{2.15}$$

$$\frac{E}{E_0} = 1 + \left(\frac{2 \cdot k \cdot T}{W_a \cdot E_0}\right) \cdot \left(\frac{\dot{\varepsilon}}{\dot{\varepsilon}_0}\right)^{0.02} \cdot \ln\left(\frac{\dot{\varepsilon}}{\dot{\varepsilon}_0}\right) \tag{2.16}$$

with $k \cdot T / W_a = 404$ MPa at the temperature of test $T = 293$°K and where E is the E-modulus obtained at a strain rate $\dot{\varepsilon}$, E_0 and $\dot{\varepsilon}_0$ are the quasi-static E-modulus and strain rate (defined here as 3×10^{-5} s^{-1}), respectively. The effect of the strain rate on the E-modulus obtained from both expression is shown in Figure 2.21. As can be seen, the values obtained from the two expressions are in good agreement between each other and are in good agreement with the results found in the literature (Wu *et al.*, 2012, Dejian and Xilin, 2008).

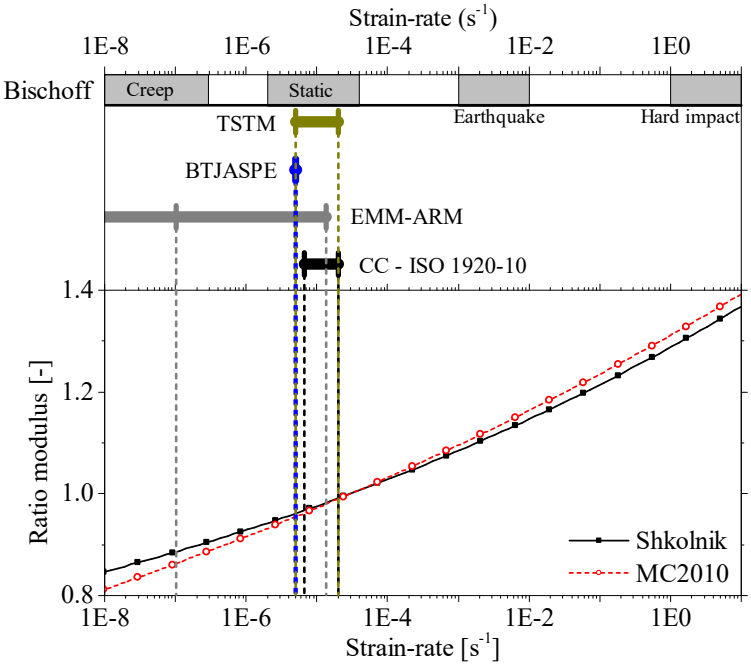

Figure 2.21. Strain rate influence on concrete E-modulus.

The strain rate ranges of the quasi-static tests presented before are presented in the top part of Figure 2.21. Additionally, the strain rate of the EMM-ARM test to the for the most requested fibre in the mid-span cross-section is also shown in the figure. The strain rate of the EMM-ARM test was computed from the peak velocity ($\dot{y}$) obtained by integration of an accelerogram from an experiment with a concrete with 35 GPa. The strain rate (ε) was computed through the equation (2.17) (Sun and Wu, 2009).

$$\dot{\varepsilon} = \dot{y} \cdot \frac{\pi^2}{L^2} \cdot h \tag{2.17}$$

where L is span of the beam and h is distance between the neutral axis and the point of interest in the cross-section (defined here as half of the cross section height).

As can be observed in Figure 2.21 all the strain rate ranges of the quasi-static methods lie within the static range defined previously. Furthermore, the EMM-ARM maximum strain rate is also within the quasi-static range. In fact, from the obtained results the strain rate obtained for the EMM-ARM tests seems to be lower than the cyclic compression tests. However, one shown note that the strain rate computation might have a poor accuracy due to the indirect measure of the beam's peak velocity. Nevertheless, one should not expect any differences in the E-modulus estimation between the EMM-ARM and the quasi-static methods due to the strain rate effect since all these methods lie within the static range. Lastly, the identification of the stress/strain rate of the ultrasonic wave transmission methods is a hard task due to the low level of disturbance of the material. Still according to Tatsuoka (2011) the strain rate of an ultrasonic wave transmission method is in a range between 10^2 and 10^4 s^{-1}. Therefore, due to the much higher strain rate of the ultrasonic wave transmission methods when compared to the other methods one obtain higher E-modulus estimations that can be classified as dynamic E-modulus.

2.7.1. Stress level effect on E-modulus estimation

Another effect on E-modulus estimation that needs to be discussed is related with the stress level used in each experimental method. It is well known that the stress-strain relationship is in fact non-linear, and can be described by a quadratic equation such as equation (2.18), where *b* is the non-linear parameter (Shkolnik, 2008, Delsaute *et al.*, 2016). This expression is not based on any mechanical concept but it is the result of a mathematical fitting on basis of the experimental results. As it was shown in the work of Shkolnik (2008), the non-linear parameter *b* in the stress-strain relationship is dependent on the concrete mix design and the degree of hydration. As concrete hardens and the E-modulus increases, the slope of this stress-strain relationship decreases.

$$\sigma = E_0 \cdot \varepsilon - b \cdot \varepsilon^2 \tag{2.18}$$

where b = $E_0/2 \cdot \varepsilon_c$ and ε_c is the strain of breaking the interatomic bonds.

The nonlinearity of the stress-strain curve can have an important rule since difference of ~9% between the linear behaviour and the nonlinear one are expected to happen at 1/3 of the ultimate compressive strength. However, contrary to the statements of Shkolnik (2008) and despite the common agreement in the scientific community regarding the fact that the static E-modulus is smaller than that obtained by dynamic methods, Popovics *et al.* (2008) state that there is no evidence of non-linear behaviour in the stress-strain curves of the cyclic compression tests.

Regarding the experimental methods presented before, the stress level used is indeed very different between each other. In the first group, the cyclic loading methods, the stress level is usually 1/3 of the ultimate compressive strength of the material at the age of testing. This recommendation is mainly due to the lack of accuracy of the longitudinal strain measurement of the specimens at low levels of applied stress. Therefore, in the remaining methods, since the strain measurement accuracy is not an issue, the stress levels used are much lower (almost negligible). Despite this different stress levels used as stated by Popovics *et al.* (2008) no differences should be observed from this fact. However, one should remark that if one experiment is performed at a stress level higher than 1/3 of the ultimate compressive strength nonlinear effects might be observed.

This page intentionally left blank

Chapter 3

Enhancements of EMM-ARM test setup

3.1. Introduction

Despite the successful results obtained through the studies involving EMM-ARM before the work of this dissertation, the method could still be considered to be at an early development in view of a potentially generalized application in both research and industry fields. In fact, at the current state of development, the method still requires the operator to be somewhat experienced to ensure the capacity to carry out the experiment. There are indeed several special cares (normally resulting from experience) that need to be taken to ensure that the experiment occurs in conditions that do not negatively affect the quality of E-modulus estimation. In fact the user needs to be aware of all the techniques used during the whole experimental procedure to be able to perform the experiment correctly, as opposed to several commercial systems that frequently almost allow a 'one-button' operation framework (Brouwers *et al.*, 2011, Proceq, 2014, Grant, 2012). Furthermore, due to the sizes, materials and/or geometry of the EMM-ARM beams, there are still some limitations for a simple application of the method. These limitations are still

currently hindering a widespread systematic application of EMM-ARM among concrete researchers and practitioners.

This Chapter presents a comprehensive study of several improvements to EMM-ARM, which aimed to mitigate the problems and limitations of the method at the state of development shown in Chapter 2 (i.e. before the research work reported in this thesis). The improvements to EMM-ARM are initially reported for the version of this method that allows testing concrete testing, and afterwards for cement paste testing. It should be noted that part of the content of this Chapter has already been published in (Azenha *et al.*, 2012b, Granja and Azenha, 2015) and submitted to (Granja and Azenha, 2016).

3.2. Concrete testing

The main limitations that the methodology presents are related to the mould (acrylic tube – Figure 2.16) used in the tests, which tends to pose some problems when a systematic application is considered: (*i*) due to the 2.0 m length, the handling and casting operations are relatively complex to carry out; (*ii*) the mould material (acrylic) in combination with the need for connectors placed along the beam disable the access of a vibrating needle to the inside of the mould; (*iii*) acrylic is a quite brittle material that tends to shatter under direct contact with the vibrator needle, thus demanding specific protective procedures during casting, such as the interposition of a cloth between the vibrator needle and the mould, as to avoid damages; (*iv*) the accuracy of E-modulus predictions tends to be influenced by the vertical stiffness of the supports of the beam that need to be meticulously setup and verified by the test operator.

The following subsections will present several proposed improvements to EMM-ARM, together with a parallel experimental study for validation purposes. The description and validation of improvements is started with adaptations to the geometry/material of the testing mould, followed by the development of a new support system. In the end a new reusable mould is suggested. All the experiments reported in this sub-section, comprise measurement of accelerations at mid span of the beams, acquired through an accelerometer PCB 393B12 (sensitivity: 10 V/g; range: ±0.5 g), which was in turn connected to a dynamic acquisition system NI 9234 with 24 bit resolution. The accelerations were recorded at an acquisition frequency of 500 Hz in packages of 300 seconds each 10 minutes. To validate EMM-ARM, the

classical approach of testing E-modulus in cylinders under cyclic compressive loading (here termed as CC) was also taken for all the tested concretes, following the recommendations LNEC E397 (1993).

3.2.1. Mould geometry and material

3.2.1.1. First attempt

As stated the original implementation of EMM-ARM described above carries several drawbacks. Therefore, it was decided to explore the possibilities and pitfalls of using an alternative mould which could be re-used, while allowing easy access of a vibrating needle to the entire specimen. The basic conception of the mould for the new test setup followed the same principles as those already adopted for the acrylic tube and presented in the work of Azenha *et al.* (2010a):

1. The resonant frequency of the composite beam should preferably range from 10 Hz (with concrete in fresh state) to less than 50 Hz at the hardened state, as to avoid the introduction of electricity noise in the acquired signals at such stage. This demand causes the beam to be relatively slender, which carries the interesting feature of being easily excitable by ambient vibrations, thus facilitating the use of output-only modal identification techniques.
2. The centre of gravity of the mould must coincide with the centre of gravity of the tested concrete to simplify the analysis procedures.

It was also decided to increase the minimum cross-sectional dimension of the specimen to 150 mm in order to be able to test the same types of concretes that are used in the traditional cylinders (150 mm diameter) and cubes (150 mm edges) (CEN, 2000), in terms of maximum admissible aggregate size. In order to simplify the casting operations, it was decided to use a square section for the tested concrete, with the mould being open at the top, as can be seen in Figure 3.1. This ‘U-shaped’ section has the advantage of allowing concrete to be cast from the top of the beam, with the mould already set into its final testing position. It further allows the easy access of the vibrating needle to all parts of concrete, and ensures that the cross-sectional

centres of gravity of the mould and concrete coincide. Additionally, to eliminate the risk of damage the mould during casting this new mould was manufactured in steel.

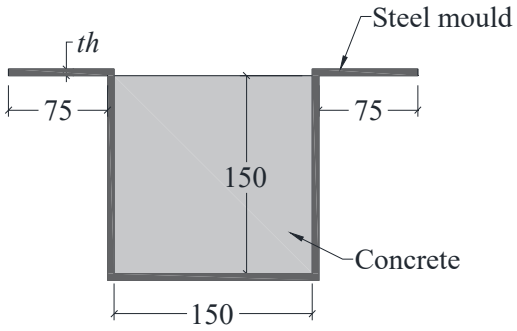

Figure 3.1. 'U-shaped' section adopted [units: mm].

A parametric study using equations (2.11) and (2.12) was performed in order to define the thickness (*th*) of the mould and the span of the beam in order to meet the requirements set out above. Thus, two scenarios were considered: one for the beginning of the curing period of concrete when the stiffness of the material was considered null, and the second one for a hardened concrete with $E = 30$ GPa. This study also considered that concrete has a density of 2400 kg/m^3 and the steel of the mould has $E = 210$ GPa and $\rho = 7800$ kg/m^3.

The variation of the first resonance frequency with the thickness of the mould and with the span of the beam is shown in Figure 3.2 for the two different scenarios under study. In this figure, it is possible to observe that the decrease of the span of the beam span causes the first resonance frequency of the beam to increase exponentially. On the other hand, increasing the thickness of the mould increases the resonance frequency of the beam. This effect is more pronounced on the scenario when the concrete is in the fresh state and has zero stiffness. Therefore, the reduction of the thickness of the mould increases the resolution of the method, since the frequency variation along the stages curing is increased. Based on these results, it was decided to adopt a 1 mm thick mould. In order to limit the maximum frequency of the beam below 50 Hz when the concrete is hardened ($E = 30$GPa) it was decided to use a 2.4 m span beam. Thus the maximum expected frequency will be around 46.9 Hz and the frequency evolution along the concrete curing should be around 22.3 Hz.

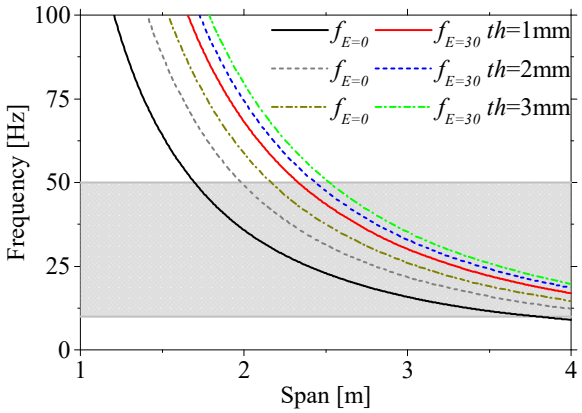

Figure 3.2. Dependency of the first resonance frequency of the new 'U-shaped' beam with the mould thickness and span.

The developed mould was based on 1 mm thick steel alloy plates, which were bent to meet the geometry shown in Figure 3.3. The mould has a total length of 2.6 m and a 'U-shaped' cross section that assures inner cross-sectional dimensions for the specimen of 150×150 mm^2. Extremity lids are placed at 100 mm distance from the extremities of the mould, causing the length of the concrete specimen to be of 2.4 m, which is coincident with the free span of the simply supported beam assured by the bottom supports.

These bottom supports solely sustain the bottom part of the mould along its 150 mm width. Aluminium stiffeners are placed on top of the beam in order to assure that the geometry of the mould remains unchanged after casting (i.e. the mould does not suffer cross-sectional deformations associated to the lateral pressure caused by fresh concrete). Casting procedures are relatively straightforward, with possible use of vibrating needles, and the interesting feature of being conducted with the mould placed in its final structural arrangement (simply supported). Upon the end of casting operations (total concrete height of 150 mm), a plastic cover should be placed in order to assure proper curing conditions and prevent water loss from the specimen (which would affect its overall mass). During the experiment, accelerometers are placed at 3 spots throughout bottom surface of the beam, allowing a more accurate modal identification as compared to a single-accelerometer setup (as shown in Section 4.4.1).

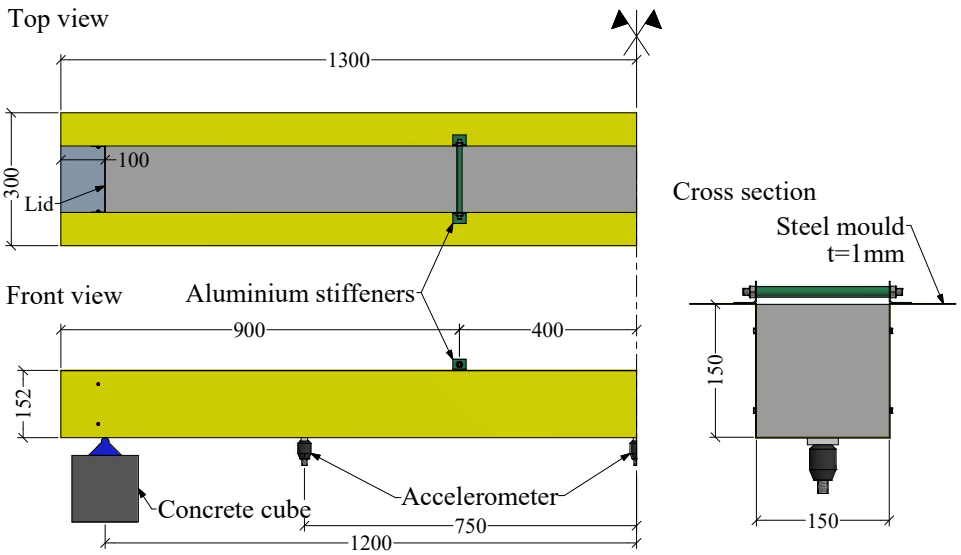

a)

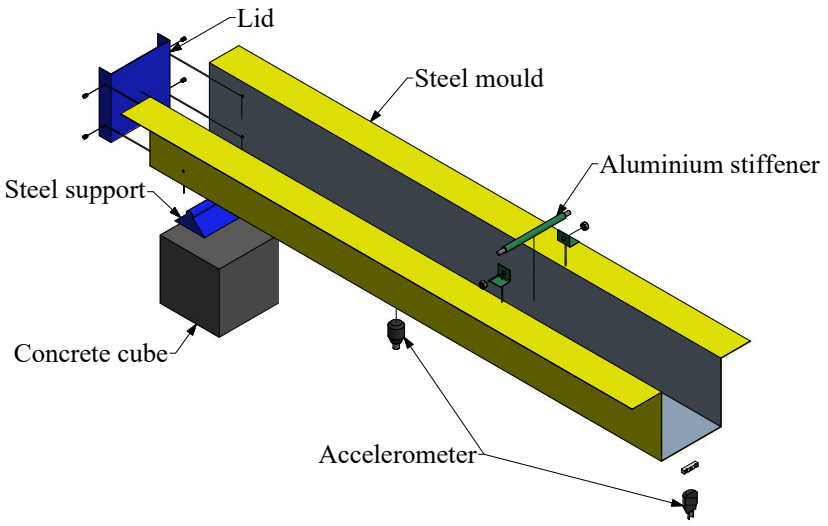

b)

Figure 3.3. EMM-ARM steel 'U-shaped' beam: a) Scheme; b) 3D exploded view [units: mm].

After the end of the experiment, the set composed by the accelerometers, the extremity lids and the aluminium stiffeners are removed from the mould. Then, the mould is turned upside down, allowing the easy removal of the concrete specimen through slight bending of the lateral walls of the mould. It should be remarked that this experimental setup causes the experiment to have no expendable parts: everything is re-usable.

In order to validate the new devised 'U-shaped' mould an experiment was performed in a prefabrication industry plant. The overall experiment consisted in casting two EMM-ARM specimens: one with the original acrylic tube version (O-ACR-1.8-CS), and the other in the 'U-shaped' steel mould (U-STL-2.4-CS). The geometrical and mechanical characteristics of the beams are summarized in Table 3.1. The concrete used in these tests, named as Mix 1, has the composition as shown in Table 3.2.

Table 3.1. Parameters used for the transformation of the frequencies in E-modulus.

	Test 1 – concrete mix 1	
Reference	*O-ACR-1.8-CS*	*U-STL-2.4-CS*
Geometry		
Cross-section	Circular	'U'
$\varnothing_i$/Height	91.50 mm	146.7 mm
$\varnothing_e$/Width	99.92 mm	150.3 mm
Span	1800 mm	2405 mm
Connectors	Yes	No
(spacing)	(300 mm)	
Supports	$Ø_{TR}$=5 mm Concrete cubes	Concrete cubes
Mould		
Material	Acrylic	Steel
Density	1180.0 kg/m^3	7800.0 kg/m^3
E-modulus	3.50 GPa	170.0 GPa
Concrete density	2450.0 kg/m^3	2450.0 kg/m^3

Table 3.2. Concrete compositions used.

Component	*Mix 1 (kg/m^3)*	*Mix 2 (kg/m^3)*	*Mix 3 (kg/m^3)*	*Mix 4 (kg/m^3)*	*Mix 5 (kg/m^3)*
Sand	418 (fine) 377 (coarse)	621 (0/8) 306 (4/8)	739 (0/4) –	245 (0/2) 786 (0/6)	250 (0/2) 460 (0/4)
Gravel	1006 (5/15) –	438 (10/16) 449 (14/12)	1072 (8/22) –	417 (6/14) 478 (14/20)	1140 (4/16) –
Cement	430 (CEM I 42.5R)	224 (CEM I 42.5R)	340 (CEM I 52.5N PMES CP2)	280 (CEM II 42.5R)	218 (CEM II/A-L 42.5R)
Fly ash	–	96	–	40	112
Water	143 l/m^3	170 l/m^3	184 l/m^3	143 l/m^3	155 l/m^3
Super plasticiser	3.90 (Polycarboxylic ether polymers)	2.20 (Pozzolith 390S)	–	6.25 (Rheobuild 1000)	3.3 (Sikament 400+)

As concrete could not be classified as self-compacting, the casting operations inside the acrylic tube had to be done with external vibration (handheld vibrator coated with a cloth and slightly pressed against the mould), as shown in the photo of Figure 3.4a. In the case of concrete inside

the steel mould, casting operations were easier because of the direct access of the vibrator (see Figure 3.4b).

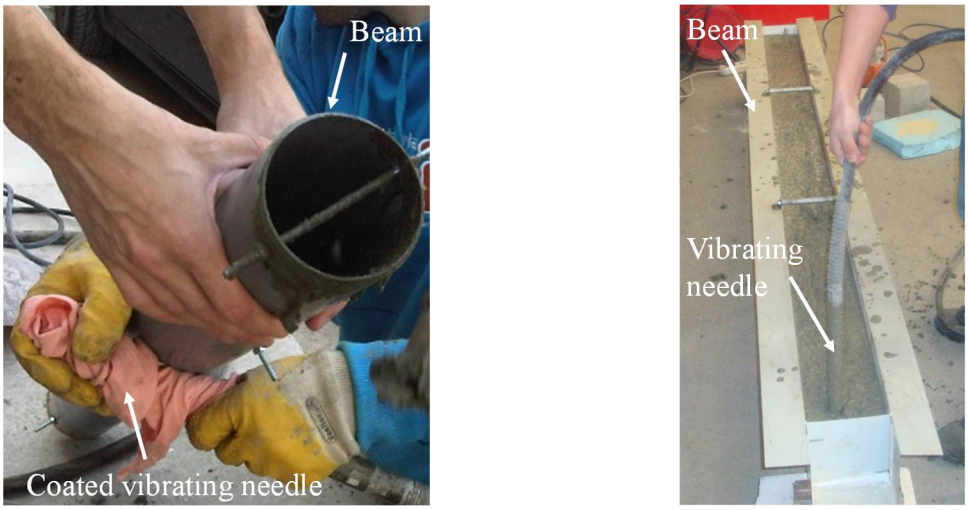

a) b)

Figure 3.4. Examples of how to vibrate the concrete: a) Acrylic EMM-ARM beam with a vibrator coated with a cloth and slightly pressed against the mould; b) 'U-shaped' steel EMM-ARM.

Fans were placed in the vicinity of EMM-ARM specimens to increase the ambient vibration associated to air movement (random turbulent motion). A photo of the experiment is shown in Figure 3.5. Alongside with these experiments, the static E-modulus of concrete was determined through classic cyclic compression tests (CC) in 150 mm diameter and 300 mm long cylinders at the ages of 1, 4, 7, 14 and 28 days (three cylinders tested at each age) according to LNEC E 397 (1993).

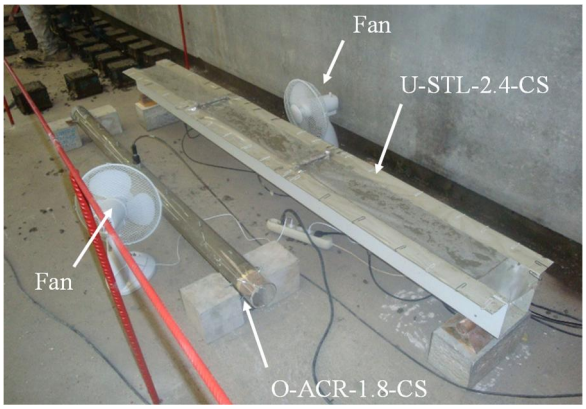

Figure 3.5. Photo of the test.

The raw data in terms of identified resonant frequencies along time, collected in both EMM-ARM specimens, is shown in Figure 3.6a. It can be observed that a wide range of frequencies is covered during concrete hardening in both cases, ranging from 9 to 40 Hz in the acrylic beam and from 20 to 45 Hz in the steel alloy beam. Both evolution curves seem plausible, exhibiting an initial dormant period (where frequency remains almost unchanged) in the first two hours, and then having steep evolutions until approximately 2 days age. After that, both beams exhibit a significantly smaller rate of resonant frequency growth in time.

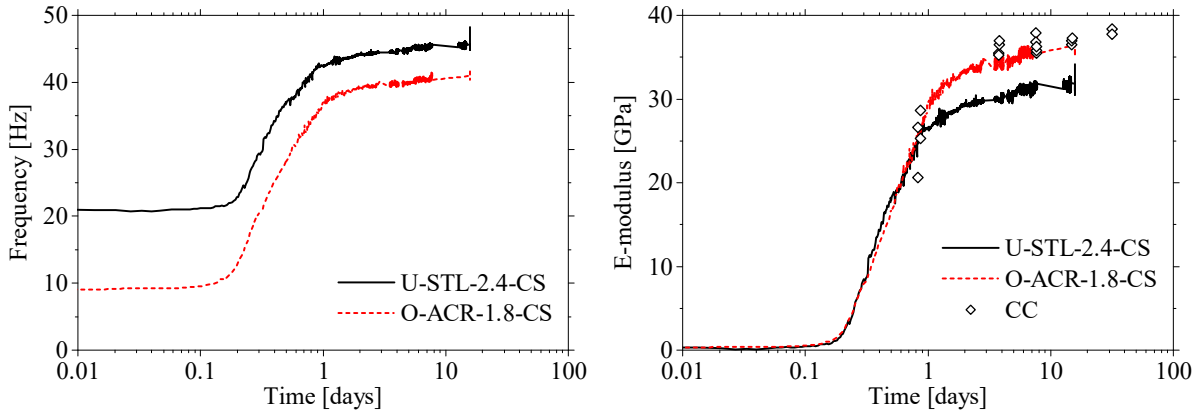

a) b)

Figure 3.6. a) Identified resonant frequencies in the EMM-ARM specimens; b) E-modulus obtained through EMM-ARM and through compressive cyclic testing.

The analysis of interest in the scope of this thesis is centred in the E-modulus of concrete, which was estimated with recourse to equations (2.11) and (2.12) applied to the data of Figure 3.6a, together with the information forwarded in Table 3.1. The estimated evolution of E-modulus

based on the resonant frequencies for both beams is shown in Figure 3.6b. The results obtained through classic cyclic testing are also shown in the figure. Regarding the E-modulus estimation by the acrylic mould EMM-ARM, it can be stated that an excellent coherence in regard to classic cyclic testing was obtained, within an error margin that relies below ~2 GPa. This situation is consistent with the kind of accuracy already reported before for laboratory application of EMM-ARM (Azenha *et al.*, 2010a). It is also noticeable that the initial E-modulus amounts to ~0 GPa, which denotes the feasibility of the assumption of zero initial stiffness (this observation is also valid in the case of the steel alloy mould).

The use of the initially devised version of EMM-ARM for acrylic is thus considered valid in view of its ability of estimating E-modulus values very similar to the static E-modulus estimated by the classic cyclic compression test. However, the same conclusion of adequate performance cannot be withdrawn by observation of the results for the steel alloy EMM-ARM in Figure 3.6b. In fact, after an initial period where the estimated E-modulus evolution was remarkably similar to that obtained from the acrylic EMM-ARM, at 0.7 days, the behaviour started to deviate. After such instant, the steel alloy EMM-ARM led to significant underestimations of concrete E-modulus up to the final age of 15.5 days. The reason for this deviation was successfully determined at the end of the experiment, as it was possible to remove the plastic sealing from the top of the beam and observe it. It was seen that some parts of the edge between concrete and the steel mould were slightly separated, thus pointing to the debonding of the two materials, as shown in Figure 3.7. This debonding is bound to have been caused by the effect of autogeneous shrinkage of concrete (as drying was prevented), and it has probably occurred at the equivalent age of 0.7 days mentioned above.

a) b)

Figure 3.7. Evidence of debonding in the 'U-shaped' steel mould: a) Position of the debonding problem; b) Detail A.

In order to make sure that the concrete in the specimen was actually well cast and that its stiffness was adequate (thus ruling out the possibility of internal voids or defects), it was removed from the steel mould and tested individually as simply supported, with a span of 2.3 m (this beam was named S-CON-2.3). The measured resonant frequency was of 49.8 Hz. By application of equations (2.11) and (2.12), together with the analysis parameters shown in Table 3.3, the measured resonance frequency led to an estimation of 35.1 GPa for the E-modulus at such instant of testing (t = 15.5 days). As the E-modulus of concrete obtained through classic cyclic compression testing at a similar age (t = 14.7 days) had the comparable value of E = 36.9 GPa, this satisfactory coherence rules out the possibility of the error in steel alloy EMM-ARM being caused by the concrete itself. Therefore, these findings confirm the plausibility of appointing the loss of bond between the materials as a cause of the under-estimation of E-modulus with the steel-alloy EMM-ARM. In fact, the occurrence of debonding may induce overall stiffness loss of the system and/or motivate the occurrence of local modes of vibration (that may lie within the frequency range of the experiment) in the bottom steel plate that supports the accelerometer.

Table 3.3. Physical characteristics of the demoulded concrete beam.

Reference	*S-CON-2.3*
Geometry	
Cross-section	Square
Height	146.7 mm
Width	150.3 mm
Span	2300 mm
Supports	Concrete cubes
Concrete density	2392.0 kg/m^3

Bearing in mind the reported problem with the 'U-shaped' EMM-ARM steel mould, it was decided to perform a second experiment with measures being taken to mitigate the possibility of debonding. In an attempt to overcome this problem, 16 steel connectors were placed along the sides of the steel mould (8 in each side). The connectors are stainless screws with 3.55 mm in diameter and 37.76 mm in length were laced in the beam according to the scheme shown in Figure 3.8.

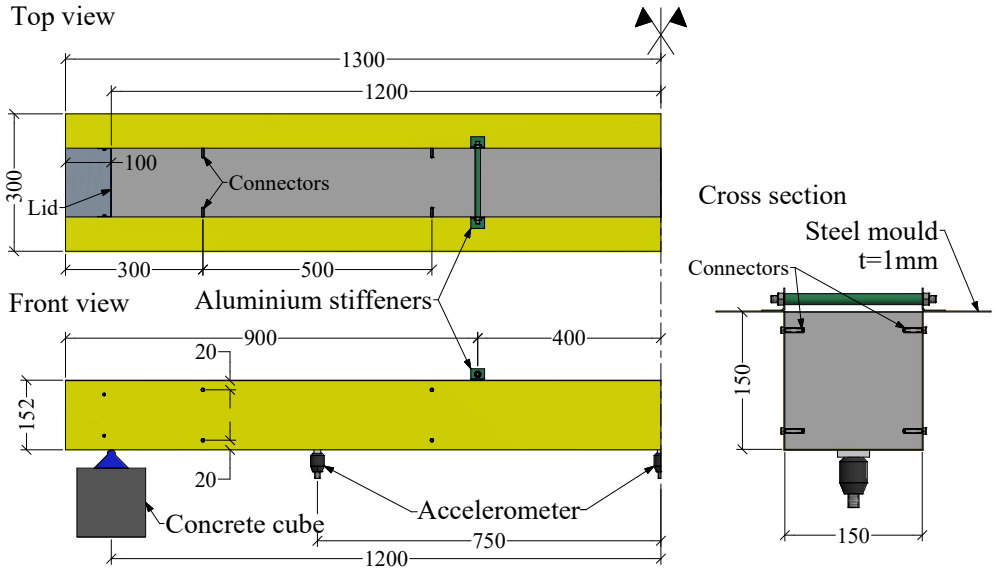

a)

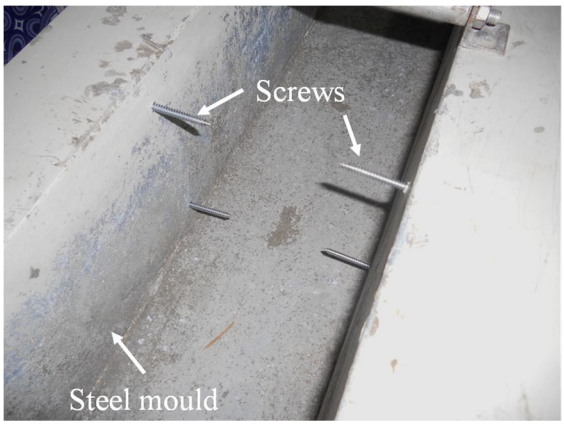

b)

Figure 3.8. Overall scheme of the steel 'U-shaped' beam [units: mm].

This second test with the 'U-shaped' steel alloy mould containing connectors took place at a distinct construction site, and with a distinct type of concrete. The characteristics are presented in Table 3.4 and the concrete composition was the mix 2 shown in Table 3.2. Additionally classic cyclic compression testing (CC) were conducted in cylinders (Ø = 150 mm and 300 mm height) at ages of 1, 3, 7, 14 and 29 days, performed according to LNEC recommendations E397 (1993).

Table 3.4. Beam characteristics used in test 2.

Reference	*Test 2 – concrete mix 2* *U-STL-2.4-CS*
Geometry	
Cross-section	'U'
Height	150.40 mm
Width	151.58 mm
Span	2404 mm
Connectors	Yes
(spacing)	(500 mm)
Supports	Concrete cubes
Mould	
Material	Steel
Density	7800.0 kg/m^3
E-modulus	170.0 GPa
Concrete density	2300.0 kg/m^3

The raw results of the resonance frequencies identified from the 'U-shaped' steel beam are shown in Figure 3.9a. Once more, the resonance frequency evolution has similar kinetics to the previous EMM-ARM applications, with a dormant period in the first 7 hours, after which the resonance frequency evolved significantly until two days of concrete curing. From that point, the evolution rate was significantly reduced.

The estimated concrete E-modulus and the corresponding comparison with CC results for this test is shown in Figure 3.9b. The results show similar coherence to that which had been previously obtained in the acrylic EMM-ARM application. This leads to the conclusion that the addition of drive screws in the steel mould avoids the debonding problems, and thus allows proving the steel alloy EMM-ARM as a feasible alternative to the initially devised acrylic mould. It is further remarked that the inclusion of these screws does not endanger the re-usability of the mould, as they can be easily unscrewed before concrete removal.

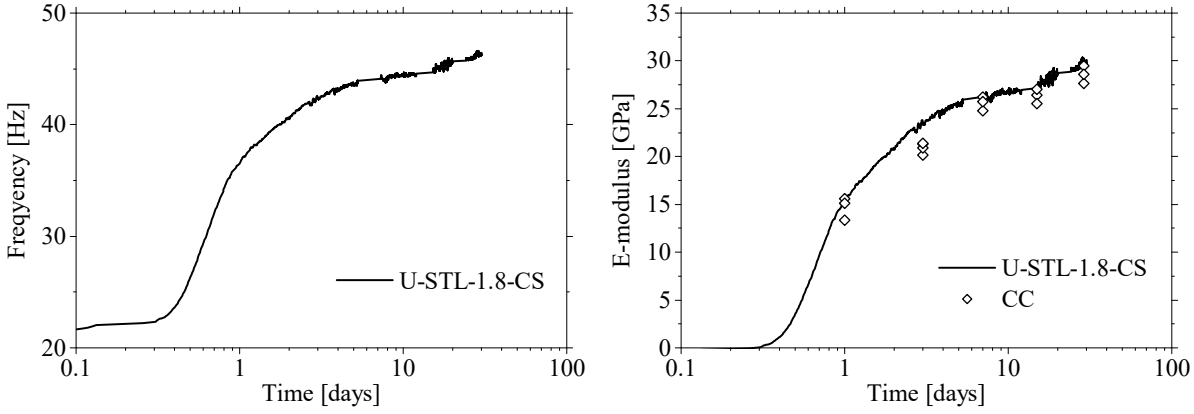

a) b)

Figure 3.9. Results of test 2: a) Identified frequency evolution in the EMM-ARM specimen; b) E-modulus obtained through steel alloy EMM-ARM with connectors and through compressive cyclic testing.

However, despite this successful feasibility demonstration, the steel-alloy mould revealed to be somehow impractical for systematic application due to its large size (2.6 meter long). Furthermore, due to the reduced thickness of its steel plate, the mould tended to suffer sectional deformations with repeated use. In fact, in just one reuse of the mould the cross-sectional geometry changed 0.78% (1.28 mm) in the width and 2.46% (3.70 mm) in the height. These changes in the geometry tended to compromise the accuracy of the stiffness estimations, which is a quite undesirable effect. Thus if these changes were not properly taken into account they would have had an impact in the E-modulus estimations of 1.8% (0.53 GPa).

3.2.1.2. Second attempt

As previously stated, a major limitation of EMM-ARM in the 2 meters long acrylic beam setup is related to the difficulty to cast inside the long mould from its extremity and the inherent difficulties in handling the test beam. Despite the previous attempt, where the use of an open 'U-shaped' beam solved the problem of casting, the 'U-shaped' mould continues to be an obstacle due to its considerable size that is not manageable by a single operator. Therefore, it was decided to adapt the original tubular mould by reducing its total length, making casting/handling operations easier. However, it is necessary to take into account that the reduction of the beam span increases the overall stiffness of the system and thus decreases the

amplitude of ambient-induced vibrations of the beam, which ultimately poses difficulties for the accurate measurement of accelerations.

Therefore, an analytical parametric study was performed in order to optimize the span of the beam. In this study, it was established that the maximum resonance frequency of the first vibration mode of the beam should be around 150 Hz. This value, which was based on the accumulated experience of previous applications, should be appropriate to ensure vibration levels that can be detected by the adopted accelerometers without accuracy issues (e.g. avoiding high noise-to-signal ratios). It was also considered relevant to limit the maximum resonance frequency, as to prevent the EMM-ARM test from reaching resonance frequencies that could induce a dynamic-type response (therefore obtaining dynamic E-modulus measurements as opposed to the current capacity of capturing static E-modulus values as discussed in section 2.7.2) (Shkolnik, 2008). Thus, a scenario for a hardened concrete with 30 GPa and 2400 kg/m^3 density was considered. By conserving the cross-sectional characteristics to the original implementation (see Figure 2.16), while reducing the span to 0.9 m, the resulting calculated resonance frequency of the EMM-ARM beam was found to fill the intended requirements (i.e. $f < 150$ Hz). It should also be noted that this smaller span increases the resolution of EMM-ARM by increasing the range of variation of the resonance frequencies during testing. In fact, since the instants right after casting (0 GPa) to the hardened stage of concrete (30 GPa), the original implementation of EMM-ARM covered an evolution range of 7.4-38.6 Hz, whereas the reduced span version covers a range of 28.8-147.7 Hz. It is noted that further alternatives to the 'U-shaped' cross-section were no longer studied due to the robustness problems that the thin plate of the mould has brought.

Therefore, two laboratory test programs were performed to study the feasibility of reducing the total length of the testing beams (Figure 3.10), while conserving a tubular cross-section for the mould. Both test programs included additional specimens in which the material of the mould was changed to PVC, which is both cheaper than acrylic and less prone to being damaged during casting operations. Each of the two test programs is briefly summarized in Table 3.5, whereas the corresponding concrete compositions are shown in Table 3.2. The first test program comprised three beams (Figure 3.10a): one corresponding to the original implementation with acrylic beam that had 1.8 m span (O-ACR-1.8-CS); another with the 'U-shaped' steel mould of 2.4 m span as reported in Figure 3.8 (U-STL-2.4-CS); and a new 0.9 m span PVC mould with

inner/outer diameter of 86/90 mm (O-PVC-0.9-CS). The second test program was solely dedicated to the tubular shaped beams and included (Figure 3.10b): one beam corresponding to the original implementation (O-ACR-1.8-CS); one acrylic beam with the same cross section as the previous one, but 1.0 m span (O-ACR-1.0-CS); and a beam with PVC mould that was quite similar to the one of the first test program, but had 1.0 m span instead of 0.9 m (O-PVC-1.0-CS). In both test programs, additional cylinder specimens (Ø = 150 mm and 300 mm height) have been cast as to allow the evaluation of E-modulus through CC testing. In the first test, two specimens were cast and tested at 2.7, 7, 14 and 28 days. In the second test, three specimens were cast and tested at 41 days. The tests were performed in the laboratory of the University of Minho under almost isothermal environmental conditions (at 20±2 ºC).

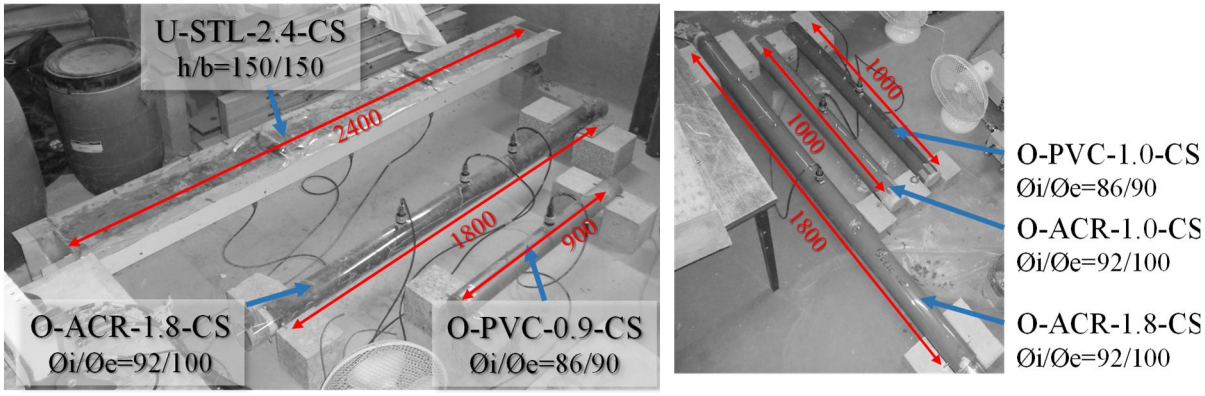

a) b)

Figure 3.10. Photos of the studied EMM-ARM beams: a) Test 3; b) Test 4.

Table 3.5. Beam characteristics for the tests 3 and 4.

	Test 3 – concrete mix 3			*Test 4 – concrete mix 4*		
Reference	*O-ACR-1.8-CS*	*U-STL-2.4-CS*	*O-PVC-0.9-CS*	*O-ACR-1.8-CS*	*O-ACR-1.0-CS*	*O-PVC-1.0-CS*
Geometry						
Cross-section	Circular	'U'	Circular	Circular	Circular	Circular
$\varnothing_i$ /H	92 mm	150 mm	86 mm	92 mm	92 mm	86 mm
$\varnothing_e$ /B	100 mm	150 mm	90 mm	100 mm	100 mm	90 mm
Span	1800 mm	2400 mm	900 mm	1800 mm	1000 mm	1000 mm
Connectors (spacing)	Yes (300 mm)	Yes (500 mm)	Yes (180 mm)	Yes (300 mm)	Yes (200 mm)	Yes (200 mm)
Supports	$Ø_{TR}$=5 mm Concrete cubes	Concrete cubes	$Ø_{TR}$=5 mm Concrete cubes	$Ø_{TR}$=5 mm Concrete cubes	$Ø_{TR}$=5 mm Concrete cubes	$Ø_{TR}$=5 mm Concrete cubes
Mould						
Material	Acrylic	Steel	PVC	Acrylic	Acrylic	PVC
Density	1286.9 kg/m^3	7800.0 kg/m^3	1463.5 kg/m^3	1400.0 kg/m^3	1200.0 kg/m^3	1400.0 kg/m^3
E-modulus	3.30 GPa	170 GPa	4.3 GPa	3.60 GPa	4.00 GPa	3.50 GPa
Concrete density	2340.3 kg/m^3	2362.9 kg/m^3	2295.7 kg/m^3	2382.6 kg/m^3	2347.1 kg/m^3	2311.3 kg/m^3

The resonance frequencies identified by EMM-ARM for test programs 3 and 4 are shown in Figures 3.11a and 3.11b, respectively. It is noticeable in both figures that both the initial resonance frequency and the amplitude of resonance frequency variation of EMM-ARM tests is increased in the specimens with smaller span (0.9 m and 1.0 m) as expected. In fact, the frequency variation along testing was 9.7-44.5 Hz in the 1.8 m span original beam (ACR-O-CS-1.8), whereas it shifted to 30.1-139.2 Hz for the 0.9 m span beam (PVC-O-CS-0.9). Moreover, all frequency evolution curves appear to be plausible, showing an initial dormant period (where the frequency remains almost constant within ±0.3 Hz). After this threshold, the frequencies evolved significantly for all tested specimens until approximately 21 and 19 hours of curing period for the mix 1 and 2, respectively, after which a dramatic reduction in the slope of frequency evolution occurs.

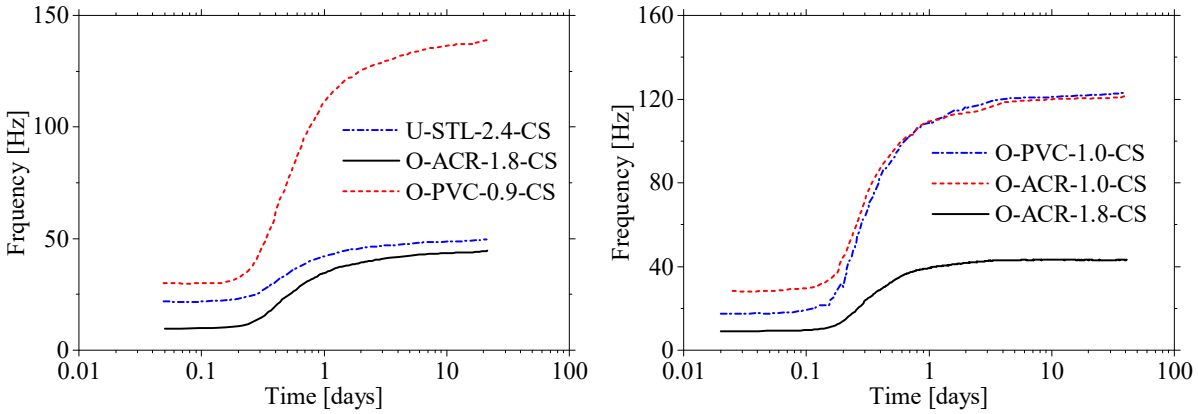

a) b)

Figure 3.11. Comparison between the frequency evolutions obtained through the different EMM-ARM beams: a) Test 3; b) Test 4.

The elasticity modulus of the two concretes was estimated by applying equations (2.11) and (2.12) to the resonant frequencies presented in Figure 3.11. In a first approach, it was assumed that the vertical stiffness of the supports of the beams (k – in equation (2.11)) was infinite. The resulting E-modulus evolution estimates, along with the results of CC testing, are shown in Figures 3.12a and 3.12c for tests 3 and 4, respectively. There is a good coherence between the results of the original EMM-ARM beam (O-ACR-1.8-CS) and the 'U-shape' steel beam (U-STL-2.4-CS) with the results of cyclic compression, corroborating the validity of results presented in previous works (Azenha *et al.*, 2010a, Azenha *et al.*, 2012b, Boulay *et al.*, 2013a). Nevertheless, when the results of the reduced span EMM-ARM beams (O-ACR-1.0-CS, O-

PVC-1.0-CS and O-PVC-0.9-CS) are added to the comparison, a large discrepancy between the results of these beams can be seen. In fact, the estimated concrete stiffness through these test beams is consistently lower than that of the previous implementations and that of CC. A careful analysis of the experimental setup at the end of the experiments allowed observing that the assumption of infinite rigidity for the supports might not be truly valid due to: (*i*) a small gap between the mould and the concrete cube support; and to (*ii*) precarious support conditions due to misalignments of the horizontal rods in the beam in combination with the small stiffness of the horizontal rods. Then, the consideration of infinite of k in equation (2.11) would require a corresponding correction, as to obtain accurate estimates of concrete E-modulus.

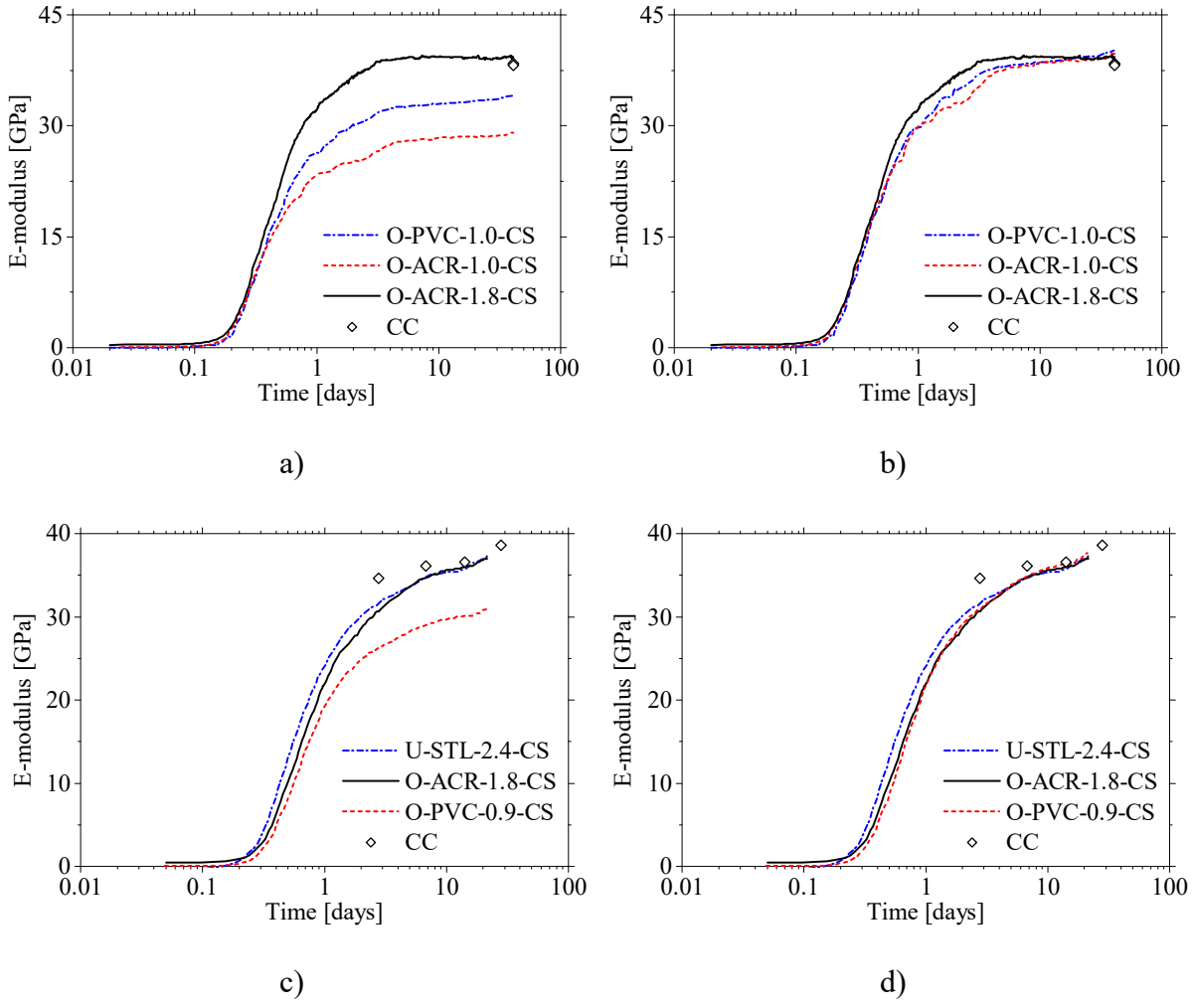

Figure 3.12. Comparison between the E-modulus evolutions obtained through the different EMM-ARM beams: a) Test 3 with $k=\infty$; b) Test 3 with real value of k; c) Test 4 with $k=\infty$; d) Test 4 with real value of k.

Thus, the spacing between the effective point where the rods touch the supports and the concrete beams (see Figure 3.13) was carefully measured and the actual stiffness of the support beams with circular cross-section was estimated in accordance with the procedure present in the work of Azenha *et al.* (2010a).

$$k = 3 \cdot E \cdot I \cdot \left(\frac{1}{l_1^3} + \frac{1}{l_2^3} \right) \tag{3.1}$$

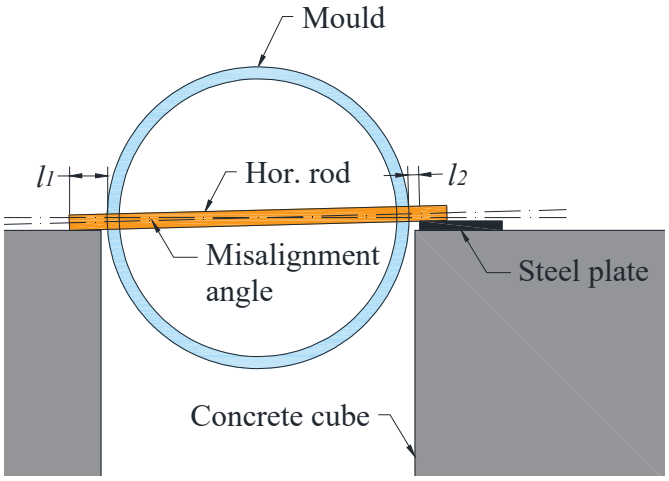

Figure 3.13. Effective point where the rods touch the supports.

The following values for the vertical stiffness of the supports were obtained: 25×10^6 N/m for the PVC beams (O-PVC-0.9-CS and O-PVC-1.0-CS) as a result of an average 8.1 mm gap in both sides of the beams; 17×10^6 N/m for the beam O-ACR-1.0-CS as a result of an average 9.2 mm gap; and 848×10^6 N/m for the beam O-ACR-1.8-CS as a result of an average 2.0 mm gap. The vertical stiffness of the supports of the 'U-shaped' steel beam was assumed to be infinite due to their direct standing on concrete blocks without intermediate supporting bars (flexible). These values were introduced in equation (2.11) (page 35) and the concrete E-modulus for all tested beams was recomputed based on the frequencies of the Figures 3.11a and 3.11b.

The corrected curves of stiffness evolution of the concrete for the test programs 3 and 4 are shown, respectively, in Figures 3.12b and 3.12d. It can be observed that the E-modulus estimation of all beams and CC testing has become quite coherent. It is interesting to notice that

the estimates of E-modulus of the longer span test specimens (original implementation) were marginally affected by this correction, with modifications always below 0.1% in comparison to the initial estimates in which the rigidity of the supports had been considered infinite. However, the new reduced spans have strongly increased the dependency of E-modulus estimates on the stiffness of the supports, thus justifying the changes of more than 15.1% of estimates when the support stiffness was corrected. Despite this stiffness support sensitivity issue, these two test programs have allowed confirming that the reduction of beam span and alteration of mould material to PVC are feasible changes.

3.2.2. New supports

Taking into account the added sensitivity to support conditions that the reduced span of ~1.0 m carries to EMM-ARM E-modulus estimations, it became necessary to ensure adequate support conditions of the tested beams as to guarantee the desirable robustness for testing. Thus a new support system was developed in which the dependency on the operator skill to ensure stiff supports is strongly reduced. The new support system was developed in steel to ensure adequate stiffness and durability.

The sketch of the new steel supports is shown in Figure 3.14. The supports have specially devised round depressions to receive the horizontal rods from the specimen, and their geometry is such that the slacks between the specimen and the supporting system are kept to a minimum (i.e. under 0.5 mm, when the specimen is centred with the support). As mentioned in the previous subsection, slight alignment mismatches had been observed between the pairs of supporting rods of the beams at their extremities. These mismatches demanded that slight corrections were made in the height of the support blocks in some occasions (e.g. with thin metal sheets – see Figure 3.13). To avoid such type of operator-dependent corrections with potential impact on the stiffness of the supports, the new developed supports encompass a longitudinal bearing in one of them (pivoted support), which allows fine-tuning its transversal rotation as to compensate any potential misalignment between the supporting rods of the beam.

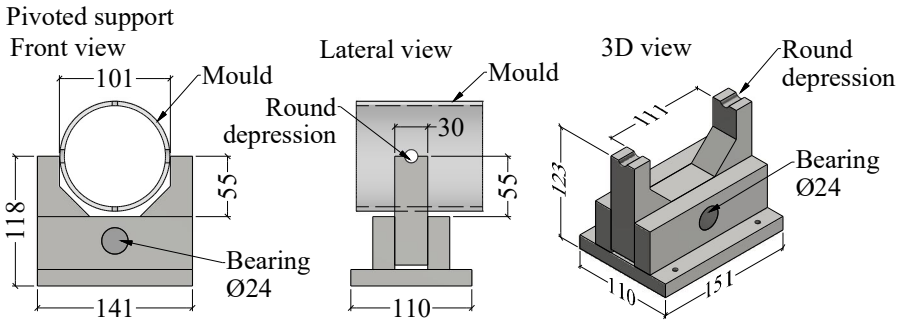

a)

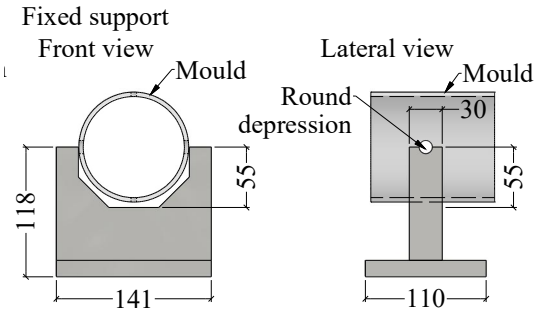

b)

Figure 3.14. New EMM-ARM steel supports: a) Pivoted; b) Fixed [units: mm].

In addition to the development of the new supports, to increase the vertical stiffness of the whole support system, the horizontal threaded rods (TR) with $\varnothing_{TR}$ = 5 mm that were used in previous implementations of EMM-ARM where replaced with plain steel rods (PR) with $\varnothing_{PR}$ = 12 mm. These adaptations increased the vertical stiffness of the supports to a minimum of 8.79×10^{12} N/m. In the worst-case scenario of the shortest beam O-ACR-09 (most sensitive to the stiffness of the support), this stiffness has an impact of less than 0.0001% on the estimation of composite beam stiffness, when compared to the assumption of infinite rigidity of the support.

To assess the performance of the newly devised support system, a test program was performed. This test program intended to compare two different EMM-ARM beams: an original EMM-ARM beam (O-ACR-1.8-CS) with 1.8 m span and supported over concrete cubes (Figure 2.16) and an acrylic beam with 1.0 m span (O-ACR-1.0-MS), which is equal to the first beam, except for its span and the fact that it uses the new support system (Figure 3.15). Besides

the EMM-ARM experiments, E-modulus had already been measured for a previous batch of this concrete in cylinder specimens through CC at the age of 41 days.

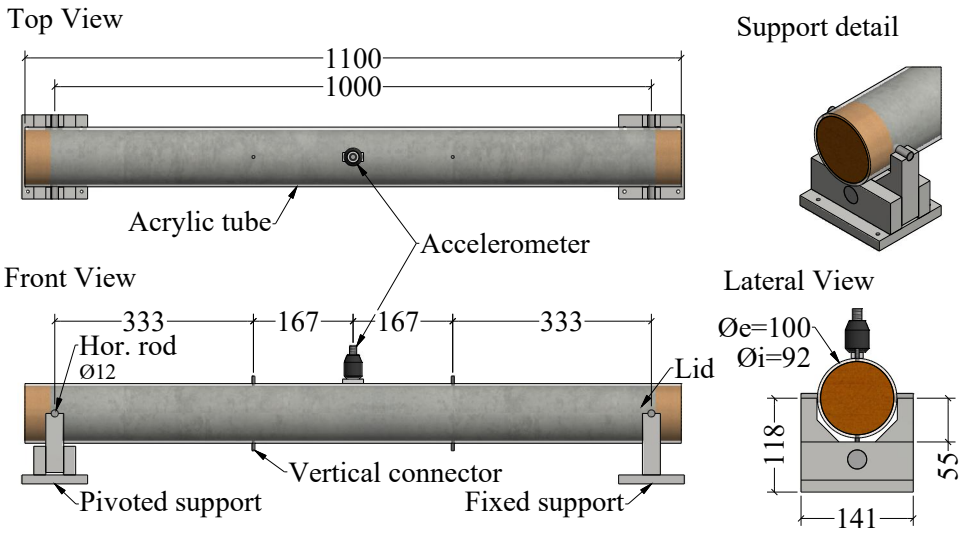

Figure 3.15. Scheme of the reduced span mould for EMM-ARM tests with new steel supports [units: mm].

The characteristics of the beams used in this experiment are shown in Table 3.6. The concrete used in this experiment was mixture 4 shown in Table 3.2.

Table 3.6. Beam characteristics used in the test 5.

	Test 5 – concrete mix 4	
Reference	*O-ACR-1.8-CS*	*O-ACR-1.0-MS*
Geometry		
Cross-section	Circular	Circular
$\varnothing_i$	91.65 mm	91.46 mm
$\varnothing_e$	100.19 mm	100.17 mm
Span	1825 mm	1019 mm
Connectors	Yes	Yes
(spacing)	(300 mm)	(330 mm)
Supports	$Ø_{TR}$=5 mm Concrete cubes	$Ø_{PR}$=12 mm Steel supports
Mould		
Material	Acrylic	Acrylic
Density	1160.0 kg/m^3	1160.0 kg/m^3
E-modulus	5.70 GPa	6.20 GPa
Concrete density	2316.8 kg/m^3	2317.4 kg/m^3

The evolutions of the identified resonance frequencies of the two beams as presented in Figure 3.16a. Once more, as can be observed, the evolutions kinetics displays similar shape to previous

implementations of EMM-ARM. The estimated elastic modulus evolutions from these resonance frequencies for concrete are shown in Figure 3.16b. Both EMM-ARM results seem to slightly over-estimate the value of E-modulus as compared to CC testing. The reader is however reminded that these CC results pertained to a previous batch of the same concrete, and that this difference is likely to be related to variance between different concrete batches. Furthermore there is an almost perfect overlap of the E-modulus estimations obtained with the original beam (O-ACR-1.8-CS) and with the reduced span beam with the new support system (O-ACR-1.0-MS).

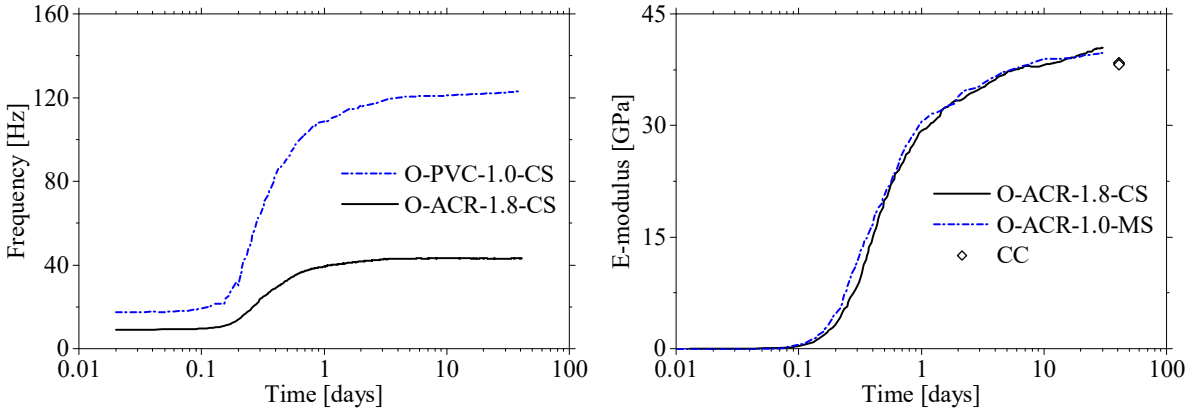

Figure 3.16. Comparison between the E-modulus evolutions with different support systems.

Therefore, it is possible to conclude that the new support system for EMM-ARM beams is feasible and provides sufficient stiffness for the assumption of infinite support stiffness in the scope of application of the E-modulus predictive formulae. Thus, the dependency of the operator in the results was strongly reduced by eliminating the problem of controlling the gap between the supports and the testing beam and by allowing the correction of some geometric imperfections in the alignment between the horizontal rods that support the beam (pivoted support).

3.2.3. Development of a new reusable mould

In previous subchapters, new moulds for EMM-ARM were studied by varying both the geometry, the mould material and the supports. However, none of the tested moulds is reusable

(except for the 'U-shaped' steel mould, with its negative points raised earlier), which would definitely be a desirable situation to perform systematic applications of EMM-ARM. Based on the previous developments, and taking into account the intention of making a reusable mould, a new PVC mould reinforced with aluminium rings, with the geometry shown in Figure 3.17, was developed and tested. To enable the reuse of the PVC tube, it was sliced in two halves along its longitudinal direction through a vertical plane. The longitudinal cut was made in this position as to avoid undermining the composite behaviour of the beam. Indeed, the shear stresses are minimum in the top and bottom parts of the beam. In order to ensure constancy of geometry of the PVC mould, three lightweight aluminium rings were glued to the tube, which also ensure adequate connection between the two PVC halves.

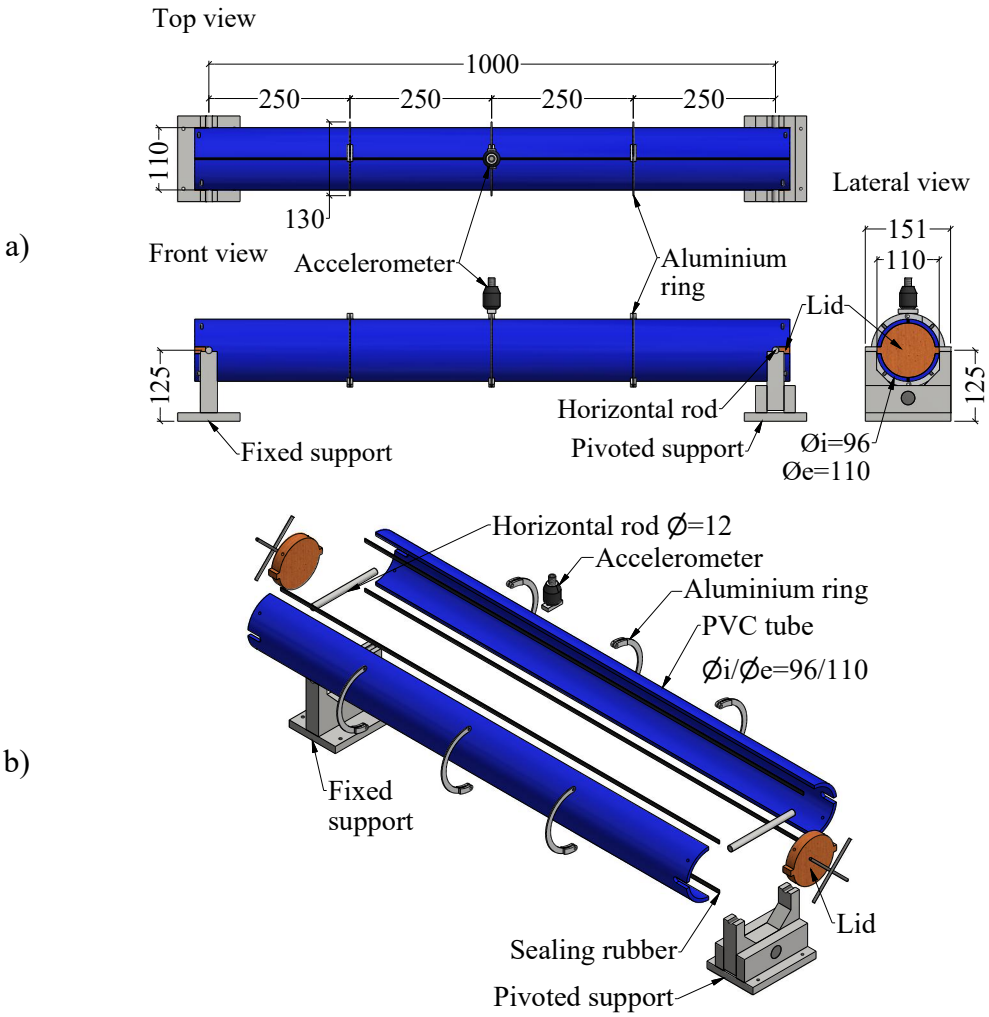

Figure 3.17. Reusable mould for EMM-ARM tests: a) Scheme; b) 3D exploded view [units: mm].

The combination of several factors in the design of this re-usable mould make it advantageous in comparison to the previous attempt of re-usability through the 'U-shaped' mould: (*i*) its circular cross section and the aluminium ring allow a better control of geometry constancy along repeated use; (*ii*) the smaller span makes it easier to handle, particularly in regard to demoulding operations at the end of the experiment, together with specimen disposal; (*iii*) much less concrete volume is necessary to deploy the same type of characterization. Additionally, the use of PVC as mould material, together with the absence of internal connectors and the small length of the beam, allows the access of a vibrator needle inside the mould without danger of damaging it, which is a significant advantage in comparison to the original implementation of EMM-ARM.

To test this new mould, an additional test program experiment with three EMM-ARM beams was carried out: a 0.9 m span acrylic beam similar to the original supported with the new supports (O-ACR-0.9-MS); the new reusable beam (R-PVC-1.0-MS); and a beam similar to the newly devised reusable but with the PVC tube intact, i.e. without cutting it in halves, nor placing the aluminium rings (O-PVC-1.0-MS, which is not re-usable). This test allowed, in addition to the validation of the reusable beam, to check if the elimination of the vertical connectors could lead to the loss of the composite behaviour of the beam due to slippage. The characteristics of the beams used in this test are given in Table 3.7. In addition to the EMM-ARM testing, cyclic compression testing (CC) was made at 7 days of curing. This new mould was tested with the concrete mix 5 shown in Table 3.2.

Table 3.7. Beams characteristics used in the test 6.

	Test 6 – concrete mix 5		
Reference	*O-ACR-0.9-MS*	*O-PVC-1.0-MS*	*R-PVC-1.0-MS*
Geometry			
Cross-section	Circular	Circular	Circular
$\varnothing_i$	92.11 mm	96.05 mm	96.04 mm
$\varnothing_e$	99.82 mm	110.19 mm	110.11 mm
Span	900 mm	1000 mm	1000 mm
Connectors	Yes	No	No
(spacing)	(300 mm)		
Supports	$Ø_{PR}$=12 mm Steel supports	$Ø_{PR}$=12 mm Steel supports	$Ø_{PR}$=12 mm Steel supports
Mould			
Density	1239.9 kg/m^3	1469.4 kg/m^3	1492.6 kg/m^3
E-modulus	4.68 GPa	3.40 GPa	3.06 GPa
Reusable	No	No	Yes
Concrete density	2361.8 kg/m^3	2380.0 kg/m^3	2381.3 kg/m^3

The identified evolution of resonance frequencies for the three tested beams is presented in Figure 3.18a, where it is possible to observe the three phases of the concrete hardening. First the dormant period, followed by a fast evolution of the frequencies and after 2 days of curing a slow grow period. Based on this information, the elastic modulus evolutions of concrete monitored in this test program were computed and are shown in Figure 3.18b. The Figure highlights a good coherence between the results obtained with three different beams, with a variation of only 0.97 GPa (3%) at 7 days. The results of the EMM-ARM and cyclic compression tests also show only a deviation of 1.25 GPa (4%) at such age. This similarity in the results allows the validation the removal of vertical connectors. In fact, despite the removal of the vertical connectors placed along the beam, concrete remains mechanically connected to the mould through the horizontal rods placed at the extremities of the beam, which in addition to support the beam, also end up operating as extremity connectors. These results also validated the reusable beam during its first use. It is noted that after the end of this experiment, the mould was easily removed and re-assembled. The geometry of the reassembled mould was verified after the test and the geometry variation from the state prior to the test was less than 0.25% in both the internal and external diameters. It is also pointed that the demoulded specimen did not exhibit any kind of damage or cracking.

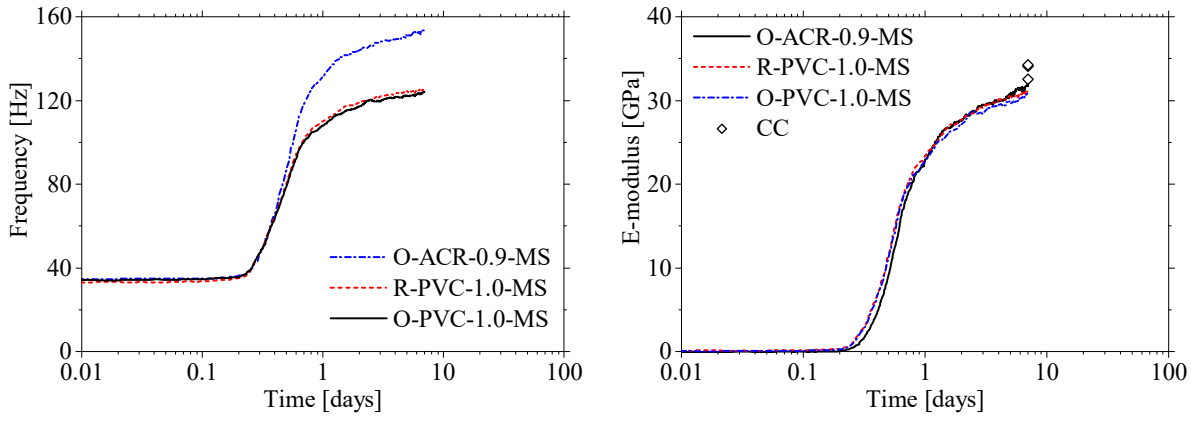

a) b)

Figure 3.18. Comparison between the E-modulus evolution obtained through reusable and non-reusable beams.

3.3. Cement paste testing

Since its first application, the EMM-ARM applied to cement paste has yielded successful results and has been extensively used in materials research (Maia *et al.*, 2011a, Maia *et al.*, 2011b, Maia *et al.*, 2012b, Maia *et al.*, 2012c). However, contrary to the concrete version in which the mould had some practical issues and major user-dependency problems that prevented the systematic use of the method, the original test apparatus applied to cement pastes has less user-dependency problems and did not reveal any relevant problematic issues. Nevertheless the clamping device of the beam is still quite insufficiently developed, as it may cause a non-expert user to make mistakes in the assembly, with potentially relevant impacts in the support conditions. It is also hard to ensure the verticality of the accelerometer placed at the free end of the composite beam and the stiffness of the support is dependent on how the user attaches the clamping device of the beam to the support base of the testing system. Additionally, although it is possible to obtain good quality and repeatable results with the version of EMM-ARM for cement paste, when compared with the version for concrete, it has a much lower resolution. This lower resolution is related to the higher slenderness of the beam and the higher relevance of the accelerometer's mass in the free end of the beam when compared with the mass of the beam.

The following section presents the implementation of a new clamping device that allows a simple assembly of the whole testing apparatus. Then a study on the possibility of using moulds with shorter spans and the use of very lightweight accelerometers to increase the resolution method will be presented.

3.3.1. New support system

As mentioned the beam's camping system has some shortcomings that make it unreliable when appropriate attention is not taken during the assembly of the testing system. This happens because the original clamping device consists of two halves of a steel tube that embrace the testing beam and do not actually have any connection to a rigid base to stand the entire testing system. Such connection is normally made through an external clamp that presses the beam against a metallic heavy base, as shown in Figure 3.19.

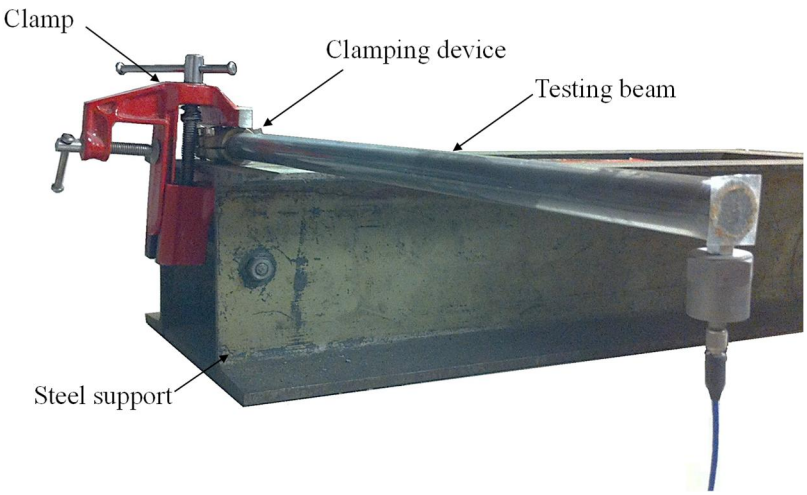

Figure 3.19. EMM-ARM for cement paste original support system.

It is this connection that renders the support system potentially unreliable, and extreme caution is needed during the clamp adjustment to ensure proper support of the beam and guarantee the verticality of the measuring axis of the accelerometer placed at the free end. Therefore, in order to limit the user's dependency, a new support system was developed, as shown in Figure 3.20. It consists of a new clamping device composed of two parts: the lower part is fixed to a rigid base for supporting the entire structural system; and the top paste fixing the beam to the clamping device. Both parts of the support have a semi-circular groove with a diameter equal to the outer diameter of the testing beam (20 mm). In order to avoid any problems with geometric imperfection in the outer diameter of the beam, the clamping device was designed to have a 1 mm gap between the two parts of the support (see Figure 3.20b). This gap allows it to continue to be effective even when the beam has an outer diameter of 19 mm.

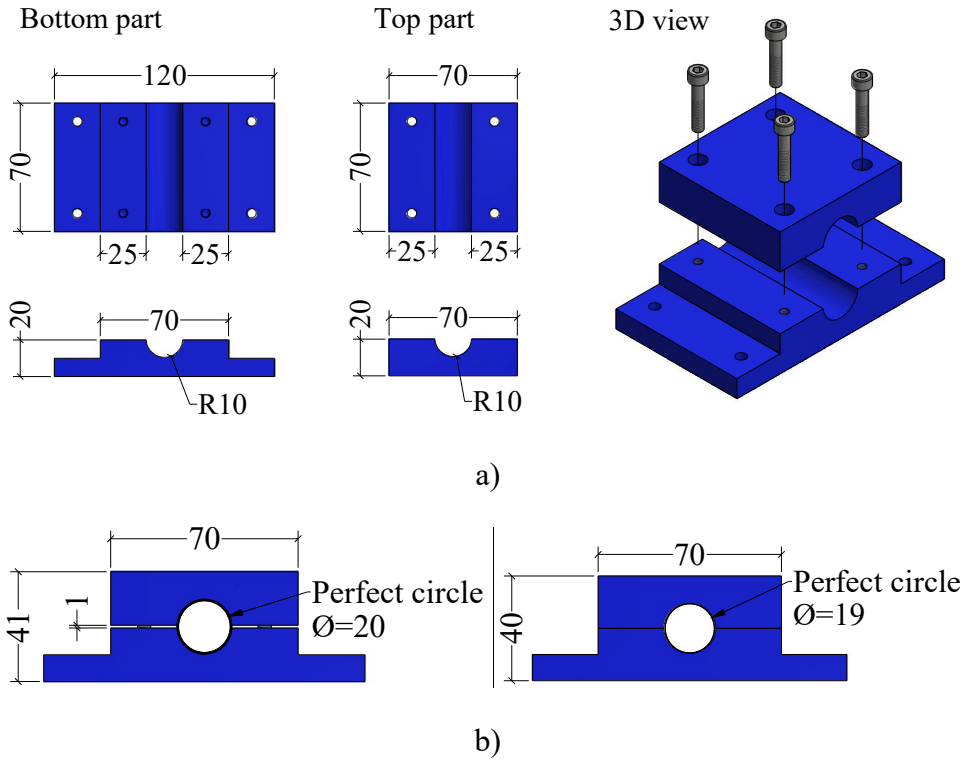

Figure 3.20. New EMM-ARM supports for cement paste tests: a) Disassembled scheme; b) Assembled scheme.

In order to verify if the new support is stiff enough to allow the consideration of a perfect cantilever a small experimental test was performed. In this test a small weigh of 0.54 kg was suspended at the free end of a EMM-ARM acrylic beam ($\varnothing_i$ = 16 mm $\varnothing_e$ = 20 mm and E = 4.2 GPa) with 250 mm of span filled with an epoxy adhesive with E = 8.55 GPa (estimated by an EMM-ARM test). The deflexion of the beam was measured in 4 different points along its free span and these measurements were compared to a numerical curve. To compute the numerical curve was computed assuming a perfect cantilever. The results of this validation test are shown in Figure 3.21. As can be observed there is almost a superposition of the two curves proving that the support is stiff enough to allow the consideration of a perfect cantilever.

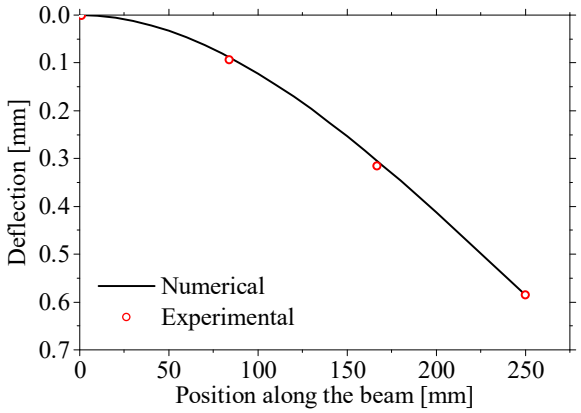

Figure 3.21. Results of the support stiffness validation test.

The final testing apparatus is presented in Figures 3.22a and 3.22b. This new clamping device is then attached to a steel support as shown in Figure 3.22c. Thus with this new testing apparatus the test assembly process is much simpler, and the stiffness of the beam support is increased.

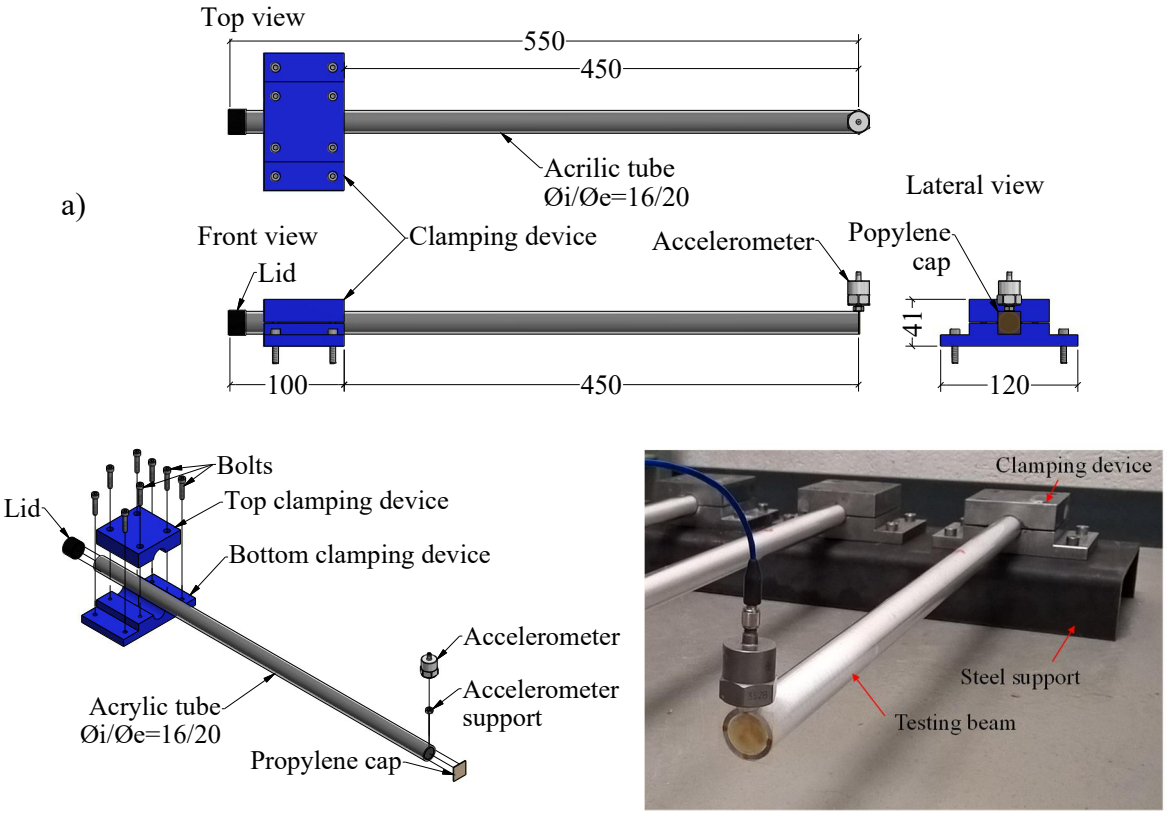

Figure 3.22. EMM-ARM final assembly for cement pastes tests: a) Scheme; b) 3D exploded view; c) Photo [units: mm].

To validate the use of this new support, a test was made where four different beams were evaluated: three beams identical in every aspect to the original presented in Figure 2.18 (45-OS-A1-C1-1, 45-OS-A1-C1-2, 45-OS-A1-C1-3) and one beam similar to the previous ones but with the support provided by the new system (45-NS-A1-C1). The characteristics of the beams as well as the tested cement paste are shown in Table 3.8. It is noted that in all experiments reported in these subsection 3.3.1, the accelerations at free end of the beams were acquired through an accelerometer PCB 352C04 (sensitivity: 1 V/g; range: ±5 g) connected to a dynamic acquisition system NI 9234 with 24-bit resolution. The accelerations were recorded at an acquisition frequency of 500 Hz in packages of 60 seconds each 10 minutes.

Table 3.8. Beam's characteristics for the cement paste tests.

Reference	*45-OS-A1-C1-1*	*45-OS-A1-C1-2*	*45-OS-A1-C1-3*	*45-NS-A1-C1*	*45-OS-A2-C1*	*25-OS-A1-C1*	*45-OS-A1-C2*	*25-OS-A1-C2*
Geometry								
$\varnothing_i$ (mm)	16.305	16.313	16.313	16.145	16.313	16.100	16.410	16.683
$\varnothing_e$ (mm)	20.025	20.135	20.135	20.138	20.135	20.000	20.068	20.008
Span (mm)	450.0	450.0	450.0	450.0	450.0	250.5	449.0	250.5
Supports	Original	Original	Original	New	Original	Original	Original	Original
Mould								
Density (kg/m^3)	1285.9	1238.9	1238.9	1231.7	1238.9	1255.1	1314.9	1339.7
E-modulus (GPa)	4.70	5.00	5.00	4.20	5.00	4.70	4.75	4.80
Accelerometer								
Mass (grams)	23.25	23.25	23.25	23.25	5.80	23.25	23.25	23.25
Sensitivity (mV/g)	1000	1000	1000	1000	10	1000	1000	1000
Cement paste								
Cement type	CEM I 42.4R	CEM I 42.4R	CEM I 42.4R	CEM I 42.4R	CEM I 42.4R	CEM I 42.4R	CEM I 52.5N	CEM I 52.5N
w/c	0.50	0.50	0.50	0.50	0.50	0.50	0.54	0.54
Density	1740.9	1789.6	1789.6	1797.9	1789.6	1774.3	1712.6	1700.2

The resonant frequencies identified by the EMM-ARM for the four studied beams are shown in Figure 3.23a. It is worth mentioning the good coherence between the frequency evolutions identified in the different beams, ranging from ~14.9 Hz to 24.9 Hz within the testing period. Moreover, all the frequency evolution curves exhibit an initial dormant period where the frequency remains almost constant with standard deviation (*SD*) of 0.076 during the first 5 hours. After this threshold, the frequencies evolved significantly for all tested specimens until approximately 48 hours of curing period, after which a dramatic reduction in the slope of frequency evolution occurs. The consistency of the identified frequency evolutions indicates right away for the suitability of the new support system. However, the EMM-ARM experiments are targeted to the estimation of the elastic modulus of the material inside the mould, which

should then be assessed. Thus the elasticity modulus of the tested cement paste was estimated by applying equations (2.14) and (2.12) to the resonant frequencies presented in Figure 3.23a. The resulting E-modulus evolution is shown in Figure 3.23b.

Firstly, it is possible to verify that the E-modulus evolution curves estimated from the beams with the same testing apparatus have very good coherence with each other, demonstrating adequate repeatability of EMM-ARM. Furthermore, when comparing the results obtained with the beam with the new support (45-NS-A1-C1), it can be seen that there is an almost perfect superposition of the curves, with a differences always under $SD < 0.25$. Additionally, it can be seen that during the initial dormant period, the estimated E-modulus of the cement paste is almost zero (6.35×10^{-4} GPa with $SD = 0.104$) in all the tests. These results are in agreement to previous applications (Azenha *et al.*, 2012a, Maia *et al.*, 2011a, Maia *et al.*, 2011b, Maia *et al.*, 2012b, Maia *et al.*, 2012c). The similarity of the E-modulus evolutions during the whole curing process of the cement paste allow the validation of the new support system of the EMM-ARM beams.

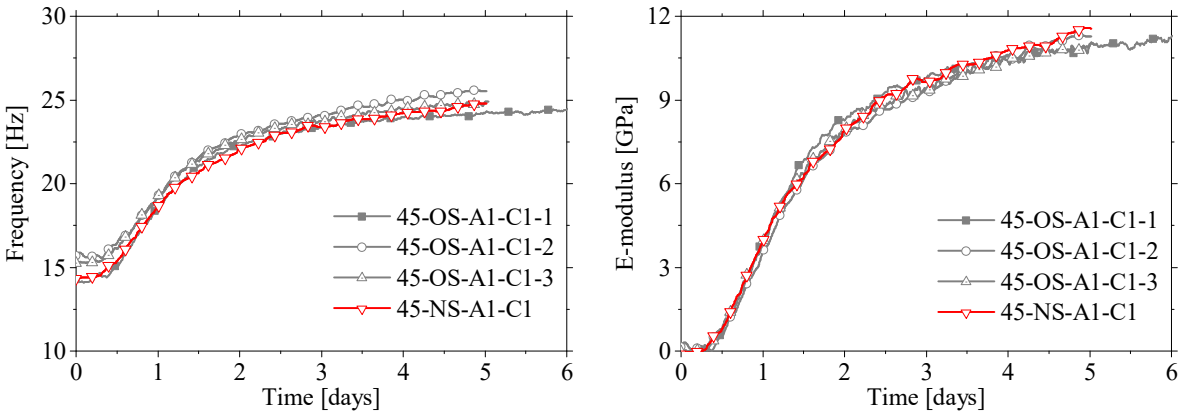

a) b)

Figure 3.23. Cement paste EMM-ARM test 1: a) Identified first resonance frequency evolutions; b) Estimated elastic modulus evolutions.

3.3.2. Mould geometry and accelerometer

In the previous subsection, the issue of supporting the EMM-ARM testing beam has been addressed. However, as mentioned above, the initial version of EMM-ARM applied to cement

paste testing still has problems related to the resolution that can be achieved in the E-modulus measurement. This problem is mainly related to the high slenderness of the test beam and to the ratio between the beam's mass and the mass of the accelerometer on the free end of the beam. Thus, in an attempt to increase the resolution of the method, this subsection presents a study aimed to reduce the slenderness of the beam by reducing its free span. The reduction of the size of the beam is also interesting from the point of view of the study of expensive materials, such as synthesized pure compounds (for example pure Alite) which have considerable manufacturing costs and as such it is intended to use the least possible amount of material.

In order to support the decision about the new span of the beam it was established as a principle that it should have a slenderness closer to the original beam applied to concrete. However, it was necessary to take into consideration that the beam response to the environmental excitation has to be higher when compared to the version for concrete due to lower accuracy of the light weight accelerometers. Therefore, a compromise was established that led to the choice of a 250 mm span which reduces the slenderness (λ) of the beams from 140.56 to 78.09, value rather close to the value used in the original beam applied to concrete (52.99). The slenderness values of the different EMM-ARM moulds are summarised in the Table 3.9.

Table 3.9. EMM-ARM moulds slenderness.

Mould	*Concrete*		*Cement paste*	
characteristics	*O-ACR-1.8*	*O-PVC-1.0*	*45-OS-A1*	*25-OS-A1*
$Ø_i$ (mm)	92.0	96.0	16.0	16.0
$Ø_e$ (mm)	100.0	110.0	20.0	20.0
Span (mm)	1800	1000	450	250
λ_{mould}	52.99	27.40	140.56	78.09

To validate the use of this new geometry test beam, two tests were conducted with two different cement pastes (C1 and C2). The characteristics of the beams as well as the tested cement pastes are shown in Table 3.8. The first resonance frequency evolutions obtained in these two tests are shown in Figure 3.24a. It is noticeable that both the initial resonance frequency and the range of variation of the resonant frequency of EMM-ARM tests is increased in the specimens with 250 mm span (25-OS-A1-C1 and 25-OS-A1-C2) as expected. Moreover, all frequency evolution curves appear to be plausible, showing a shape similar to the ones obtained in previous applications.

Again the elasticity modulus of the two cement pastes was estimated by applying equations (2.14) and (2.12) together with the information shown in Table 3.8 to the resonant frequencies presented in Figure 3.24a. The resulting E-modulus evolution estimates are shown in Figure 3.24b for the two tests. In this figure, it can be observed that the evolution curves of each cement paste are almost overlapping with each other, regardless of the test setup that was used, with differences always under $SD_{C1} < 0.288$ and $SD_{C2} < 0.289$ for cement pastes C1 and C2 respectively. Additionally, it can be seen that even during the initial dormant period the E-modulus estimations were not affected by the span reduction and the initial values obtained at this stage were almost zero (9.20×10^{-4} GPa with $SD = 0.104$ and 3.95×10^{-2} GPa with $SD = 0.0069$ for the cement paste C1 and C2 respectively). Furthermore, when comparing the results obtained with the two pastes (C1 and C2), it can be seen that the E-modulus evolution is a bit faster in the cement paste C2 (CEM I 52.5N and w/c 0.54) in the beginning of the cement hydration and until 1.35 days. Then the cement paste C1 (CEM I 42.5R and w/c 0.5) starts to develop higher stiffness. In the end of the tests, at 10 days, the difference between the two cement pastes is ~1.5 GPa. These results emphasize the ability that the EMM-ARM has to evaluate the kinetics of cement hydration. Furthermore the similarity of the E-modulus evolutions during the whole curing process of the cement paste allow the validation of the reducing the span of the beam to perform EMM-ARM tests.

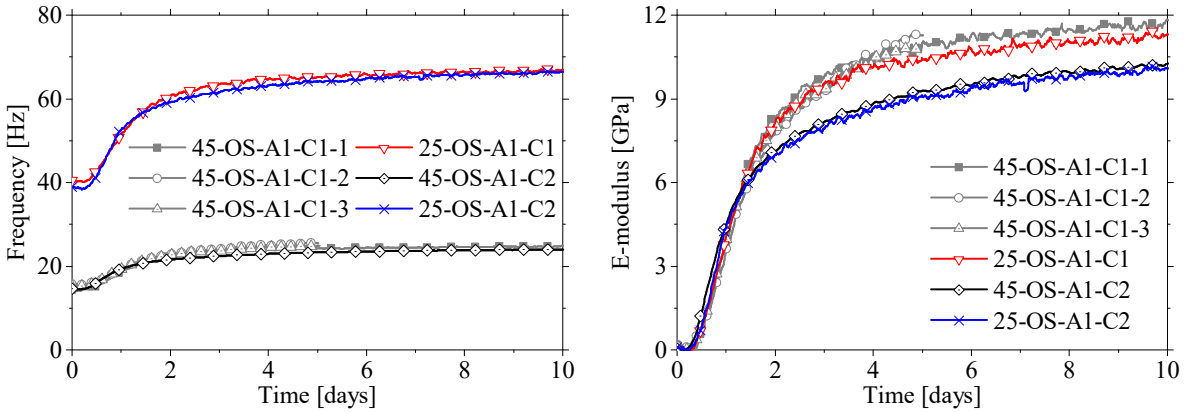

a) b)

Figure 3.24. Results of the cement paste test 2: a) Identified natural frequencies; b) Estimated E-modulus.

As stated before, another important aspect in the test setup is related to the mass placed on the free end of the beam. As can be seen in Table 3.10 the ratio between the mass of the

accelerometer used in the tests and the beams is much higher in variant for cement pastes (45-OS-A1) when compared with the variant for concretes (O-ACR-1.8 and O-PVC-1.0) which leads to a reduction in the resonance frequency variation range along the test and consequently to the reduction of the method resolution.

Table 3.10. Mass ratio between the beam and the accelerometer.

	Concrete		*Cement paste*	
Reference	*O-ACR-1.8*	*O-PVC-1.0*	*45-OS-A1*	*45-OS-A2*
Mould				
γ_{mould} (kg/m^3)	1300	1300	1300	1300
$Ø_i$ (mm)	92.0	96.0	16.0	16.0
$Ø_e$ (mm)	100.0	110.0	20.0	20.0
Testing material				
$\gamma_{material}$ (kg/m^3)	2400	2400	1700	1700
Mass				
$\overline{m}$ (kg/m)	17.52	20.32	0.489	0.489
m_{accel} (kg)	0.22	0.22	0.025	0.0058
$m_{accel}/\overline{m}$ (%)	1.26	1.08	5.11	1.19

Thus a new test was performed in which was intended to investigate the feasibility of using a very light weight accelerometer (PCB 352C04 with 5.8 grams). However, this type of light weight accelerometers typically has very low sensitivity (10 mV/g) which can significantly hinder the identification of the beam vibrations. Therefore, in an attempt to not excessively undermining the identification of the beam resonance frequencies, instead of using a short span beam tested before (which would lead to a reduction in the vibration amplitude), the test beam in this experiment has the same span as shown in Figure 3.22. In this new test the accelerations at the free end were monitored by this new accelerometer here called A2 (45-OS-A2-C1). The test was performed with the cement paste C1.

The identified first resonance frequency of the EMM-ARM beams is shown in Figure 3.25a. First, it is possible to observe the increase in both the resonant frequencies and the variation range of the beam with the lighter accelerometer relative to the previously tested beams. In fact, for the beams with the heavier accelerometers (45-OS-C1-1-A1, 45-A1 OS-C1-2-45 and OS-A1-1-3), the resonance frequencies ranged between 14.9 Hz during the dormant period and 24.9 Hz in the end of the test (that corresponds to a 10 Hz range). In the beam with the lightweight accelerometer A2, the resonance frequencies ranged from 16.8 Hz to 27.9 Hz (11.1 Hz range).

After converting the resonance frequency to the E-modulus of the cement paste the obtained results are shown in Figure 3.25b. There is an almost perfect superposition of the different evolutions, with differences lower than $SD < 0.044$. From this good coherence between the results it can be concluded that the use of low-mass accelerometers improves the resolution of the EMM-ARM tests as the resonance frequency range changed from 9.96 Hz in the beams with the heavier accelerometer (45-OS-A1-C1-1, 2 and 3) to 11.15 Hz (+11.9%) in the beam 45-OS-A2-C1.

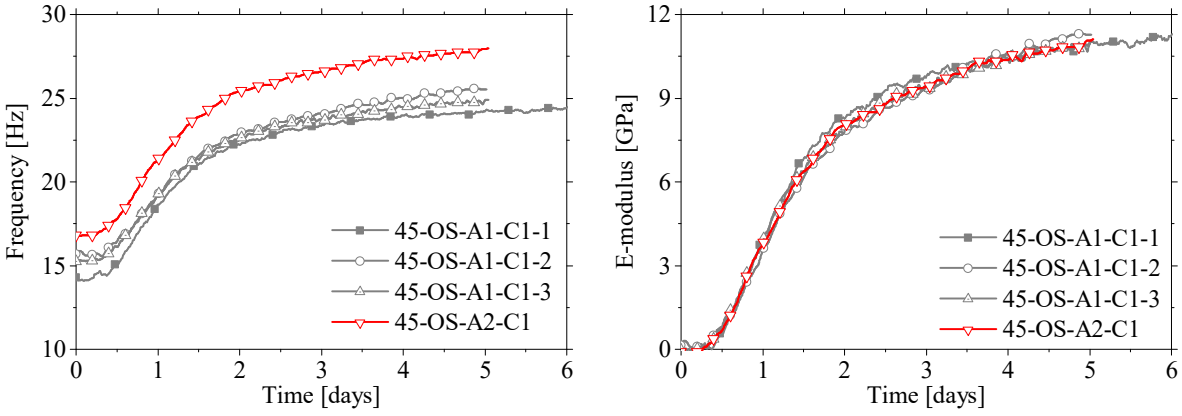

a) b)

Figure 3.25. EMM-ARM results of the cement paste test 3: a) Resonance frequency evolution; b) Estimated cement paste E-modulus.

Chapter 4

Identification of modal parameters

4.1. Introduction

In the previous Chapter, the limitations EMM-ARM were studied in view of issues related to the experimental setup, namely: moulds geometry, materials and support systems, as well as the development of a reusable mould for concrete testing. However, in addition to the aforementioned improvements that solved limitations of the initial versions of EMM-ARM, the method presents another potential problem. The original implementations of EMM-ARM were conducted in laboratorial conditions where the selection of an appropriate place to perform the experiments (where the ambient noise on average in periods of 10 minutes can easily be assumed as a white noise) was quite easy. Nonetheless if this premise is not valid, i.e if the vibrations of the beam are contaminated by noises with well-defined frequencies within the first natural frequency range of the EMM-ARM test the frequency spectra can be affected by these noises that have potential to hinder the frequency identification. However, these issues can be easily avoided by the use of different modal identification techniques where a small excitation is applied to the test specimen (Goodwin and Payne, 1977).

In view of the issue raised in the previous paragraph, this Chapter present a study on the possibility of using different types of vibration tests for EMM-ARM, such as environmental vibration testing and forced vibration. Together with this study will be also evaluated the use of new modal parameters identification techniques. But first a short literature review on dynamic models of structures will be presented to better frame the topic under study.

4.2. Dynamic models of structures

The dynamic structural models aim to characterize the behaviour of structures under dynamic actions. Two different approaches are available for evaluating the structural dynamic behaviour: deterministic and stochastic (Chopra, 1995, Clough and Penzien, 1995, Reynders, 2012, Peeters and De Roeck, 2001, Mendes and Oliveira, 2008). The difference between these two approaches depends upon how the excitation of the structure is defined. To use a deterministic approach, the time variation of the excitation needs to be fully known. On the other hand, if the time variation of the excitation is not completely known (random dynamic/stochastic excitation) but can be defined in a statistical sense a stochastic analysis should be used.

4.2.1. Deterministic systems

4.2.1.1. Linear Equations of Motion

Consider a linear time-invariant vibrating structure with general viscous damping with n_y output degrees of freedom (DOFs) and n_u DOFs of interest. Newton's equations of motion for this type of structures are a set of m second-order differential equations, where m is the number of independent DOFs, given by the equation (4.1) (Chopra, 1995, Mendes and Oliveira, 2008, Reynders, 2012).

$$M \cdot \frac{d^2 v(t)}{dt^2} + C \cdot \frac{dv(t)}{dt} + K \cdot v(t) = B_2 \cdot u(t) \tag{4.1}$$

with M, C and $K \in \Re^{m \times m}$ respectively the mass, damping and stiffness matrices, $v(t) \in \Re^m$ the vector with modal displacements and $B_2 \in \Re^{m \times n_u}$ a selection matrix such that the vector with externally applied forces, $u(t) \in \Re^{n_u}$ has only elements that are not identically zero.

4.2.1.2. Impulse Response

The Impulse Response Function (IRF) $H(t) \in \Re^{n_y \times n_u}$ is defined as the response at DOF l due to an impulsive input along DOF m, applied at $t = 0$ under zero initial conditions on the outputs. Once IRF is determined, the response $y(t)$ at the outputs due to any input vector $u(t) \in \Re^{n_u}$ can be computed by convolution, since any $u(t)$ ca be written as equation (4.2) (Reynders, 2012).

$$u(t) = \int_{\Re} H(t-\tau) \cdot u(\tau)\, d\tau \tag{4.2}$$

Using the assumption that the structure is linear and time-invariant one can obtain:

$$y(t) = \int_{\Re} H(\tau) \cdot u(t-\tau)\, d\tau = H(t) * u(t) \tag{4.3}$$

4.2.1.3. Transfer function

Consider a damped harmonic input at DOF m, $u_m = e^{s \cdot t}$ with $s \in \mathbb{C}$. Using (4.3), the response at DOF l can be computed according to equation (4.4) (Reynders, 2012).

$$y_l(t) = \int_{\Re} H_{lm}(t-\tau) \cdot e^{-s \cdot (t-\tau)}\, d\tau e^{s \cdot t} = H_{lm}(s) \cdot e^{s \cdot t} \tag{4.4}$$

where $H(s)$ is the Laplace transform of $H(t)$. The Laplace transform of the impulse response is called the transfer function and can be written as (Cauberghe, 2004):

$$y(s) = H(s) \cdot u(s) \tag{4.5}$$

The transfer function of a discrete system is defined as the z-transform $H(z)$ of its impulse response (H_k), and the relationship $y(z) = H(z) \cdot u(z)$ still holds. The frequency response function (FRF) $H(\omega)$ is defined as the Fourier transform of the IRF (Cauberghe, 2004).

4.2.1.4. Continuous-Time State-Space Model

The state formulation allows to explore structures where damping is not proportional to the distribution of stiffness and mass, also allowing the construction of mathematical models where the characteristics of the experimental data are specifically considered. This formulation allows the modelling of noise always existent in experimental testing, as well as the construction of models in discrete time, adapted to the use of time series obtained in experimental studies.

State-Space equation

In the state of formulation, the system of differential equations of 2nd order is converted into a system of differential equations of 1st order. By rearranging (4.1) and assuming that M has full rank, a continuous-time state space model (4.6) is obtained (Reynders, 2012).

$$\frac{dx(t)}{dt} = A_C \cdot x(t) + B_C \cdot u(t) \tag{4.6}$$

where

$$x(t) = \begin{bmatrix} v(t) \\ \dfrac{dv(t)}{dt} \end{bmatrix}, \quad A_C = \begin{bmatrix} 0 & I \\ -M^{-1} \cdot K & -M^{-1} \cdot C^v \end{bmatrix}$$

$$\text{and} \quad B_C = \begin{bmatrix} 0 \\ M^{-1} \cdot B_2 \end{bmatrix}$$

The vector $x(t) \in \Re^n$ is called the state of the structure. The number of elements of $x(t)$, n, is called the model order. The state matrix A_C have the following the relationship:

$$A_C = \Psi \cdot \Lambda_C \cdot \Psi^T \tag{4.7}$$

This relationship is very important since shows that the matrices Λ_C and Ψ have, respectively, the eigenvalues and eigenvectors of the state matrix. The dynamic characteristics of a system are in fact described in its state matrix.

Observation equation

If the output quantities of interest are linear combinations of displacements, velocities or accelerations DOFs, it is possible to obtain the equation (4.8) (Reynders, 2012).

$$y(t) = C_{\ddot{v}} \cdot \frac{d^2 v(t)}{dt^2} + C_{\dot{v}} \cdot \frac{dv(t)}{dt} + C_v \cdot v(t) \tag{4.8}$$

where $C_{\ddot{v}} \in \Re^{n_y \times n}$, $C_{\dot{v}} \in \Re^{n_y \times n}$, $C_v \in \Re^{n_y \times n}$ are selection matrices. Considering equation (4.1) and the state vector definition (4.6), the expression (4.8) can be transformed into the equation (4.9) designated by observation equation (Reynders, 2012).

$$y(t) = C_C \cdot x(t) + D_C \cdot u(t) \tag{4.9}$$

where

$$C_C = \begin{bmatrix} C_v - C_{\ddot{v}} \cdot M^{-1} \cdot K & C_{\dot{v}} - C_{\ddot{v}} \cdot M^{-1} \cdot C^v \end{bmatrix}$$

$$\text{and} \quad D_C = C_{\ddot{v}} \cdot M^{-1} \cdot B_2$$

Impulse Response and transfer function

Combining the equations (4.6) and (4.9), a state-space parametrization of the impulse response can be obtained (Reynders, 2012):

$$H(t) = C_C \cdot e^{A_C \cdot t} \cdot B_C + D_C \cdot \delta(t) \tag{4.10}$$

A Laplace transform of both sides of the equations (4.6) and (4.9) results in a parametrization of the transfer function:

$$y(s) = \left(C_C \cdot \left(s \cdot I - A_C\right)^{-1} \cdot B_C + D_C\right) \cdot u(s) = H(s) \cdot u(s) \tag{4.11}$$

4.2.1.5. Discrete-time State-Space Model

Since for a given input $u(t)$, solving the equations (4.6) or (4.8) analytically is usually impossible in the time domain, it seems natural to convert these models to discrete time (Reynders, 2012). Thus, the following equations are obtained:

$$x_{k+1} = A \cdot x_k + B \cdot u_k \tag{4.12}$$

$$y_k = C \cdot x_k + D \cdot u_k \tag{4.13}$$

where

$$A = e^{A_C \cdot \Delta t} \quad ,$$

$$B = \left(A - I\right) \cdot A_C^{-1} \cdot B_C \quad ,$$

$$C = C_C$$

and $D = D_C$

Impulse response

The state equations (4.12) and (4.13) can be solved as (Reynders, 2012):

$$y_k = C \cdot A^k \cdot x_0 + \sum_{l=1}^{k} C \cdot A^{l-1} \cdot B \cdot u_{k-l} + D \cdot u_k \tag{4.14}$$

From this relationship the impulse response (H_k) is then obtained:

$$H_0 = D \quad , \qquad H_k = C \cdot A^{k-1} \cdot B \quad , \quad k > 1 \tag{4.15}$$

Transfer function

The transfer function ($H(z)$) can be obtained by performing the z-transform of both sides of equations (4.12) and (4.13) as shown in the following equation (Reynders, 2012):

$$y(z) = \left(C \cdot \left(z \cdot I + A\right)^{-1} \cdot B + D\right) \cdot u(z) = H(z) \cdot u(z) \tag{4.16}$$

4.2.2. Stochastic systems

The term stochastic excitation is associated with the unknown dynamic action, whose temporal variation is random in nature, i.e. when is impossible to predict the future behaviour of the excitation (Rodrigues, 2004). In these circumstances, the characterization of the dynamic behaviour of structures can only be achieved through the adoption of probabilistic concepts (Chopra, 1995, Clough and Penzien, 1995). Thus, the dynamic behaviour characterization is based on the analysis and interpretation of the structure response, and are specially devoted to the experimental side. In this section some basic concepts of statistics and stochastic processes are introduced, which aim at the study of analytic representation of spectral density functions, a key element in addressing this type of process in the frequency domain (Chopra, 1995, Rodrigues, 2004).

If a stochastic process is stationary and ergodic, the autocorrelation function only includes a realization r and a time lag τ, and can be determined simply by the following expression (Clough and Penzien, 1995, Rodrigues, 2004):

$$R_{xx}(\tau) = \lim_{T \to \infty} \frac{1}{T} \int_{-T/2}^{T/2} x_r(t) \cdot x_r(t+\tau)\, d\tau \tag{4.17}$$

The autocorrelation functions associated with a stationary stochastic processes with zero mean are symmetric functions with a maximum at the origin. By applying a Fourier transform these functions can be converted to the frequency domain. Thus, the auto-spectrum or power spectrum functions are obtained (Rodrigues, 2004):

$$S_{xx}(\omega) = \int_{-\infty 2}^{\infty} R_{xx}(\tau) \cdot e^{-i \cdot \omega \cdot \tau} \, d\tau \tag{4.18}$$

These spectrums are real function that quantifies the distribution of energetic content of the signal along the frequencies. Thus, the area below the graph represents the total energy of the signal.

The response spectral density functions for structures with several degrees of freedom can be defined based on the following expression (Rodrigues, 2004):

$$S_q(\omega) = H(\omega) \cdot S_p(\omega) \cdot H^H(\omega) \tag{4.19}$$

where $S_q(\omega)$ represents the frequency spectrum matrix of the structure, $H(\omega)$ the frequency response function matrix $()^H$ denotes the complex conjugate transposed of the matrix) and $S_p(\omega)$ is the excitation spectrum matrix.

4.2.2.1. Discrete-time stochastic state-space model

By applying model reduction, sampling and modelling the noise, equation (4.1) can be converted to following discrete-time stochastic state-space model (see the detailed derivation in (Peeters and De Roeck, 1999)):

$$x_{k+1} = A \cdot x_k + w_k \tag{4.20}$$

$$y_k = C \cdot x_k + v_k \tag{4.21}$$

where x_k is the discrete-time state vector with the sampled displacements and velocities in instant $k \cdot \Delta t$; y_k is the response vector and contains the sampled accelerations in instant $k \cdot \Delta t$; A is the state matrix; C is the output matrix; w_k is defined as process noise resulting from input perturbations and modeling inaccuracies; and v_k is measurement noise due to transducers and data acquisition disturbances. Both stochastic vectors (w_k and v_k) are impossible to measure but their statistic properties can be assumed as: zero mean and white noise (Rodrigues, 2004, Peeters, 2000).

The modal parameters can be obtained from the matrices A and C. the derivation starts with the eigenvalue deposition of A (Peeters, 2000):

$$A = \Psi \cdot \Lambda_d \cdot \Psi^{-1} \tag{4.22}$$

where Ψ is the eigenvector matrix and Λ_d is a diagonal matrix containing the discrete time eigenvalues. The eigenfrequencies ω_i and damping coefficients ξ_i can be computed from:

$$\mu_i = e^{\lambda_i \cdot \Delta t} \quad , \quad \lambda_i, \lambda_i^* = -\xi_i \cdot \omega_i \pm j\sqrt{1-\xi_i} \cdot \omega_i \tag{4.23}$$

Where Δt is the sampling time. Finally, the mode shapes ϕ can be obtained from:

$$\phi = C \cdot \Psi \tag{4.24}$$

4.3. Modal analysis tests

The identification of modal parameters through dynamic test was originally developed in the fields of mechanics and aerospace engineering (Juang, 1994a). Modal testing is an experimental technique used to derive the modal model of a linear time-invariant vibratory system (He and Fu, 2001). The theoretical basis of the technique is secured upon establishing the relationship between the vibration response at one location and excitation at the same or another location as a function of excitation frequency. Modal analysis involves three constituent phases: data collection, system identification and modal parameter extracting from the identified system.

For the dynamic monitoring structures, depending on the source of excitation are currently used two different groups techniques: experimental modal analysis – EMA (He and Fu, 2001, Ewins, 2000) and operational modal analysis – OMA (Rainieri and Fabbrocino, 2014, Reynders, 2012, Peeters and De Roeck, 2001, Overschee and Moor, 1996).

4.3.1. Experimental modal analysis (EMA)

The EMA tests essentially consists in applying a controlled excitation to the structure under study with low intensity, so that the produced vibration levels do not affect the integrity of the structure, and measuring its response. The forced excitation can be induced by mechanical vibrators or low power explosive. Since in these tests, both the excitation forces and the structure response are measured it becomes possible to perform the evaluation of the impulse response functions (IRF) and the frequency response function (FRF). The first EMA techniques were Single Degree Of Freedom (SDOF) methods like Peak-Picking (PP) or Circle Fitting (He and Fu, 2001). In these methods, it is assumed that each mode can be estimated independently from the other modes, and consequently they are not useful when some modes of interest are closely spaced. This disadvantage was later removed with the introduction of Multiple Degree Of Freedom (MDOF) methods for EMA. Nowadays EMA is a well-established and often-used approach in mechanical engineering, as documented in (Ewins, 2000, He and Fu, 2001). Table 4.1 presents a summary of several algorithms for experimental modal identification. Detailed information about these methodologies may be found in (Caetano, 1992, Ewins, 2000, He and Fu, 2001, Pintelon *et al.*, 1994, McKelvey *et al.*, 1996, Juang and Suzuki, 1988, Juang and Pappa, 1985, Chen *et al.*, 1993)

Table 4.1. EMA system identification methods.

Type of formulation	*Method*
Frequency domain	Peak-picking
	Circle-fit
	Inverse
	Dobson
	Nonlinear LSFD
	Orthogonal Polynomial
	ERA
Time domain	Complex Exponential
	LSCE
	Ibrahim
	ERA
	ARMA

4.3.2. Operational modal analysis (OMA)

OMA is based on the measurement of a structure response to dynamic excitations imposed on the structure due to environmental factors such as wind and urban traffic, which can be defined as the operational conditions. The dynamic response of the structure is acquired through the measurement of the accelerations, velocities or displacements in relevant points of the structure. From the acquired signals the dynamic system is identified, using stochastic modal analysis techniques, and the modal parameters can be estimated based on that system, namely the eigenfrequencies, damping coefficients and modes shapes (Reynders, 2012).

The OMA techniques have the major advantage of not using explicit excitation of structures (Ren and Zong, 2004). This type of modal identification methods, by means of measurements of ambient vibration, has become a very attractive approach to the area of civil engineering structures. In fact these methods has been successfully applied in monitoring the conservation status of many major structures, such as the Golden Gate Bridge (Kim *et al.*, 2007), the Vasco da Gama bridge (Cunha *et al.*, 2001), the suspended roof of the stadium of Braga (Magalhães *et al.*, 2006), among others.

The responses induced by environmental actions have small amplitudes, which requires the use of very sensitive equipments to acquire the response of the structure (Rodrigues, 2004). Fundamentally can be considered two sets of OMA methods: the first group comprises the signal analysis methods, where the measured response series at different points of the structural systems are analysed and related to each other based on the its transformation to the frequency domain – frequency domain methods; the second group corresponds the methods were the acquired repose time series are analysed directly in the time domain – time domain methods. Figure 4.1 shows a summary of the OMA methods.

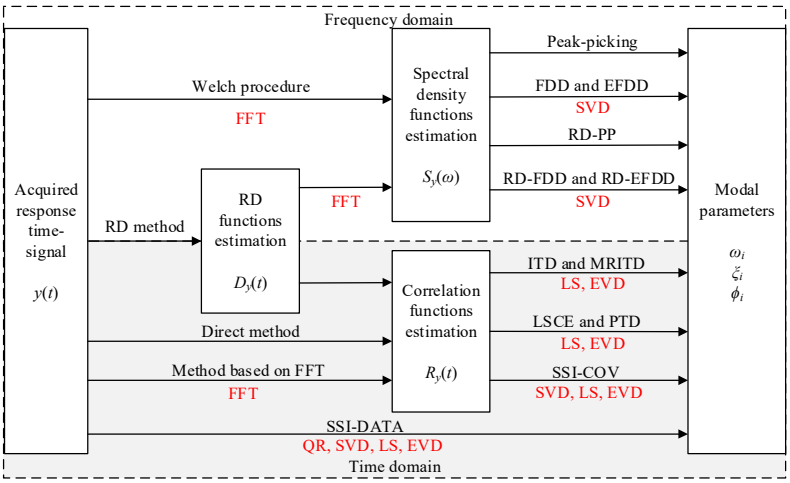

Figure 4.1. General outline of the main OMA methods (FFT – Fast Fourier Transform; SVD – Singular Value Decomposition; LS – Least Squares algorithm; EVD – Eigenvalue Decomposition ; QR – Orthogonal decomposition). Adapted from Rodrigues (2004).

4.4. EMM-ARM adaptations to the modal analysis technique

As already mentioned, EMM-ARM is based on a simple OMA technique of a composite beam called peak-picking. However, the robustness of this technique can be compromised when the tests are performed in places with high contaminations of the ambient noise. In fact, at locations such as construction sites, there frequently exists heavy machinery being operated, which may induce significant environmental vibration at a certain frequency or set of frequencies (e.g. vibrations conducted through air or ground), thus having potential to interfere with in the range of resonant frequencies to be identified with EMM-ARM. In this subchapter the possibility of using both different OMA techniques as well as EMA techniques will be addressed. But first the original OMA technique used in EMM-ARM in the first application will be presented. It should be noted that part of this study was already published in (Granja and Azenha, 2015) and submitted to publication in (Granja and Azenha, 2016).

4.4.1. Operational modal analysis (OMA) tests

4.4.1.1. OMA nonparametric modal identification

The response frequency spectra are the starting point of this group of identification methods, so this subsection start with the demonstration of the algorithm to perform its estimation from the acquired response time series.

Response spectral density function estimation

The most efficient way of evaluating the spectral density functions of a structural system response involves the determination of the Discrete Fourier Transform (DFT) of the response signals (Welch, 1967). However the application of this algorithm result in *leakage* errors (for more information see (Dishan, 1995, Thompson and Tree, 1980)). To reduce the effects of *leakage* before the DFT calculation it should be apply signal processing windows, or windows of data, to the response signals. In the case of random type signals usually *Hanning* window are used. The Fourier Transforms of the discrete-time response signals y_k to which a data window w_k has been applied, are given by:

$$Y(\omega,T)=\Delta t\cdot\sum_{k=0}^{N-1}w_k\cdot y_k\cdot e^{-j\cdot\omega\cdot k\cdot\Delta t} \tag{4.25}$$

where N is the number of discrete signal values y_k, Δt is the time interval between the discrete signal values y_k, ω is the arbitrary frequency and T is the total duration of the signal y_k. The usual choice of discrete values to calculate the Fourier Transform is (Welch, 1967):

$$\omega_n=\frac{m}{N}\cdot\frac{2\pi}{\Delta t},\ m=0,\ 1,\ 2,\ \ldots,\ N-1 \tag{4.26}$$

The frequency resolution in the DFT is therefore equal to the inverse of the total duration of the signals, namely:

$$\omega_n = \frac{m}{N} \cdot \frac{2\pi}{\Delta t} \text{ [rad.s}^{-1}\text{]} \leftrightarrow \Delta f = \frac{1}{N \cdot \Delta t} \tag{4.27}$$

In discrete frequencies ω_m the processed values provide the Fourier components defined by (Rodrigues, 2004):

$$Y_m = \frac{Y_m(\omega_n)}{\Delta t} = \sum_{k=0}^{N-1} w_k \cdot y_k \cdot e^{-j \cdot \frac{2\pi \cdot m \cdot k}{N}} \quad , \quad m = 0, 1, 2, \ldots, N-1 \tag{4.28}$$

An efficient way of making the determination of the DFT is via the Fast Fourier Transform algorithm (FFT). The estimated spectral density functions matrix $\hat{S}_y(\omega_m)$ of y_k responses can then be calculated from its DFT $Y(\omega_m)$ through expression (4.29) (Rodrigues, 2004).

$$\hat{S}_y(\omega_m) = \frac{1}{N \cdot \Delta t \cdot \sum_{k=0}^{N-1} |w_k|^2} \cdot Y_i^*(\omega_m) \cdot Y_i^T(\omega_m) \quad , \quad m = 0, 1, 2, \ldots, N-1 \tag{4.29}$$

However, the application of the Fourier Transforms to discrete signals with finite duration results in spectra with a high variance (see (Welch, 1967) for more information). To reduce this variance, the response records y_k are divided into n_d samples, to each a *Hanning* windows is applied and the corresponding DFT is computed. Finally, the average of all spectra is calculated being obtained a smoothed estimation of the response spectral density functions. To take advantage of all the information contained in the acquired data is usual to overlap in the data division procedure. When *Hanning* windows are used is usual to use an overlap value near half the segment length (50% overlapping) (Welch, 1967).

Pick-picking (PP) method

The Pick-picking (PP) method, systematized in the work Felber (1993), the eigenfrequencies of a structure are identified from the selection of the peaks with highest amplitude in the spectral

density functions. The modal parameters are obtained through the amplitude and phase relationship between a reference point and the measured points. This method is quite simple and fast execution.

The OMA tests may require the acquisition of the structure response in several notable points. Therefore, the spectral analysis of these records will lead to the same number of auto-spectra and also to the cross-spectra between each two response records obtained in different instrumented points. The analysis of these spectral density function, to identify the eigenfrequencies can become extremely laborious. One way to synthesize all of this information is through the Normalized Power Spectrum Density – NPSD (Felber, 1993). These spectra are calculated from the auto-spectra of each record through the following equation:

$$NPSD(\omega_m) = \frac{\hat{S}_y[i,i](\omega_m)}{\sum_{m=1}^{N/2} \hat{S}_y[i,i](\omega_m)} \tag{4.30}$$

The damping coefficient relative to a SDOF oscillator can be determined by the half-power method (Clough and Penzien, 1995). In this method to compute the damping coefficient of each eigenfrequency, it is only necessary estimate the two points with spectral ordered equal to $\alpha_{max}/2$, half the maximum frequency amplitude (α_{max}), defined as ω_b and ω_a. The damping coefficient of the vibration mode i, can then be estimated by the following expression (Chopra, 1995):

$$\xi_i = \frac{\omega_b - \omega_a}{\omega_b + \omega_a} \tag{4.31}$$

However, the damping coefficients estimated by this method are not very accurate (Rodrigues, 2004). This is mainly due to the uncertainty that exists in the selection of half-power points, the frequencies ω_b and ω_a, since the spectral ordinates are defined with a resolution finite frequency $\Delta\omega$.

Case study

In order to compare the accuracy of the methods of identification of modal parameters of an EMM-ARM beam hereinafter all methods will be used in the same case study. This case study consists on a series of OMA and EMA tests in a reusable EMM-ARM beam similar to that shown in Figure 3.17 (page 72) with its characteristics shown in Table 4.2. The tests were performed after 8 days of casting when the concrete casted inside de tube could be considered stable, i.e. without E-modulus evolution in the time-span of the experiments (~3 hours). The resonance frequency, defined here as reference, and the E-modulus of the concrete inside the mould was estimated through an EMM-ARM test using EMA SSI technique as will be presented in section 4.4.2.3.

Table 4.2. Physical and mechanical characteristics of the EMM-ARM beam.

Reference	*OMA-1*
Geometry	
Cross-section	Circular
$\varnothing_i$	95.64 mm
$\varnothing_e$	110.11 mm
Span	1000 mm
Supports	$\varnothing_{PR}$=12 mm Steel supports
Reusable	Yes
Mould	
Density	1239.9 kg/m^3
E-modulus	3.10 GPa
Concrete	
Density	2335.2 kg/m^3
E-modulus	26.56 GPa
Expected frequency	117.20 Hz

In this specific case, the beam was tested under OMA conditions with one fan paced in the vicinity of the tests to increase the air movement and therefore increate the ambient excitation of the beam. The response of the beam was acquired with one high precision accelerometer PCB 393B12 (sensitivity: 10 V/g; range: ±0.5 g) attached to the top part of the beams mid-span connected to a data acquisition system NI 4431 with an analogue to digital converter with 24 bits. The test was performed during 30 min with a sampling rate of 10 kHz. A part of the acquired signal is shown in Figure 4.2.

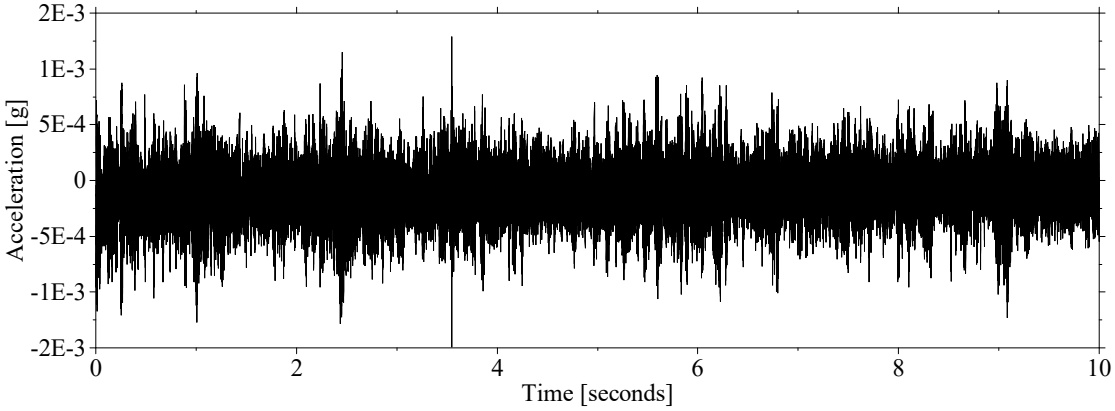

Figure 4.2. Raw acquired data in OMA.

From Figure 4.2 it possible to observe that the amplitude of vibration of the EMM-ARM beam under OMA testing is very low. Nevertheless, the sensitivity of the accelerometer together with the data acquisition system resolution used in the tests seems to be adequate since the whole system has a sensitivity of 2.4×10^{-5} g. However, one can extrapolate that is not for the signal to be contaminated with ambient noises with the same amplitude or even higher.

Regarding the signal processing, the FFT algorithm was performed with 2^{14} points (16 384). *Hanning* windows were used to decrease the *leakage* effect with 50% overlap. By using equation (4.27) is possible to verify that the final NPSD has a resolution of 0.6103 Hz. The resulting NPSD is shown in Figure 4.3a. As can be seen, the NPSD shows several peaks that correspond to different vibration modes of the beam. However, together with peaks that correspond to modes of vibration, it is possible to observe several peaks from ambient noise, despite lower amplitude than the peak of the resonance frequency of the beam's first mode of vibration. Nevertheless, these noisy peaks can easily hinder the automatic peak identification, and more advanced techniques might be necessary to be applied.

Through the use of PP method is possible to estimate the frequency and damping coefficient of the first mode of vibration, as shown in Figure 4.3b. The estimated frequency was 117.798 Hz, value that has a non-negligible difference, 0.598 Hz (+0.51%), form the expected 117.20 Hz. However, the difference between the two values is lower than the frequency resolution of the NPSD, showing that although the method's precision is adequate, the frequency resolution plays a very important rule and is an issue difficult to solve. The resolution can be increased by

increasing the acquisition time which, however, is not a feasible operation when the material inside the beam is in the hardening process.

As shown in Figure 4.3b the damping coefficient was accessed using equation (4.31). The value obtained was 1.202%. This value also allows to validate the assumption on which the identification of the frequencies in the original implementation EMM-ARM was based on which it is assumed that the damped frequencies are equal to the undamped ones. In fact, if the estimated damping coefficient value is valid, the difference between the two frequencies, undamped and damped, is only 0.007%.

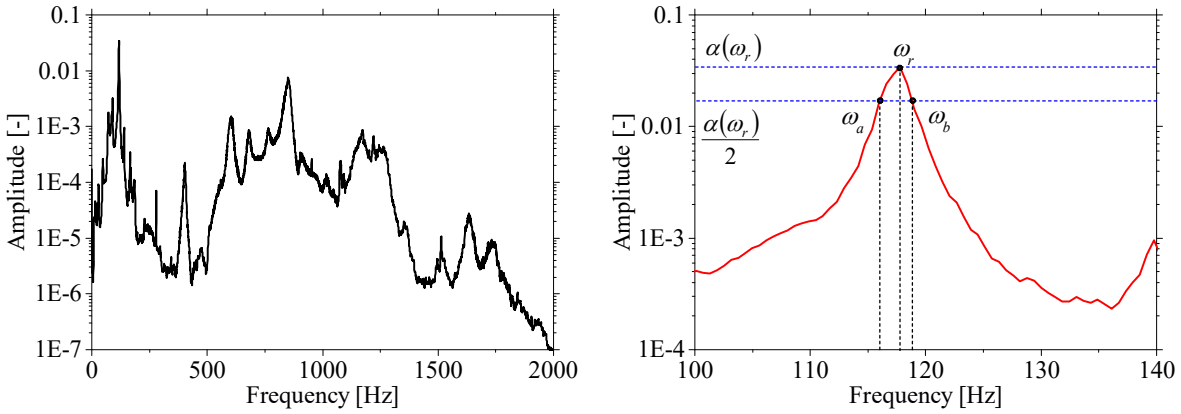

Figure 4.3. a) Normalized Power Spectrum Density (NPSD); b) Peak-picking OMA identification method.

Inverse Fourier Transform (IFT)

Another method to identify the modal parameters of a system based on its response frequency spectra is by using the Inverse Discrete Fourier Transform (IDFT). Transforming spectral density functions of a SDOF system to the time domain by IDFT (with the Inverse Fast Fourier Transform (IFFT) algorithm), one obtains the corresponding auto-correlation functions from which it is possible to estimate the eigenfrequencies and damping coefficients. The damping coefficient is determined using the logarithmic decrement δ of the positive and negative maximum of the auto-correlation function which is defined by the following expression (Brinker *et al.*, 2001):

$$\delta = \frac{2}{k} \cdot \ln\left(\frac{r_0}{|r_k|}\right) \tag{4.32}$$

where r_0 is the initial value of the auto-correlation function and r_k is the value of the logarithmic decrement in the point k. Both the logarithmic decrement and the initial value of the auto-correlation function can be obtained through a linear regression in $k \cdot \delta$ and $\ln(|r_k|)$ and the damping coefficient is obtained from (Brinker *et al.*, 2001):

$$\xi = \frac{\delta}{\sqrt{\delta^2 + 4 \cdot \pi^2}} \tag{4.33}$$

The frequency is estimated by linear regression of the time where the auto-correlation function crosses the zero.

Case study

Regarding the same case study presented before, only the frequency spectrum between 0 and 395 Hz was selected in order to eliminate the influence of vibration modes higher than the first. By applying the IFFT algorithm to the selected region of the spectrum is possible to obtain the auto-correlation function shown in Figure 4.4.

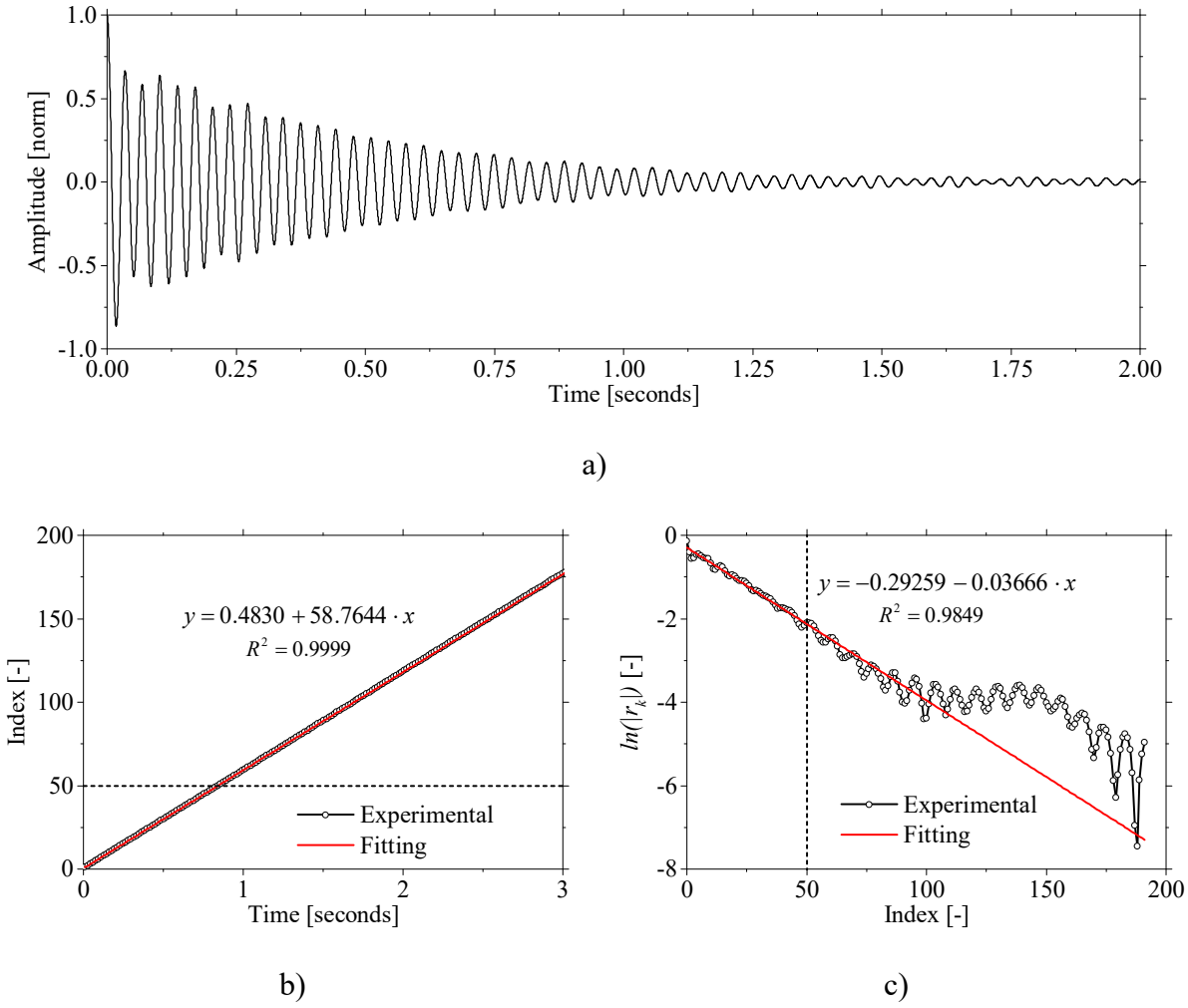

Figure 4.4. OMA IFT results: a) Auto-correlation function; b) Zero-crossing of the auto-correlation function; c) Evolution of the logarithm of the positive and negative maximums.

As mentioned, from the auto-correlation function of a SDOF oscillator is possible to determine the eigenfrequency and the correspondent damping coefficient. The variation of the zero crossing points with the time instant at which they occur (for the frequency determination) and the evolution of the logarithm of the positive and negative maximums with the number of indexes (for the damping coefficient determination) are shown, respectively, in Figures 4.4b and 4.4c. From the slope of a linear curve fit at the first 50 points of the curves it was possible to estimate the frequency of 117.529 Hz and the damping coefficient of 0.583%. The estimated frequency is more accurate than the one identified through the PP method when compared with the reference value. However, the estimation of the damping coefficient if strongly influenced by the noise level present in the response frequency spectrum.

Despite the problems in the damping coefficient estimation, with this method it is possible to eliminate the uncertainty about what is the peak in the frequency spectrum that is related with the structural response of the structure (problem of the PP method).

4.4.1.2. OMA parametric subspace system identification

Until this point all the modal identification used in EMM-ARM tests were based only on frequency domain modal identification methods (non-parametric methods). However, the accuracy of these methods has high sensitivity to the noise level of the measuring environment, as already observed in the first work with EMM-ARM (Azenha *et al.*, 2010a) and also in the previous subchapter. The time domain methods (also known as parametric methods) (Peeters, 2000, Peeters and De Roeck, 1999, Overschee and Moor, 1996) are usually more robust and less sensitive to noise levels (Rodrigues, 2004).

In the approach devised here, the Stochastic Subspace Identification (SSI) parametric method (Peeters and De Roeck, 1999) was chosen to estimate the modal parameters in EMM-ARM. Time discrete models require that the continuous response (e.g. structural accelerations recorded along a time interval) can be represented with a certain fixed sampling period Δt. Then, the response can be discretized and solved at every instant t_k, where $t_k = k \cdot \Delta t$ and k is an integer. If it is assumed that excitation forces are unknown but exhibit white noise properties, the discrete-time state model presented by the equations (4.20) and (4.21) can be assumed (Juang, 1994b).

The main objective of the SSI method is the identification of the state matrix A and the output matrix C (equations (4.20) and (4.21)) which contain the information about the resonant frequencies, mode shape vectors and damping coefficients (Deraemaeker *et al.*, 2008, Rodrigues, 2004, Peeters, 2000, Peeters and De Roeck, 1999).

Considering that the output covariance Λ_ι and the state-output covariance G matrices are defined as (Reynders, 2012):

$$\Lambda_\iota = E\left[y_{k+1} \quad y_k^T\right] \tag{4.34}$$

$$G = E\left[x_{k+1} \quad y_k^T\right] \tag{4.35}$$

where y_k are the recorded outputs of the system. Stochastic system realization starts with gathering output correlation matrices in a block Hankel matrix (Reynders, 2012):

$$L_{1|\iota} = \begin{bmatrix} \Lambda_1 & \Lambda_2 & \cdots & \Lambda_\iota \\ \Lambda_2 & \Lambda_3 & \cdots & \Lambda_{\iota+1} \\ \vdots & \vdots & \ddots & \vdots \\ \Lambda_\iota & \Lambda_{\iota+1} & \cdots & \Lambda_{2\cdot\iota-1} \end{bmatrix} \tag{4.36}$$

where $\imath$ is chosen in such a way that, if n is the expected system order, $n_y \cdot \imath \geq n$, $n_u \cdot \imath \geq n$ and $\imath \geq 2$. The block Hankel matrix decomposes into the extended observability matrix O_ι and the stochastic controllability matrix C_ι (Reynders, 2012):

$$L_{1|\iota} = O_\iota \cdot C_\iota \tag{4.37}$$

where

$$O_\iota = \begin{bmatrix} C \\ C \cdot A \\ \vdots \\ C \cdot A^{\iota-1} \end{bmatrix} \tag{4.38}$$

$$C_\iota = \begin{bmatrix} G & A \cdot G & \cdots & A^{\iota-1} \cdot G \end{bmatrix} \tag{4.39}$$

The matrices O_t and C_t can be obtained from $L_{1|t}$, up to a similarity transformation of the A matrix, using reduced singular value decomposition (Zeiger and McEwen, 1974):

$$L_{1|t} = U \cdot S \cdot V^T \tag{4.40}$$

$$O_t = U \cdot S^{1/2} \tag{4.41}$$

$$C_t = S^{1/2} \cdot V^T \tag{4.42}$$

where S contains only the nonzero singular values and U and V contain the corresponding singular vectors. The C matrix can be determined as the first n_y rows of O_t and the G matrix as the first n_u columns of C_t. For the determination of A, there are several different algorithms (Kung (Kung, 1978), Zeiger-McEwen (Zeiger and McEwen, 1974) and Eigensystem Realization Algorithm (ERA) (Juang and Pappa, 1985)). Kung's algorithm makes use of the shift structure of the matrix O_t (Reynders, 2012)

$$A = \underline{O_t}^{\dagger} \cdot \overline{O_t} \tag{4.43}$$

where "†" denotes the Moore-Penrose pseudo-inverse, $O_{\underline{t}}$ is equal to O_t without the last n_y rows and $O_{\overline{t}}$ is equal to O_t without the first n_y rows.

The results from the SSI method can be observed in a stabilization diagram (Figure 4.5 computed from the case study presented before), which results from the information of matrices A and C (Peeters and De Roeck, 1999). In this diagram the parameters in a range of model orders, the so-called stochastic state-space realizations, are presented. The horizontal axis regards to the frequencies, whereas the vertical axis is related to all model orders (also known as the state space dimension, which is the dimension of the matrix A). The physical modes reveal themselves as straight vertical lines, according to several criteria (isolated or combined), such as: frequency, mode shape, and damping. In opposition, noise modes will appear scattered all over the diagram. At this stage, and based in the stabilization diagram, the user should select a model order, according to the stable vertically aligned poles. Normally this procedure is not straightforward, as the selection of the model order depends on the experience of the user and on the quality of data.

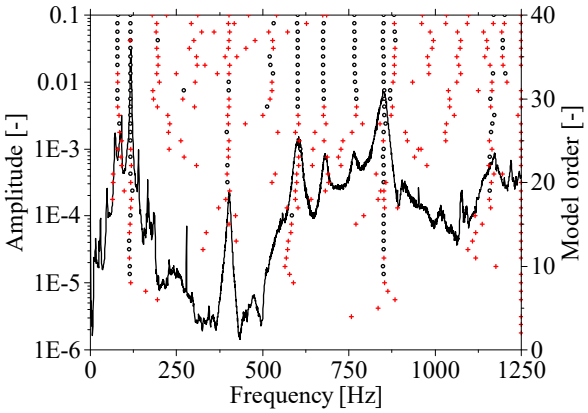

Figure 4.5. Stabilization diagram of the Stochastic Subspace Identification method (Symbols: '○' stable pole: damping coefficient between 0.1 and 10%, relative frequency variation < 3% and relative damping coefficient variation < 15% (Reynders, 2012); '+' unstable pole).

Case study

Considering the same case study presented in the section 4.4.1.1, the SSI OMA technique was applied to the acquired response accelerogram presented in Figure 4.2. The stabilization diagram of the SSI method is shown in Figure 4.5. For the definition of a stable pole it was defined that the damping coefficient should be between 0.1 and 10% and the relative variation of the frequency and damping coefficient between two consecutive model orders should be under 3% and 15%, respectively. Taking in to consideration these criteria, one can observe that there are 6 stable poles, denoted in the diagram as a series of sable poles vertically aligned. However, in this method with the use of only one monitoring point of the structure's response is impossible to select the pole that corresponds to the first mode of vibration of the EMM-ARM beam. Thus a preprocessing step is taken to allow the identification of the desired pole. This preprocessing step corresponds to the use of the nonparametric IDFT technique presented before to identify the frequency (or at least a closer frequency) and then use this information to select the desired pole.

By using a model order of 40 a frequency of 117.321 Hz was identified. This value is significantly more accurate than the one obtained from the previous nonparametric OMA techniques with a difference from the expected of 0.10%. Additionally, a damping coefficient of 0.383% was identified, value that is considerably different from the previous ones. However, one should keep in mind that the previous values could have a high estimation error.

4.4.1.3. Comparison between the OMA techniques

The identified modal parameters though the OMA techniques are surmised in Table 4.3. From this table it is clear that the Subspace System Identification (SSI) technique is the more accurate one and the peak-picking (PP) techniques, the one in which the original EMM-ARM method was based, is the less accurate, when compared with the reference value. However, despite the increase in accuracy with the use of SSI techniques to perform the modal parameters identification, these techniques are still very sensitive to the ambient noise.

Table 4.3. Identified modal parameters though the OMA techniques.

Method	*Frequency (Hz)*		*Damping (%)*
		Dif. from ref.	
PP	117.798	0.51%	1.202
IFFT	117.529	0.28%	0.583
SSI	117.321	0.10%	0.383
Reference	117.200		

Second case study

To further validate the OMA techniques presented before a second case study was used. This second case study had two purposes: first validate the accuracy of the techniques along an entire EMM-ARM tests where the frequencies of the testing beam evolve; and second to check the sensitivity to the ambient noise of each technique. In this second case study the 'U-shaped' version of EMM-ARM described in the section 3.2.1.1 was tested inside a prefabrication industry plant, in parallel with the production/testing of a 27.4 m long prestressed concrete beam for a bridge in Portugal. The characteristics of the beam are shown in Table 4.4. It was decided to perform the test in a prefabrication industry plant to intentionally contaminate the response signals with harmonic noises, difficult to separate from the signal.

Table 4.4. Physical and mechanical characteristics of the EMM-ARM beam tested in the second case study.

Reference	*OMA-1*
Geometry	
Cross-section	'U'
$\varnothing_i$/Height	150 mm
$\varnothing_e$/Width	150 mm
Span	2405 mm
Connectors (spacing)	No
Supports	Concrete cubes
Mould	
Material	Steel
Density	7800.0 kg/m^3
E-modulus	170.0 GPa
Concrete density	2450.0 kg/m^3

The previous implementation of EMM-ARM relied on the use of a single accelerometer for the modal identification. In this case study the use of three accelerometers to record the beams response was also checked. The two additional accelerometers were attached to the beam at 750 mm for each side from the center accelerometer placed at mid span of the beam as shown in Figure 3.3 (page 54). The use of three accelerometers allows modal identification to be easier, as more information can be perceived in regard to relative ordinates in the modal shape. Thus, the first flexural resonant frequency can be much easier to recognize due to the well-known expectable mode shape.

The same accelerometers presented in the first case study were used (sensitivity of 10 V/g, within the range ±0.5 g). Fans were placed in the vicinity of EMM-ARM specimen to increase the ambient vibration associated to air movement (random turbulent motion). The conrete used in these tests had the composition shown in Table 4.5

Table 4.5. Concrete composition tested in the second case study.

Component	*Mix (kg/m^3)*
Sand	418 (fine) 377 (coarse)
Gravel	1006 (5/15)
Cement	430 (CEM I 42.5R)
Water	143 l/m^3
Super plasticiser	3.90 (Polycarboxylic ether polymers)

The identified resonant frequencies and damping coefficients along time, that were identified with the three OMA techniques presented before (PP, IFT, SSI computed with information provided with only one accelerometer SSI-1A) and with the additional SSI technique SSI-3A (computed with the use of the information form the three accelerometers) from the EMM-ARM specimen are shown in Figures 4.6a and 4.6a. It can be observed that all the techniques were able to identify the frequency evolution of the EMM-ARM beam with a very plausible shape. However, it is clear that the accuracy of the different identification techniques is quite different. To illustrate the accuracy and precision of each technique the normal distribution of the identified frequencies was computed. But first the all the values were normalized to a reference value at the age of testing computed from a curve fitting of the equation (4.44) (Carette, 2015) to the identified frequency evolution with the SSI-3A technique, as shown in Figure 4.6c.

$$f(t) = a_1 \cdot e^{-\left(\frac{\tau_1}{t}\right)^{\beta_1}} + a_2 \cdot e^{-\left(\frac{\tau_2}{t}\right)^{\beta_2}} + a_3 \qquad (4.44)$$

$$f_0 = a_3 \quad , \quad f_{ult} = a_1 + a_2 + a_3$$

The normal distributions of the frequency identification along the whole EMM-ARM tests form the four distinct techniques are shown in Figure 4.6d.

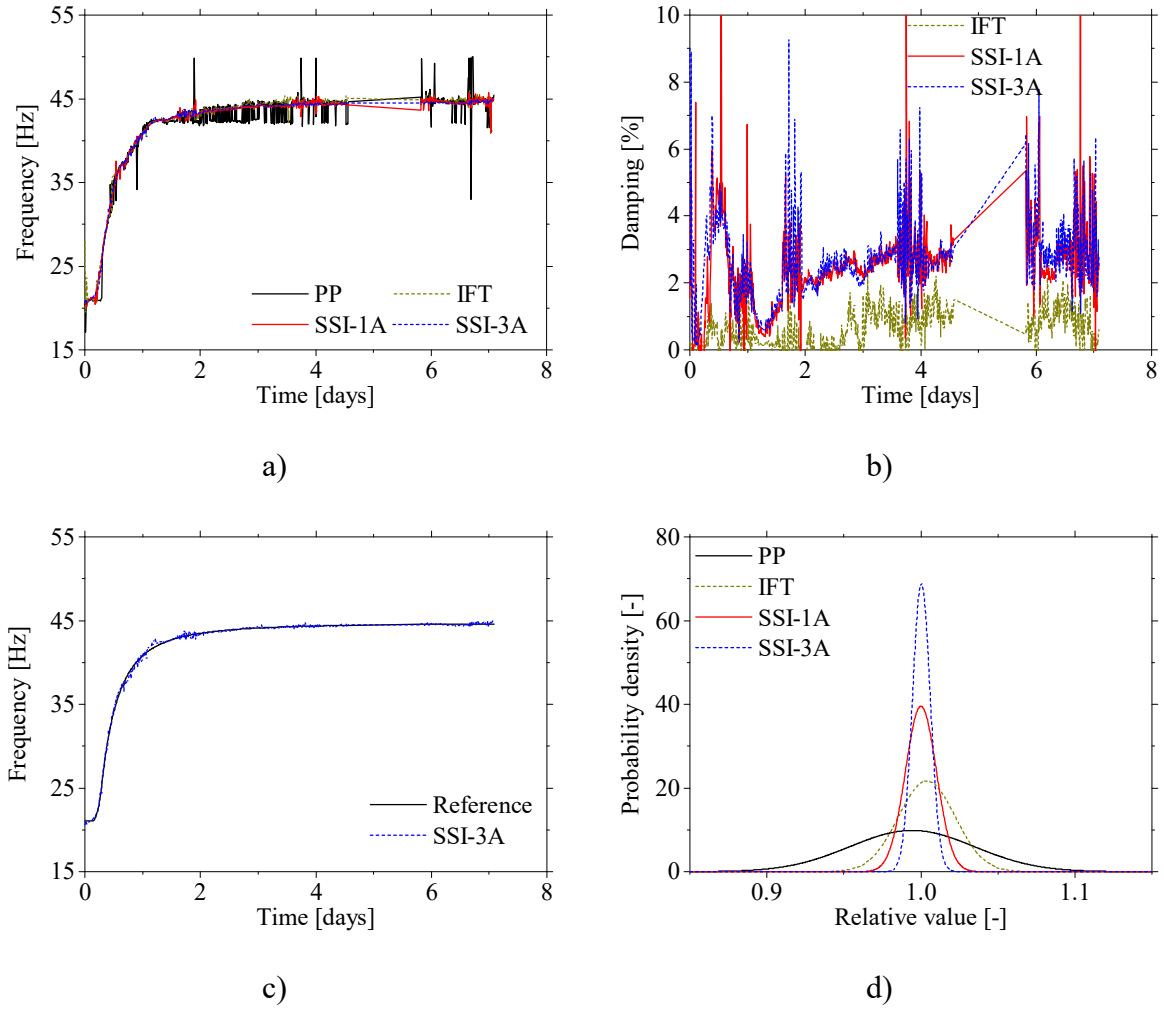

Figure 4.6. Second case study OMA results: a) Fully automatic frequency evolution identified with four distinct approaches; a) Fully automatic damping coefficient evolution identified with IFT, SSI-1A and SSI-3A; c) Curve fitting of the frequency evolution obtained through SSI-3A; d) Accuracy and precision of the OMA methods.

As can be seen the more accurate and precise technique was the SSI-3A with an average (μ) of 1.000 and a Standard Deviation (SD) of 0.0058 and on the opposite side is the PP with $\mu = 0.993$ and $SD = 0.0316$. However, the use of three accelerometers to perform the modal identification only marginally improved the identification precision since the SSI-1A had $\mu = 1.000$ and $SD = 0.0101$.

Regarding the identification of the damping coefficient evolution, shown in Figure 4.6b, one should remark that only the parametric identification methods were able to identify the evolution even with a big dispersion of the results.

These results enable to conclude that the use of parametric SSI techniques improve the accuracy of the EMM-ARM frequency estimation and allow to estimate, even with high dispersion, the damping evolution, when compared with the original identification technique used in EMM-ARM tests.

4.4.2. Experimental modal analysis (EMA) tests

As stated in Chapter 2, the EMM-ARM is based on OMA of a composite beam. However, as presented before, the robustness of these techniques can be compromised when the tests are performed in places with high contaminations of the ambient noise. In fact, at locations such as construction sites, heavy machinery being operated frequently exists, which may induce significant environmental vibration at a certain frequency or set of frequencies (e.g. vibrations conducted through air or ground), thus having potential to interfere with the EMM-ARM resonant frequencies identification. This section the potential to change the modal identification technique used in EMM-ARM through the use of EMA techniques will be investigated. By application of these techniques, the sensitivity of the modal identification to the ambient noise is strongly reduced and the response of the beam is amplified which simplifies the identification process of resonance frequency, and opens pathways for a fully automated procedure, regardless of the testing site.

4.4.2.1. Excitation issue

Even though EMA techniques can increase the accuracy of the modal identification of the composite beam, it has to be taken into account that the induction of an external vibration during the curing period of the cementitious materials may potentially affect the development of the mechanical properties, particularly during the setting time when bonds are being formed in the cement matrix that can be damaged due to the vibrations. This issue was studied by several authors (Dunham *et al.*, 2007, Hong and Park, 2015, Fernandes *et al.*, 2011) and it was found that excessive vibration during the curing process can affect the elastic modulus by almost 10%. Also in the work of Hong and Park (2015) it was found that even small vibrations (with maximum accelerations of 14.4 mg at 5 Hz) can have a relevant impact in the concrete curing process and affect its mechanical properties. Based on these evidences it was established that the use of forced vibrations techniques should be quite limited in terms of vibration intensity

applied to the material, as to make the impact of such vibration negligible on the setting and hydration processes.

In addition to the excitation intensity issue, it is also necessary to take into consideration that the application of equation (2.11) presented in section 2.5.3 demands a structural system comprised of a simply supported beam with an added mass at mid-span, but does not include any potential interaction issues with an actuator system. Therefore, the actuator must not introduce any added vertical stiffness to the system, otherwise a spring would have to be considered (and dully quantified) in the boundary conditions used to derive the equation.

In this way a custom electromagnetic actuator was developed, specially designed to be able to apply a very small dynamic force to the testing beam without physical contact between the actuator and the beam. A representation of this custom made electromagnetic actuator is shown in Figure 4.7. The force is applied to the beam through a magnet (made of neodymium N50 with remanence: B_r=1.4T; ∅ = 8 mm; height = 20 mm) that is physically attached to the bottom of the beam at mid span. On the opposite side, the magnet is surrounded by a coil (made with copper wire with 0.22 mm in diameter and 3140 turns; $\varnothing_{int}$ = 10 mm $\varnothing_{ext}$ = 25 mm). When subjected to a given current intensity, this coil creates a magnetic field dependent on the current polarity and intensity. The coil's frame was built in a non-ferromagnetic material (plastic) to prevent interaction between the magnet attached to the beam and the body of the actuator, which could again introduce an effect similar to that of an elastic spring at mid span of the beam.

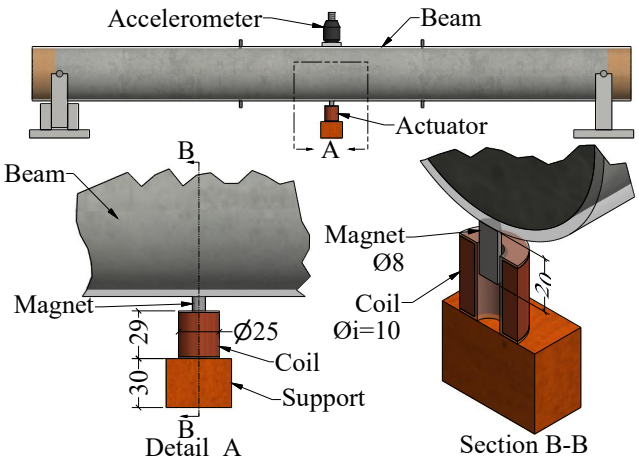

Figure 4.7. Custom made non-contact electromagnetic actuator attached to an EMM-ARM beam [units: mm].

Before starting the implementation of a different modal analysis testing technique to EMM-ARM, a test was performed to characterize the excitation that the developed actuator can exert on an EMM-ARM acrylic beam with the same characteristics of the beam O-ACR-0.9-MS shown in Table 3.7 (page 73). Before the beginning of the test the E-modulus of concrete inside the acrylic mould was accessed through OMA with PP method of the beam. The concrete inside the beam had 63 days of age and it was verified that it had an E-modulus of 30.8GPa (obtained through an EMM-ARM OMA test with PP identification technique) at the time of testing. Regarding the test procedure with forced excitation, a sine function was sent in a continuous sweep of frequencies with 40 seconds duration between 20 and 200 Hz with an amplitude of ±2.4 V, through a dynamic signal analyser NI 4431 with 24-bit resolution, at a sampling frequency of 20 kHz. To measure the force applied to the beam and the level of induced accelerations, a piezoelectric impedance sensor (PCB 288D01 with sensitivity to accelerations of 100 mV/g in the range of reading ±50 g and sensitivity to forces of 22.4 mV/N in the range of reading ±222.4 N) was placed between the magnet and the beam.

Figure 4.8 depicts the induced voltage, as well as the resulting forces and accelerations that were input to the beam during 16 cycles that operated in the vicinity of the resonance frequency (163.0 Hz). It can be observed that the amplitude of the excitation force ranged ±8 mN and is constant throughout this specific stretch of the frequency sweep. Despite the very low excitation force range, as can be seen in Figure 4.8b, it is sufficient to create a response with enough acceleration amplitude to be detectable by the accelerometer. The maximum response of the beam was in a range of ±6 mg, value that according to the study of Hong and Park (2015) is small enough to avoid changes in the mechanical properties. Based on the level of excitation and maximum response of the beam it can be concluded that this test procedure should be suitable for application to an EMM-ARM beam along the concrete curing, without disturbing/damaging the microstructural development.

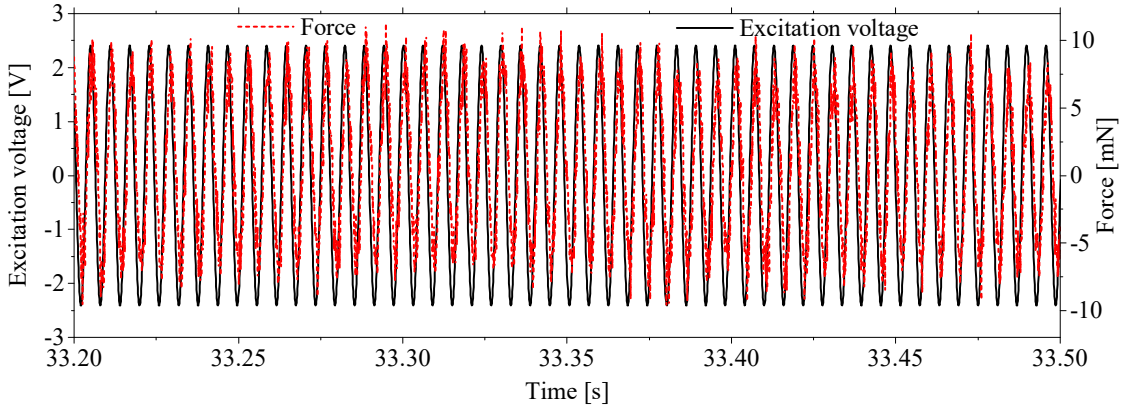

a)

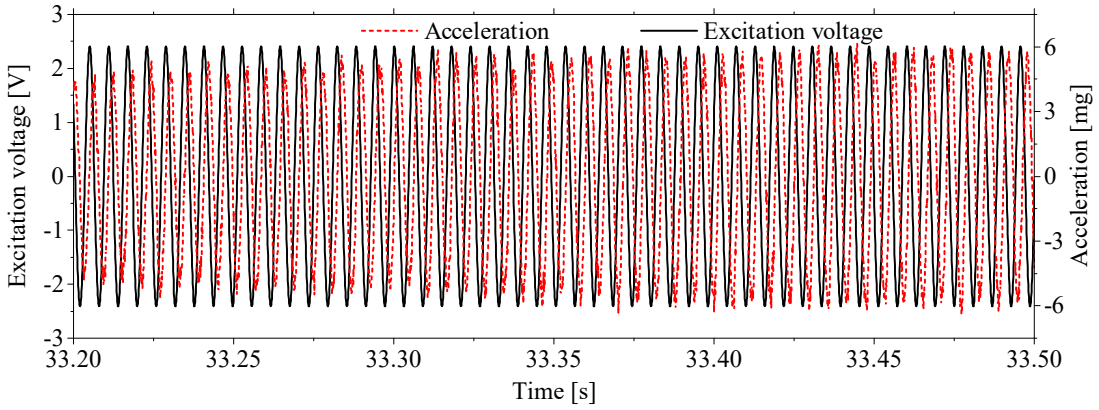

b)

Figure 4.8. Excitation imposed to the EMM-ARM beam: a) Excitation voltage and force applied; b) Excitation voltage and acceleration response.

4.4.2.2. EMA nonparametric modal identification

Pick-picking (PP) method

This method is identical to the PP method presented previously in OMA techniques. However, in this group of methods the modal identification is made from the estimated IRF or FRF of the system rather than through the structure response spectra (He and Fu, 2001). In the context of this thesis the modal parameters were estimated through the FRF that, in the frequency domain (defined here as $H(\omega)$), can be defined by the ratio of the cross-spectrum excitation-response $S_{fy}(\omega)$ and the auto-spectrum of the excitation $S_{ff}(\omega)$ (Oppenheim *et al.*, 1989), as shown in the equation (4.45).

$$H(\omega)=\frac{S_{fy}(\omega)}{S_{ff}(\omega)} \tag{4.45}$$

For estimating damping, the half power points at ω_a and ω_b are obtained from each side of the identified peak with amplitude $\alpha_{max}/\sqrt{2}$, where α_{max} is amplitude of the identified peak. The damping coefficient is then computed by applying equation (4.31).

Case study

Consider the same beam presented in the first case study of this Chapter. The EMM-ARM beam was also tested with EMA techniques. The excitation of the beam was made by the custom made electromagnetic actuator presented in Figure 4.7 at the mid span of the beam. The excitation signal was a sine sweep with linear frequency variation between 10 and 2000 Hz during 100 seconds with constant maximum force amplitude of 8 mN. The test was made during 400 seconds at an acquisition rate of 10 kHz. A segment of the acquired data, force and acceleration, both at mid span, is shown in Figure 4.9.

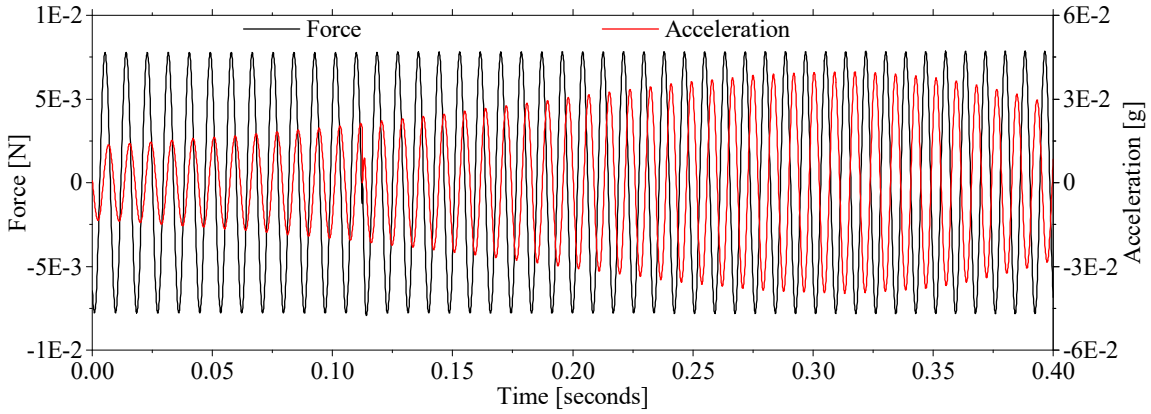

Figure 4.9. Raw acquired data in EMA.

From the raw acquired data, it is possible to compute the Normalized Power Spectrum Density (NPSD) of both the excitation and the response of the beam. The FFT algorithm was performed with 2^{15} points (32 768). *Hanning* windows were used to decrease the leakage effect with 50% overlap. Through the use of equation (4.27) is possible to verify that the final NPSD has a resolution of 0.3051 Hz. The obtained spectra are shown in Figures 4.10a and 4.10b. From these

spectra one can conclude that the amplitude of the excitation was enough to eliminate the effect of all the contaminations in the frequency spectra from the ambient noise, even when a lower acquisition time and a higher number of points in the FFT algorithm were used. However, despite the NPSD of the response being much cleaner and with a higher frequency resolution, since the excitation of the beam was explicitly measured it is possible to compute the FRF of the system through the use of equation (4.45). The amplitude and phase angle of the FRF are shown in Figures 4.10c and 4.10d, respectively.

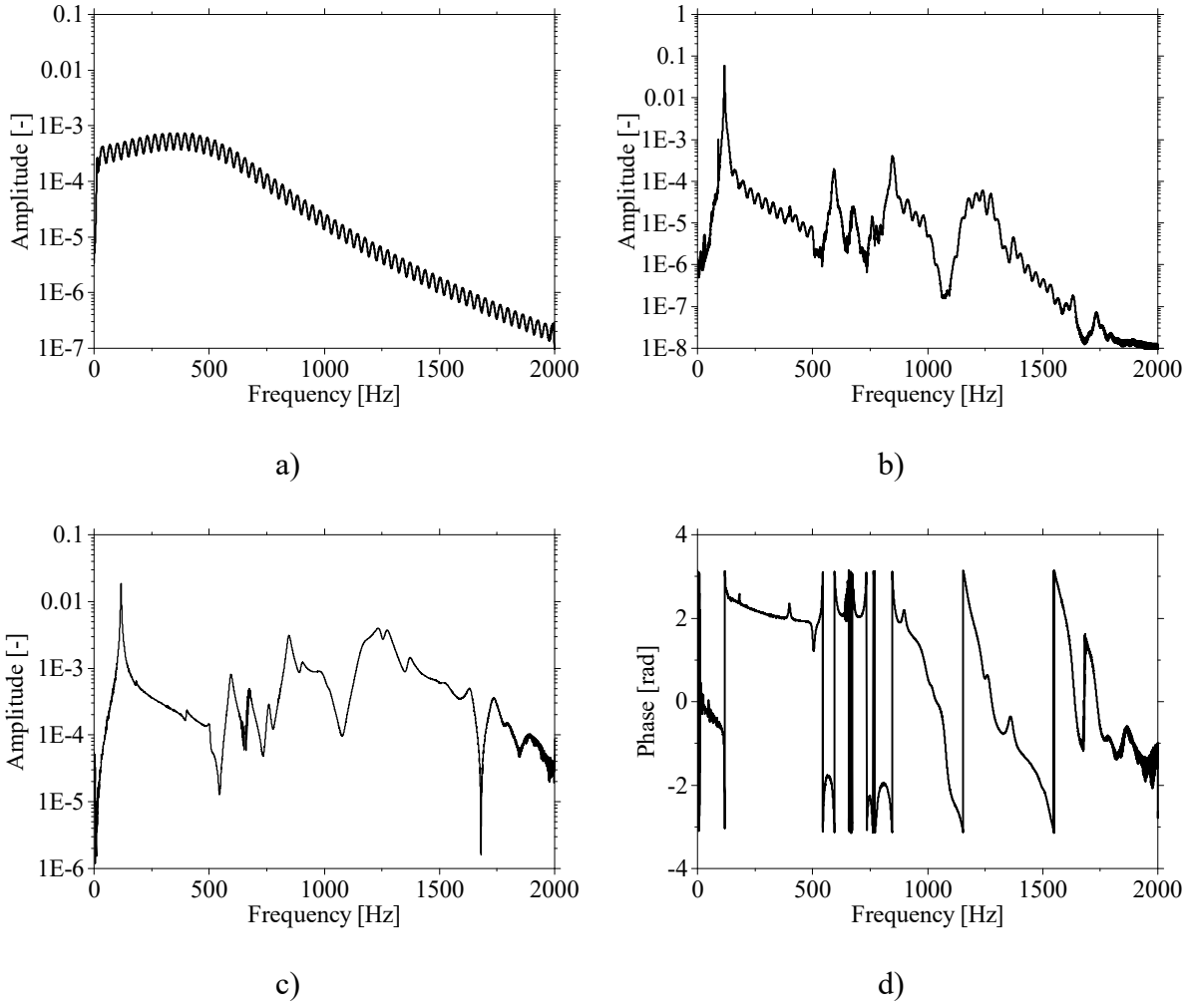

Figure 4.10. EMA EMM-ARM results: a) NPSD of the excitation; b) NPSD of the response; c) Amplitude of the Frequency Response Function (FRF); c) Phase of the FRF.

Looking to the FRF amplitude in Figure 4.10c it became clear what is the peak with higher amplitude, that corresponds to the first mode of vibration of the EMM-ARM beam. By selecting that peak it was possible to identify a frequency of 117.493 Hz that is a better approximation of

the expected frequency than the one identified by the OMA PP technique. However, the difference is still not negligible (0.25%). After the section of the frequency of the first mode of vibration, the damping coefficient was estimated, as can be seen in Figure 4.11. The estimated value was 1.169% that is close to the value obtained in the OMA PP technique.

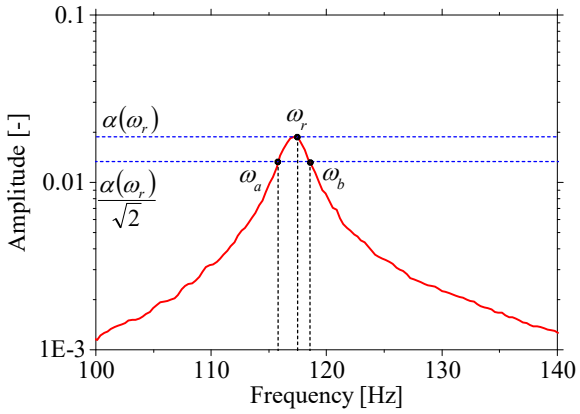

Figure 4.11. EMA PP technique frequency and damping coefficient identification.

Inverse Fourier Transform (IFT)

Similar to the OMA IFT technique, in EMA the same strategy can be followed by simply replacing the NPSD of the response by the amplitude of the FRF. Apart from that change all the procedure remains the same.

Case study

In the case study, the IFFT algorithm was applied to the FRF spectrum. However, it should be noted that only the spectrum frequency between 0 and 395 Hz was used in order to eliminate the influence of the vibration modes higher than the first. The obtained Auto-correlation function is shown in Figure 4.12a.

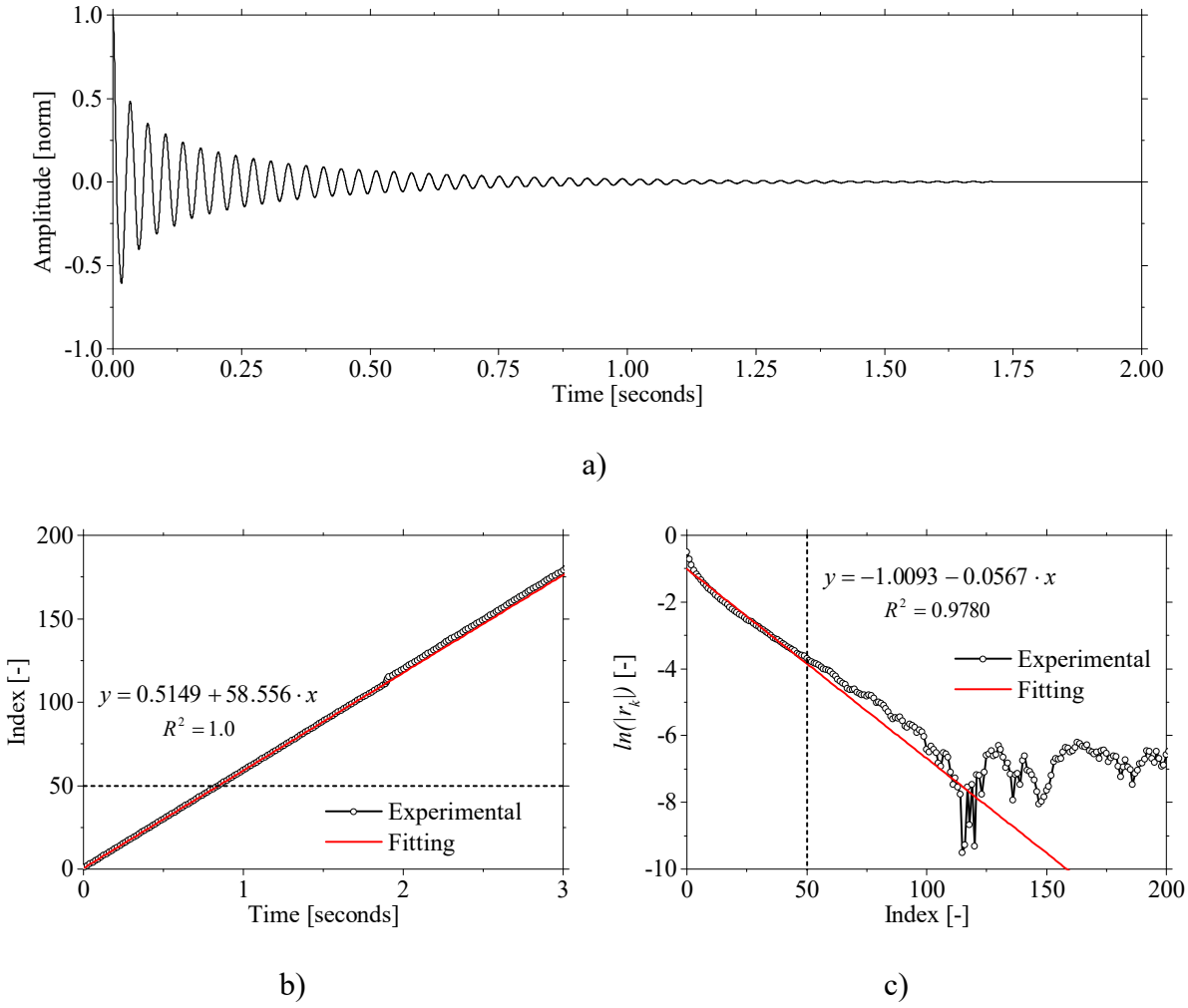

Figure 4.12. EMA IFT results of case study: a) Auto-correlation function; b) Zero-crossing of the auto-correlation function; c) Evolution of the logarithm of the positive and negative maximums.

From a linear curve fitting to the evolution of the zero crossing points with of the time instant at which they occur and the evolution of the logarithm of the positive and negative maximums with the number of indexes, shown in Figures 4.12b and 4.12c, at the first 50 points it is possible to estimate the frequency of 117.112 Hz and the damping coefficient of 0.903%, respectively. The identified frequency is very close to the expected with a difference of only 0.06%. Also the estimated damping is reasonable close to the value obtained from the OMA PP and EMA PP.

4.4.2.3. EMA parametric modal identification

Despite the increase in the identification accuracy by using very simple EMA techniques, this improvement can be enhanced through the use of more advance EMA identification techniques. Instead of looking to the FRF data, by using parametric identification techniques is possible to identify the properties of the system that is under test and from that system extract the modal parameters. There are several parametric techniques available to perform the system identification, based on time domain or in frequency domain. However the frequency domain methods has the following advantages (Pintelon *et al.*, 1994): it is easy to reduce the noise; the non-excited frequency lines are eliminated; the processing time is reduced since a large number of time-domain samples are replaced by a small number of spectral lines; no initial state estimation of the system is needed; and when periodic excitations are used the quality of estimated FRF is increased. Thus in the context of these thesis only frequency domain methods will be presented.

In frequency domain there are two different methods to perform the system identification: the Parametric Identification of the Transfer Function and the Deterministic Subspace Identification. In the following section the identification procedures will be presented and its performance will be verified with a case study.

EMA Parametric Identification of the Transfer Function (TF)

Consider the linear dynamic time-invariant continuous-time system. The objective is to estimate the real coefficients $P = (\alpha_0, \alpha_1, \ldots, \alpha_n, \beta_0, \beta_1, \ldots, \beta_n)^T$ of the rational transfer function model $H(s,P)$, equation (4.46), of order n/d using a discrete set of measured input-output spectra $(X_m(\omega_k), Y_m(\omega_k) : k = 1, 2, \ldots, F)$ or measured frequency response data $(H_m(\omega_k) : k = 1, 2, \ldots, F)$ (Pintelon *et al.*, 1994).

$$H(s,P) = \frac{N(s,P)}{D(s,P)} = \frac{\sum_{k=0}^{n} \alpha_k \cdot s^k}{\sum_{k=0}^{d} \beta_k \cdot s^k} \tag{4.46}$$

The estimates are found by minimizing (in each step) a "quadratic-like" cost function K (Pintelon *et al.*, 1994):

$$K = E^T \cdot E \tag{4.47}$$

where E is a nonlinear vector function of the measurements and the model parameters. Often a Newton-Gauss type algorithm is used to minimize equation (4.47). The i^{th} iteration step of this algorithm is given by (Pintelon *et al.*, 1994):

$$\left(J^{(i)}\right)^T \cdot \left(J^{(i)}\right) \cdot \Delta P^{(i+1)} = -\left(J^{(i)}\right)^T \cdot E^{(i)} \tag{4.48}$$

here $J^{(i)}$ denotes the Jacobian of the vector E evaluated at $P^{(i)}$ ($J^{(i)} = \partial E/\partial P^{(i)}$). To estimate the model parameters, the objective is to minimize the following cost function (Pintelon *et al.*, 1994):

$$K = \sum_{k=1}^{F} \left| H_m(\omega_k) - H(\omega_k, P) \right|^2 \tag{4.49}$$

which is nonquadratic in the parameters. Finally, the poles of the structure are obtained by computing the roots of the denominator polynomial of the estimated transfer function. From the poles, the modal parameters (eigenfrequencies and damping coefficients) can be estimated using equation (4.23).

Case study

The FRF estimated in the previous section, shown in Figure 4.10c, was processed using the strategy presented before. First, to check the most adequate orders of the numerator and denominator polynomials, a stabilization diagram was constructed. It was assumed that the orders of the two polynomials should remain equal and the maximum order was defined as 50. To define a pole as stable the following roles were followed: the damping coefficient should be between 0.1 and 10% and the relative frequency and damping coefficient variations should be less than 3 and 15%, respectively. The resulting stabilization diagram is presented in Figure

4.13a together with the FRF amplitude estimated through the TF model of 50th order. It is clear that only 7 stable poles are present in the diagram (defined as a series of consecutive stable poles in a vertical alignment).

The estimated FRF from the 50th order model was compared with the FRF experimentally obtained, as shown in Figures 4.13b, 4.13c and 4.13d. An almost perfect fitting of the FRF was obtained. From the identified TF model one can obtain the frequency and the damping coefficient of the first mode of vibration of 117.160 Hz and 1.109%, respectively. The identified frequency is very close to the expected value with an error of only 0.04%. It should also be noted that the damping coefficient estimation in this technique is very stable and the value is considerable close (taking in to account the variance that the parameter exhibit in the current case study) to the one identified in by the OMA PP, EMA PP and EMA IFT techniques.

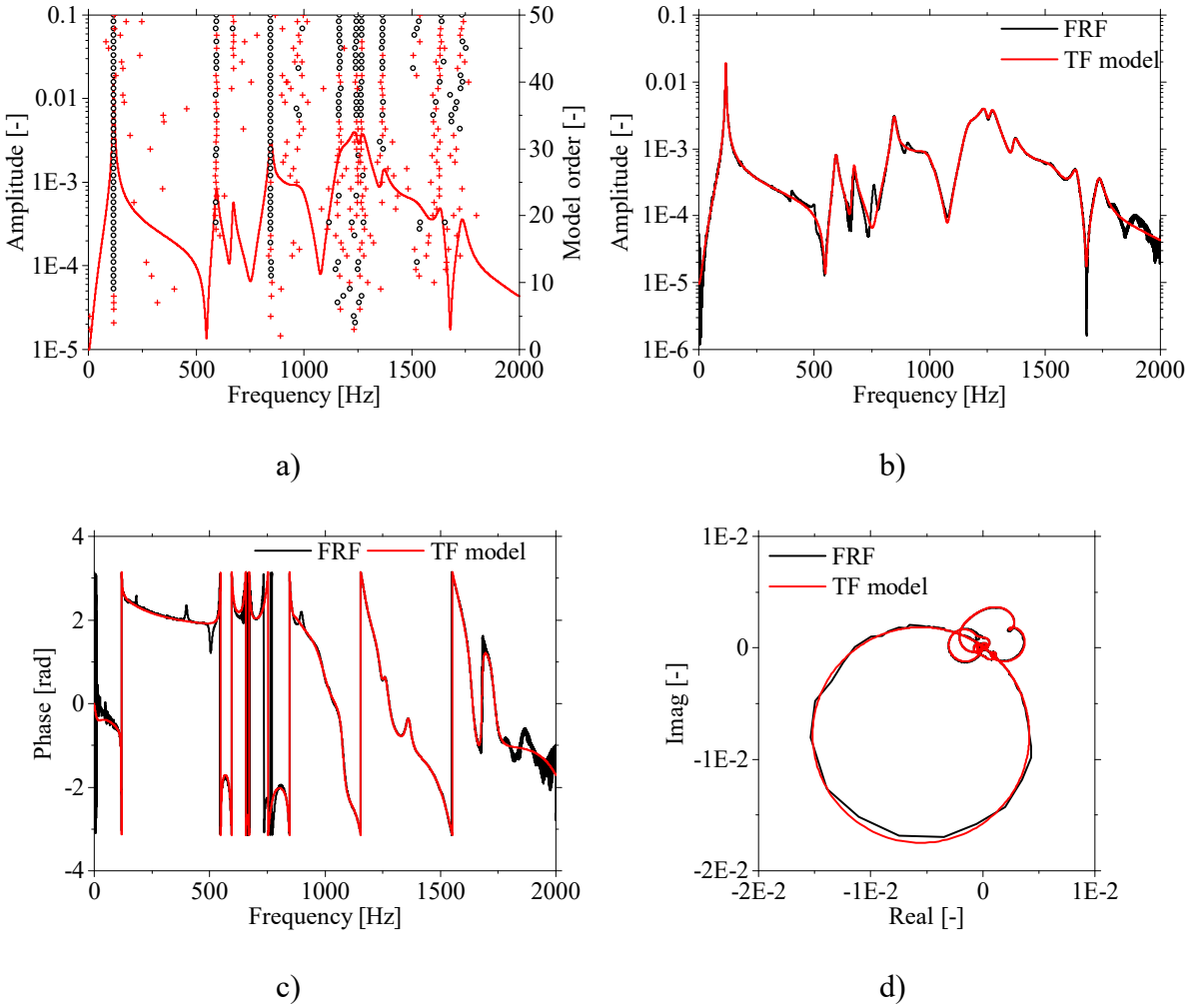

Figure 4.13. EMA TF results: a) Stabilization diagram (Symbols: '○' stable pole: damping coefficient between 0.1 and 10%, relative frequency variation < 3% and relative damping coefficient variation < 15%); b) FRF amplitude fitting; c) FRF phase fitting; d) FRF real *vs* imaginary fitting.

Deterministic Subspace System Identification (SSI)

The objective of a parametric identification is to identify state space models (equations (4.12) and (4.13)) from the given frequency response data. The relation between the state-space model and the Frequency Response Function (FRF) $G(\omega_i)$ is (Chen *et al.*, 1993):

$$G(\omega_i) = C \cdot \left(e^{j \cdot \omega_i \cdot \Delta t} \cdot I_n - A\right)^{-1} \cdot B + D \tag{4.50}$$

Where ω_i are the frequencies in rad/second and Δt the sampling time interval. Given $G(\omega_i)$, the problem of parametric identification is to find a set of matrices, denoted by $\hat{A}$, $\hat{B}$, $\hat{C}$ and $\hat{D}$ (hereafter "^" denotes and estimated value), such that the estimated FRF ($\hat{G}(\omega_i)$) (4.51) matches $G(\omega_i)$ optimally under some optimally criterion (Chen *et al.*, 1993).

$$\hat{G}(\omega_i) = \hat{C} \cdot \left(e^{j \cdot \omega_i \cdot \Delta t} \cdot I_n - \hat{A}\right)^{-1} \cdot \hat{B} + \hat{D} \tag{4.51}$$

Note that $G(\omega_i)$ is a matrix of dimension $m \times r$. If the 2-norm of the error is to be minimized, then an appropriate error index is (Chen *et al.*, 1993):

$$J = \sum_{i=0}^{l} \varpi^2(\omega_i) \left\| G(\omega_i) - \hat{G}(\omega_i) \right\|_2^2 \tag{4.52}$$

Where $\varpi(\omega_i)$ is a specified frequency weighting function and l is the total number of frequencies. However, minimizing equation (4.52) with the respect to the state-space parameters directly is a nonlinear problem, which may be difficult to solve. To avoid the difficulties associated with the nonlinear optimization, one possible alternative is to optimize first with respect to the Markov parameters and then convert the Markov parameters to a space-state model, as optimizing equation (4.52) with respect to the Markov parameters is a linear problem. To formulate this alternative mathematically, it begins with expanding equation (4.50) (Chen *et al.*, 1993):

$$\begin{aligned} G(\omega_i) &= D + C \cdot B \cdot e^{-j \cdot \omega_i \cdot \Delta t} + C \cdot A \cdot B \cdot e^{-j \cdot 2 \cdot \omega_i \cdot \Delta t} + C \cdot A^2 \cdot B \cdot e^{-j \cdot 3 \cdot \omega_i \cdot \Delta t} + \ldots \\ &= \sum_{k=0}^{\infty} Y_k \cdot e^{-j \cdot k \cdot \omega_i \cdot \Delta t} \end{aligned} \tag{4.53}$$

where $Y_0 = D$, $Y_k = C \cdot A^{k-1} \cdot B$ ($k = 1, 2, \ldots, \infty$) are the Markov parameters.

Replacing the equation (4.53) in to equation (4.52) yields (Chen *et al.*, 1993):

$$J = \sum_{i=0}^{l} \varpi^2(\omega_i) \left\| G(\omega_i) - \sum_{k=0}^{\infty} \hat{Y}_k \cdot e^{-j \cdot k \cdot \omega_i \cdot \Delta t} \right\|_2^2 \tag{4.54}$$

However, the problem associated with this approach is that theoretically the number of Markov parameters is infinite. To avoid the problem of excessive number of parameters in the optimization, an intermediate step should be taken. That is, curve-fit the FRF data using a finite-ordered matrix-fraction first and then construct the Markov parameters from this result.

Linear Curve-fitting

The transfer function matrix of the system described by equations (4.12) and (4.13) the transfer can be expressed by a Left Matrix-Fraction Description(LMFD) as (Chen *et al.*, 1993):

$$G(z^{-1}) = R^{-1}(z^{-1}) \cdot S(z^{-1}) \tag{4.55}$$

where both $R(z^{-1})$ and $B(z^{-1})$ are matrix polynomials:

$$R(z^{-1}) = I_m + R_1 \cdot z^{-1} + \ldots + R_p \cdot z^{-p} \tag{4.56}$$

$$S(z^{-1}) = S_0 + S_1 \cdot z^{-1} + \ldots + S_p \cdot z^{-p} \tag{4.57}$$

This factorization is also not unique. For convenience one can choose the orders of both polynomials to be equal (= p) (Chen *et al.*, 1993). Pre-multiplying equation (4.55) by $R(z^{-1})$ one has:

$$R^{-1}(z^{-1}) \cdot G(z^{-1}) = S(z^{-1}) \tag{4.58}$$

which can be rearranged to become:

$$\begin{aligned} G(z^{-1}) = &-R_1 \cdot G(z^{-1}) \cdot z^{-1} - ... - R_p \cdot G(z^{-1}) \cdot z^{-p} + S_0 \\ &+ S_1 \cdot z^{-1} + ... + S_p \cdot z^{-p} \end{aligned} \tag{4.59}$$

Because $G(z^{-1})$ is known at $z = e^{j\omega_i \Delta t}$, ($i = 1, \ldots, l$), the equation (4.59) is linear and there are a total of l equations available (Chen *et al.*, 1993). Denoting $e^{j\omega_i \Delta t}$ by z_i and stacking up the l equations, one has:

$$\Phi \cdot \Theta = \Psi \tag{4.60}$$

where

$$\Phi = \begin{bmatrix} G^T(z_1^{-1}) \cdot z_1^{-1} & \cdots & G^T(z_1^{-1}) \cdot z_1^{-p} & I_r & z_1^{-1} \cdot I_r & \cdots & z_1^{-p} \cdot I_r \\ G^T(z_2^{-1}) \cdot z_2^{-1} & \cdots & G^T(z_2^{-1}) \cdot z_2^{-p} & I_r & z_2^{-1} \cdot I_r & \cdots & z_2^{-p} \cdot I_r \\ \vdots & \vdots & \vdots & \vdots & \vdots & \vdots & \vdots \\ G^T(z_l^{-1}) \cdot z_l^{-1} & \cdots & G^T(z_l^{-1}) \cdot z_l^{-p} & I_r & z_l^{-1} \cdot I_r & \cdots & z_l^{-p} \cdot I_r \end{bmatrix}$$

$$\Theta^T = \begin{bmatrix} -R_1 & \cdots & -R_p & S_0 & \cdots & S_p \end{bmatrix}$$

$$\Psi^T = \begin{bmatrix} G(z_1^{-1}) & G(z_2^{-1}) & \cdots & G(z_l^{-1}) \end{bmatrix}$$

Equation (4.60) is a normal equation, where a least-squares solution of Θ can be found.

Estimation of Markov parameters

After obtaining a solution to equation (4.60), it is now necessary to construct the system Markov parameters (Chen *et al.*, 1993). Equation (4.58) can be written as:

$$\left(\sum_{i=0}^{p} R_i \cdot z^{-i} \right) \cdot \left(\sum_{i=0}^{\infty} Y_i \cdot z^{-i} \right) = \sum_{i=0}^{p} S_i \cdot z^{-i} \tag{4.61}$$

From this relation, the following equations are derived by equating terms of like powers and recalling equations (4.56) and (4.57):

$$Y_0 = S_0 \tag{4.62}$$

$$Y_k = S_k - \sum_{j=1}^{k} R_j \cdot Y_{k-j} \quad \text{for } k = 1, \ldots, p \tag{4.63}$$

$$Y_k = -\sum_{j=1}^{p} R_j \cdot Y_{k-j} \quad \text{for } k = p+1, \ldots, \infty \tag{4.64}$$

Identification of state-space models

Once the Markov parameters are constructed, the Eigensystem Realization Algorithm (ERA) can be used to obtain a state-space model (Chen *et al.*, 1993). The ERA uses singular value decomposition to decompose a data matrix (referred to as the general Henkel matrix) and to compute a state-space model from the decomposed matrices (Bayard, 1994, Juang and Pappa, 1985).

The Eigensystem Realization Algorithm in Frequency Domain (ERA-FD) begins by forming the $r \times (N+1)$ complex block matrix, called Henkel matrix (H). If one consider any r and s such that $r+s \leq N$ and $\min(r, s) \geq 2 \cdot p$, the Hankel type matrices H_0, H_1 can be defined as (Bayard, 1994):

$$H_0 = \begin{bmatrix} Y_1 & Y_2 & \cdots & Y_s \\ Y_2 & Y_3 & \cdots & Y_{s+1} \\ \vdots & \vdots & \ddots & \vdots \\ Y_r & Y_{r+1} & \cdots & Y_{r+s-1} \end{bmatrix} \tag{4.65}$$

$$H_1 = \begin{bmatrix} Y_2 & Y_3 & \cdots & Y_{s+1} \\ Y_3 & Y_4 & \cdots & Y_{s+2} \\ \vdots & \vdots & \ddots & \vdots \\ Y_{r+1} & Y_{r+2} & \cdots & Y_{r+s} \end{bmatrix}$$

After the formation of the Henkel matrices a balanced state-space realization using the ERA algorithm needs to be computed. First the Singular Value Decomposition (SVD) of H_0 is performed (Bayard, 1994):

$$H_0 = U \cdot \Sigma \cdot V^T \tag{4.66}$$

where $\Sigma = \text{diag}[\sigma_1, \ldots, \sigma_\mu]$, and $\mu = \min(r \cdot n_y, s \cdot n_u)$. By plotting the Hankel singular values σ_i the trade-off between model order and identification accuracy can be visualized, and one can truncate to keep only q singular values. From the q-th order state-space realization as (Bayard, 1994):

$$x_{k+1} = A_q \cdot x_k + B_q \cdot u_k \tag{4.67}$$

$$y_k = C_q \cdot x_k + D \cdot u_k \tag{4.68}$$

where

$$A_q = \Sigma_q^{-1/2} \cdot U_q^T \cdot H_1 \cdot V_q \cdot \Sigma_q^{-1/2} \tag{4.69}$$

$$B_q = \Sigma_q^{1/2} \cdot V_q^T \cdot E_u \tag{4.70}$$

$$C_q = E_y^T \cdot U_q \cdot \Sigma_q^{1/2} \tag{4.71}$$

$$D = H_0 \tag{4.72}$$

$$E_y^T = \begin{bmatrix} I_{n_y \times n_y} & O \end{bmatrix} \tag{4.73}$$

$$E_u^T = \begin{bmatrix} I_{n_u \times n_u} & O \end{bmatrix} \tag{4.74}$$

$$\Sigma_q = diag\left\{\sigma_1, \ldots, \sigma_q\right\} \tag{4.75}$$

U_q – submatrix formed from first q columns of U

V_q – submatrix formed from first q columns of V

Then from the eigenvalue decomposition of the matrix A tis possible to estimate the modal parameters of the system: damped angular eigenfrequencies and damping coefficients of the eigenmodes from the imaginary and real parts respectively.

Case study

Similarly to the previous case, the EMA SSI technique was applied to the FRF data. First to check the most adequate model order a stabilization diagram was constructed. The maximum order was again defined as 50 and the same criteria as used to define a pole as stable. In the stabilization diagram, shown in Figure 4.14 (with the FRF estimated from the 50^{th} order SSI model), it is possible to observe 14 stable poles (represented as a series of stable poles vertically aligned).

In Figures 4.14d, 4.14c and 4.14d the estimated FRF from the 50^{th} model order obtained through the SSI technique is compared to the acquired FRF. As can be observed fitting that can be considered perfect of the FRF was obtained. From the identified SSI model one can obtain the frequency of the first mode of vibration of 117.20 Hz and the corresponding damping coefficient of 1.103%.

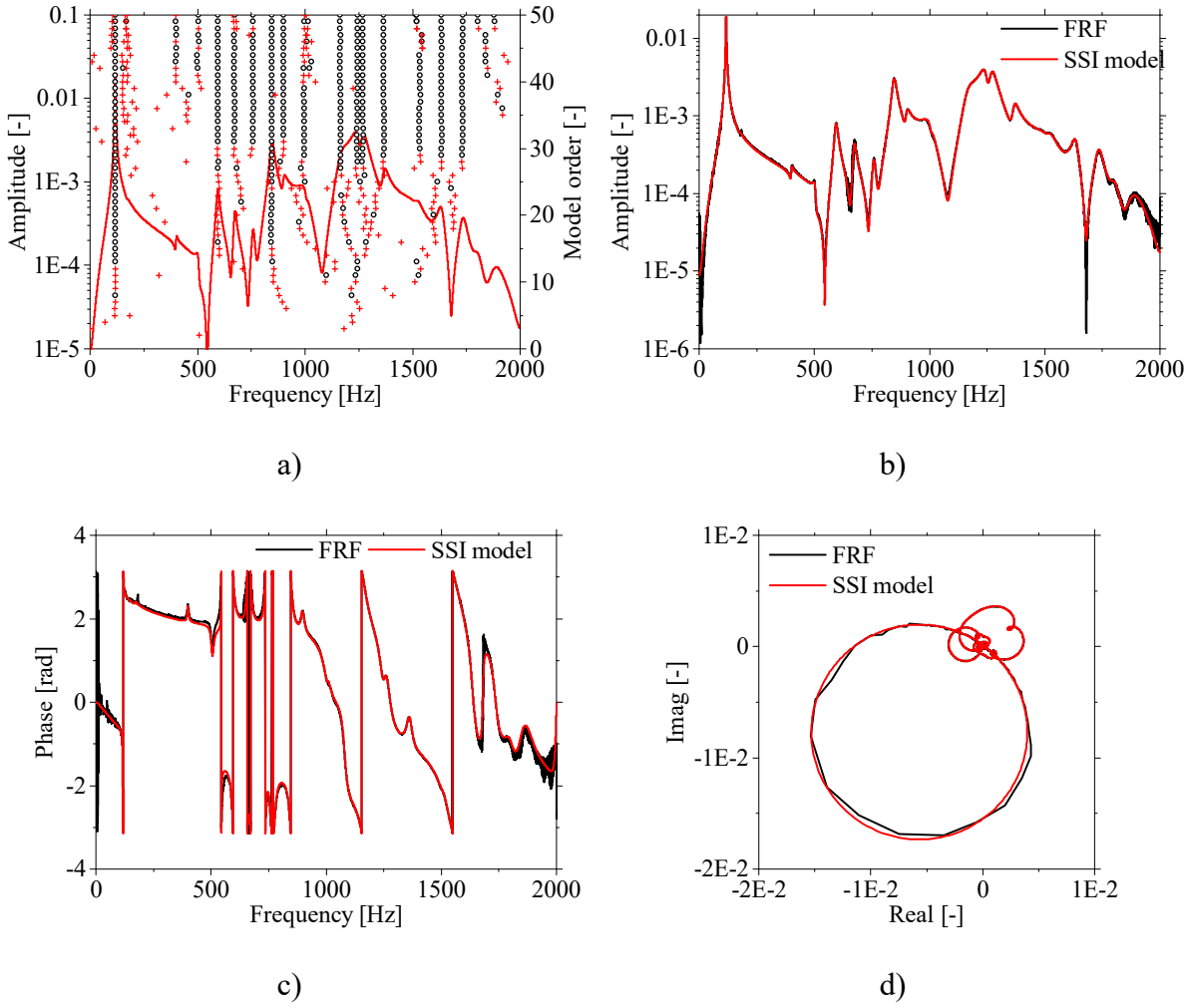

Figure 4.14. EMA SSI results: a) Stabilization diagram (Symbols: '○' stable pole: damping coefficient between 0.1 and 10%, relative frequency variation < 3% and relative damping coefficient variation < 15%); b) FRF amplitude fitting; c) FRF phase fitting; d) FRF real *vs* imaginary fitting.

4.4.2.4. Comparison between the EMA techniques

The identified modal parameters through the EMA techniques are summarized in Table 4.6. By the analysis of the table one can note that the modal parameters (frequency and damping) identified by the SSI and TF techniques exhibit no significant differences between them. The PP technique was the one with the worst performance in the frequency identification.

Regarding the estimated damping coefficients, it is possible to observe that all the techniques were quite close when compared with the OMA test. However, is difficult so state what is the more accurate one since no reference value could be defined.

Table 4.6. Identified modal parameters though the EMA techniques.

Method	*Frequency (Hz)*	*Dif. from ref.*	*Damping (%)*
PP	117.49	0.250%	1.169
IFT	117.11	0.075%	0.903
TF	117.16	0.035%	1.109
SSI	117.20	-	1.103

Second case study

In the case study presented before the test was performed in lab conditions with very low ambient noise. Thus to check the accuracy of the Experimental Modal Analysis (EMA) tests under very noisy conditions a new case study was used. In this new test a 1.0 meter PVC EMM-ARM beam with geometry similar to the one presented in Figure 3.15 (page 70) was used with the physical and mechanical characteristics shown in Table 4.7. The experiment was performed in a construction site where heavy machinery was used during the experiment.

Table 4.7. Physical and mechanical characteristics of the EMM-ARM beam used in the second case study.

Reference	*EMA-2*
Geometry	
Cross-section	Circular
$\varnothing_i$	96.42 mm
$\varnothing_e$	110.01 mm
Span	998 mm
Connectors (spacing)	No
Supports	$\varnothing_{PR}$=12 mm Steel supports
Mould	
Material	PVC
Density	1434.1 kg/m^3
E-modulus	3.50 GPa
Concrete density	2327.9 kg/m^3

The conrete used in these tests had the composition shown in Table 4.8.

Table 4.8. Concrete compositions used

Component	*Mix (kg/m^3)*
Sand	300 (0/2) 540 (0/6)
Gravel	550 (6/14) 420 (11/22)
Cement	320 (CEM II/A-L 42.5R)
Fly ash	100
Water	165 l/m^3
Super plasticiser	3.36 (Polycarboxylic ether polymers)
Adjuvant	0.84 (Basf Pozzolith 540)

To monitor the beam response at mid span PCB 393B12 accelerometers (sensitivity of 10 V/g, within the range ±0.5 g) were used. The excitation of the beam was made by the custom made electromagnetic actuator presented in Figure 4.7 connected to a NI 4431 dynamic signal analyzer with 24-bit of resolution. The excitation signal was a sine sweep with linear frequency variation between 10 and 200 Hz during 40 seconds with constant maximum force amplitude of 8 mN. Each test was made during 300 seconds at an acquisition rate of 500 Hz and repeated every 600 seconds.

The identified resonant frequencies and corresponding damping coefficients along time, that were identified with the four EMA techniques presented before (PP, IFT, TF and SSI), are shown in Figures 4.15a and 4.15b. At first it is possible to observe that despite the high amplitude of the ambient noises, three of the identification techniques (PP, TF and SSI) were able to identify the frequency evolution of the first mode of vibration with a very plausible shape. However, the IFT technique proved to be very sensitive to the noise and the identification resulted in a big scatter of erroneous values. Additionally, regarding the other three techniques, it is clear that the identification accuracy is different. To illustrate the accuracy and precision of each technique the normal distribution of the identified frequencies was computed. But first the all the values were normalized to a reference value at the age of testing computed from a curve fitting of the equation (4.44) to the identified frequency evolution with the TF technique, as shown in Figure 4.15c.

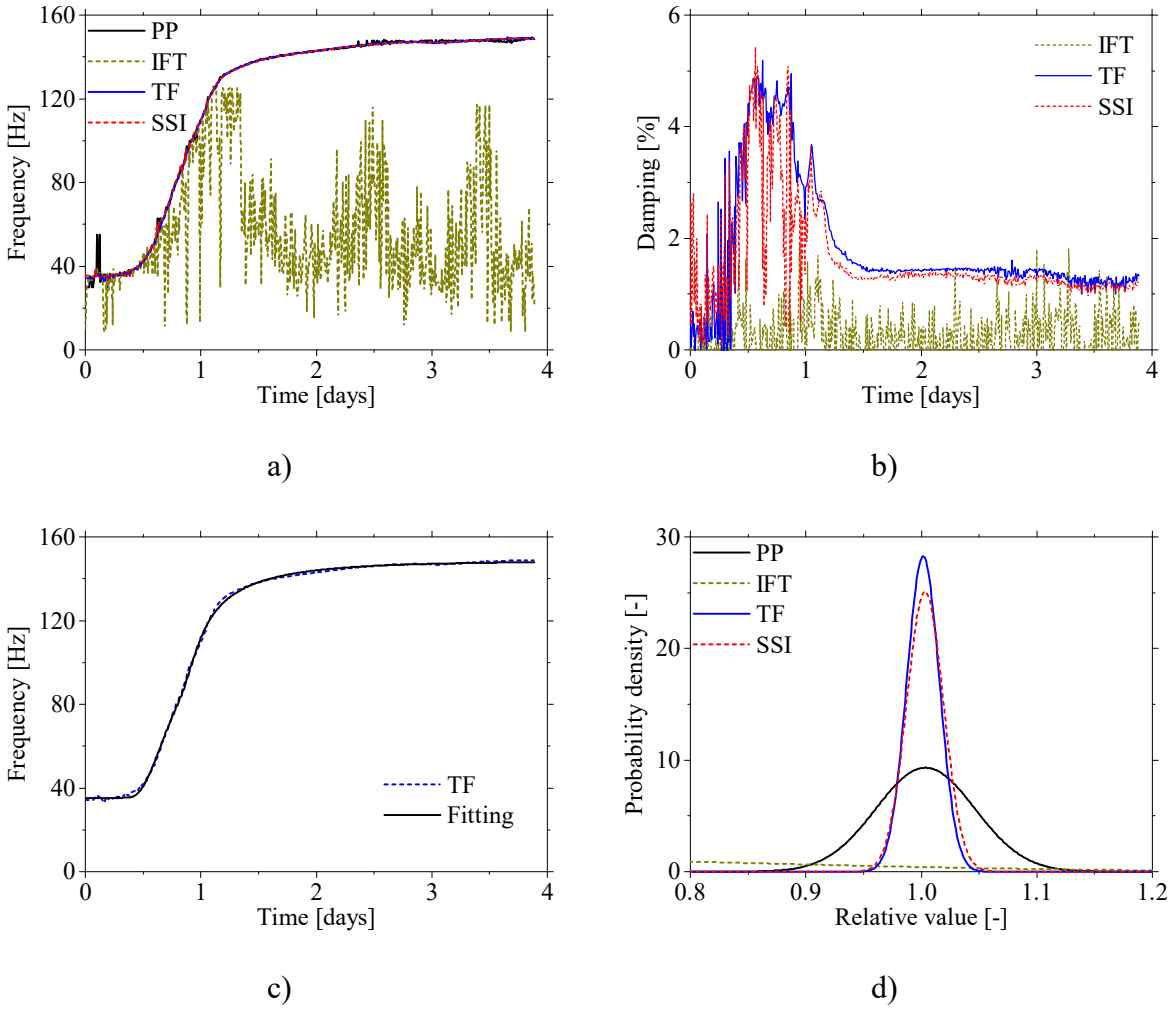

Figure 4.15. Second case study EMA results: a) Fully automatic frequency evolution identified with four distinct approaches; a) Fully automatic damping coefficient evolution identified with IFT, TF and SSI c) Curve fitting of the frequency evolution obtained through TF; d) Accuracy and precision of the EMA methods.

The normal distribution of the frequency identification accuracy of each method is shown in Figure 4.15d. As can be observed in the figure the more accurate and precise technique was the TF with an average (μ) of 1.0015 and a Standard Deviation (SD) of 0.0141 followed with very similar values by the SSI technique.

Regarding the identification of the damping coefficient evolution, shown in Figure 4.15d, one should remark that only the parametric identification methods were able to identify the evolution, despite some dispersion of the results during the first day. The damping evolution seems to start with a constant low value around ~0.5% and remains stable during the first 6

hours. After this point the damping of the EMM-ARM beam evolve rapidly reaching a maximum value of ~4.6% at 14 hours. After this point the kinetic of the evolution change again and the value starts to drop reaching ~1.3% at 1.5 days after casting and remains more or less constant after this point. Despite these evolution, the use of the damping to explore the viscoelastic behaviour of the material inside the mould remains a challenge, since the separation of the contribution of the mould to the final response is not a trivial operation.

From these results one can conclude that with the use of EMA testing techniques and the modal parameters estimation TF or SSI methods the sensitivity of the EMM-ARM to the ambient noise is substantially reduced as well as the accuracy in increased even when the experiments are performed in a very noisy place. Also the EMA parametric identification techniques allow the identification of the beam's damping along the material curing that might be used in the future to estimate some viscoelastic properties of the material under test.

4.4.3. Validation of EMA applied to EMM-ARM

As mentioned before, the use of excitation during a EMM-ARM tests could lead to damage of the material during the early age of curing. Therefore, to validate the use of this alternative testing technique, during the last case study presented before one additional beam was tested under OMA conditions. Therefore, one of the beams was tested through the original ambient vibration technique (OMA-2) and the other was tested through the forced vibration technique (EMA-2) as presented before. The characteristics of the OMA-2 tested beam are shown in Table 4.9. Together with EMM-ARM testing, E-modulus was assessed through CC testing at the ages of 1, 2 and 7 days (kept at the same curing conditions).

Table 4.9. Beams characteristics for the test 5.

Reference	*OMA-2*
Geometry	
Cross-section	Circular
$\varnothing_i$	96.47 mm
$\varnothing_e$	110.00 mm
Span	998 mm
Connectors (spacing)	No
Supports	$Ø_{PR}$=12mm Steel supports
Mould	
Material	PVC
Density	1460.9 kg/m^3
E-modulus	3.50 GPa
Modal analysis	Ambient
Concrete density	2335.5 kg/m^3

The colour maps obtained in this experiment are shown in Figure 4.16. It is possible to observe that, although it is possible to identify the resonance frequency evolution along the concrete curing in both beams, the evolution is considerably clearer and more evident in the beam EMA-2. In fact, this beam that endured forced excitation exhibits almost no influence of environmental noises, which are clearly seen as horizontal lines in Figure 4.16a (indicated by red arrows) for the beam tested without explicit excitation. To better understand this idea, the response spectra obtained by the two beams (NPSD of the beam OMA-2 and FRF of the beam EMA-2) were normalized to their maximum amplitude at two different ages (0.57 and 3.87 days), and represented in Figure 4.17. While at 3.87 days the resonance peak can be easily identifiable in both spectra, this does not happen in the spectra at the age of 0.57 days. In fact, the peak of highest amplitude does not match the resonant frequency peak in the NPSD spectrum of the beam OMA-2. This fact compromises the use of simple automatic algorithms for the identification of resonant frequencies. Therefore, if OMA methods are to be used (i.e. without specific known excitation), it becomes necessary to perform the identification manually using the surfaces shown in Figure 4.17, where it is possible to interpret the graph and separate the noise harmonic frequencies from the system resonance frequency.

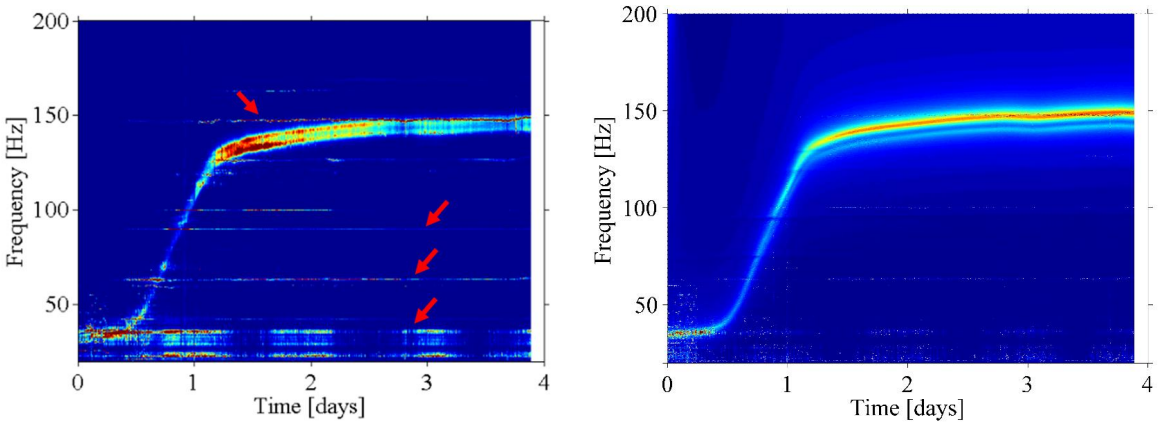

a) b)

Figure 4.16. Evolution of the frequency spectrum: a) NPSD of the beam OMA-2; b) FRF of the beam EMA-2.

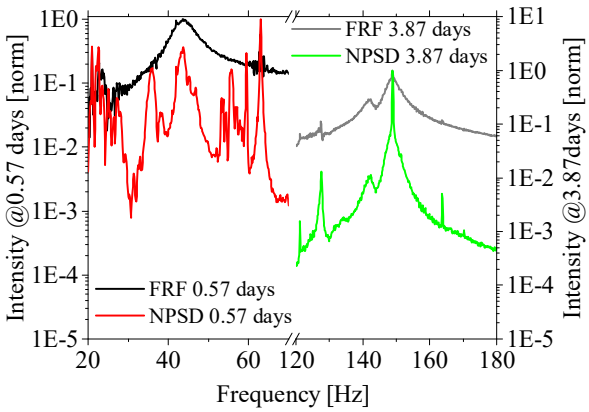

Figure 4.17. NPSD and FRF frequency spectrums at 0.57 and 3.87 days.

The resonant frequencies identified in the two different beams are shown in Figure 4.18a. It is worth mentioning that the results of the two beams are almost superimposed. The elasticity modulus of the concrete was estimated by applying equations (2.11) and (2.12) to the resonant frequencies presented in Figure 4.18a. The resulting E-modulus evolution is shown in Figure 4.18b. Firstly, it is possible to verify that the E-modulus evolution curves have very good coherence with each other, with differences lower than 0.25%. Furthermore, the values obtained through EMM-ARM are similar to those collected in CC tests in terms of magnitude and evolution kinetics. These results suggest that the level of excitation applied to the beam EMA-2 is not sufficient to damage the weak connections in the beginning of the cement hydration and decrease the estimated concrete stiffness. Thus this test allowed to confirm the viability of the use of EMA techniques to perform EMM-ARM tests, with significant advantages in terms

of robustness and possibility of automated data processing without any kind of intervention on behalf of the operator.

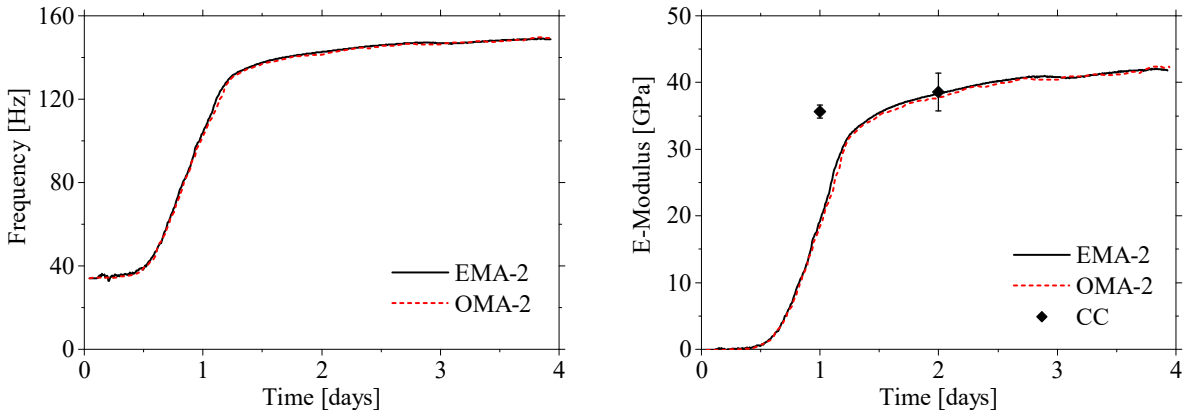

a) b)

Figure 4.18. Comparison of the results obtained with OMA and EMA tests: a) Frequency evolution; b) E-modulus evolution.

Chapter 5

Validation of the ambient vibration method

5.1. Introduction

Despite the successful results obtained through the studies involving EMM-ARM before the research work of this thesis (Maia *et al.*, 2012b, Maia *et al.*, 2012c, Maia *et al.*, 2012a, Azenha *et al.*, 2012a, Azenha, 2009, Azenha *et al.*, 2010a, Azenha *et al.*, 2010b), as well as the improvements introduced in σs 3 and 4, the method still requires an extensive and systematic validation of the attained E-modulus estimations. In fact, the EMM-ARM was only compared with classical cyclic compression tests (CC). Furthermore, all the comparison tests were made by the same operator. The obtained results have pointed that EMM-ARM is able to measure E-modulus values are similar to those obtained through cyclic compression tests at the same ages and same curing conditions. However, there is still the need for conducting a more profound and systematic study to analyse the performance of the EMM-ARM for characterising cement-based materials since early ages, more specifically concrete and cement paste, focusing on its relative behaviour to other methods. That is precisely the initial aim of this Chapter (in sections 5.2.1 and 5.2.2).

After the comparison of EMM-ARM with the competing methods, this Chapter addresses issues related to the repeatability, reproducibility and accuracy of the E-modulus estimations. In the end of this Chapter, a sensitivity analysis of the input parameters needed to compute the material E-modulus on the final estimation will be presented.

5.2. Comparison with other methods

Upon the beginning of this thesis, EMM-ARM was in a prototype stage with very few experiments performed. Therefore, and as stated before, an extensive comparison of the results obtained with EMM-ARM and the comparable or competing methods was needed. In this subchapter two different experimental campaigns will be presented, where the E-modulus estimations through EMM-ARM for two different variants (concrete and cement paste) will be compared with several other methods used in the bibliography for the E-modulus estimation of cement-based materials.

In fact, there are already some studies regarding the comprehensive comparison of different experimental methods to access the behaviour of cement-based materials at early ages (Bullard et al., 2006, Sant et al., 2009). However, these works focused mainly on the detection of the setting time, rather than the evolution of stiffness itself. Thus, this subchapter aims also to fulfil this gap through an extensive comparison between several experimental methodologies capable of quantifying the stiffness of concrete and cement paste, such as: EMM-ARM, cyclic compression/tension tests (CC, BTJASPE, TSTM), ultrasonic wave transmission (UWT), bender-extender elements (BE), and penetration resistance.

5.2.1. Concrete

The work that will be presented here was the result of part of an international collaboration between three research centres (University of Minho (UM), *Institut Français des Sciences et Technologies des Transports, de l'Aménagement et des Réseaux* (IFSTTAR) and *Université libre de Bruxelles* (ULB)). The results are already published in two papers (Boulay *et al.*, 2013a, Delsaute *et al.*, 2016).

Additionally to the EMM-ARM technique presented and enhanced in the previous two Chapters used in the Laboratory of Structures of the University of Minho (UM), eight different techniques have been implemented in the three involved laboratories. They can, a priori, be sorted in two classes, according to their respective ranges of loading rates: four techniques of quasi-static loadings (cyclic compression tests: classical CC (all three labs), automated with BTJASPE (IFSTTAR), classical automated (ACC) using BTJASPE protocol (IFSTTAR), automated with a TSTM (ULB)); and four techniques of high frequency loadings: three classical UPV measurements with PunditLab (UM), FreshCon (ULB), and BTPULS (IFSTTAR); and Smart Aggregates SMAGs (ULB). All these experimental methods were applied without a rigorous temperature history control history of the specimens due to practical limitations associated to the test setups and the size of specimens themselves. That is why observations are compared after having expressed results at the same concrete maturity using the equivalent time method.

5.2.1.1. Mixing and material characterization

The same material is used in the three laboratories. The mixture proportions are given in Table 5.1.

Table 5.1. Mixture proportions of the concrete (w/c = 0.54).

Components	*Mass (kg/m^3)*
Cement	340 (CEM I 52.5 N PMES CP2)
Sand	739 (0/4)
Gravel	1072 (8/22)
Total water	184
Density	2335

The concrete was mixed mechanically or manually depending on the volume of the batch (from 2 litres to approximately 40 litres). Even though these differences can lead to scattered results, no significant effect was observed in the performed experiments on this concrete as presented in section 5.2.1.3.

The strength evolution was useful for quantifying the limits of the automatic loadings (tests presented in section 5.2.1.2) applied at early age in order to avoid any damage of the samples.

The samples were cylinders (Ø = 110 mm×220 mm). They were cured inside adhesive aluminium tape at 20°C, and capped with sulphur mortar. The corresponding results are reported in Figure 5.1.

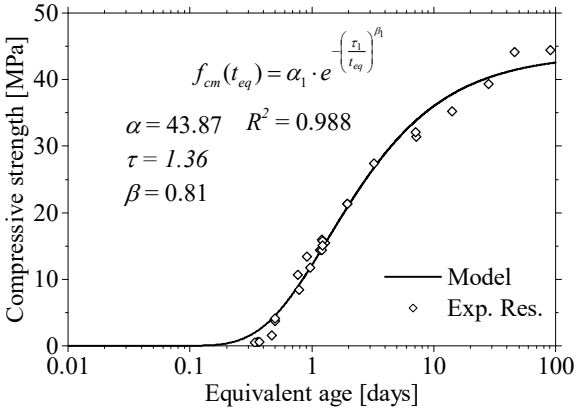

Figure 5.1. Compressive strength results obtained by the teams of IFSTTAR and ULB.

For the sake of these calculations, the compressive strength (f_{cm}) is modelled by the following equation:

$$f_{cm}(t_{eq}) = \alpha_1 \cdot e^{-\left(\frac{\tau_1}{t_{eq}}\right)^{\beta_1}} \tag{5.1}$$

with: $\alpha_1 = 43.87$, $\tau_1 = 1.36$ and $\beta_1 = 0.81$. t_{eq} is the equivalent age at 20°C.

The apparent activation energy was determined through calorimetric testing and a value of 32.2 kJ/mol was obtained (Boulay *et al.*, 2013a). Together with temperature recordings, the apparent activation energy allowed the calculation of the equivalent age (t_{eq}) (D'Aloia, 2003), according to Arrhenius laws. These calculations were performed at an arbitrary reference temperature equal to 20°C, allowing all experimental results to be normalized to temperature effects.

An important issue to remark pertains to the consideration of the instant of setting, which is of paramount importance for the analysis of results reported herein. The setting period corresponds to a period between the time when a needle penetrates completely a sample of mortar or cement

grout and the time when it does not penetrate anymore the sample (Sant *et al.*, 2009). As penetration tests do not apply specifically for concrete, the work of reference of Robeyst *et al.* (2008) compared transmitted ultrasonic P-waves to penetration tests performed on thieved concrete. They found that the final setting occurs when the value of the derivative of the P-wave velocity evolution decreases down to 80% of the peak value. This technique was applied here. It is worth underlining that the final setting corresponds to a time when a sample can be manipulated, but gently to avoid any rupture. Before this time, any manipulation would be likely to induce rupture of specimens. It is also the time when the stiffness of the material begins to increase significantly. This final setting is, here, called t_0 (Bentur, 2003). An estimation of this time is required for starting tests just after concrete setting. According to the assessment that will be presented in section 5.2.1.3, the final setting t_0 estimated for this concrete was 5.4 hours (0.226 days).

5.2.1.2. Experimental techniques and protocols

EMM-ARM

In the context of this collaborative research, three different EMM-ARM beams were used to characterise the tested concrete: one cylindrical acrylic beam (O-ACR) similar to the original as presented in Figure 2.16 (page 32); one 'U-shaped' metallic beam (U-STL) as shown in Figure 3.3 (page 54); and one cylindrical PVC beam (O-PVC) with geometry similar to the one presented in Figure 3.15 (page 70). The physical and mechanical characteristics of the beams are presented in Table 5.2.

The three beams were tested under OMA conditions with a fan pointing to the beams to increase the amplitude of vibration. Accelerations of the monitored points have been measured for 28 days with sampling frequency of 200 Hz and PCB accelerometers with 10 V/g sensitivity, 0.15 to 1000 Hz frequency range and 225 grams of mass. Packets of 60 seconds of data have been taken every 15 minutes with a 24-bit data logger (NI 9234). Regarding the frequency identification, the OMA SSI technique was used with a model order of 4.

Table 5.2. Physical and mechanical characteristics of the EMM-ARM beams.

	Test 3 – concrete mix 3		
Reference	*O-ACR*	*U-STL*	*O-PVC*
Geometry			
Cross-section	Circular	'U'	Circular
$\varnothing_i$ /H	92 mm	150 mm	86 mm
$\varnothing_e$ /B	100 mm	150 mm	90 mm
Span	1800 mm	2400 mm	900 mm
Connectors	Yes	Yes	Yes
(spacing)	(300 mm)	(500 mm)	(180 mm)
Supports	$\varnothing_{TR}$=5 mm Concrete cubes	Concrete cubes	$\varnothing_{TR}$=5 mm Concrete cubes
Mould			
Material	Acrylic	Steel	PVC
Density	1286.9 kg/m^3	7800.0 kg/m^3	1463.5 kg/m^3
E-modulus	3.30 GPa	170 GPa	4.3 GPa
Concrete density	2340.3 kg/m^3	2362.9 kg/m^3	2295.7 kg/m^3

Classical cyclic compression tests (CC)

Classical tests, considered as reference, were performed at UM, IFSTTAR and ULB on cylinders at different ages. For each test, strains were measured by extensometers. Three transducers (LVDTs) measured the relative displacement between 2 rings fixed to the specimen, as presented on Figure 2.1 (page 10). The specimens were kept in a curing chamber at 20ºC. However, the protocol of loading, the size of the specimen and the extensometers used for the determination of E are different. These differences are synthesized in Table 5.3. The selected testing ages associated to the results are given also in this table.

Table 5.3. Classical test setup in the different laboratories.

Lab	*UM*	*IFSTTAR*	*ULB*
Extensometer spacing (mm)	100	120	120
Specimen			
Height (mm)	300	220	220
Diameter (mm)	150	110	110
Protocol of loading			
Loading range	0.8 to 33% of f_{cm}	5% to 30% of f_{cm}	20% of f_{cm}
Stress rate (MPa/s)	0.3	0.5	0.20 to 0.55
Testing ages (days)	3, 7, 14, 28	0.4, 0.5, 0.8, 1, 7, 14, 28, 90	0.8, 1, 2, 5

At the University of Minho, cylinder specimens, 150 mm in diameter and 300 mm in length, have been tested under cyclic compression according to (LNEC, 1993). The protocol of loading consisted in applying 5 cycles between 0.8 MPa and 33% of the ultimate strength at the age of

testing. The loading rate was set to 0.3 MPa/s. The testing equipment included a hydraulic actuator with 2000 kN of maximum load capacity.

At IFSTTAR, sample geometries were the same as the ones used for strength measurements (cylinders with 110 m in diameter and 220 mm in length). The first tests were performed 7 hours after casting. Strains were measured by extensometers. The protocol of loading consists in applying 4 cycles between 5 and 30% of the strength measured on other cylinders (with the same geometry) just before the test (Torrenti *et al.*, 1999). The loading rate was set to 0.5 MPa/s. The testing equipment included a hydraulic actuator with 500 kN of maximum load capacity.

At ULB, similar cylinders and the same extensometer were used. 20% of the concrete strength at the time of the test was applied within 10 seconds, on 4 different samples. Corresponding stress rates were ranging from 0.2 to 0.55 MPa/s, depending on the age of the sample. The testing equipment included a hydraulic actuator with 1000 kN of maximum load capacity.

BTJASPE device

BTJASPE is a relatively recent device, developed at IFSTTAR (Boulay *et al.*, 2012, Boulay *et al.*, 2010, Boulay *et al.*, 2013b), as already presented in section 2.2.2. It allows the automatic monitoring of the stiffness of a concrete cylinder remaining in its mould. Measurements start just after concrete casting and continue up to a few days. The device is placed between the plates of an automatic testing machine. The temperature of the sample is kept at a constant value thanks to a circulation of water inside a double walled mould. The sample is 100 mm in diameter and 200 mm in length. This sample is loaded at a constant strain rate of 5×10^{-3} m/m·s until a relative strain equal to 100×10^{-3} m/m·s. Then, at this point the ramp is reversed in order to unload the sample. This strain value is chosen to avoid any damage of the sample in compression. This protocol allows starting the tests shortly after the concrete casting as the device has a LVDT in the top to detect the contact between the actuator and the sample. A new loading cycle is triggered after a delay of about 15 to 30 minutes.

Automated cyclic compression tests (ACC) using BTJASPE protocol

In order to check the accuracy of this test setup (sample confined in the stainless steel mould), other tests using the same loading protocol were performed on concrete cylinders removed from their cardboard mould just after the concrete setting (detected by ultrasonic measurements). The sample is capped with sulphur mortar, equipped with an extensometer and placed between the upper and the lower bearings used for BTJASPE (Figure 5.2). A ball joint is placed between the upper face of the sample and the upper bearing. In that case, the sample is not confined thus the results are not affected by any lateral effect and they can be considered as validation tests for BTJASPE study (called ACC hereafter). Strain measurement is performed with the same technique adopted by IFSTTAR for the reference tests in cylinders (classical testing).

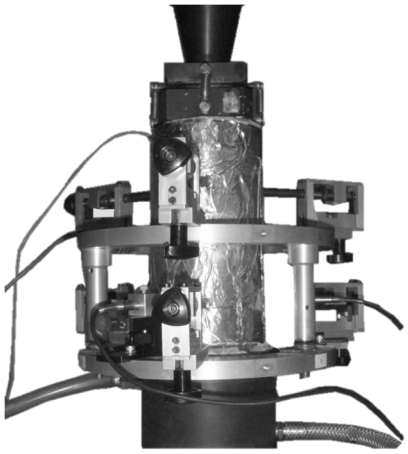

Figure 5.2. Validation test for results obtained with BTJASPE (Delsaute *et al.*, 2016).

Temperature Stress Testing Machine (TSTM)

Since 2006, a revisited TSTM has been under development in ULB for testing concrete since t_0, under free and restraint conditions (Boulay *et al.*, 2013b, Staquet *et al.*, 2012). The testing machine is a Walter+Bay LFMZ 400 kN electromechanical testing setup. The machine is composed by a fixed steel head, a central part where the testing specimen is placed and a moving end (Figure 5.3a). In the central part, where the measurements of the displacements are taken, the stress field is assumed to be homogenous (Figure 5.3b) and the cross-sectional dimensions are 100×100 mm^2. The displacements are recorded by Foucault current's sensors (contact free sensors). Before casting, a plastic sheet is placed in the mould to ensure sealed conditions.

Moreover, the plastic sheet helps also to reduce the friction between the sample and the mould, within a system that also encompasses a Teflon plate. The machine is equipped with a double walled mould allowing a thermal regulation and, in particular, ensuring isothermal curing conditions. Temperature measurements took place in the central part of the specimen and in each heads. The experiment was conducted in a climatic chamber with temperature of 20 ± 1ºC.

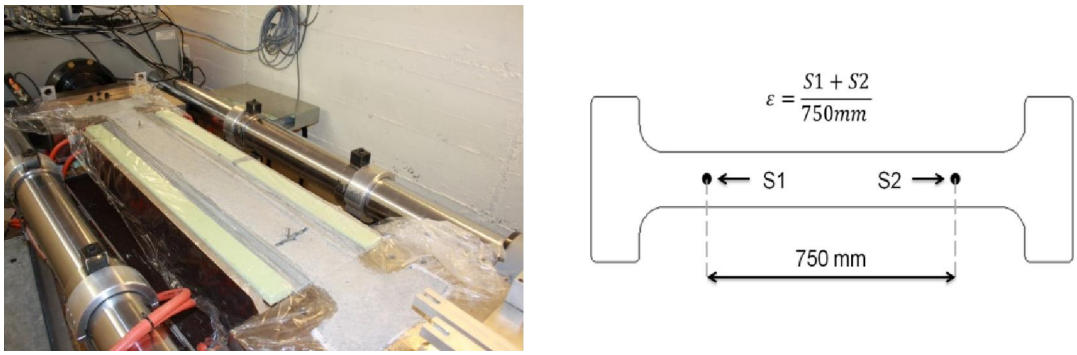

a) b)

Figure 5.3. a) TSTM equipment for cyclic loadings; b) Measurement of displacement in TSTM device (Delsaute *et al.*, 2016).

A new methodology was developed for measurement of the Young's modulus. The test is controlled at a constant loading rate, thanks to the software "DION®" (Walter & Bai). The test begins shortly after t_0. For each cycle of loading, the moving end of the testing machine is controlled by the force sensor, up to 20% of the compressive strength at the age of testing. The sample is then unloaded till a null force. Recordings (displacements, force and temperature) are taken during the cycles and more specifically during each loading and unloading. These displacement measurements can then be directly used to compute the Young's modulus. The duration between each loading was approximately 60 minutes. The relation between the stresses and the strains is quasi linear during the loading. In order to keep the strictly linear zone of the stress/strain curve, the Young's modulus is calculated between 30 and 80% of the maximum load reached in each cycle.

Classical ultrasonic wave transmission (UWT) measurements

Three classical techniques of UWT were performed on this concrete. First, the PunditLab device (Proceq, 2014) was used in the UM laboratory. This device is equipped with two probes

with a resonance frequency of 54 kHz that were placed in two opposite sides of a concrete cube with 150 mm edge. Single period pulses were generated with 500 V of amplitude. The measurements stated immediately after casting, however due to the fluid like behaviour of the concrete in fresh state the first measurements were taken only at 6 hours after casting.

The FreshCon device (see Figure 5.4) developed at the University of Stuttgart was used due to its ability to detect very early age signals. Ultrasonic pulses of 5 μseconds at 800 V are sent through ultrasonic transducers (0.5 MHz resonant frequency). The ultrasonic pulse velocity (UPV) can therefore be computed before setting. These technique was used by the ULB team in the context of these research work. In addition, the UPV was measured with a BTPULS device developed at IFSTTAR (Boulay *et al.*, 2013b). This additional test, performed after the setting, was performed for comparative purposes between these two techniques.

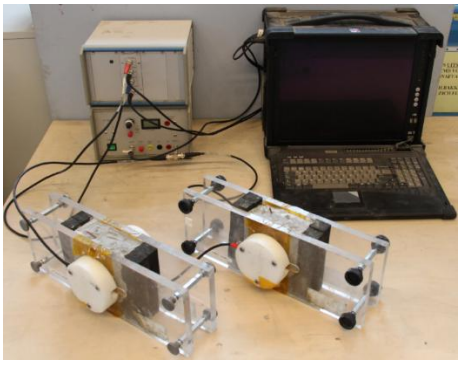

Figure 5.4. FreshCon System (Delsaute *et al.*, 2016).

In the FreshCon system, the sample thickness is 47 mm. Two samples are cast inside two similar containers: one for P-waves measurements and one for S-waves measurements. Samples are placed in a thermally regulated chamber and their temperatures are measured continuously during the test. Detailed information about this method can be found in (Krüger *et al.*, 2013).

The P-waves (V_p) and S-waves (V_s) velocities can be used to compute the dynamic Poisson's ratio (ν_{dyn}) and E-modulus (E_{dyn}) through equations (2.4) and (2.5) (page 16).

Smart aggregates (SMAGs)

The main drawback of the PunditLab, FreshCon and BTPULS systems is the use of a fixed sized mould which strongly limits the possible testing conditions of the sample. In particular, it does not allow applying specific hygral and/or mechanical boundary conditions on the concrete sample. An alternative is to perform ultrasonic testing directly inside a concrete specimen of an arbitrary shape and size using embedded piezoelectric transducers. The use of embedded transducers, also called "Smart Aggregates" (SMAGs) can be used to monitor the elastic mechanical properties of concrete in (Li *et al.*, 2009). At ULB, transducers based on a similar design were recently developed. Each SMAG consists in a flat piezoelectric patch which is wrapped in a waterproof coating and embedded in a small cube or cylinder made of mortar (as already shown in Figure 2.7 – page 20). One of the advantages of this technique is that no coupling agent is needed between the sensor and concrete. The SMAGs fabricated at ULB have been used for the monitoring of the P-wave velocity in early age concrete (Dumoulin *et al.*, 2012). The results for early age testing are used in this paper and compared to the results obtained with the other techniques presented. More detail about the testing procedure is detailed in the work of Dumoulin *et al.* (2012).

A prismatic mould, containing a pair of *SMAGs* with a distance d = 56 mm is used (Figure 5.5). The FreshCon system is used to excite the emitter with a pulse of 800 Volts and 2.5 µs and record the wave at the receiver's side. The testing procedure is therefore identical to the one described before for FreshCon, except for the fact that piezoelectric transducers of the mould are replaced by SMAGs directly embedded inside the concrete specimen.

Figure 5.5. Prismatic mould with SMAGs before casting the concrete (Delsaute *et al.*, 2016).

5.2.1.3. Results and discussions

The results are cumulatively presented below, beginning with the results of classical cyclic compression tests (CC), the EMM-ARM results, followed by a comparison between the low frequency techniques (CC, EMM-ARM, BTJASPE, ACC and TSTM). The comparison proceeds with the results obtained through the wave propagation methods. Finally, a comparison between the data collected through all analysed testing methodologies is presented.

Classical cyclic compression tests (CC)

Measurements of the modulus of elasticity were performed by means of classical extensometry in the 3 laboratories (Table 5.4). Strain rates were ranging from 0.2 to 0.55 MPa/s for the 3 laboratories.

Table 5.4. Classical cyclic compression tests (mean values).

UMinho[*]		*IFSTTAR*[*]		*ULB*[**]	
t_{eq} *(days)*	*E (GPa)*	t_{eq} *(days)*	*E (GPa)*	t_{eq} *(days)*	*E (GPa)*
2.78	34.66	0.36	2.72	0.79	16.8
6.80	36.10	0.47	7.32	0.92	20.5
14.11	36.60	0.79	18.76	1.96	29.5
27.98	38.59	0.97	22.86	4.88	35.2
		1.16	26.14		
		7.23	36.41		
		14.23	37.43		
		28.23	39.66		
		90.23	39.62		

[*]Mean values of 3 specimens
[**]Values of 1 specimen

As loading protocols are very similar, these results are mixed in order to obtain a single description of the evolution of the Young's modulus by these classical means. For the sake of the analysis of our results, the following mathematical model was used (Carette, 2015) (Figure 5.6):

$$E(t_{eq}) = \alpha_1 \cdot e^{-\left(\frac{\tau_1}{t_{eq}}\right)^{\beta_1}} + \alpha_2 \cdot e^{-\left(\frac{\tau_2}{t_{eq}}\right)^{\beta_2}} \quad (5.2)$$

where $E(t_{eq})$ is expressed in GPa, t_{eq} in days, $\alpha_1 = 32.35$, $\beta_1 = 1.81$, $\tau_1 = 0.63$ $\alpha_2 = 11.30$, $\beta_2 = 0.34$ and $\tau_2 = 6.16$.

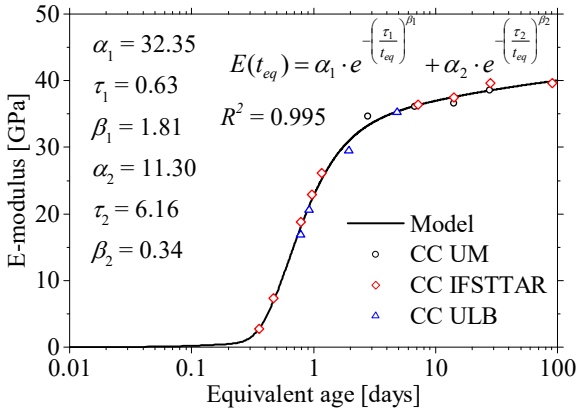

Figure 5.6. Evolution of the E-modulus obtained with classical methods. A model is adjusted to the data.

This function is accepted as the reference for the comparisons between the different methods and will thus be used recurrently in the following sections. This kind of test does not provide an accurate estimation of t_0; as the first measurement could only be made 3 hours after t_0.

EMM-ARM results

The resonant frequency evolutions for the three composite beams (concrete-filled moulds), resulting from processing the recordings of the accelerometers are shown in Figure 5.7a. All the data of EMM-ARM is plotted according to the equivalent age, normalized to 20°C (see temperature history in Figure 5.7b). By observation of Figure 5.7a, it is clear that all composite beams endured a significant frequency shift ranging between 27.49 Hz in the beam U-STL and 109.12 Hz in the beam O-PVC.

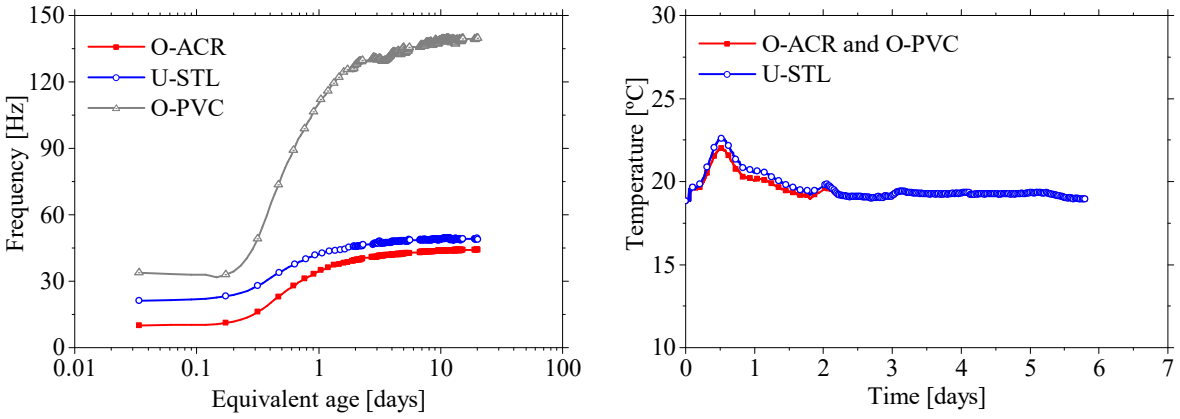

a) b)

Figure 5.7. a) Resonant frequency evolution for the acrylic, metallic and PVC EMM-ARM composite beams (O-ACR, U-STL and O-PVC); b) Temperature history observed in the EMM-ARM specimens.

The overall results of E-modulus measured by the three EMM-ARM composite beams and the reference curve of classical tests are shown in Figure 5.8. It is evident that the coherence of the four curves is very good at most ages of testing, once more confirming the feasibility and robustness of EMM-ARM. It is however remarked that the E-modulus obtained from the metallic mould test is slightly higher than the E-modulus obtained from the other beams (acrylic and PVC) from the beginning of the evolution until ~3 days of age. This may be partially explained by some uncertainties in the geometry of the metallic beam due to its high local deformability (1 mm thick plates) that resulted in some local warping due to previous uses of the mould. After this point the values estimated by the different beams are quite similar with an average value of 36.06 GPa with a standard deviation $SD = 0.98$. A slight under-estimation of the final E-modulus value of all EMM-ARM specimens in regard to the model can also be observed in Figure 5.8.

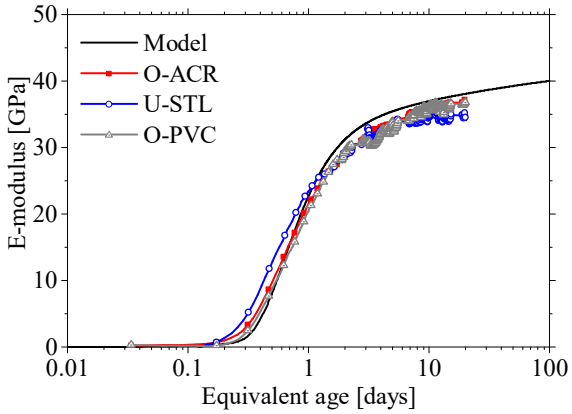

Figure 5.8. E-modulus obtained through EMM-ARM (acrylic, metallic and PVC composite beams - O-ACR, U-STL and O-PVC) compared to calibrated model for quasi-static E-modulus.

Comparison between low frequency testing methods

The average E-modulus evolutions obtained will all low frequency (or quasi-static) methods are shown in Figure 5.9. In all the results the overall evolution kinetics is similar, with an initial dormant period until ~5 hours after mixing. At this point the E-modulus starts to increase whatever the testing method. After setting, the kinetic of the E-modulus looks very similar, whatever the testing method whereas a limited scattering is observable between the results, especially very early ages. It appears that the difference of protocol of loading (strain rate, stress amplitude) and the type of testing method did not induce any strong effect on the kinetic and the amplitude of the E-modulus. Furthermore, all low frequency testing methods have revealed a good correspondence with classical cyclic compression results.

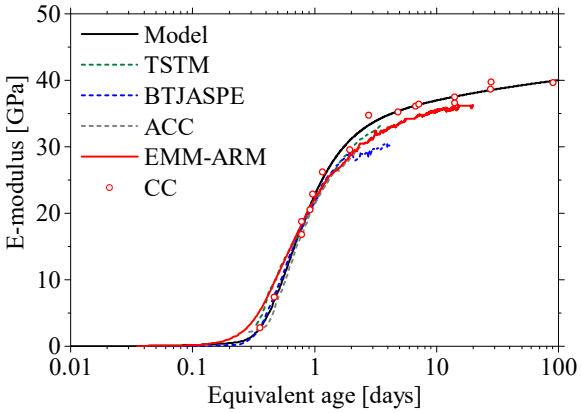

Figure 5.9. E-modulus obtained with low frequency testing methods.

To illustrate the accuracy and precision of each method the normal distribution of the estimated E-modulus was computed. But first all the values were normalized to a reference value at the age of testing computed from the model (fitting of CC results). The normal distributions of the E-modulus estimations along the whole duration of the tests form the five distinct techniques are shown in Figure 5.10 and the mean values and standard deviations are summarized in Table 5.5.

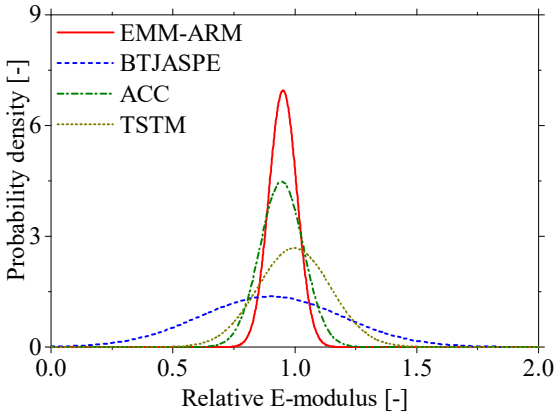

Figure 5.10. Accuracy and precision of the low frequency experimental methods.

Table 5.5. Summary of the mean values (μ) and standard deviations (SD) of the E-modulus estimated with the low frequency experimental methods.

Method	*EMM-ARM*	*BTJASPE*	*ACC*	*TSTM*
μ	0.952	0.902	0.946	0.997
SD	0.0618	0.2914	0.0888	0.1490

It can be observed that, the most accurate was the TSTM method with an average (μ) of 0.997, though the precision was low since the Standard Deviation (SD) is 0.1490. Regarding the EMM-ARM results, it is possible to state that the method is able to estimate the so-called quasi-static E-modulus of the concrete with a very high precision and a good accuracy. This results enable the validation of the E-modulus estimations obtained with EMM-ARM since the accuracy and precision of the estimations are within the range of the competing static methods.

High frequency testing

The P-wave velocity results obtained, for the same concrete, with the PunditLab, SMAGs, the BTPULS and FreshCon systems are plotted on Figure 5.11. Additionally, with the FreshCon it was also measured the velocity of S-waves transmission. In the figure, the average of three samples is shown for FreshCon and BTPULS.

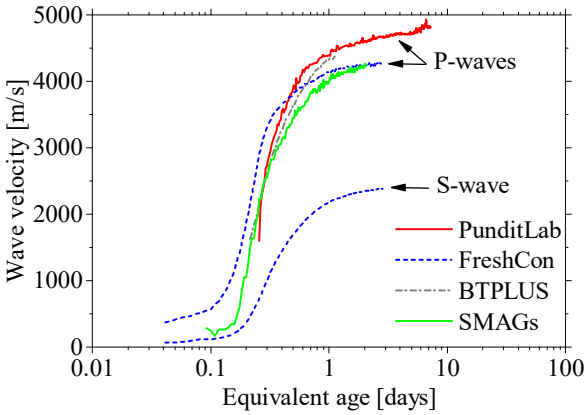

Figure 5.11. Measured P-wave velocities using PunditLab, FreshCon, BTPULS, and SMAGs.

In the FreshCon results the P-waves velocity increases rapidly during setting and stabilizes after the final setting time to a value slightly superior to 4000 m/s. However, the S-waves hardly propagate though fluids. It is only at the beginning of the hardening that the S-waves velocity increases. Then, it slowly reaches a value close to 2500 m/s. These observations are in good agreement with the few results found in the literature (Van Den Abeele *et al.*, 2009, Benmeddour *et al.*, 2012). It seems also that this system gives slightly different results of P-waves velocity, in the first part of the curve when compared to the others. However, this difference mainly occurs before t_0. These differences could be related to errors on the distance between the probes (Carette *et al.*, 2012). From 12 hours onward, the overall tendency is the same for all techniques, however with some differences in the magnitude of the velocity. In fact, one can identify two groups, the first one (PunditLab and BTPLUS) has a velocity at 24 hours of 4350 m/s and the second group has 4070 m/s. These discrepancies can be due to different air content in the different moulds, since different techniques are used for placing the concrete in the moulds. Indeed, it is known that a strong dependency of the early age P-waves velocity to the air content of the mix exists. In aired mixes, the initial velocity is around 250 m/s, whereas for de-aired mixes, initial values close to 1500 m/s can be observed (Zhu *et al.*, 2011a).

Additionally, these differences could be related to the different mould and probes sizes and different distances between probes of the different methods. Further analysis should be made to study the origin of these differences.

In order to evaluate the relevance of the PunditLab, SMAGs and BTPULS methods compared to usual UPV measurements, a constant Poisson's ratio of 0.3 has been considered as no S-wave measurements were performed with these techniques. The dynamic E-modulus (E_{dyn}) estimations with the high frequency methods are shown in Figure 5.12. The values for the FreshCon curve with a constant v_{dyn} equal to 0.3 and the SMAGs curve seem to stabilise after 30 hours, whereas the values of the FreshCon curve with consideration of the evolution of v_{dyn}, the PunditLab and BTPLUS follows the trend of the static E-modulus given by the model with increasing values after 30 hours.

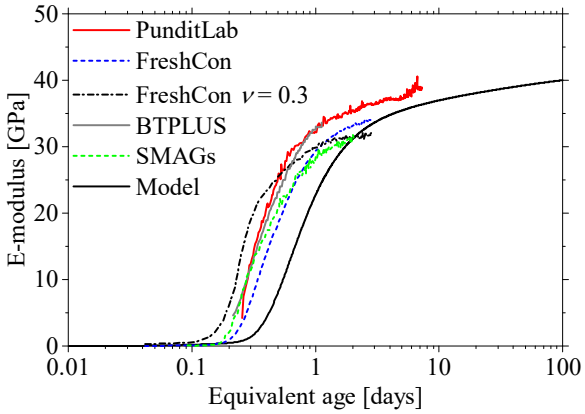

Figure 5.12. Comparison of the dynamic E-modulus computed from the P-wave velocity only with v_{dyn} = 0.3 (PunditLab, SMAGs, FreshCon, BTPULS) and from the P-wave and S-wave velocity (FreshCon) with the static E-modulus model.

Before the setting time, a scattering is observable between all the dynamic testing methods. The results FreskCon considering the real v_{dyn} exhibit the lowest amplitude because before t_0, the values of v_{dyn} are much higher than 0.3. After t_0, again one can separate the methods in two groups: the first one (PundilLab and BTPLUS) the E-modulus estimations follows the static model but with a gap of ~1.6 GPa; the second one (FreshCon, BTPULS with constant v_{dyn}) the E-modulus estimations seems to stabilize with tendency to underestimate the so-called static E-modulus. Only the FreshCon with consideration of the real v_{dyn} seems to enable the estimation of the static E-modulus but only after ~3 days after mixing. Therefore, as observed in (Van Den

Abeele *et al.*, 2009), the computation of E_{dyn} only from P-wave velocity should be considered as a qualitative indicator of the E-modulus development.

Overall comparison

Figure 5.13 presents the synthesis of all results. Only mean values of each testing method are shown here. As expected, clear differences appear between static and dynamic results. Dynamic modulus with consideration of the evolution of v_{dyn} is always higher than static results. A faster evolution of dynamic results is also observable.

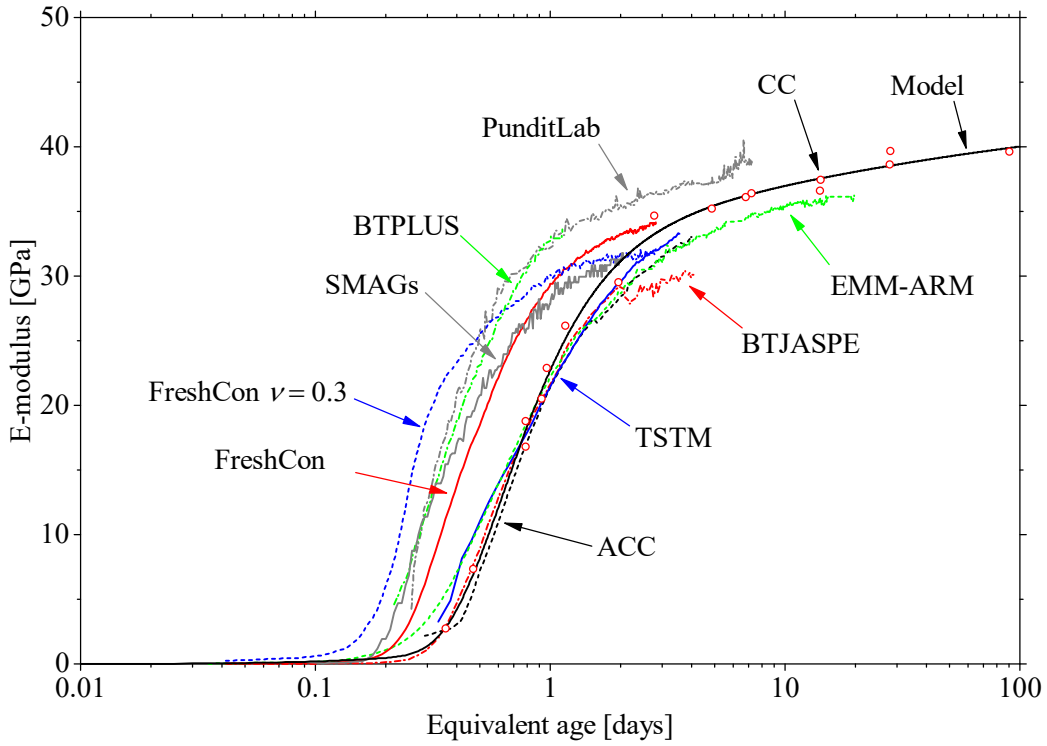

Figure 5.13. Comparison of E-modulus obtained with static and dynamic testing methods.

Final setting time

With the results obtained from FreshCon the final setting time was computed from derivative of the wave velocity evolution according to the procedure described in section 5.2.1.1. Due to the acquisition noise the experimental data was fitted by the equation (5.3) to enable the computation of the first derivative of the P-wave velocity.

$$V_p(t) = \alpha_1 \cdot e^{-\left(\frac{\tau_1}{t_{eq}}\right)^{\beta_1}} + \alpha_2 \cdot e^{-\left(\frac{\tau_2}{t_{eq}}\right)^{\beta_2}} + \alpha_3 \tag{5.3}$$

where $\alpha_1 = 1445.98$, $\alpha_2 = 2445.72$, $\alpha_3 = 409.06$, $\tau_1 = 0.207$, $\tau_2 = 0.182$, $\beta_1 = 6.113$, $\beta_2 = 1.548$ and $R^2 = 0.9994$. The wave velocity and the corresponding first derivative along time is shown in Figure 5.14. After the selection of the peak of the derivative of the P-wave velocity, the point when the derivative of the velocity decreases to 80% of the peak value is identified, that corresponds to the final setting time in accordance to the work of (Robeyst *et al.*, 2008). As already presented before, a value of 5.4 hours (0.226 days) was obtained.

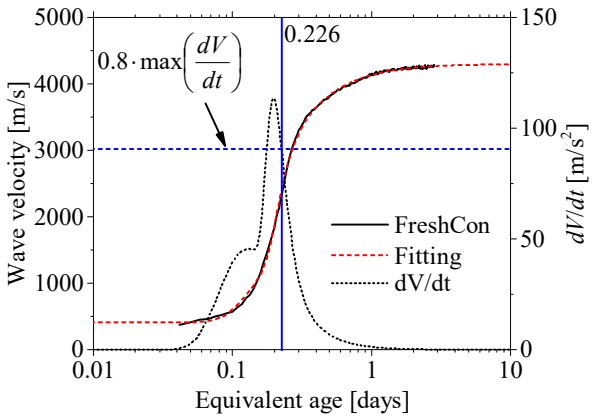

Figure 5.14. Final setting time estimation with FeshCon.

Nonetheless, since EMM-ARM also provides information about the E-modulus evolution since casting, the setting time obtained from FreshCon is compared here with the first derivative of the E-modulus evolution obtained with EMM-ARM. Similarly, to the previous method, the experimental data (average of the three specimens) was again fitted to enable the computation of the derivative of the E-modulus evolution. To the fit the experimental the equation (4.1) was

used with the following parameters: $\alpha_1 = 27.95$, $\alpha_2 = 9.26$, $\tau_1 = 0.657$, $\tau_2 = 0.517$, $\beta_1 = 0.977$, $\beta_2 = 2.464$ and the R^2 was 0.9993. The E-modulus evolution and the corresponding first derivative along time are shown in Figure 5.15. It is observed that there is a very good agreement between the final setting time obtained with FreshCon (0.226 days) and a setting time computed by selecting the first point with 50% of the peak value of the DE/dt curve (0.211 days).

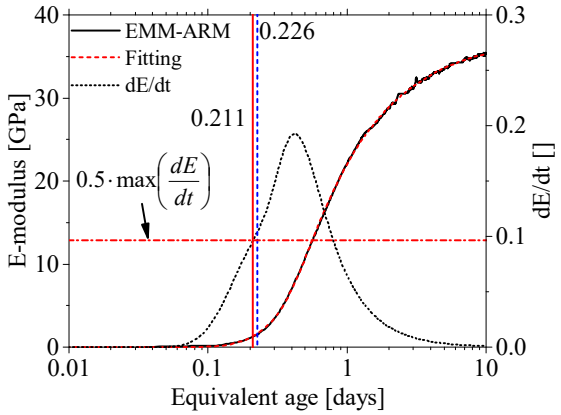

Figure 5.15. Final setting time estimation with EMM-ARM.

Despite a good agreement between the two setting times estimations, further experiments will be necessary to validate the feasibility of assuming that the final setting time corresponds to the first point with 50% of the peak value of the first derivative of the E-modulus.

5.2.2. Cement paste

In this subchapter, the EMM-ARM version for cement paste will be validated through comparison with a set of directly or indirectly competing methods, such as: classical cyclic compression (CC), ultrasonic pulse velocity (UPV), bender-extender elements (BE) and Vicat needle. It should be noted that this work is the continuation of the work carried out by the author during the master's thesis (Granja, 2011). It is also remarked that some of these results were already published in (Granja *et al.*, 2014a, Granja *et al.*, 2012).

5.2.2.1. Experimental Program

Materials

The experiments were conducted on cement pastes containing Type I and Type II Portland cement. Table 5.6 presents the compositions and properties of the two cements, based on information provided by the cement producer (average analysis of the month in which the cement was produced). The Bogue composition was calculated according to ASTM C150 (2004).

Table 5.6. Tested cements: chemical and Bogue composition together with other cement characteristics (percentages with respect to mass).

Cement	*CEM II/B-L 32.5N*	*CEM I 42.5R*
Loss of ignition [%]	13.50	2.69
Insoluble residue [%]	3.02	1.34
Silicon Oxide [%]	15.91	19.58
Aluminate Oxide [%]	4.21	4.72
Iron Oxide [%]	2.56	3.24
Calcium Oxide [%]	58.02	63.42
Magnesium oxide [%]	1.38	2.12
Sulphates [%]	2.71	3.52
Potassium oxide [%]	-	-
Sodium oxide [%]	-	-
Chlorides [%]	0.04	0.05
Free lime [%]	-	1.05
N/D (no dosed) [%]	-	-
C_3S [%]	42.47	51.63
C_2S [%]	13.58	17.18
C_3A [%]	6.82	7.03
C_4AF [%]	8.84	9.86
Limestone filler [%]	-	-
Gypsum [%]	-	-
Blaine [cm^2/g]	4899	3891
Specific gravity [g/cm^3]	2.99	3.13

In the scope of this experimental program, two cement paste compositions with two different water/cement ratios (w/c = 0.45 and w/c = 0.50) were adopted. The mixture proportions of the cement pastes as well as the corresponding nomenclatures are presented in Table 5.7. For both cement pastes with w/c = 0.5, more than one batch was tested. Therefore, the density value indicated in Table 5.7 corresponds to the average value and the observed variation (less than 0.23%). This care in the determination of density is particularly important due to its role in the

evaluation of E-modulus of the cement paste through the EMM-ARM method, as shown in equations (2.12) and (2.14) (page 35).

Table 5.7. Cement pastes adopted in this research work.

Reference	*Cement type*	*w/c ratio*	*Density (kg/m³)*
c32.5wc0.5	CEM II/B-L 32.5 N	0.50	1787.4±4.0
c42.5wc0.5	CEM I 45.5 R	0.50	1840.3±4.1
c42.5wc0.45	CEM I 45.5 R	0.45	1926.8

The acrylic tubes used for the EMM-ARM had an average elastic modulus of 4.72 GPa at 20°C (with a variation of ±0.02 GPa in all tested moulds) and an average density of 1172 kg/m^3. The values of E-modulus and density of the acrylic were verified in the laboratory through modal identification of the empty moulds, which were weighed before the start of each test.

Experimental program and procedures

The experimental program involved the measurement of the cement pastes E-modulus with 4 distinct methods: EMM-ARM, ultrasonic pulse velocity (UPV), bender-extender elements (BE) and classic cyclic compression (CC) tests. Penetration resistance was also measured through Vicat needle testing, according to EN 196-3 (2005b). The details about the procedures used in each method is presented in the next section. All EMM-ARM tests involved simultaneous testing of two specimens for repeatability checking. The list of all the specimens used during this experimental program, comprising the three cement pastes previously mentioned, is presented in Table 5.8. EMM-ARM, BE and UPV tests were performed continuously since casting, whereas the cyclic compression tests were conducted at the ages of 2, 3, 7, 14 and 28 days.

Table 5.8. Specimens used in the study.

Specimen	*Cement paste*	*Monitoring method*	*Curing temperature (ºC)*
32.5-Vic	c32.5wc0.5	Vicat	20
32.5-CC	c32.5wc0.5	CC	20
32.5-UPV	c32.5wc0.5	UPV	20
32.5-BE	c32.5wc0.5	BE	20
32.5-EMM1	c32.5wc0.5	EMM-ARM	20
32.5-EMM2	c32.5wc0.5	EMM-ARM	20
42.5-Vic	c42.5wc0.5	Vicat	20
42.5-CC	c42.5wc0.5	CC	20
42.5-UPV	c42.5wc0.5	UPV	20
42.5-BE	c42.5wc0.5	BE	20
42.5-EMM1	c42.5wc0.5	EMM-ARM	20
42.5-EMM2	c42.5wc0.5	EMM-ARM	20
42.5A-EMM	c42.5wc0.45	EMM-ARM	20
32.5-EMM40	c32.5wc0.5	EMM-ARM	40
42.5-EMM40	c42.5wc0.5	EMM-ARM	40

In specific regard to the preparation of the cement pastes, the mixing operations were performed in an automatic mixer, according to the following procedure that conforms the recommendations of EN 196-1 (2005a): (i) introduce the cement and immediately after add water (instant defined as "*t=0*"); (ii) start mixing at 500 rpm for 90 seconds; (iii) stop mixing during the following 90 seconds; (iv) resume mixing operation at 500 rpm for another 30 seconds. After the mixing process, the resulting cement pastes were poured into the moulds, which were simultaneously slightly vibrated for removal of air bubbles during the casting process. The time elapsed between mixing and the beginning of monitoring did not exceed 20 minutes for any of the continuous methods (EMM-ARM, UPV and BE).

All these tests on c32.5wc0.5, c42.5wc0.5 and c42.5wc0.45 were performed under moist sealed conditions at 20°C and carried out for at least 7 days. The only exception to the mentioned situation corresponded to the CC specimens that were demoulded right before the first test (t = 2days) and were placed, unsealed, in a controlled environment with T = 20ºC and RH = 60%. The temperature inside the distinct samples was assessed through embedded K-type thermocouples. In the EMM-ARM samples, the maximum temperature increase with respect to the registered room temperature was lower than 0.5°C, thus rendering temperature variation effects negligible. In the remaining specimens, maturity corrections were necessary to take into account the temperature effects during the cement hydration process shown in Figure 5.16.

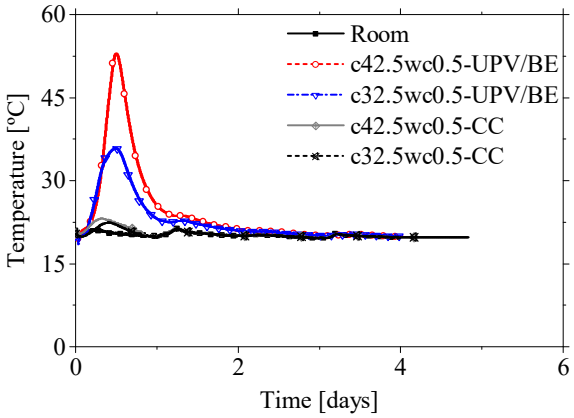

Figure 5.16. Specimens temperature history.

The comparative results to be presented in the next section refer to their equivalent age (t_{eq}), at a reference temperature adopted as 293.15°K = 20°C. In order to assess the apparent activation energy, two additional tests were performed with the EMM-ARM. These additional experiments were conducted on cement pastes c32.5wc0.5 and c42.5wc0.5, in a temperature-controlled room that guaranteed an average temperature of 40.2±0.2°C. The obtained E_{act} values that were used for maturity corrections in the scope of this study are discussed in section 5.2.2.3.

5.2.2.2. Experimental techniques and protocols

EMM-ARM

In this experimental program the cement pastes presented before were tested with the EMM-ARM version for cement pastes testing (see section 2.5.3). Here, the original test apparatus shown in Figure 2.18 (page 36) was used. The geometry of the tested beams is presented in Table 5.9.

Table 5.9. EMM-ARM beams' geometry.

	32.5-EMM1	*32.5-EMM2*	*32.5-EMM40*	*42.5-EMM1*	*42.5-EMM2*	*42.5-EMM40*	*42.5A-EMM*
$\varnothing_i$ (mm)	16.18	16.13	16.13	16.18	16.13	16.13	16.14
$\varnothing_e$ (mm)	20.13	20.11	20.10	20.14	20.13	20.11	20.12
Span (mm)	450.0	450.0	450.0	450.0	450.0	450.0	450.0

Classical cyclic compression tests (CC)

Classical cyclic compression tests (CC) with on-sample strain measurements were performed to quantify the E-modulus of cylindrical specimens. The cement paste cylindrical specimens utilized in this study had a diameter/height of 50/100 mm. The testing apparatus includes a hydraulic actuator with 50 kN capacity and 3 displacement transducers (LVDTs), supported by 2 aluminium rings attached to the specimens (spaced 40 mm), as presented in Figure 2.1 (page 10). The test protocol adopted in this work was based on the experiments reported by Maia *et al.* (2012b). Each test involved 3 loading/unloading cycles, with a loading rate of 200 kPa/s, and the E-modulus was computed in the loading branch of the last load/unload cycle. The maximum cyclic load reached 33% of the compressive strength of the cement paste at the age of testing, obtained through destructive compressive tests in 50×50×50 mm^3 cubes.

Ultrasound Pulse Velocity (UPV)

In the present work, the method for monitoring the velocity of ultrasonic waves in cement pastes is based on the generation and transmission of a single-period sine wave through an ultrasonic probe transmitter, according to the test configuration shown in Figure 5.17a. The setup consists of an ultrasonic transmitter placed on one side of the sample, as depicted in Figure 5.17b, and a receiver positioned on the opposite side. The wave, defined in a function generator (model TTI - TG1010A) with 0.1 mHz resolution, an accuracy of <10 ppm and a range of 0.1 mHz to 10 MHz, is transmitted to the sample through a contact probe (P-wave probe with operating frequency of 150 kHz and diameter of 25 mm), and received in the opposite side of the sample by another contact probe (identical to the source probe). The size of the probes is considered to be adequate for application to cement pastes since its diameter is greater than the largest expected heterogeneity. An oscilloscope with 16-bit resolution and a sensitivity of 10 mV/div to 20 V/div (PicoScope 4424) performs the analog-to-digital conversion of both emitted and received waves and transmits the digitized waves to the computer for signal processing.

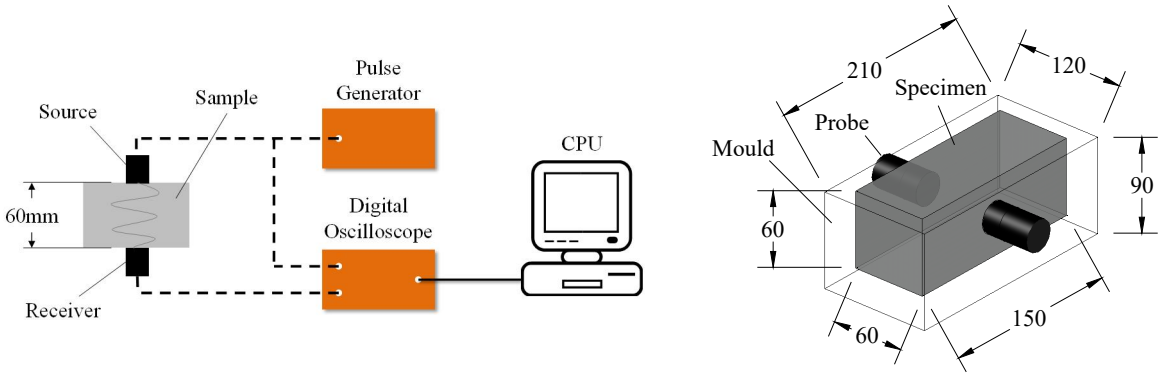

a) b)

Figure 5.17. UPV method: a) experimental set-up; b) container.

A prismatic mould, made of extruded polystyrene, with dimensions 60×60×150 mm^3 was used, as seen in Figure 5.17b. To allow measurements immediately after mixing, the UPV probes were positioned in advance in the opposite faces of the cross-section of the mould. Preliminary tests allowed to confirm that the adopted solution performed well, without any noticeable negative effects on the quality of the received wave.

Bender-extender elements (BE)

In the present work, the adopted test configuration for this methodology is quite similar to the one described in the previous section for UPV, except for the use of BE probes instead of ultrasonic probes (Figure 5.18a). In this study, T-shaped bender-extender elements made in the University of Western Australia (Brignoli *et al.*, 1996) were used, and they are schematically depicted in Figure 5.18b. These BE enable the measurement of P and S waves and operate in a wide frequency range, common for this type of probes.

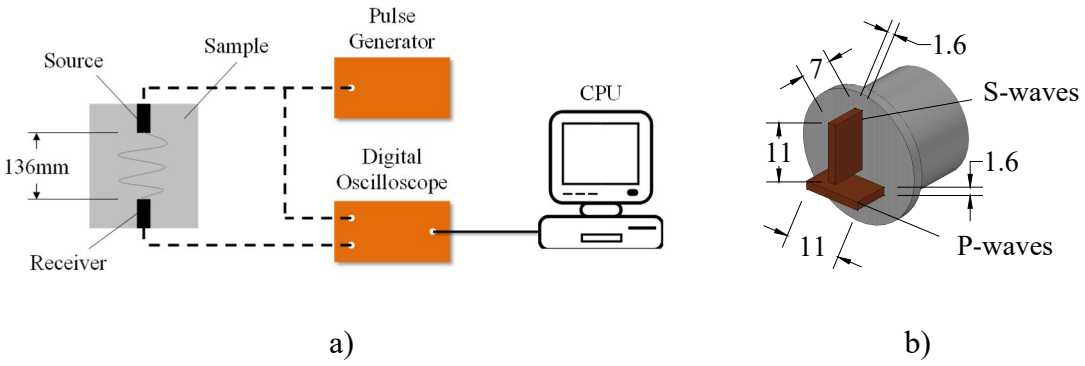

Figure 5.18. BE method a) experimental set-up; b) BE probe [units: mm].

In order to avoid errors in the identification of the wave propagation time, special attention must be given to the mould used for the BE methodology, due to the possible existence of "cross talk" parasite waves (Santamarina *et al.*, 2001). However, as the usual operation of BE elements involves a wide frequency range that can start as low as 1 kHz, the distance between the probes must hence be higher, in comparison with the distance adopted for the UPV method. Preliminary tests in the scope of this research work have shown that the adopted geometry for the UPV (60×60×150 mm^3, as shown in Figure 5.19) made in extruded polystyrene is also suitable for BE experiments on cement pastes. However, in this case the probes were placed in the opposite faces of the mould that are separated by 210 mm. Similarly to the UPV, the BE probes were fixed to the mould in order to allow measurements immediately after mixing.

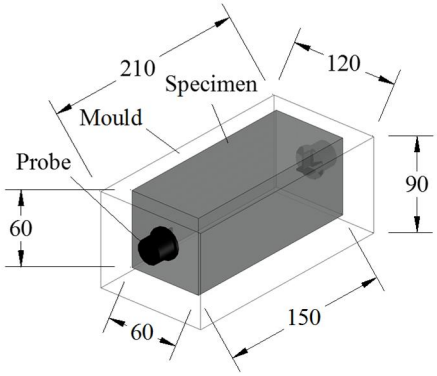

Figure 5.19. Container for the use of bender-extender elements. [units: mm].

The choice of the best frequency for wave velocity assessment at each instant of testing was made by manually sweeping the frequency to obtain the highest output signal amplitude. At such frequency, the identification of the wave arrival time is facilitated, since the noise-to-signal

ratio is at its lowest. It is reasonable to assume that within the range of frequencies used in this method, the travel time is independent of frequency, that is, the travel time remains the same regardless of the applied input frequency (Viana da Fonseca *et al.*, 2009).

5.2.2.3. Results and discussion

The results are cumulatively presented below, beginning with the results of classic methods (Vicat test and cyclic compression), followed by the EMM-ARM results. The comparison proceeds with the results obtained through the wave propagation methods (UPV and BE). Finally, a comparison between the data collected through all analysed testing methodologies is presented.

Penetration tests and cyclic compression tests

The Vicat and cyclic compression tests conducted on the cement pastes c32.5wc0.5 and c42.5wc0.5 yielded the results presented in Figures 5a and 5b. The results of penetration testing (Figure 5a) show that the structural setting time occurs earlier for the cement paste prepared with the higher cement class (c42.5wc0.5) – see Table 5.10. Cyclic compression testing of c42.5wc0.5 also yielded higher elastic modulus than of c32.5wc0.5 during the whole period of study as shown in Figure 5b.

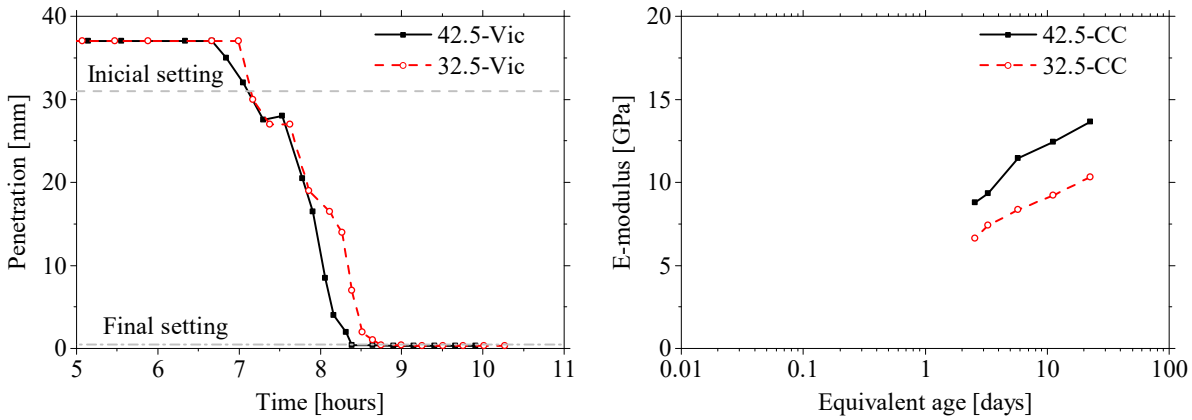

a) b)

Figure 5.20. Results obtained through the classic methods a) Penetration resistance (Vicat needle) b) Cyclic compression.

Table 5.10. Structural setting time of the cement pastes.

Cement paste	*Initial setting (hours)*	*Final setting (hours)*
c42.5wc0.5	7.05	8.39
c32.5wc0.5	7.17	8.75

EMM-ARM

The resonant frequencies identified by the EMM-ARM method for the three studied cement paste mixtures are shown in Figure 5.21a. It is worth mentioning that a wide range of frequencies was covered throughout the curing process of the cement pastes, ranging from ~14.6 Hz to 26.0 Hz within the testing period. Moreover, all frequency evolution curves appear to be plausible, showing an initial dormant period (where the frequency remains almost constant within ±0.3 Hz). After this threshold, the frequencies evolved significantly for all tested specimens until approximately 48 hours of curing period, after which a dramatic reduction in the slope of frequency evolution occurs.

The elasticity modulus of the tested cement pastes was estimated by applying equations (2.11) and (2.12) (page 35) to the resonant frequencies presented in Figure 5.21a. The resulting E-modulus evolution is shown in Figure 5.21b.

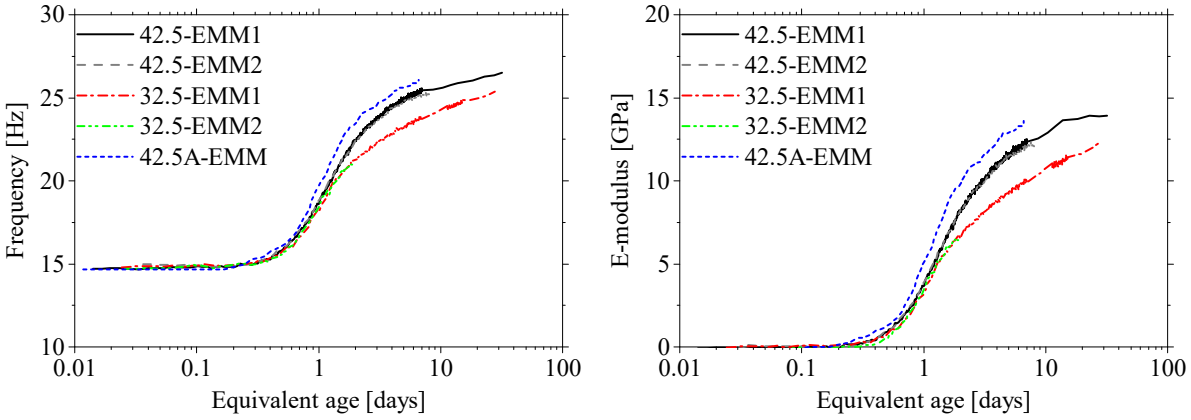

a) b)

Figure 5.21. EMM-ARM results: a) Frequency evolution; b) E-modulus evolution.

Firstly, it is possible to verify that the E-modulus evolution curves of the same cement pastes have very good coherence with each other, demonstrating adequate repeatability of EMM-

ARM. Furthermore, when comparing the results obtained with the two pastes containing the same w/c ratio (c42.5wc0.5 and c32.5wc0.5), it can be seen that the cement paste containing the CEM I 42.5R cement has a higher stiffness, with a difference of ~2 GPa at the age of 7 days (168 hours) - see Figure 5.21b. However, even though the cement paste c42.5wc0.5 has reached a higher stiffness after the first day of curing, the E-modulus evolution at very early ages is fairly similar to that of paste c32.5wc0.5. In fact, this would not be expected by strictly considering the chemical composition of the utilized cements, namely due to the higher C_3S content of cement CEM I 42.5R. Nonetheless, another important characteristic might justify this behaviour at very early ages: the specific surface or Blaine index. In fact, the Blaine index of CEM I 42.5 R is lower than that of CEM II/B-L 32.5N (3891 against 4899 cm^2/g according to Table 5.6). The similarity of the E-modulus evolution at very early ages between the two pastes can thus be considered reasonable, taking into account these two aspects that justify the apparent inverse trends: clinker composition and specific surface.

A further comparative interpretation can be made by observing the behaviour of the two pastes containing the same type of cement: c42.5wc0.5 and c42.5wc0.45. The corresponding results are shown in Figure 5.21b, where the expected trend was confirmed: the reduction of the w/c ratio increases early hydration velocities, and leads to higher values of E-modulus (after 6 days of curing, there is a difference of approximately 1.3 GPa).

The comparison between the elastic modulus results obtained by EMM-ARM and by classic methods (CC and Vicat) for the cement pastes c32.5wc0.5 and c42.5wc0.5 is shown in Figure 5.22. It can be seen that the values obtained through the EMM-ARM are similar to those collected in CC tests in terms of magnitude and evolution kinetics. However, the results for c32.5wc0.5 (Figure 5.22a) show a non-negligible difference of 1.4 GPa at t_{eq} = 22.4 days (538 hours). This deviation may possibly be explained by differences in the curing conditions of the samples. In fact, the EMM-ARM samples remained in perfectly sealed conditions during the whole test, while the samples used for the CC tests were exposed to drying during the testing period. This small variation in the curing conditions may have influenced the hydration process at the surface of the CC specimens (Parrott, 1990), which may have significant effects in view of the small size of the specimen, thus resulting in lower stiffness. As the porosity of c32.5wc0.5 is higher than that of c42.5wc0.5, it is plausible that this deficient curing of CC specimens may have affected c32.5wc0.5 more significantly, as opposed to c42.5wc0.5.

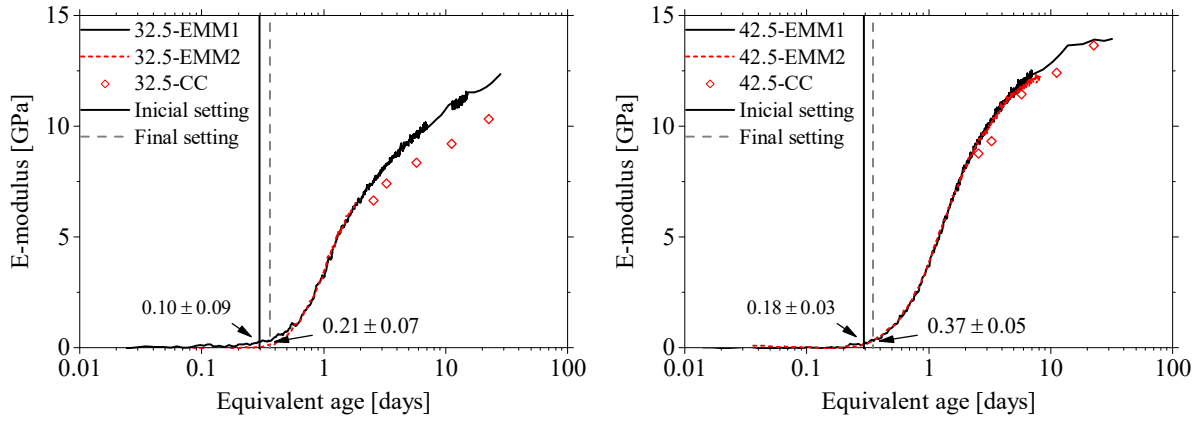

a) b)

Figure 5.22. Comparison of the results of EMM-ARM, Vicat, and cyclic compression for cement pastes: a) c32.5wc0.5 b) c42.5wc0.5.

The results presented in Figure 5.22 also show good agreement between EMM-ARM and the data collected by the Vicat needle, in the sense that the end of setting determined by Vicat testing coincides with the end of the dormant period observed in EMM-ARM, followed by a strong acceleration of the hydration kinetics.

With the results obtained from EMM-ARM the final setting time was computed from the derivative of the E-modulus evolution according to the procedure described in the previous section 5.2.1.3. Again, due to the acquisition noise the experimental data was fitted by the equation (4.1) to enable the computation of the first derivative of the E-modulus evolution. To the fit the experimental the parameters shown in Table 5.11 were used.

Table 5.11. Parameters used to fit the EMM-ARM results.

Parameter	*32.5-EMM*	*42.5-EMM*
α_1	9.218	2.830
α_2	3.584	11.512
τ_1	0.980	1.184
τ_2	7.652	1.299
β_1	1.601	2.619
β_2	1.087	0.954
R^2	0.999	0.999

The E-modulus evolutions and the corresponding first derivative along time are shown in Figure 5.23. From these graphs the final setting time was computed by selecting the first point with

50% of the peak value of the first derivative of the E-modulus evolution. The following values were obtained for final setting: 8.10 and 10.48 hours for the cement pastes c42.5wc0.5 and c32.5wc0.5, respectively. The values obtained for the cement paste c42.5wc0.5 are in very good agreement with ones obtained with Vicat needle presented in Table 5.10. However, for the cement paste c32.5wc0.5 the coherence between the two values is poor with a difference of 1.43 hours. This difference could be related to differences in the curing temperatures since the tests were performed at room temperature without a precise control.

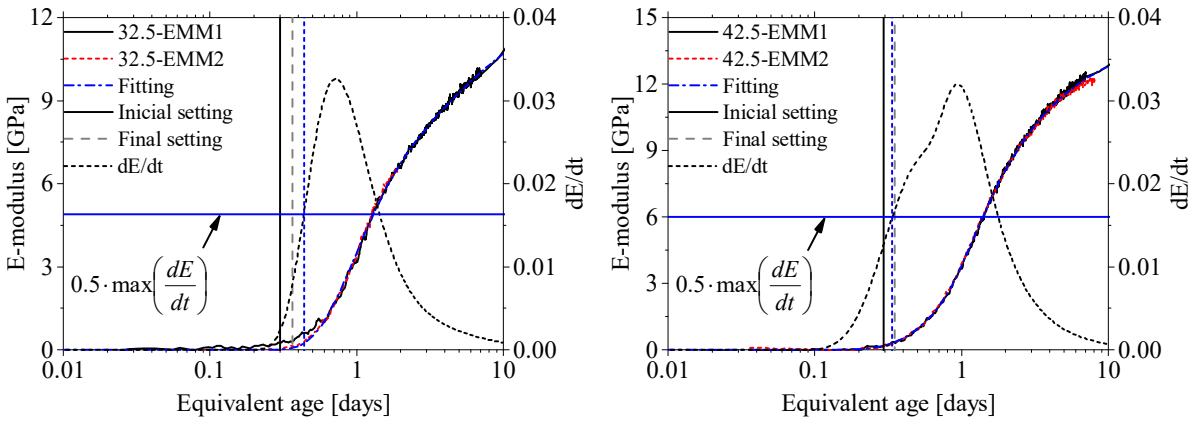

a) b)

Figure 5.23. EMM-ARM final setting time determination: a) Cement paste c32.5wc0.5; b) Cement paste c42.5wc0.5.

Ultrasonic Pulse Velocity (UPV)

The evolution of the P-wave velocity for c42.5wc0.5 and c32.5wc0.5 is shown in Figure 5.24, together with information collected by Vicat testing.

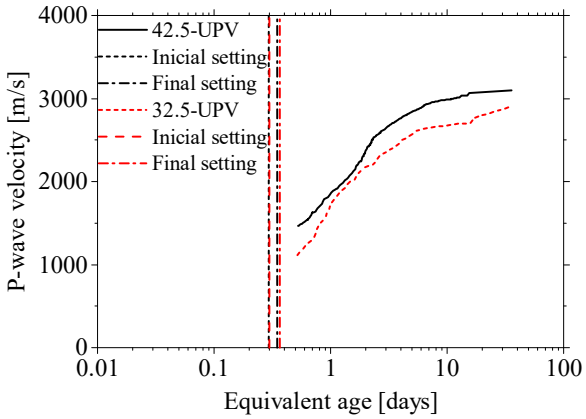

Figure 5.24. P-wave velocity evolution for cement pastes c42.5wc0.5 and c32.5wc0.5.

Firstly, it should be noted that UPV was unable to provide measurements of P-wave velocity in the cement pastes at very early ages, including the setting period. The earliest measurement was only possible at t_{eq} = 12.4 hours, when EMM-ARM already exhibited E-moduli above 0.8 GPa for both pastes (see Figure 5.22). The reason for this problem can be attributed to the presence of air bubbles in the samples, which have been reported to attenuate and delay the wave propagation, as well as due to the high impedance mismatch between the transducers and the fresh cement paste (Zhu *et al.*, 2011a). In fact, in order to monitor the evolution of the P-wave velocity in cement pastes, some authors (Boumiz *et al.*, 1996, Zhu *et al.*, 2011a) used de-aired samples (previously placed in vacuum) with successful results. However, since the 'real' cement pastes always contain some air bubbles the de-airing of the samples may end up producing unrealistic results. In order to avoid this drawback in UPV, some authors (Reinhardt and Grosse, 2004) successfully performed measurements during the setting by using smaller distances between the probes and more energetic excitation signals (with higher voltage) even with the wave attenuation. Such alternative was not available in this research work. Another solution to this problem, currently under research, involves adjusting the input frequencies to lower values (below the reference frequency of the ultrasonic transducers) at very early ages. Despite the reduction in the performance of the transducer, this procedure would enable to comply with the initially low stiffness of the tested material. However, despite the absence of UPV measurements in this initial period (~12 hours), the wave velocity measurements of Figure 5.24 exhibit an evolution which can be considered plausible. In fact, the various stages usually observed in the cement hydration kinetics after the dormant period can be identified: (i) an initial stage where a substantial increase in wave velocity occurs; (ii) a subsequent stage in which the velocity evolution becomes less significant. Lastly, it can be noted that the

c42.5wc0.5 paste shows a greater increase in wave velocity, which is consistent with the results of the EMM-ARM that were already reported.

Bender-extender elements (BE)

The application of BE for studying the evolution of the stiffness characteristics of cement pastes is still taking its first steps, with very few published works so far (Zhu and Kee, 2010, Zhu *et al.*, 2011b). However, the success already achieved in the application of BE to cement-stabilized soils at the University of Minho (Azenha *et al.*, 2011, Silva *et al.*, 2013b) has justified the interest on this testing methodology.

As opposed to the UPV method, the use of BE easily allows to perform high quality measurements immediately after casting. This is mainly due to the high efficiency over a wide frequency range that the BE probes possess, which enables an adjustment of the input frequency to provide better results at each instant of measurement. However, despite this benefit, the use of BE is often accompanied by difficulties associated with a high sensitivity to external disturbances (such as the existence of electrical noise in the testing room), which obscure and compromise the interpretation of test results. This high sensitivity can be partly explained by the relatively low power of the signal generator adopted in this research that solely allowed a maximum excitation amplitude of 20 V. On the other hand, the use of power amplifiers (to boost the input signal) is limited by the transducer itself, which depolarises approximately above 60 V.

Figure 5.25 shows four S-wave signal readings performed for the paste c42.5wc0.5 at ages of 2.9, 9.0, 26 and 172 hours. These readings were conducted at optimum increasing frequencies between 1 kHz at 2.9 hours and 50 kHz at 172 hours (see Figure 5.25a). In the four measurements presented in Figure 5.25b, one can clearly observe the difficulty the identification of the first arrival of the wave. This problem was already mentioned in the works of Ferreira (2009) and Viana da Fonseca *et al.* (2009) regarding the performance of BE in stiff materials.

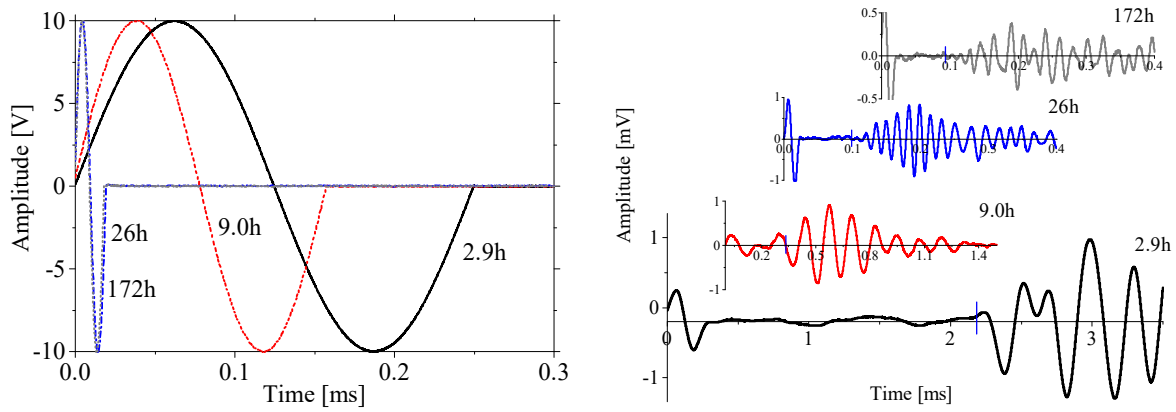

a) b)

Figure 5.25. Signal readings during the use of the BE method in the paste c42.5wc0.5 at 2.9, 9, 26 and 172 hours of curing: a) Input signal at the transmitter BE; b) Output signal registered by the receiver BE.

The BE used in these tests have the capability of measuring compressional (P) and shear (S) waves, hence initially all tests included the recording of both wave types. However, after some measurements, it was found that both sensors measured exactly the same type of wave: S-waves (noted by the same wave shape and the order of magnitude of the recorded velocities). The justification for this phenomenon is due to the characteristics of the BE probes, as mentioned by Lee and Santamarina (2005), and schematically shown in Figure 5.26: the probe generates two P-wave side lobes normal to their plane and a S-wave frontal lobe. Therefore, since the generation of response signal in the receiver demands that the sensor itself bends, when the BE transmitter and BE receiver are perfectly aligned (which is the case in our work), the P-waves are parallel to the longitudinal axis of the receiving transducer, thus being unable to flex it. On the other hand, the S waves disturb the transducer in the direction perpendicular to its longitudinal axis, thus causing a larger bending motion and as a result a larger signal output. This feature causes them to lose the ability to adequately receive P-waves, while having a significant resolution in the measurement of S-waves. Additionally, at very early ages, i.e. in fresh pastes, the propagation of P-waves is difficult, as already mentioned in regard to UPV tests, due to the presence of entrapped air and to the high stiffness impedance between the transducer and the material. As the paste hardens, the compressional wave velocity increases rapidly and the frequency required to measure such high velocity causes the BE to vibrate in complex mode shapes, which in turn strongly reduces the amplitude of the effectively propagated wave and makes it difficult to detect the P-wave in the received signal.

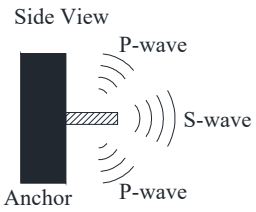

Figure 5.26. Waves generated by a BE probe. Adapted from Lee and Santamarina (2005).

Consequently, the attempt to measure P-waves with BE in the scope of this research work was abandoned. Moreover, these results demonstrate that the use of S-waves is more suited to monitor these complex evolving processes than P-waves, since shear waves only propagate through the solid skeleton of the specimens, providing a higher sensitivity towards the structural changes that occur during setting.

After obtaining the propagation time of the S-waves, the evolution of the wave velocity was computed, as shown in Figure 5.27. It can be observed that there are no significant differences in the recorded wave velocities for the two types of pastes. However, the S-wave velocity is higher in the c42.5wc0.5 paste throughout the entire curing period. It should also be noted that the difference in the wave velocity increases along the curing process, which is in agreement with the results of the previous methods. Therefore, the application feasibility of this methodology to cement pastes was confirmed in coherence with the conclusions of the research work conducted by Zhu *et al.* (2011b). It should also be noted that, in the very early ages of curing (before setting), this method is more sensitive than the EMM-ARM. In fact, the measurements with BE method begin ~2hours after mixing, which is significantly sooner than the initial setting time that only occurred at 7 hours of age. This is a clear indication that a robust solid skeleton for S-wave transmission exists much sooner than the conventional initial setting time (Sant et al., 2009), thus highlighting the potential of S-waves for measuring pre-setting behaviour. In fact, any potential analysis of the viscoelastic properties at pre-setting stages (for example through a rheometric test (Sun *et al.*, 2006)) can lead to the observation that significant changes occur during this period. However, the EMM-ARM results still remain unaffected at this stage (i.e. constant), while there is already evolution of the velocity of the propagated wave measured with the BE.

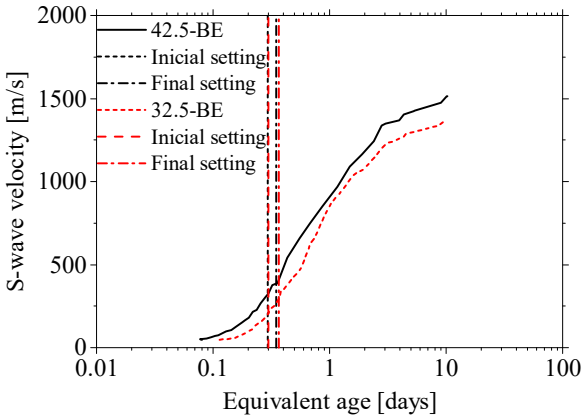

Figure 5.27. S-waves velocity evolution in the c32.5wc0.5 and c42.5wc0.5 cement pastes.

Overall comparison

Taking into account that the methodologies based on wave propagation measure dynamic parameters, for the purpose of comparison of all methodologies under study, the results were normalized ('Norm' in Figure 5.28) by dividing all results of each specimen/methodology by their corresponding values at t_{eq} = 7 days. Moreover, in order to simplify the analysis and to compare both methods based on wave propagation (BE and UPV) with the results of quasi-static methods, the velocity values were squared (V^2) prior to normalization, as V^2 is proportional to the elasticity modulus (see equation (2.4) – page 16).

The results of all experimental methods involved in this comparison is given in Figure 5.28, which demonstrates a quite reasonable reciprocal agreement, thus mutually validating the studied methodologies. The good performance of EMM-ARM in the scope of this comparative study, together with its ability to provide precise, continuous and quantitative estimates of E-modulus confirms the versatility and applicability of this methodology.

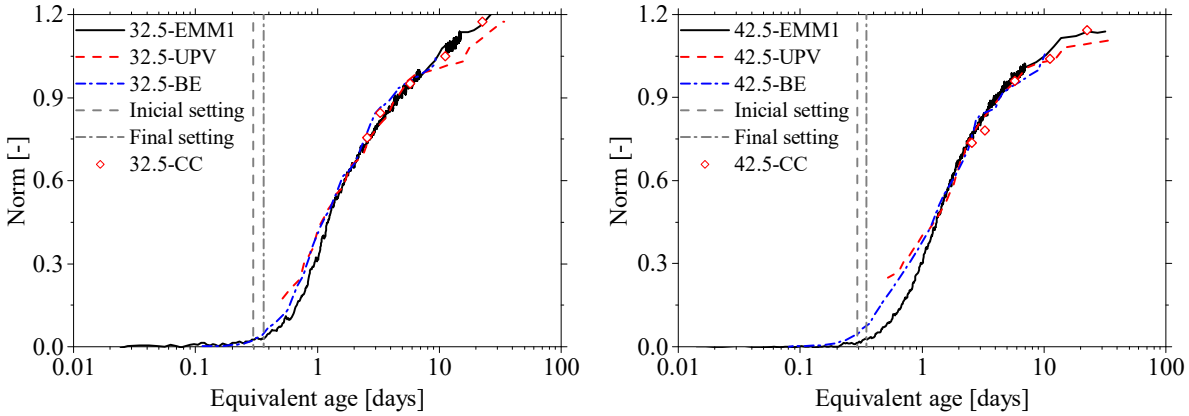

a) b)

Figure 5.28. Comparison of the results of all methodologies used in this study for cement pastes a) c32.5wc0.5 and b) c42.5wc0.5.

In regard to setting times, there is also a good coherence between Vicat, EMM-ARM and BE, as observable in Figure 5.28. Thus, these results have confirmed the applicability of the wave propagation methods to monitor the stiffness of cement pastes since the fresh state and throughout the entire hardening process, as already mentioned by other authors (Boumiz *et al.*, 1996, Reinhardt and Grosse, 2004). Despite this fact, the results obtained by these wave-propagation based methods should be regarded qualitatively, since these refer to dynamic properties, whose conversion to static properties is often arguable, particularly at very early ages, due to the evolution of Poisson's ratio during curing (Popovics *et al.*, 2008).

However, it should be noted that these wave velocity methods (UPV and BE) seem to exhibit a slightly more accelerated evolution kinetics than EMM-ARM, which is more evident for the c42.5wc0.5 paste, as shown in Figure 5.28b. This fact may be related to the early evolution of Poisson's ratio. Similar findings have been reported in other research works, where the consideration of constant Poisson's ratios led to apparent earlier acceleration of stiffness when estimated through pulse velocity methods (Boulay *et al.*, 2013a).

Activation energy

The two additional EMM-ARM tests that were performed at 40°C allowed obtaining the apparent activation energy of c42.5wc0.5 and c32.5wc0.5. Given the influence of temperature

variations on the stiffness of the acrylic (Schirrer and Goett, 1982), an initial modal identification test was performed on the acrylic hollow beam to obtain the E-modulus of the acrylic at 40ºC. An E-modulus of 3.6±0.2 GPa was obtained.

The results collected during the apparent activation energy experiments are shown in Figure 5.29a. It is noted that the test conducted inside the temperature-controlled chamber at ~40°C lasted only 10 hours for the c32.5wc0.5 paste and 16 hours for the c42.5wc0.5 paste. The limited duration of these tests was due to an electrical problem in the data acquisition system. Nonetheless, despite the short duration of the tests, the repetition of the tests was considered unnecessary because the extracted information was sufficient for determining the apparent activation energy of the tested cement pastes. The results show that the initial setting in specimens exposed to 40°C occurred much earlier (~2 hours) than the initial setting observed in the tests at 20°C (~7 hours). Moreover, the reaction rate was also more significant, since it can be observed that, for example, the time needed to growth the elastic modulus from 1 to 5 GPa is approximately 5.49 hours at 40°C, as opposed to the approximately 18.24 hours required for the test conducted at 20°C.

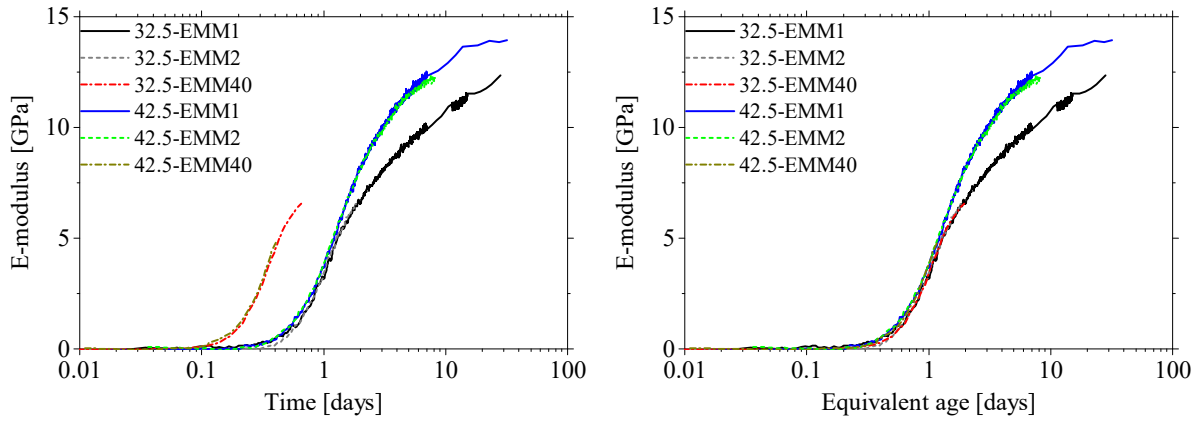

Figure 5.29. E-modulus evolution of the cement pastes c32.5wc0.5 and c42.5wc0.5 cured at different temperatures (20°C and 40°C), obtained through the EMM-ARM: a) plotted in order to the curing age b) plotted in order to the equivalent age at 20°C.

The data collected through these particular tests enabled the possibility of determining the apparent activation energy (E_{act}) by the successive application of equation (6.1) (page 194) with distinct E_{act} values until the E-moduli evolution at both temperatures (20°C and 40°C) matched

when presented in order to their equivalent age (t_{eq}) (see Figure 5.29b). This procedure is usually referred to as the "superposition method" (D'Aloia, 2003, D'Aloïa *et al.*, 2001). The following values of E_{act} were computed: 42 kJ/mol and 41 kJ/mol for pastes c32.5wc0.5 and c42.5wc0.5, respectively.

5.3. Repeatability of E-modulus estimations

In the previous subchapter it was shown that EMM-ARM capable of very consistent results when compared with the competing methods. However, the repeatability of the method still needed to be assessed in order to make the measurement method valid (Dotson, 2015). According to JCGM (2012) repeatability in the context of a physical measurement is "*the measurement precision under a set of repeatability conditions of measurement (...) that includes the same measurement procedure, same operators, same measuring system, same operating conditions and same location, and replicate measurements on the same or similar objects over a short period of time*". In accordance to the previous subchapter, the repeatability study was divided in two parts: the first one dedicated to the version of EMM-ARM for concrete testing and the second on to the cement paste version.

5.3.1. Concrete

To assess the repeatability of EMM-ARM a series of seven tests were performed in five different concrete mixes with at least 2 beams tested simultaneously. The list of all the tests performed with the information of the concrete mix tested, the number of specimens and temperature of testing is presented in Table 5.12. All the tests were performed at room temperature with exception to the test T7 that was performed under imposed variable temperature. The mean temperature history measured in the specimens tested in test T7is shown in Figure 5.30.

Table 5.12. Tests performed in the repeatability study for the EMM-ARM concrete version.

Test	*Concrete*	*Number of tests*	*Testing temperature*
T1	C1	3	Room temperature 20±2°C
T2	C2	3	Room temperature 20±2°C
T3	C3	3	Room temperature 20±2°C
T4	C4	3	Room temperature 20±2°C
T5	C5	6	Ambient temperature 17±7°C
T6	C6	3	Ambient temperature 23±8°C
T7	C1	2	Variable See Figure 5.30

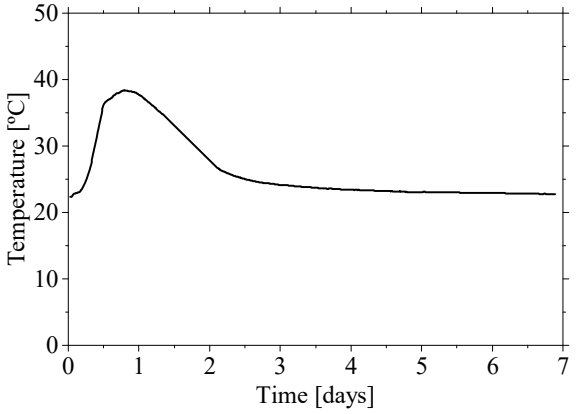

Figure 5.30. Temperature history of T7 test.

The mixture proportions for the five different concretes are given in Table 5.13.

Table 5.13. Mixture proportions of the different concrete mixes used.

Component	*Mix C1 (kg/m³)*	*Mix C2 (kg/m³)*	*Mix C3 (kg/m³)*	*Mix C4 (kg/m³)*	*Mix C5 (kg/m³)*	*Mix C6 (kg/m³)*
Sand	250 (0/2) 460 (0/4)	395 (0/2) 395 (0/6)	245 (0/2) 786 (0/6)	739 (0/4) –	300 (0/2) 540 (0/6)	330 (0/2) 560 (0/6)
Gravel	1140 (4/16) –	840 (6/22) –	417 (6/14) 478 (14/20)	1072 (8/22) –	550 (6/14) 420 (11/22)	550 (6/14) 440 (11/22)
Cement	218 (CEM II/A-L 42.5R)	320 (CEM I 42.5R)	280 (CEM I 42.5R)	340 (CEM I 52.5N PMES CP2)	320 (CEM II / A-L 42.5R)	220 (CEM II / A-L 42.5R)
Fly ash	112	–	40	–	100	130
Filler	–	260	–	–	–	–
Water	155 l/m³	160 l/m³	143 l/m³	184 l/m³	165 l/m³	160 l/m³
Super plasticiser	3.30 (Sikament 400+)	7.64 (Viscocrete 3006)	6.25 (Rheobuild 1000)	–	3.36 (BasfGlenium Sky 548)	2.45 (BasfGlenium Sky 548)
Plasticiser	–	–	–	–	0.84 (BasfPozzolith 540)	2.10 (BasfPozzolith 540)

The E-modulus evolutions obtained in the seven different tests are shown in Figure 5.31. In this figure only the mean curve (full lines), the mean curve + the standard deviation (dashed lines) and the mean curve - the standard deviation (dash dot lines) are represented. As can be observed in all the tests, the deviation from the mean curve is very small with average error of 1.5% at the end of all the test. In fact, even tests performed with the same concrete but with different temperature histories (T1 and T7), the final values measured at the age of 7 days have a very small discrepancy (a difference of 0.5 GPa or 1.8%). These results enable to state that the E-modulus estimations obtained with EMM-ARM in the version for concrete have a very good repeatability.

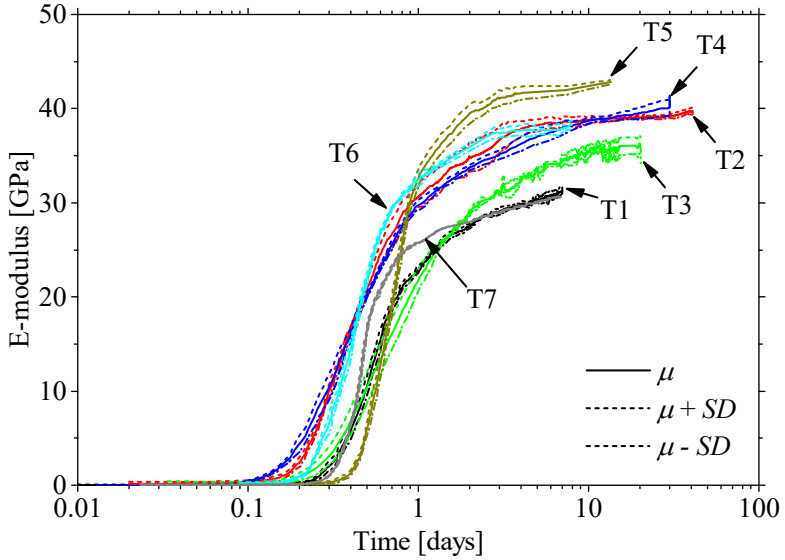

Figure 5.31. Concrete E-modulus evolutions obtained in seven EMM-ARM tests.

5.3.2. Cement paste

The repeatability of EMM-ARM for cement pastes was evaluated by performing seven tests with seven different cement pastes with at least 2 specimens. The list of all the tests performed with the information of the cement paste composition, the number of specimens and temperature of testing is presented in Table 5.14.

Table 5.14. Tests performed in the repeatability study for the EMM-ARM cement paste version.

Cement paste	*Cement*	*w/c*	*Number of tests*	*Testing temperature*
GA0.50T20	Grey type A	0.50	7	20°C
GB0.50T20	Grey type B	0.50	2	20°C
GC0.35T20	Grey type C	0.35	2	20°C
W0.32T20	White	0.32	2	20°C
W0.40T20	White	0.40	2	20°C
W0.48T20	White	0.48	2	20°C
W0.40T10	White	0.40	2	10°C

The composition and properties of the different cements used in the cement pastes are shown in Table 5.15.

Table 5.15. Composition of the different cements used in the cement pastes.

Cement	*Grey type B*	*Grey type A*	*Grey type C*	*White*
C_3S [%]	42.47	51.63	70.80	66.89
C_2S [%]	13.58	17.18	10.20	20.00
C_3A [%]	6.82	7.03	6.40	3.51
C_4AF [%]	8.84	9.86	7.30	1.00
Free lime [%]	-	1.05	-	0.31
Gypsum [%]	-	-	5.30	-

The E-modulus evolutions obtained in the seven different tests are shown in Figure 5.32. In this figure only the mean curve (full lines), the mean curve + the standard deviation (dash lines) and the mean curve - the standard deviation (dash dot lines). As can be observed in all the test results, the deviation from the mean curve is very small with average error of 1.1% at the end of all the tests. These results enable to state that the E-modulus estimations obtained with EMM-ARM in the version for cement pastes have a very good repeatability.

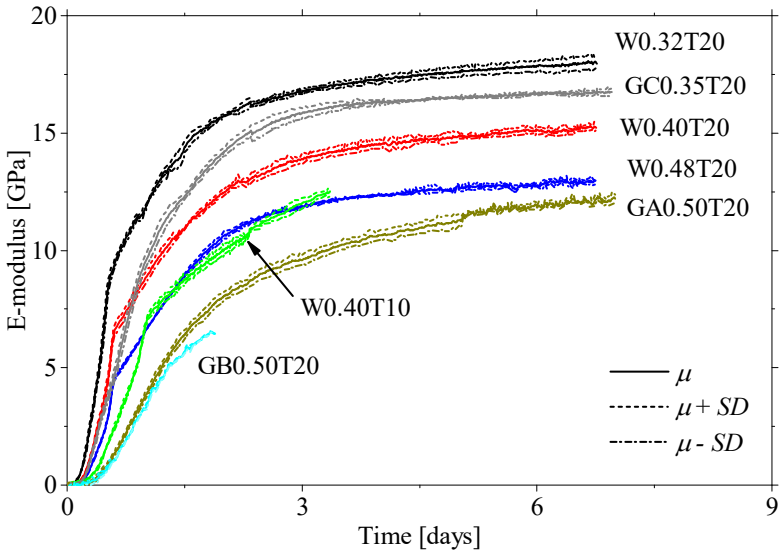

Figure 5.32. Cement paste E-modulus evolutions obtained in seven EMM-ARM tests.

5.4. Reproducibility of the EMM-ARM experiments

In metrology sciences, a measuring method is only valid if its application is reproducible (Dotson, 2015). According to JCGM (2012) measurement reproducibility is "*the measurement precision under reproducibility conditions of measurement (...) that includes different locations, operators, measuring systems, and replicate measurements on the same or similar*

objects". Therefore, in order to assist further validate the EMM-ARM, a new experimental program targeted to the study of recycled aggregates in concrete was seized to evaluate the reproducibility of EMM-ARM. This experimental program was part of an international collaboration with the University of A Coruña and was performed by Miriam Lizancos (PhD student from A Coruña university), who is henceforward referred as 'inexperienced user'. To allow the implementation of the EMM-ARM by a non-experienced operator, a user guide was made as presented in Appendix A. One should highlight that the inexperienced user had access to this manual and only had minor instructions delivered personally in order to perform the EMM-ARM application autonomously.

Regarding the experimental program, two reusable EMM-ARM beams (see Figure 3.17) were tested with the characteristics presented in Table 5.16. The tests were performed under EMA conditions. The excitation of the beams was performed through the custom made noncontact electromagnetic actuator presented in section 4.4.2.1 connected to a dynamic signal analyser NI 4431 with 24-bit resolution that generated a sine sweep between 20 and 200 Hz in 40 seconds with 7 Vpp. The response of each beam was acquired at a rate of 1250 Hz by an accelerometer PCB 393B12 (sensitivity: 10 V/g; range: ±0.5 g) connected to the same dynamic signal analyser. Each measurement had a duration of 300 seconds and was repeated each 12 minutes. The resonance frequencies were identified through the TF method presented in section 4.4.2.3 with a model order of 4.

Table 5.16. Characteristics of the EMM-ARM beams used in the reproducibility tests.

Reference	*R-PVC-1*	*R-PVC-2*
Geometry		
Cross-section	Circular	Circular
$\varnothing_i$	96.04 mm	96.35 mm
$\varnothing_e$	110.11 mm	110.20 mm
Span	1000 mm	1000 mm
Supports	$Ø_{PR}$=12 mm Steel supports	$Ø_{PR}$=12 mm Steel supports
Mould		
Density	1794.6 kg/m^3	1777.8 kg/m^3
E-modulus	3.10 GPa	3.10 GPa
Reusable	Yes	Yes
Concrete density	2400.6 kg/m^3	2375.8 kg/m^3

The two beams were tested in two different concrete batches of the same concrete with the composition presented in Table 5.17. In addition to the EMM-ARM, CC tests were performed

after 8.5 days of curing in the concrete batch of the EMM-ARM beam 1 (R-PVC-1) according to the standard EN 12390-13 (2013).

Table 5.17. Concrete composition used in the EMM-ARM reproducibility tests.

Components	*Mass (kg/m³)*
Cement	400
Sand	308 (0/2)
	608 (0/5)
Gravel	300 (4/12)
	600 (10/20)
Water	180

The identified resonance frequency evolutions had evolution kinetic similar to the results obtained in the previous implementations as can be seen in Figure 5.33a. Furthermore, the frequency evolutions of the two different beams had a good repeatability with a difference of only 0.94% (1.25 Hz) at 2.45 days. The estimated concrete E-modulus and the corresponding comparison with CC results for this test are shown in Figure 5.33b. As can be seen the E-modulus evolutions estimated by EMM-ARM had a kinetic similar to previous implementations. Additionally, the coherence between the EMM-ARM and CC results is similar to that which had been previously obtained with a difference of 3.6% (1.4 GPa). This leads to the conclusion that the EMM-ARM can easily be reproducible by a non-experienced operator with access to the EMM-ARM users guide and minor instructions.

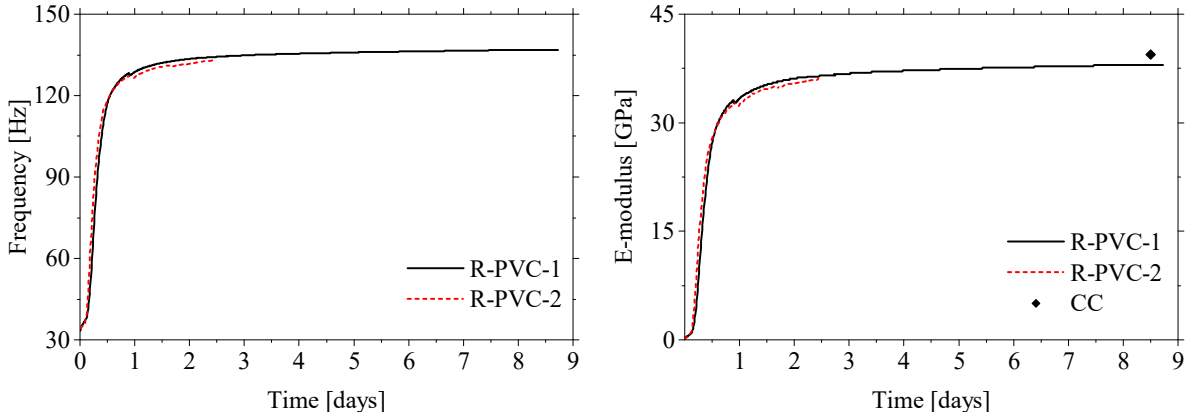

a) b)

Figure 5.33. EMM-ARM reproducibility tests results: a) Frequency evolution; b) E-modulus evolution.

After these first tests the PhD student, Miriam Lizancos, has continued to use the EMM-ARM. Until now the student has already performed 16 different tests and only 3 have faced problems not directly related to the experimental technique (one due to power loss, other due to malfunction of the custom actuator and the last one due to interference by an external person). Yet, even in these three tests the results obtained since the beginning of the test until the instant when the problem happened were recovered. In the end Miriam Lizancos was interviewed to access the perception about the EMM-ARM. The results of the interview are summarized in Table 5.18.

Table 5.18. Quality assessment of the EMM-ARM method by Miriam Lizancos.

	Questions	*Score*
1.	Do you consider that the EMM-ARM is ready to be used by an unexperienced user with only support of a user manual?	5
2.	Do EMM-ARM results have adequate the accuracy for scientific use in materials research?	5
3.	Do you consider that your implementation of EMM-ARM encountered relevant difficulties?	0
4.	Is the EMM-ARM user's manual clear?	5
5.	Does the user's manual have all the necessary information?	5
6.	Is the EMM-ARM software easy to use?	5
7.	Does the EMM-ARM software respond to your experimental needs?	5
8.	Do you think that EMM-ARM should be addressed in a standard for wild spread application?	5
Scale: 0 – Not agree; 5 – Totally agree		
How do you rate EMM-ARM as an experimental technique?		5
Scale: 0 – Very bad; 5 – Excellent		

As can be observed the results are undoubtedly outstanding with an overall rate of 'Excellent'. Only in the third question the answer was not totally convinced. In fact, the student had some minor problems during the implementation that had classified as 'non relevant'. Since then, three more research centres are now implementing the EMM-ARM: the *École polytechnique fédérale de Lausanne* (EPFL), the *Swiss Federal Laboratories for Materials Science and Technology* (EMPA) and the *Pontificia Universidad Católica del Perú* (PUCP). The first feedback provided by these research centres was positive and a scientific publication was already published (Aguilar *et al.*, 2016).

5.5. Accuracy of the E-modulus estimations

According to JCGM (2012) measurement accuracy is the "*closeness of agreement between a measured quantity value and a true quantity value of a measurand*". Thus in this subchapter the analysis of the EMM-ARM E-modulus estimations accuracy will be discussed. Once more, the analysis was divided in two parts related to the material: concrete and cement paste.

5.5.1. Concrete

From all the experiments performed during this thesis and the results of the first implementation of EMM-ARM (Azenha *et al.*, 2010a) the relation between the E-modulus obtained from the classical cyclic compression tests (CC) and the EMM-ARM estimation at the same age of testing was computed and the results are shown in Figure 5.34.

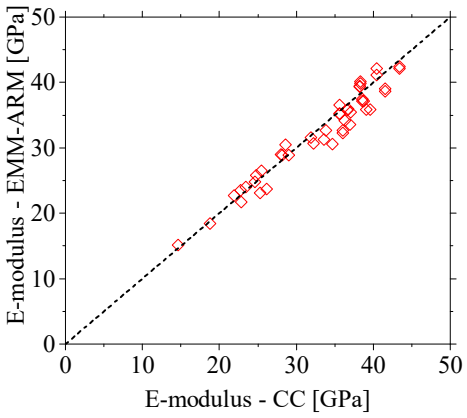

Figure 5.34. Relation between the concrete E-modulus estimated from CC and EMM-ARM.

As can be seen in the figure, the relation between the two estimations is always very close to 1, and the dispersion of the results is small. Nevertheless, to better interpret the results a normal distribution was fitted to the results as shown in Figure 5.35a. This figure shows the cumulative probability along the E-modulus estimated by the EMM-ARM divided by the E-modulus obtained from CC. A mean value of 0.981 was obtained, along with a standard deviation of 0.0496. The probability density of this normal distribution is shown in Figure 5.35b. As can be seen the accuracy of the EMM-ARM estimations is very high, with a mean error of 1.9%.

Additionally, based on this data, it is possible to observe that there is a 90% possibility that the EMM-ARM E-modulus estimations are between 0.899 and 1.062 of the CC values.

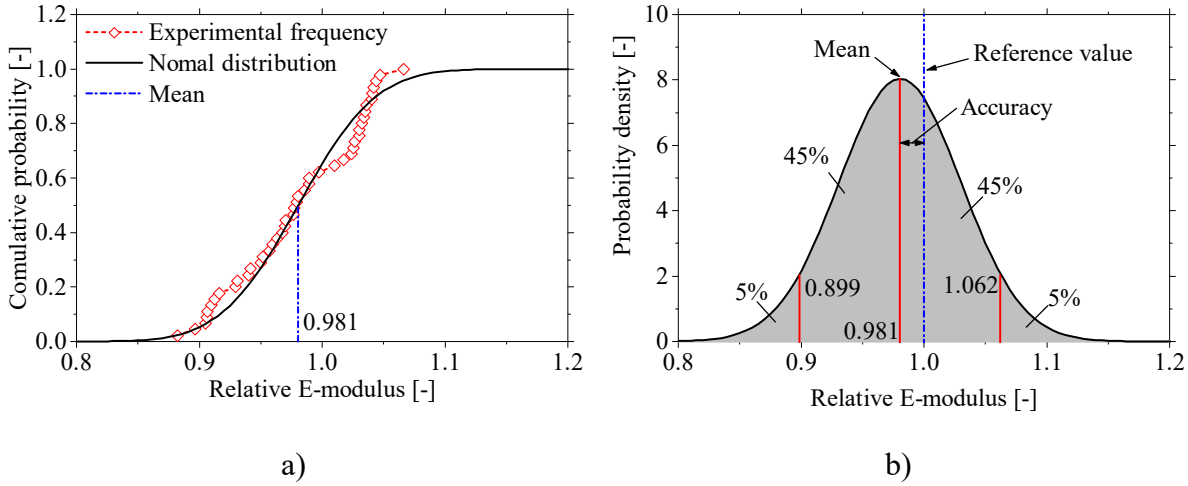

a) b)

Figure 5.35. Normal distribution of the relation between the concrete E-modulus estimations from EMM-ARM and CC: a) Cumulative probability; b) Probability density.

5.5.2. Cement paste

The relation between the E-modulus obtained from the classical cyclic compression tests (CC) and the EMM-ARM estimation at the same age of testing extracted from all the experiments performed during this thesis and the results of the first comparison of EMM-ARM with CC (Maia *et al.*, 2012b) are shown in Figure 5.34.

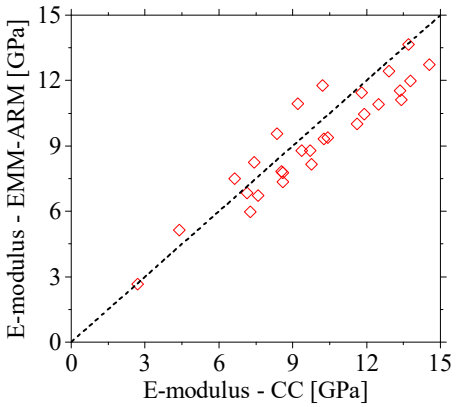

Figure 5.36. Relation between the cement paste E-modulus estimated from CC and EMM-ARM.

As can be observed the values are close to the line that represents the equality between the E-modulus estimated from EMM-ARM and CC. However, the dispersion of the results is slightly higher when compared with the results from the tests on concrete. Then again, a normal distribution of the results was fitted to the experimental data, as shown in Figure 5.37a (cumulative probability of the normal distribution). The mean value and standard deviation of the normal distribution is 0.953 and 0.1121, respectively. Therefore, one can state that the EMM-ARM in the cement paste version have a high accuracy with an average error of 4.7%. By plotting the probability density graph of the normal distribution (Figure 5.37b) one can observe that there is a 90% possibility that the EMM-ARM E-modulus estimations are between 0.769 and 1.137 of the values obtained with the classical cyclic compression tests (CC).

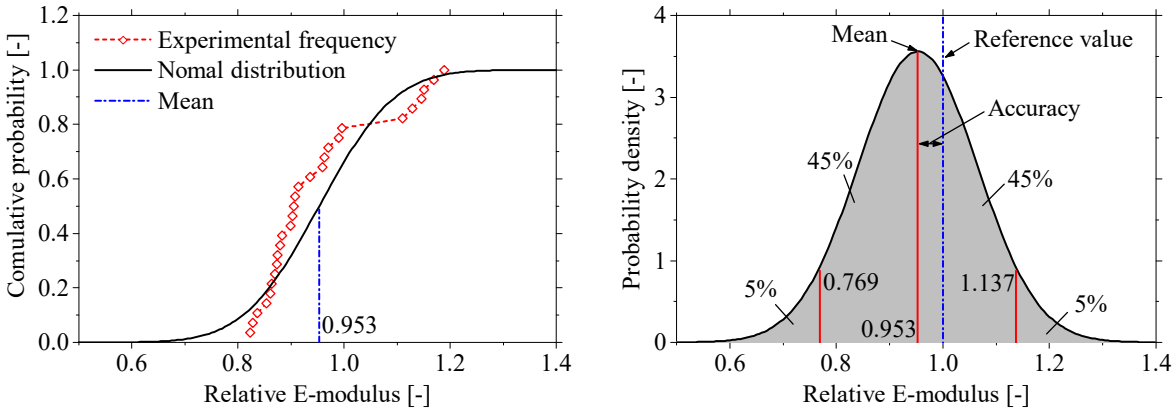

a) b)

Figure 5.37. Normal distribution of the relation between the cement paste E-modulus estimations from EMM-ARM and CC: a) Cumulative probability; b) Probability density.

5.6. Sensitivity to input parameters

In order to deepen the analysis of EMM-ARM, one should highlight the sensitivity of the E-modulus estimations to the input parameters needed to perform the estimations. To perform the sensitivity analysis, two reference scenarios were assumed for each EMM-ARM version under study (concrete and cement paste). These scenarios consisted in: (*i*) a reusable EMM-ARM beam made of PVC for the concrete version; and (*ii*) a 450 mm long acrylic tube for the cement paste version. The characteristics of both beams are summarized in Table 5.19.

Table 5.19. Characteristics of the reference beams used.

Parameter	*Concrete*	*Cement paste*
Geometry		
Cross-section	Circular	Circular
$\varnothing_i$	96 mm	16 mm
$\varnothing_e$	110 mm	20 mm
Span	1000 mm	450 mm
Mould		
Material	PVC	Acrylic
Density	1700 kg/m^3	1300 kg/m^3
E-modulus	3.10 GPa	4.50 GPa
Concrete		
Density	2370 kg/m^3	1756 kg/m^3
Final E-modulus	30 GPa	15 GPa
$\overline{EI}$		
@ E = 0 GPa	9.4 kN·m^2	20.9 N·m^2
@ E = final value	134.4 kN·m^2	69.2 N·m^2

Based on the information of Table 5.19, and based on the use of equations (2.11) (page 35) and (2.14) (page 37) for the concrete and cement paste, respectively, the initial and final resonance frequencies of the beams were computed. The concrete beam first resonance frequency starts at 32.6 Hz when the stiffness is null and reach 123.4 Hz at the end when the concrete has E = 30 GPa. In the case of cement paste the frequency range is smaller starting at 14.7 Hz and ending at 26.7 Hz when the cement paste has E = 15 GPa.

Based on these frequency values a parametric study was made to verify the influence of errors made during the measurement of the different parameters used to estimate the final E-modulus of the material inside the mould. The errors can be related to the precision of equipment used to measure the parameters (weighting machines and measure tapes) and to the user (human error). First, the parametric analysis was made with only 3 parameters used to estimate the composite beam stiffness ($\overline{EI}$): free span (L), concentrated (m_p) and distributed masses ($\overline{m}$), as shown in Figure 5.38. In this first analysis the support stiffness (k) was consider infinite. Between those three parameters, the free span is the one that shows stronger impact on the estimation error in both cases, as an error of 0.1% in the measurement leads to an $\overline{EI}$ estimation error of ~0.4%. Thus a careful estimation is needed in order to reduce the $\overline{EI}$ estimation error during the EMM-ARM tests. Contrarily the concentrated mass has a very small impact in the final $\overline{EI}$ estimation, with an error lower than 0.1% when an error of 0.3% in the parameter is made. One should also remark that this errors have a direct impact in the final E-modulus of the material.

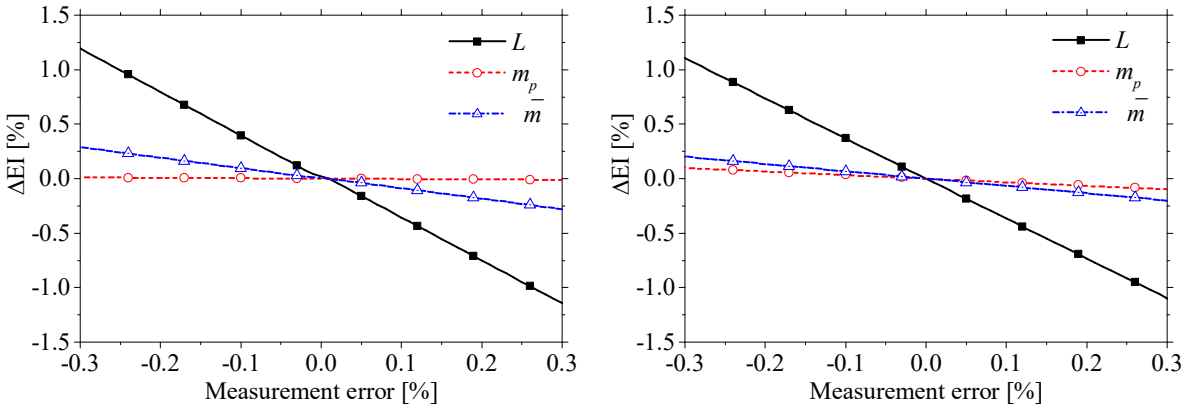

a) b)

Figure 5.38. Influence of span and masses on *EI* estimation: a) Concrete; b) Cement paste.

Another parameter that has a potential to introduce errors in $\overline{EI}$ estimations is the stiffness of the support(s) (k), as can be observed in Figure 5.39. This issue was already discussed in sections 3.2.2 and 3.3.1, however due to the big impact that it can represent, it is further evaluated herein. The parametric analysis was made for the instants when the materials (concrete and cement paste) are in the fresh state ($E = 0$ GPa) and for the hardened stage ($E = 30$ GPa for concrete and $E = 15$ GPa for the cement paste). The influence of the support stiffness increases with the increase of the material stiffness in both cases. From this analysis, in order to have an $\overline{EI}$ estimation error lower than 0.1% the supports should have a vertical and rotational stiffness of at least 5.47×10^9 N/m and 5.64×10^5 N/rad for the concrete and cement paste beams, respectively. However, despite this influence, if the new supports presented in sections 3.2.2 and 3.3.1 are used the supports stiffness is much higher that these minimum values and errors in this parameter should not influence the final E-modulus estimations.

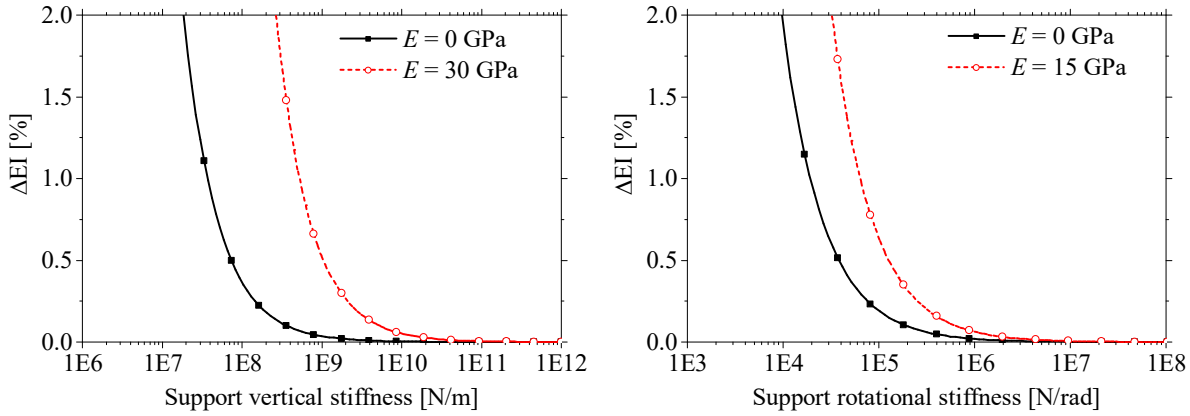

a) b)

Figure 5.39. Influence of support stiffness on $\overline{EI}$ estimation: a) Concrete; b) Cement paste.

After the estimation of the composite beam stiffness ($\overline{EI}$), it is possible to infer the E-modulus of the tested material (inside the mould) through the use of equation (2.12) (page 35). For this operation, three additional parameters are necessary: the internal ($\varnothing_i$) and external ($\varnothing_e$) diameters of the mould and the stiffness of the mould material (E_{mould}). A final parametric analysis was made for the reference scenarios and the results are shown in Figure 5.40. In equation (2.12) (page 35) the internal diameter ($\varnothing_i$) is the parameter that have the biggest impact on the E-modulus estimation since an error of 0.1% in the parameter leads to a maximum error of 0.11 and 0.04 GPa for the concrete and cement paste, respectively. Contrarily the E-modulus of the mould has a low influence in the final estimation.

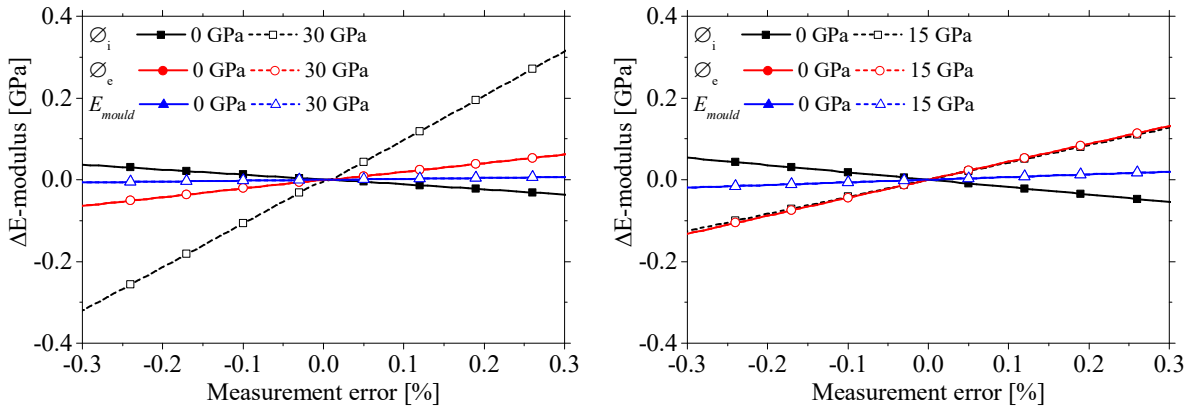

a) b)

Figure 5.40. Influence of internal and external diameters and mould stiffness on E-modulus estimation: a) Concrete; b) Cement paste.

Chapter 6

Applications and variant of EMM-ARM

6.1. Introduction

Until this stage of the thesis, the main focus of EMM-ARM experiments has been placed in metrological validations and improvements the technique to enable robust estimations of the stiffness evolution of cement-based materials since early ages. Additionally, almost all experiments were performed in laboratory and under isothermal conditions (or near-isothermal conditions), aiming at the reference temperature of 20°C. Therefore, this Chapter is dedicated to applications of EMM-ARM in different conditions: (*i*) under different curing temperatures to perform maturity analysis; (*ii*) the implementation in a construction site to support decision making; and (*iii*) under non-isothermal conditions. Furthermore, due to a construction company request a new version of EMM-ARM for monitoring the concrete viscoelasticity during the fresh state will be presented. The Chapter ends with an application of EMM-ARM to a structural non cement-based adhesive to demonstrate the versatility of the technique. This application filled a gap found in the literature, since no method was found capable of monitoring the

stiffness of epoxies adhesives that could easily be implemented in-situ during strengthening of real structures to enable a quality control of the adhesive.

6.2. Application to the study of cement hydration temperature dependence

The set of chemical reactions involved in cement hydration is exothermic and thermally activated, i.e. the reaction rate is strongly influenced by temperature. To deal with this phenomenon the concept of concrete maturity emerged in the 1950's (Saul, 1951). The concrete maturity was defined by Saul (1951) as: *"Concrete of the same mix at the same maturity has approximately the same strength whatever combination of time and temperature go to make up that maturity".* Over the last decades, the maturity concept has been used as one of the most favourable methods for estimating in-place concrete mechanical properties (Chanvillard and D'aloia, 1997). One of the most widespread formulations for concrete maturity is based on an Arrhenius law that is used to describe the effect of temperature on the rate of a chemical reaction (Poole *et al.*, 2007). This formulation allows the computation of the equivalent age (t_{eq}) of concrete, that represents the age of curing at a reference temperature (T_r adopted here as 293.15°K = 20°C) that would result in same property value as would result for curing under different temperatures (D'Aloia, 2003), as follows:

$$t_{eq} = \sum_{0}^{t} e^{-\frac{E_{act}}{R}\cdot\left[\frac{1}{T(\tau)}-\frac{1}{T_r}\right]} \cdot \Delta t \tag{6.1}$$

where E_{act} is the apparent activation energy, R is the universal gas constant (8.314 J/mol·K), t is the instant at which the equivalent age is being computed, $T(\tau)$ is the temperature at instant τ and Δt is the time interval between to measurements.

This formulation has one control variable, the apparent activation energy (E_{act}), that represents the overall temperature reactivity of the set of chemical reactions that occurs during the hydration. However, due to the complexity of the cement hydration process the apparent activation energy has to be experimentally determined through monitoring of material hydration. Usually these measurements are carried out through calorimetry tests in specimens cured at two different temperature histories (at least) (Azenha, 2009) since the methods to

measure the mechanical properties of cement-based materials do not provide continuous information during the early ages of the curing process (period where most of the changes in the materials properties happens) needed to estimate the E_{act}. However, calorimetry tests did not take into account the mechanical properties of the cement-based materials. Thus, the use of E_{act} obtained from calorimetric tests to estimate the mechanical properties could lead to wrong approximations. Therefore, this subchapter presents the use of the unprecedented data obtained by EMM-ARM to assess the apparent activation energy based on the E-modulus estimations.

6.2.1. Hydration kinetics at different temperatures

In order to assess the apparent activation energy, two EMM-ARM test programs were performed in two different materials: cement paste and concrete. In each test program, three beams were tested at three different temperatures in an isothermal temperature-controlled room with average temperatures of 16.07, 31.29 and 40.18°C for the cement paste and 20.72, 30.59 and 40.13°C for the concrete. The characteristics of the beams used in each test are shown in Table 6.1.

Table 6.1. Beams characteristics used in the maturity test

	Test program 1			*Test program 2*		
Reference	*EMMcp16*	*EMMcp31*	*EMMcp40*	*EMMc20*	*EMMc30*	*EMMc40*
Geometry						
Cross-section	Circular	Circular	Circular	Circular	Circular	Circular
$\varnothing_i$	16.14 mm	16.08 mm	16.40 mm	91.76 mm	91.43 mm	91.34 mm
$\varnothing_e$	20.11 mm	20.08 mm	20.06 mm	99.76 mm	99.79 mm	99.69 mm
Span	450 mm	450 mm	450 mm	906 mm	902 mm	902 mm
Connectors (spacing)	No	No	No	Yes (300 mm)	Yes (300 mm)	Yes (300 mm)
Supports	Steel clamps	Steel clamps	Steel clamps	$Ø_{PR}$=12 mm Steel supports	$Ø_{PR}$=12 mm Steel supports	$Ø_{PR}$=12 mm Steel supports
Mould						
Material	Acrylic	Acrylic	Acrylic	Acrylic	Acrylic	Acrylic
Density	1261 kg/m^3	1267 kg/m^3	1295 kg/m^3	1220.4 kg/m^3	1186.1 kg/m^3	1182.4 kg/m^3
E-modulus	5.16 GPa	4.63 GPa	4.31 GPa	3.92 GPa	3.83 GPa	3.71 GPa
Material						
Type	Cement paste	Cement paste	Cement paste	Concrete C4	Concrete C4	Concrete C4
Density	1745 kg/m^3	1718 kg/m^3	1724 kg/m^3	2327.7 kg/m^3	2333.6 kg/m^3	2335 kg/m^3
Average curing temperature	16.07°C	31.29°C	40.18°C	20.72°C	30.59°C	40.13°C

These tests were performed on cement paste and concrete with the compositions presented in Table 6.2.

Given the influence of temperature variations on the acrylic stiffness (Schirrer and Goett, 1982), prior to each test, the acrylic E-modulus was accessed through modal identification of the empty beams at the intended test temperature. The obtained values for temperature-dependent E-modulus of acrylic are shown in the Table 6.1. The tests presented here were performed under OMA (Operational Modal Analysis – ambient vibration) conditions. The accelerations of the beams were acquired with two different types of accelerometers: PCB 393B12 (sensitivity: 10 V/g; range: ±0.5 g) in the concrete beams and PCB 352C04 (sensitivity: 1 V/g; range: ±5 g) in the cement paste beams. In all the experiments the measurements were acquired with a dynamic acquisition system NI 9234 with 24-bit resolution at an acquisition frequency of 500 Hz in packages of 300 seconds each 10 minutes.

Table 6.2. Cement paste and concrete compositions.

Component	*Cement paste*	*Component*	*Concrete C4 (kg/m^3)*
Cement	CEM I 52.5N PMES CP2	Sand	739 (0/4)
w/c	0.54	Gravel	1072 (8/22)
		Cement	340 (CEM I 52.5N PMES CP2)
		Water	184 l/m^3

The temperature history was acquired with K-type thermocouples placed at the geometrical centre of the cross-section and at least two diameters from the extremity of the specimen. The acquired temperatures for all the specimens, along the entire duration of the tests, are shown in Figures 6.1a and 6.1b for the cement paste and concrete tests, respectively. Firstly, regarding the initial temperature of the components it is worth mention that prior to mixing all the components were placed in a temperature controlled chamber at the target temperature for 1 day. However, after the mixing process the temperature of the materials (cement paste and concrete) changed from the target due to the temperature of the mixing room and mixer. From the measured temperatures it is possible to observe that the temperature history in the specimens is almost isothermal, with a small variation during the first 18 hours after casting due to heat of hydration.

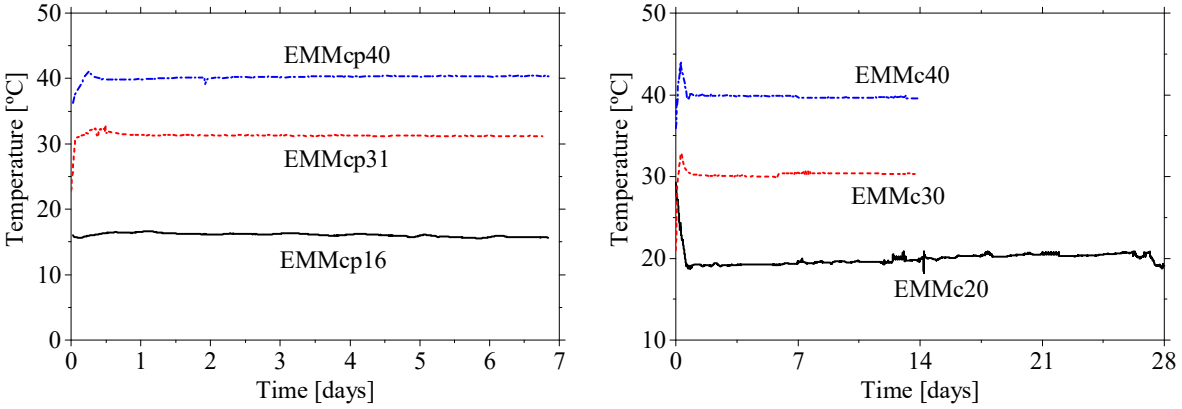

a) b)

Figure 6.1. Temperature history: a) Cement paste specimens; b) Concrete specimens.

The results collected during the EMM-ARM experiments are shown in Figures 6.2a and 6.2b for cement paste and concrete, respectively. Additionally, in the second test program, cyclic compression tests (CC) were performed in cylinders cured with same temperature history as EMM-ARM. The CC tests were performed simultaneously with the end of the experimental procedure of each EMM-ARM experiment, and followed the standard LNEC E397 (1993). The CC results are also shown in Figure 6.2b.

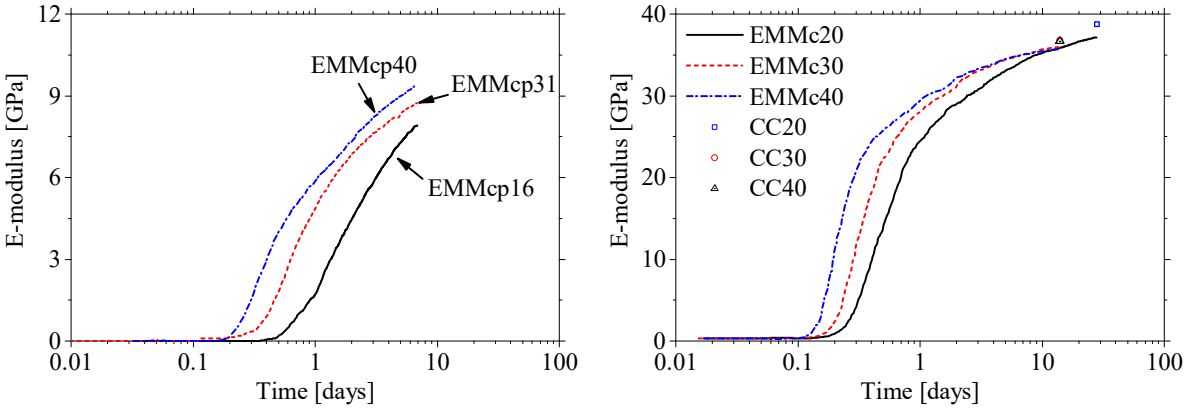

a) b)

Figure 6.2. Estimated E-modulus evolutions at different curing temperatures: a) Cement paste; b) Concrete.

Form the results of Figure 6.2 one can firstly note that all the evolution curves appear plausible with shapes similar to previous implementations of EMM-ARM. It is also possible to observe

that the effect of temperature on the E-modulus evolution kinetics is quite clear. With the increase of curing temperature, the E-modulus evolves faster. This situation is evidenced, for example, by the achievement of the cement paste elastic modulus of 3 GPa, which took 0.64 days at 40°C, as opposed to the 1.63 days required for the test conducted at 16°C. Similar conclusions can be drawn from the results for concrete. Furthermore, the final values obtained for concrete E-modulus at the end of each experiment, exhibit a good coherence with an average value of 35.87 GPa (SD = 0.061) at 14 days of curing. This value is also very close the average value obtained with CC tests – 37.35 GPa (SD = 0.962). The stiffness kinetics also show that the setting time of both the cement paste and concrete is reduced with the increase in curing temperature. These results allow the validation of the capacity of EMM-ARM to measure the E-modulus evolution of both cement paste and concrete under different isothermal curing temperatures that differ from the reference temperature of 20°C evaluated in previous Chapters, and belong to the range 16°C – 40°C.

Despite the good results reported above, it was decided to fit each of the obtained experimental curves of E-modulus by an equation similar to equation (5.2) (page 150) as shown in Figure 6.3. By using these fitted curves for the estimation of the setting time and apparent activation energy, it is possible to reduce numerical errors in estimations, which would occur due to noise (variance) in the E-modulus evolutions of each experimental curve. The parameters obtained from the fitting are presented in Table 6.3. As observable in the figure, an almost perfect fit to the experimental data was obtained with R^2 higher than 0.9997. Hereafter all the calculations will be made with basis on these analytical models. Additionally, this data fitting allows to obtain the asymptotic ultimate value for the E-modulus (E_{ult}) that will be used later to compute the evolution of the hydration degree.

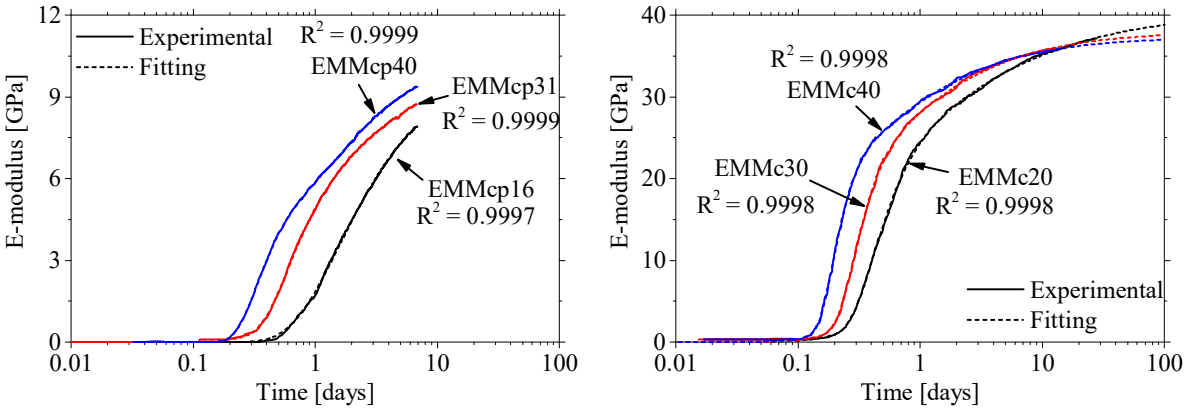

a) b)

Figure 6.3. Model fit to the E-modulus evolutions: a) Cement paste; b) Concrete.

Table 6.3. Parameters of the fitting models.

Parameter	*EMMcp16*	*EMMcp31*	*EMMcp40*	*EMMc20*	*EMMc30*	*EMMc40*
α_1	4.854	4.555	5.824	21.267	28.496	20.797
α_2	4.854	6.138	4.527	19.082	8.117	16.521
β_1	1.088	2.194	2.383	2.322	2.498	3.898
β_2	1.088	0.681	1.170	0.580	1.262	0.752
τ_1	1.591	0.574	0.337	0.412	0.290	0.191
τ_2	1.591	1.636	2.038	1.427	1.971	0.571
R^2	0.9997	0.9999	0.9999	0.9998	0.9998	0.9998

From the E-modulus evolutions the final setting time for each beam was computed according to the protocol presented in Chapter 5: the final setting time is defined as the first point for which half of the maximum value of the first derivative of the E-modulus evolution is reached, as shown in Figure 6.4.

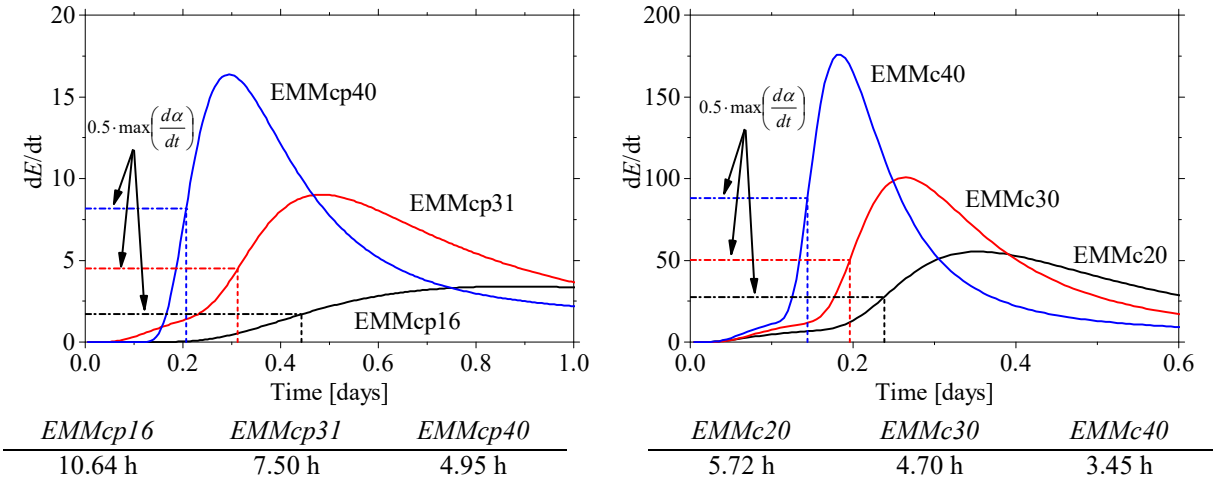

EMMcp16	*EMMcp31*	*EMMcp40*
10.64 h	7.50 h	4.95 h

a)

EMMc20	*EMMc30*	*EMMc40*
5.72 h	4.70 h	3.45 h

b)

Figure 6.4. Final setting time identification: a) Cement paste; b) Concrete.

Firstly, it is worth mentioning that the final setting time for concrete is shorter than that of cement paste for all the curing temperatures. This is probably related to the presence of rigid aggregates in concrete that fill very effectively part of the solid skeleton, increasing the connections. Additionally, it can be observed that the final setting time is strongly affected by the curing temperature with reduction of more than 50% in the cement paste with an increase of 24°C of the curing temperature.

6.2.2. Apparent activation energy

6.2.2.1. The 'speed method'

The activation energy was calculated by the so-called 'speed method' suggested by D'Aloia (2003) that is based on the analysis of hydration rates. Usually this method is not suitable to be applied to results of mechanical properties since it requires the characterization of the material property throughout the whole curing process with measurements every 5 to 15 minutes. However, with the EMM-ARM results this problem is overcome as it is possible to obtain results every 10 minutes throughout the curing process of the material. In this method, the apparent activation energy (E_{act}) is computed in each step of the hydration degree (α). according to the following equation:

$$E_{act}(\alpha) = -\frac{R}{\frac{1}{T_1(\alpha)} - \frac{1}{T_2(\alpha)}} \cdot \ln \frac{\left(\frac{d\alpha}{dt}\right)_1(\alpha)}{\left(\frac{d\alpha}{dt}\right)_2(\alpha)} \tag{6.2}$$

where T_1 and T_2 are the average temperatures of the material in each step of α in test programs 1 and 2, respectively. Here, the hydration degree is quantified as follows:

$$\alpha(t) = \frac{E(t)}{E_{ult}} \tag{6.3}$$

where $E(t)$ is the monitored E-modulus of concrete at age t and E_{ult} is the asymptotic ultimate value obtained from the data fitting presented in Figure 6.3 ($E_{ult} = \alpha_1+\alpha_2$).

The 'speed method' allows calculation of the activation energy from two different tests, and does not require any information about the hydration kinetics. The analysis of experimental results enabled to plot E_{act} as function of the hydration degree for each couple of EMM-ARM tests (see Figure 6.5). It is possible to observe that the apparent activation energy changes with temperature and this temperature dependency is more relevant for the very low and very high values of the hydration degree. The E_{act} in the concrete tests seems to stabilize during an intermediate stage between 5 and 50% hydration degrees, around an average value of 47.36 kJ/mol (SD = 1.04), for the three couples of temperatures under study. Regarding the cement paste, between 5 and 25% of hydration degree, E_{act} remains in a plateau but with different values for three temperature couples (40.24, 46.64 and 59.17 kJ/mol for the couple 16-31°C, 16-40°C and 31-40°C, respectively). Despite these plateaus, the evolution of the apparent activation energy along the hydration degree have strange evolutions with high variance. These type of results are consistence to the ones obtained with calorimetry data (Azenha, 2009, D'Aloia and Chanvillard, 2002, D'Aloia, 2003).

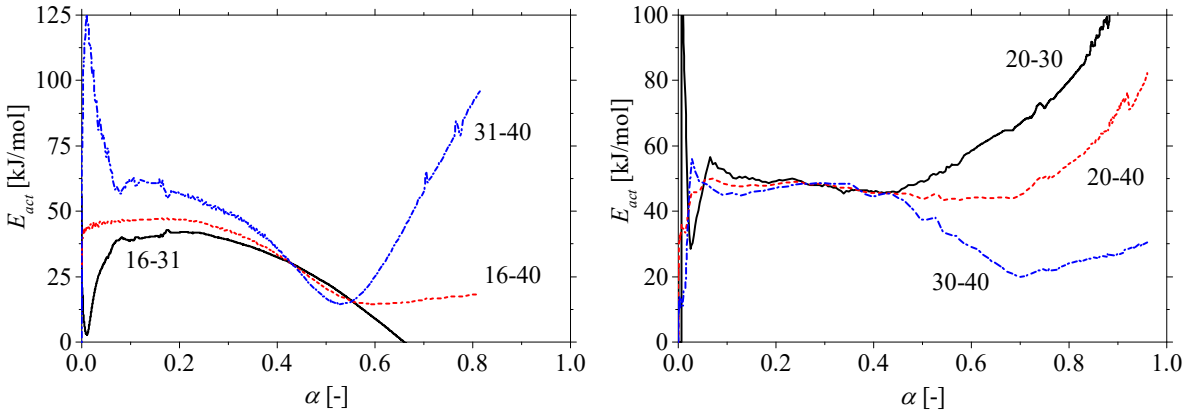

a) b)

Figure 6.5. Activation energy *versus* hydration degree obtained with 'Speed method': a) Cement paste; b) Concrete.

In Figure 6.6, the evolutions of hydration degree are plotted as function of equivalent age computed using the equation (6.1) and the values of the activation energy from Figure 6.5. It is possible to observe that an almost perfect superposition of the different evolutions is attained.

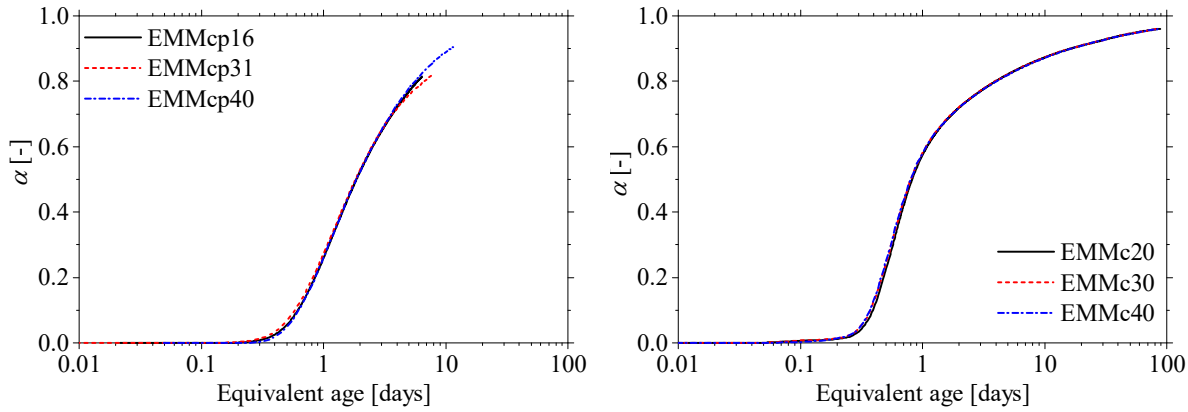

a) b)

Figure 6.6. Hydration degree *versus* equivalent age with E_{act} from 'Speed method' results: a) Cement paste; b) Concrete.

Nonetheless, despite the good superposition of the hydration degree evolutions presented in Figure 6.6 this approach to compute the apparent activation energy may lead to less-than-perfect matches if one try to superimpose the E-modulus evolutions curves. In fact, and as can be seen in Figure 6.7, due to the different E-modulus ultimate value obtained for each specimen, the E-

modulus curves are not perfectly superimposed, especially at stages when the rate of evolution starts to decrease.

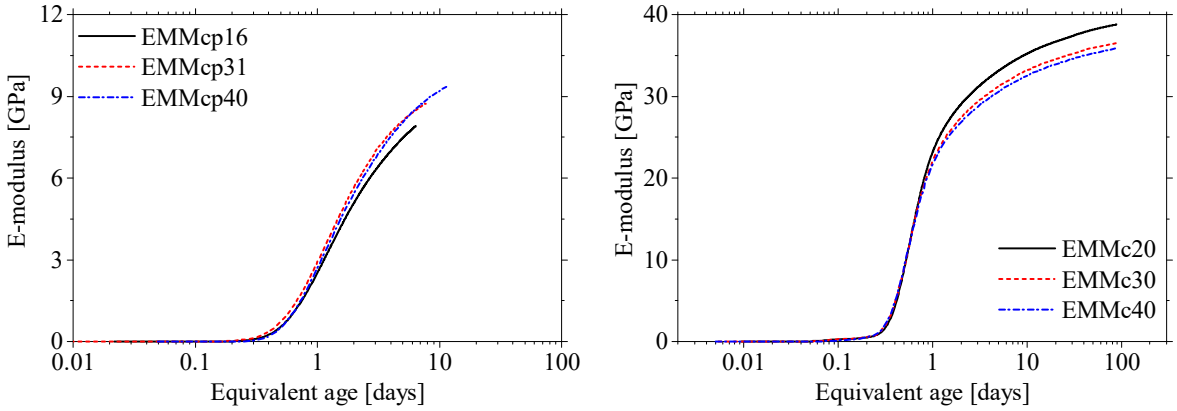

Figure 6.7. E-modulus *versus* equivalent age with E_{act} from 'Speed method' results: a) Cement paste; b) Concrete.

During the dormant period and until the final setting time, the method seems to work well. In fact, as can be seen in Figure 6.8, the equivalent age of the final setting time is very close in all the specimens, with an average of 10.05 hours (SD = 0.050) and 7.56 hours (SD = 0.061) for the cement paste and concrete, respectively. During this period the average activation energy as the following values: 10.57, 14.77 and 42.39 kJ/mol for the specimens EMMcp16, EMMcp31 and EMMcp40, respectively, and 46.96, 46.77 and 32.15 kJ/mol for the specimens EMMc20, EMMc30 and EMMc40, respectively.

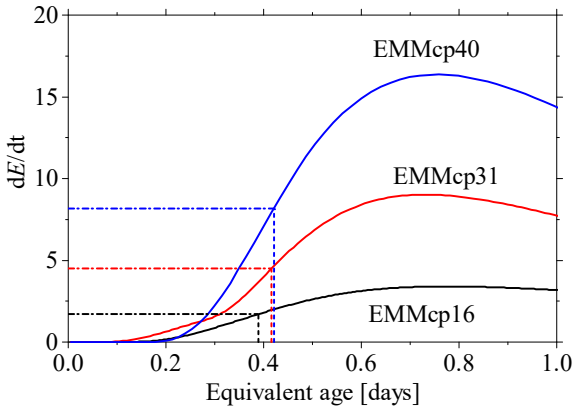

EMMcp16	*EMMcp31*	*EMMcp40*
9.34	10.00	10.10

a)

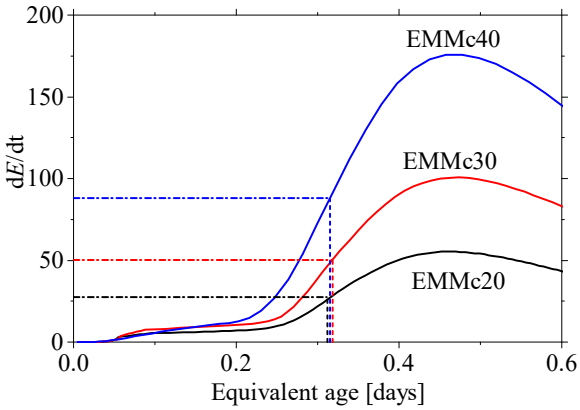

EMMc20	*EMMc30*	*EMMc40*
7.49	7.64	7.56

b)

Figure 6.8. Equivalent age of the final setting time: a) Cement paste; b) Concrete.

6.2.2.2. The 'derivate of speed method'

As any chemical reaction, the hydration reaction can be described by a rate equation given by the following expression (Vyazovkin, 2011):

$$\frac{d\alpha}{dt} = k(T) \cdot f(\alpha) \tag{6.4}$$

where α is the hydration degree, $d\alpha/dt$ is the hydration rate, T is the absolute temperature (°K), $k(T)$ is the rate constant, and $f(\alpha)$ is the function that describes the hydration reaction mechanism (for more details see (Azenha, 2009)).

Based on the EMM-ARM results, the function $f(\alpha)$ for each specimen was computed through the first derivative of the hydration degree evolution normalized to the maximum value. The obtained function as shown in Figure 6.9.

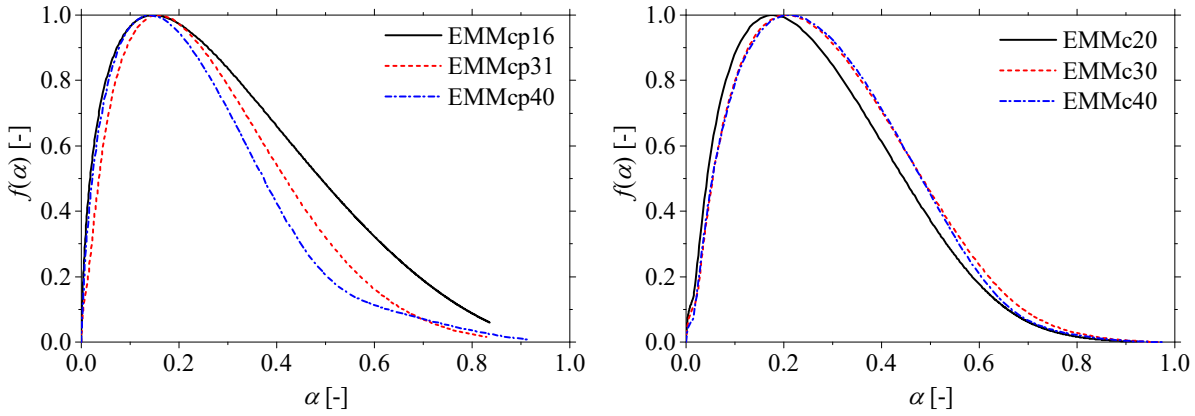

a) b)

Figure 6.9. Kinetic hydration function $f(\alpha)$: a) Cement paste; b) Concrete.

Firstly, it is seen that the hydration kinetic is different for cement paste and concrete, despite the fact that they share the same cement and w/c ratio. In the case of the cement paste the peak of the function $f(\alpha)$ happens at $\alpha = 14.9\%$ ($SD = 0.007$) of the hydration degree as opposed to the 20.4% ($SD = 0.018$) that the concrete need to reach the peak. Additionally, some temperature dependency of the hydration kinetic can be observed, especially in the cement paste during the post-peak period, as already observed by other authors (Azenha, 2009, De Schutter and Taerwe, 1995). Due to this temperature dependency of $f(\alpha)$, the basic assumptions of the 'derivate of speed method' to compute the E_{act} are jeopardized (Azenha, 2009). Nonetheless, the computation was performed anyway, but using the real $f(\alpha)$ functions for each temperature couple, instead of a single representative function.

The reaction parameter $k(T)$ was obtained from the maximum value of the hydration rate function shown in Figure 6.10 (ASTM, 2011). The obtained values are presented in Table 6.4

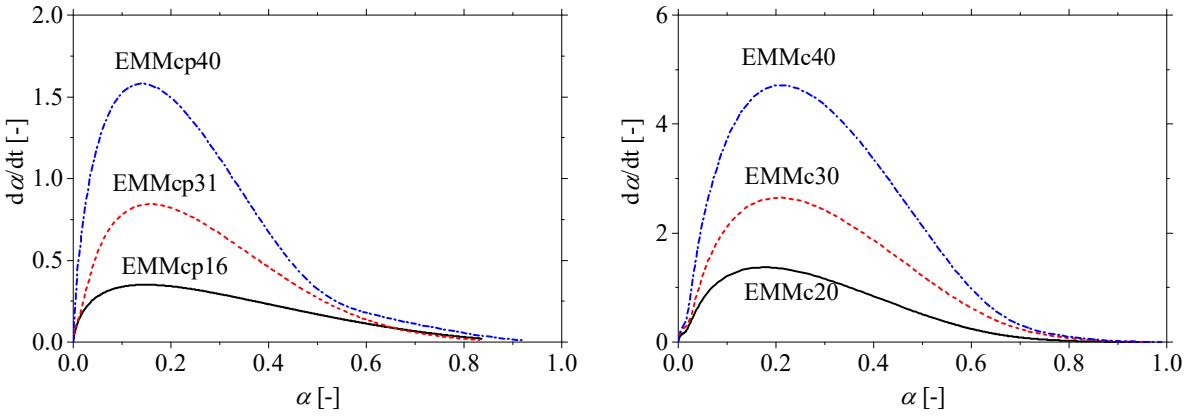

a) b)

Figure 6.10. Reaction rate as function of the hydration degree: a) Cement paste; b) Concrete.

Table 6.4. Kinetic parameters obtained from the reaction rate data.

Reference	*k(T)*
EMMc20	1.371
EMMc30	2.648
EMMc40	4.710
EMMcp16	0.351
EMMcp31	0.844
EMMcp40	1.581

The kinetic rate constant k follows an Arrhenius temperature dependence (Poole *et al.*, 2007):

$$k(T) = A_t \cdot e^{\left(-\frac{E_{act}}{R \cdot T}\right)} \tag{6.5}$$

where A_t is a proportionality constant. The kinetic rate equation can therefore be rewritten as:

$$\frac{d\alpha}{dt} = f(\alpha) \cdot A_t \cdot e^{\left(-\frac{E_{act}}{R \cdot T}\right)} \tag{6.6}$$

By plotting the logarithms of the rate constant ln(k) versus 1/T, it was possible to obtain both the apparent activation energy, E_{act}, and the natural logarithm of the pre-exponential factor, ln(A), from the slope and the y intercept of a linear fit of the results shown in Figure 6.11. The activation energy was determined to be 47.299 and 46.457 kJ/mol for the cement paste and concrete, respectively, as summarized in Table 6.5. These values are close to the average values

obtained in the ‘speed method’ for the hydration degree between 5 and 25% (48.68 kJ/mol) and 5 and 50% (47.36 kJ/mol) in the cement paste and concrete, respectively.

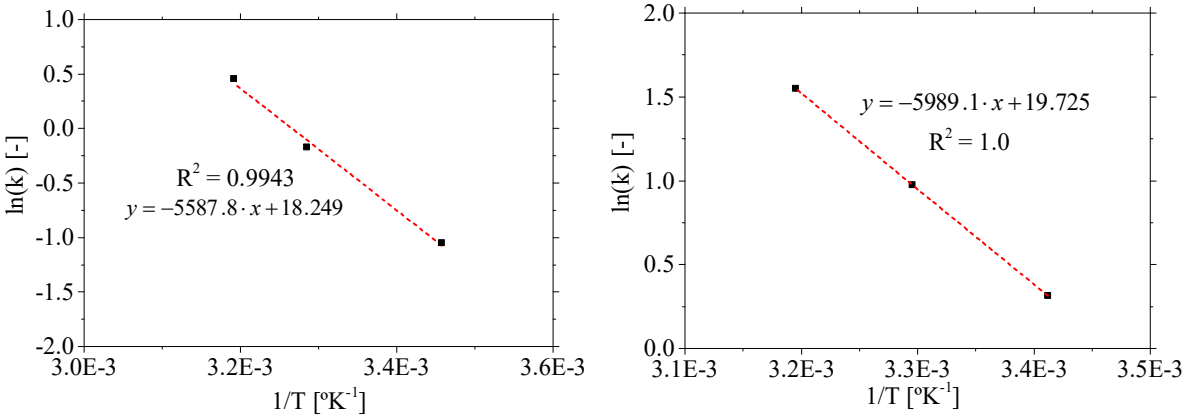

a) b)

Figure 6.11. Arrhenius plot of rate coefficient: a) Cement paste; b) Concrete.

Table 6.5. Estimated apparent activation energy E_{act} and rate constant A_t.

Reference	E_{act} *[kJ/mol]*	A_t *[min^{-1}]*
Cement paste	47.299	1.327×10^{12}
Concrete	46.457	6.570×10^{4}

In Figure 6.12, the hydration degree values are plotted as function of equivalent age. From this figure, a poor quality of the superposition can be visually identified, especially for the cement paste. This fact is due to the premises of the ‘derivate of speed method’ which allow the calculation of the average E_{act} between the beginning of the tests and the peak of the rate of reaction. Thus, as can be seen at the equivalent age of 18 and 11 hours for the cement paste and concrete (which are the instants at which the peak of the rate of E-modulus development occurs), respectively, the hydration degree values are superimposed. However, outside these points the superposition of the curves is poor.

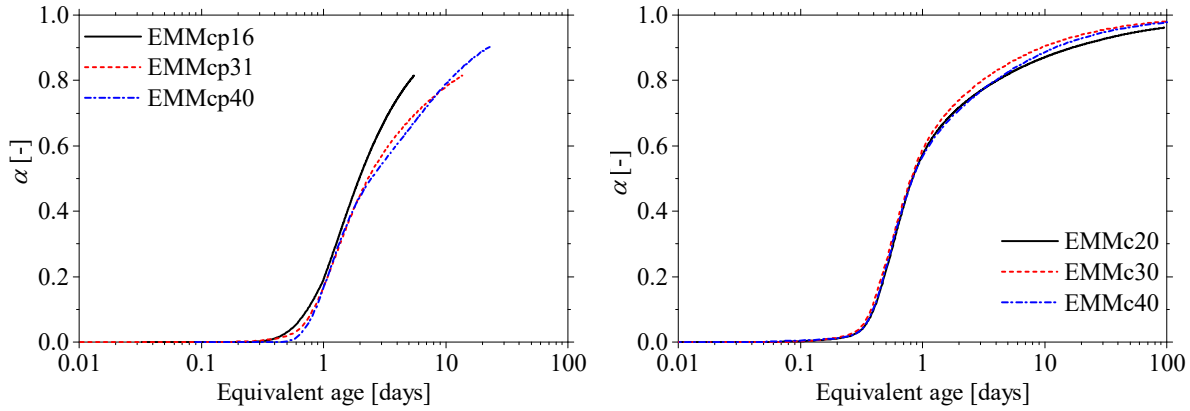

a) b)

Figure 6.12. Hydration degree *versus* equivalent age with E_{act} from derivate of speed method results: a) Cement paste; b) Concrete.

Again, by plotting the E-modulus evolutions along the equivalent age the superposition of the cure becomes a little worse, as shown in Figure 6.13. This effected is related to the same fact that occurred in the previous method: the calculations are based on the hydration degree and not directly on the E-modulus evolutions, which did not actually completely match at the end of the experiments.

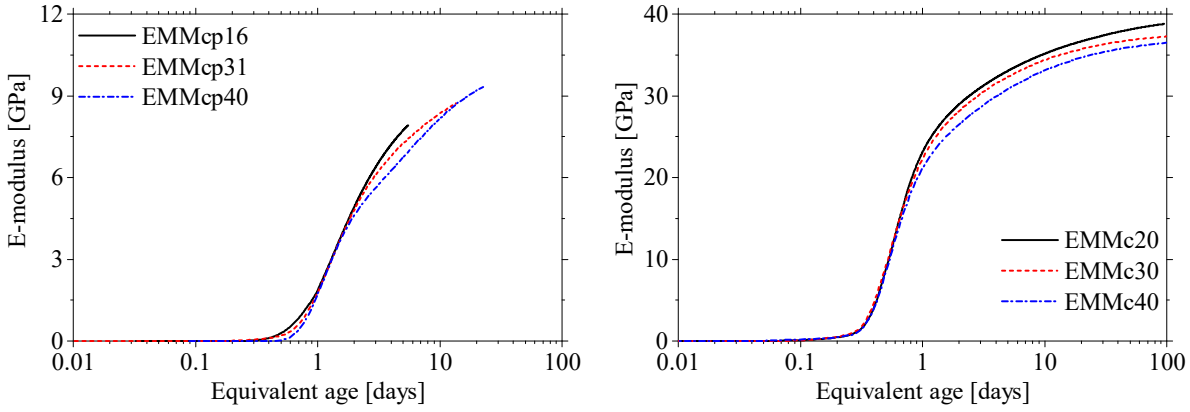

a) b)

Figure 6.13. E-modulus *versus* equivalent age with E_{act} from derivate of speed method results: a) Cement paste; b) Concrete.

6.2.3. Final remark

In this subchapter the use of EMM-ARM to compute the apparent activation energy was presented. Firstly, it was proved it is possible conduct EMM-ARM experiments at isothermal curing temperatures that differ from the reference temperature of 20ºC tested in the previous Chapters. Furthermore, the obtained results have shown the effect of the curing temperature on the E-modulus evolution kinetics. Since the EMM-ARM is able to measure the quasi-static E-modulus of the cementitious materials continuously, it gives unprecedented information to compute the apparent activation energy of a mechanical property of cement-based materials.

6.3. In-situ application to support decision making

The main objective of this this subchapter is the demonstration of EMM-ARM in an in-situ application, with the purpose of continuously monitoring of the mechanical properties of concrete to serve as support to decision making in prestressing application during the construction of a bridge. The bridge where the study took place is located in the Dão river (Portugal), and consists of three spans (100 + 170 + 120 m) supported by two intermediate columns as shown in Figure 6.14.

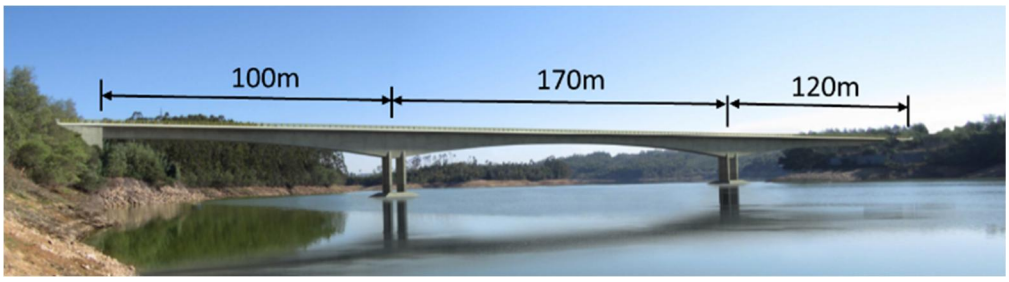

Figure 6.14. Dão river bridge (Portugal).

The deck consists of a prestressed concrete box girder, built by the balanced cantilever method. Each casting stage (4 to 5 meters long) is prestressed as soon as concrete reaches a prescribed minimum strength. Therefore, the use of a methodology that allows continuous estimates of the mechanical properties of concrete can be of significant usefulness to support decision-making processes for the prestressing operations. The next subsections present the efforts towards the in-situ implementation process, with particular emphasis on the implementation of a

temperature matched curing system, as to better follow the maturity of concrete in the regions of interest for prestressing application (near the pre-stressing heads).

6.3.1. EMM-ARM in-situ validation

Before beginning the tests to support decision-making during the construction of the bridge, a comprehensive experimental program was made to validate the EMM-ARM in construction site environment. In fact, the location of the in-situ laboratory induced significant vibrations to the EMM-ARM specimens that might potentially cause signal contamination problems in the modal identification processes. This initial experimental program was composed of three different validation tests (V1, V2 and V3) in which 9 EMM-ARM specimens were tested (see Table 6.6): 4 cylindrical acrylic beams (ACR-0.9) with geometry similar to the one shown in Figure 3.15 (page 70); 3 cylindrical PVC beams (PVC-1.0) with 1.0 m of span; and 1 reusable beam (PVCR-1.0) (see Figure 3.17 – page 72). During this study, two different concrete mixes were used (C5 and C6) and the corresponding compositions are shown in Table 6.7.

Table 6.6. In-situ validation tests of EMM-ARM

Test	*V1*	*V2*	*V3*
Beams used	ACR-0.9-V1-1	PVC-1.0-V2	ACR-0.9-V3
	ACR-0.9- V1-2	ACR-0.9-V2	PVC-1.0-V3
	PVC-1.0-V1	PVC-1.0-V2	PVCR-1.0-V3
Concrete	C5	C5	C6

Table 6.7. Concrete composition.

Component	*Mix C5 (kg/m^3)*	*Mix C6 (kg/m^3)*
Sand	300 (0/2) 540 (0/6)	330 (0/2) 560 (0/6)
Gravel	550 (6/14) 420 (11/22)	550 (6/14) 440 (11/22)
Cement	320 (CEM II / A-L 42.5R)	220 (CEM II / A-L 42.5R)
Fly ash	100	130
Water	165 l/m^3	160 l/m^3
Super plasticiser	3.36 (BasfGlenium Sky 548)	2.45 (BasfGlenium Sky 548)
Plasticiser	0.84 (BasfPozzolith 540)	2.10 (BasfPozzolith 540)

The physical and mechanical characteristics of all the beams used in the three validation tests are summarized in Table 6.8.

Table 6.8. Physical and mechanical characteristics of the EMM-ARM specimens used in the in-situ validation tests.

Reference	*ACR-0.9-V1-1*	*ACR-0.9- V1-2*	*PVC-1.0-V1*	*PVC-1.0-V2*	*ACR-0.9-V2*	*PVC-1.0-V2*	*ACR-0.9-V3*	*PVC-1.0-V3*	*PVCR-1.0-V3*
Geometry									
$\varnothing_i$ (mm)	91.96	91.96	96.17	96.42	91.78	96.47	91.81	96.04	97.86
$\varnothing_e$ (mm)	100.25	99.98	109.93	110.10	99.94	110.00	99.85	110.11	110.89
Span (mm)	900.0	900.0	1000.0	998.0	900.5	998.0	900.0	900.0	1000.0
Connectors	Yes	Yes	No	No	Yes	No	Yes	No	No
(spacing (mm))	(300)	(300)			(300)		(300)		
Supports (mm)	$Ø_{PR}$=12 MS	$Ø_{PR}$=12 MS	$Ø_{PR}$=12 MS	$Ø_{PR}$=12 MS	$Ø_{PR}$=12 MS	$Ø_{PR}$=12 MS	$Ø_{PR}$=12 MS	$Ø_{PR}$=12 MS	$Ø_{PR}$=12 MS
Mould									
Material	Acrylic	Acrylic	PVC	PVC	Acrylic	PVC	Acrylic	PVC	PVC
Density (kg/m^3)	1160	1256	1441	1434	1198	1461	1219	1493	1501
E-modulus (GPa)	3.90	3.90	3.40	3.50	3.80	3.50	4.10	3.10	3.40
Concrete density (kg/m^3)	2350	2350	2350	2328	2350	2335	2350	2374	2350
Type of identification	OMA	OMA	OMA	OMA	OMA	EMA	OMA	OMA	OMA

The tests took place inside a container placed near the discharge zone of the mixer trucks, as shown in Figure 6.15. As the container did not have a rigid floor, a small concrete slab was placed over such floor, as to reduce the effect of flexibility of the base on the resonance frequencies of the testing beams. All the tests were performed under OMA (Operational Modal Analysis – ambient vibration) conditions, except for the beam PVC-1.0-V2 that was tested under EMA (Experimental Modal Analysis – forced vibration) condition with the protocol presented in section 4.4.1. The accelerations of the beams were acquired with PCB 393B12 accelerometers (sensitivity: 10 V/g; range: ±0.5 g), connected to a dynamic acquisition system NI 4431 with 24-bit resolution at an acquisition frequency of 500 Hz in packages of 300 seconds each 10 minutes.

Figure 6.15. In-situ testing lab for EMM-ARM.

It is remarked that, in addition to the EMM-ARM tests, cyclic compression tests (CC) were performed at 1, 2, 7 and 28 days and 1, 2 and 7 days (three tests at each age) in the validation tests 1 and 3, respectively. For the CC tests cylindrical specimens (∅ = 150 mm and 300 mm height) were also cast on site and tested in the structures laboratory of the University of Minho, according to the standard LNEC E397 (1993).

The results obtained in the verification tests are shown in Figure 6.16. By analysing the results of the EMM-ARM beams is possible to confirm that the kinetics of evolution of the elastic modulus of concrete has shape and magnitude consistent with typical results obtained in previous applications. It is also possible to observe a great coherence between the results obtained by the different EMM-ARM beams, with maximum standard deviation of 1.10 GPa. There is a very good congruence between the results obtained by EMM-ARM and the classic cyclic compression method. This consistency in the results suggests that the EMM-ARM can be applied in construction site conditions at its current stage of development. Despite these good results, a remark is made regarding the early age curing temperatures. In fact, due to the lack of temperature control in the tested specimens, they endured lower temperatures than those that were experienced in the actual structure. Therefore, some extent of discrepancy would be expectable within the first 1.5 days of curing, while hydration heat still had a relevant role. This limitation can however be easily overcome by imposing the temperatures recorded in the actual structure to the tested samples in a process that is usually called temperature matched curing (Williams, 1986), and will be object of description/implementation still within this Chapter.

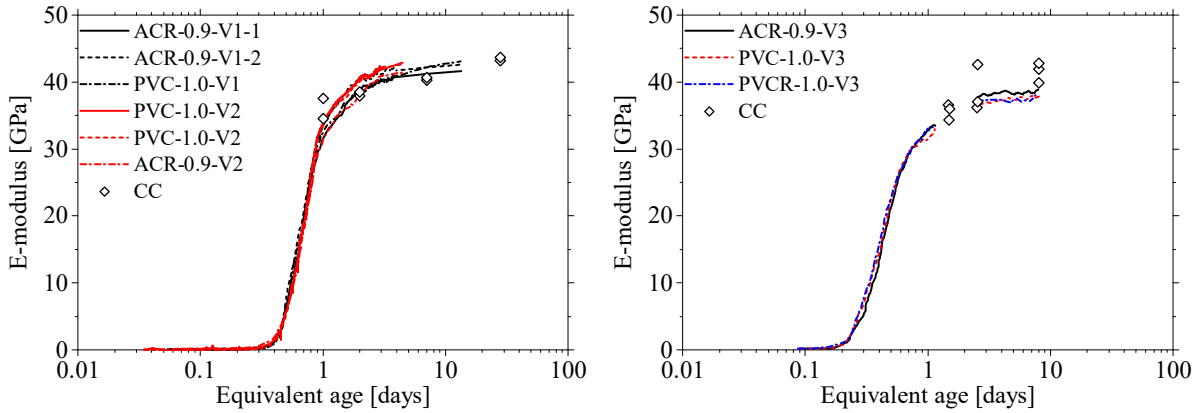

a) b)

Figure 6.16. E-modulus evolution obtained with EMM-ARM and CC: a) V1 and V2 tests; b) V3 test.

6.3.1. Temperature matched curing system

The in-situ EMM-ARM tests reported so far did not include any temperature control. However, the curing temperature plays a key role in the development of the hydration reactions and consequently on the mechanical properties. Therefore, in addition to the readily available in-situ implementation of EMM-ARM, it was necessary to develop a temperature control system to impose the temperatures observed inside the concrete in the real structure to the EMM-ARM testing specimen. This system, shown schematically in Figure 6.17a, consists of a small chamber of 1.2×1.2×0.8 m^3 made of polystyrene with a fan heater inside. The chamber's temperature control is performed by switching on or off the electrical resistance of the heating vent using in order to match the temperature inside the chamber (interior sensor) to those observed in the structure. The temperature of the concrete in the actual structure is measured by the embedment of a temperature sensor in concrete in the zone of interest newly casted (neighbourhood the prestressing head). The control unit is composed of a relay module (that switch the electrical resistance of the heating vent between the 'on' and 'off' conditions) controlled by a programmable microcontroller board (Arduino (CC, 2016)) connected to a computer with a temperature control software. The temperatures were acquired through K-type thermocouples connected to a 20-bit PicoLog data acquisition system.

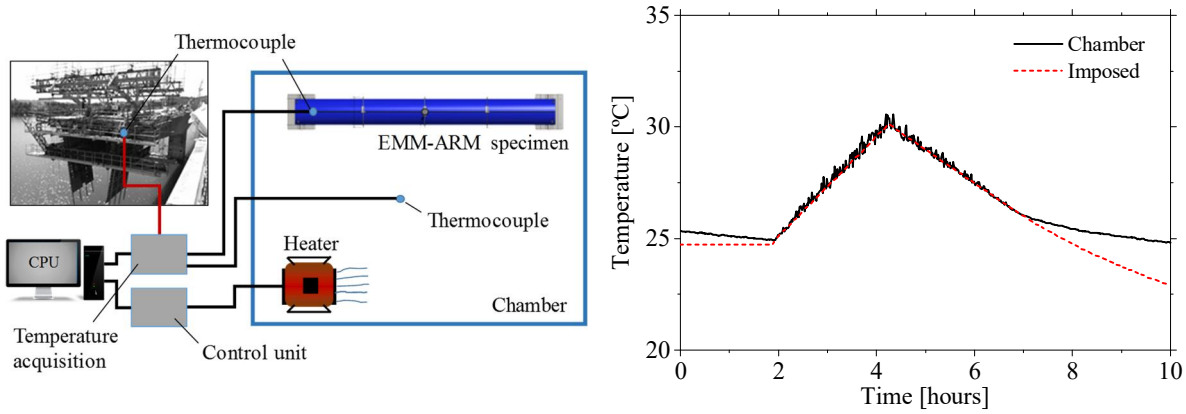

a) b)

Figure 6.17. a) Temperature match curing system scheme; b) validation test temperature evolution.

The efficiency of the system was checked by performing a small pilot test where a pre-defined temperature history was imposed to the chamber. The results of this small test are shown in Figure 6.17b, where it is possible to confirm that the temperature control was quite efficient during the temperature rise (desirable situation in temperature match curing systems of concrete).

6.3.2. E-modulus *vs* compressive strength

After the in-situ validation of EMM-ARM, it was necessary to devise a process that makes EMM-ARM results useful for the contractor to support prestress application decisions. For such purpose, an assessment was made in regard to the relationship between the concrete elastic modulus and compressive strength in the particular case of the concrete of this construction. Therefore, in addition to the EMM-ARM beams and the cyclic compression tests presented above, compressive strength tests were conducted on concrete cubes, cured in the same conditions, in accordance with the standard EN 12390-3 (2009), at 6 different ages: 0.58, 0.83, 1.33, 1.54, 1.71, and 28 days. The results of the compressive strength obtained in these tests, compared to the corresponding average elastic modulus obtained through the EMM-ARM specimens at the same age are shown in the Figure 6.18. A similar function to the one proposed by EN 1992-1 (2010) was used to fit to the experimental data. The fitting was made through

the minimization of the fitting error and the obtained coefficients (A_f, B_f and C_f) are shown in the table embedded in Figure 6.18.

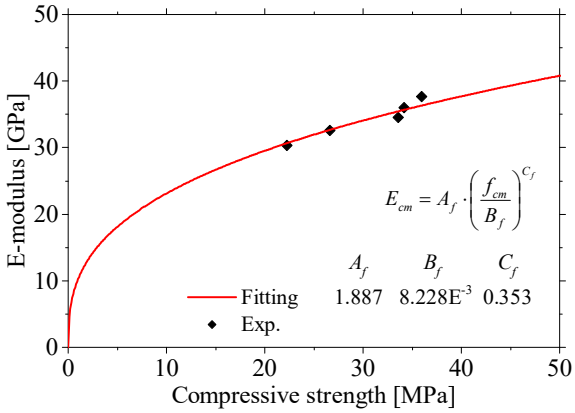

Figure 6.18. Ratio between E-modulus and compressive strength of concrete C6.

6.3.3. Support to decision making for prestressing operations

This subchapter reports the test that was performed to evaluate the ability of EMM-ARM to provide real-time information on the mechanical properties (E-modulus and compressive strength) of concrete placed in the structure, with the incorporation of the temperature match features mentioned before. To enable the user to see the results in real-time a special designed program in LabView was developed. In this program, the user can define the test (all the special characteristics of the test, like: number of specimens, type of test of each specimen, specimen's geometry, characteristics of the sensors used, etc.), see the real-time acquired data and the identified frequencies, E-modulus and compressive strength. For more details about the program see Appendix A. The test was performed during a casting operation of the bridge deck with the concrete C6 (see Table 6.7), and two reusable beams (PVCR-1.0-1 and PVCR-1.0-2) were deployed, with the characteristics shown in Table 6.9. It should be noted that beam PVCR-1.0-1 was tested under EMA conditions, with the same explicit excitation as the one presented in section 4.4.2.2. Beam PVCR-1.0-2 was tested under OMA conditions. The temperature inside the EMM-ARM specimens was measured with a K-type thermocouple placed in the geometrical centre of the cross-section and at least two diameters from the extremity of each specimen. In addition to EMM-ARM tests, concrete cubes were tested to obtain the compressive strength according to EN 12390-3 (2009) at 0.71, 1, 1.46, 1.5, 1.63 and 28 days, placed under the same curing conditions of EMM-ARM specimens.

Table 6.9. Physical and mechanical characteristics of the EMM-ARM beams used to support decision making during prestress applications.

Reference	*PVCR-1.0-1*	*PVCR-1.0-2*
Geometry		
$\varnothing_i$ (mm)	96.04	96.35
$\varnothing_e$ (mm)	110.11	110.20
Span (mm)	1000.0	1004.0
Connectors	No	No
Supports (mm)	$Ø_{PR}$=12	$Ø_{PR}$=12
	MS	MS
Mould		
Material	PVC	PVC
Density (kg/m^3)	1493	1536
E-modulus @20°C (GPa)	3.40	3.40
Concrete density (kg/m^3)	2398	2398
Type of test	EMA	OMA

Figure 6.19a shows the recorded temperature history for both the in-situ concrete and the EMM-ARM specimens. Firstly, it is possible to observe that the temperature matched curing chamber followed very precisely the temperature acquired form the real structure until 40 hours. At such age, the temperature sensor was disconnected from the data logger due to operational constraints during the bridge construction. From this point the temperature presented in the graph was measured in the air near the bridge deck and the temperature control of the test was switched off. It can be seen that the temperature histories are very similar, despite of the very small delay observed in the inner temperatures of the EMM-ARM specimen (caused by the thermal inertia of the specimen itself in regard to the surrounding environment that matched the in-situ concrete).

Because of the varying temperature on the EMM-ARM specimen, the E-modulus of the PVC mould also endured changes during the experiment (Nishi *et al.*, 1975). Therefore, the knowledge of the temperature dependent E-modulus of the mould becomes a relevant information that needs to be input to the concrete E-modulus estimation model. Therefore, before the actual experimental program reported in this section, a calibration test was performed in the beam PVCR-1.0-V3 (which was hardened and available from a previous test series). It should be noted that the beams PVCR-1.0-V3 and PVCR-1.0-1 shared the same mould and the PVCR-1.0-2 was made from the same piece of PVC tube, thus surely sharing the same mechanical properties. In this test the beam PVCR-1.0-V3 was placed in a temperature controlled room and the temperature was raised from the ambient temperature (29°C) to 50°C in 5 steps (30, 35, 40, 45 and 50°C). The temperature was kept constant in each step for at least

1 hour to ensure that the mould reached the air temperature. To get the variation of the E-modulus of the mould it was assumed that during the test the E-modulus of the concrete inside the beam remained constant at 38.7 GPa (obtained through EMM-ARM test at 29°C right before the beginning of the test). Figure 6.19b shows the PVC E-modulus variation as function of the temperature of the mould. To simplify the correction of the EMM-ARM E-modulus estimations the experimental data was fitted with a linear equation, as presented in the same figure.

Additionally, the varying temperature induce stresses in the specimen, due to the different thermal-expansion coefficients. In fact, the concrete has a thermal-expansion coefficient of $\sim 1\times10^{-5}$ K^{-1} (Sellevold and Bjøntegaard, 2006) and the PVC of $\sim 5\times10^{-5}$ K^{-1} (Nishi *et al.*, 1975). These have the potential to cause debonding between the mould and the material inside and in an extreme scenario cracking of the concrete. However, in all the experiments performed with EMM-ARM these issue was never observed. Nevertheless, in the end of the test performed to get the variation of the E-modulus of the mould the temperature was decreased again to 29°C and an EMM-ARM test was performed. The estimated E-modulus was very similar to the value obtained before the beginning of the test proving that no debonding or cracking problem happened during the temperature variation.

The E-modulus and compressive strength evolutions identified during the test are shown in Figures 6.19c and 6.19d, respectively. Due to a power failure during the night, the measurements were lost between 1.73 and 14.7 hours after the beginning of the test. However, despite this power failure the results of the E-modulus evolution are consistent with the results of cyclic compression tests obtained for the same concrete in the V3 test.

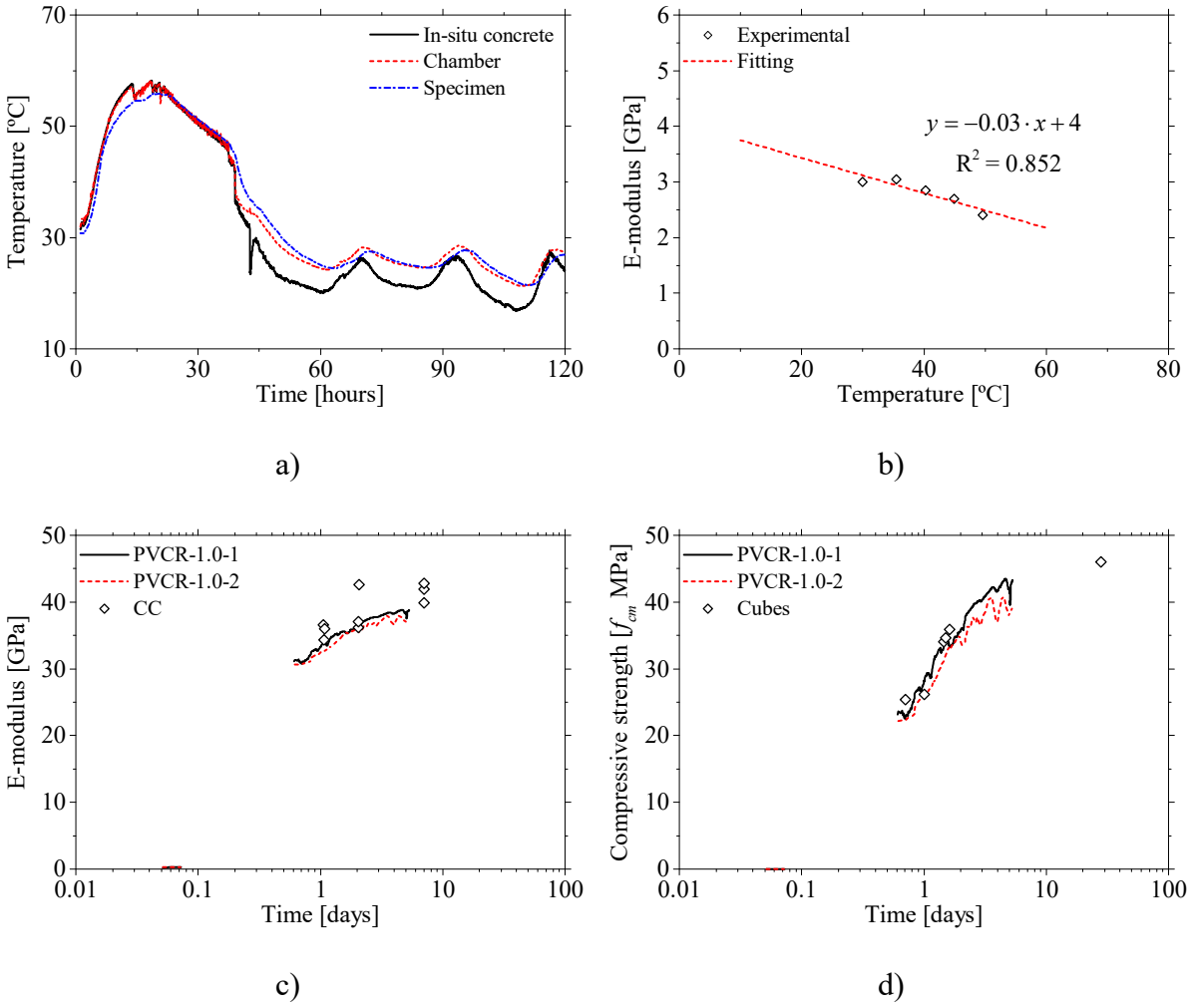

Figure 6.19. Results used in support decision making: a) Temperature history; b) Temperature dependency of the mould E-modulus c) E-modulus evolution; d) Estimated compressive strength evolution.

After application of the ratio between the E-modulus and compressive strength presented in section 6.3.2, it was possible to estimate the compressive strength evolution based on the EMM-ARM results, as shown in Figure 6.19d. The figure presents the results of the compressive strength obtained from the uniaxial loading of concrete cubes. As can see the results are in very good coherence, thus proving that the EMM-ARM can serve as a tool to support decision-making in constructions sites. However, the lack of a specific standard to the application of EMM-ARM technique is currently hindering its wide spread application.

6.4. New variant EMM-ARM, targeted to fresh state characterization

It is known that the viscoelastic properties of cement-based materials endure significant changes during the so-called dormant period (fresh state) (Banfill, 2006, Hanehara and Yamada, 2008). The knowledge of these properties can provide fundamental information about the physical status of a solid particle suspension system transforming to a viscous semi-solid and subsequently to a solid system (Kovler and Roussel, 2011). Still the viscoelastic properties evolution during the fresh is of upmost importance for the practical and scientific communities since provide information about the workability and viscosity of the material crucial for predictions of casting processes, estimate the pressure over the formworks and verify the ability of the concrete to correctly fill the formworks (Roussel, 2007, Kovler and Roussel, 2011). Additionally, the quality of the concrete structure is also dependent on the rheological behaviour of the fresh concrete during placement into formwork during construction (Wallevik, 2009). Thus, several researchers are studying evolution of the material properties during this phase (Sun *et al.*, 2006, Subramaniam and Wang, 2010, Banfill, 2006, Hanehara and Yamada, 2008). Usually the fresh properties of the cement-based materials are only assessed qualitatively by performing flowability or slump tests (Banfill, 2006, Hanehara and Yamada, 2008).

In view of the above mentioned matters, several authors have been using rheological methods to characterize the evolution of the viscoelastic properties during the fresh stat of the cement-based materials (Banfill, 2006, Hanehara and Yamada, 2008, Wallevik, 2009). However, these methods have several disadvantages since they are destructive and as the material hardens the ability to perform tests decrease rapidly. Additionally, dynamic methods are also being used to characterize the fresh properties (Sun *et al.*, 2006, Subramaniam and Wang, 2010) but they still have the disadvantages presented in section 2.3.

Based on lack of methods and deep knowledge on the fresh properties of cement-based materials, the use of vibration based methods to study the evolution of the viscoelastic properties of cement-based materials during the fresh state will be investigated in this Chapter.

6.4.1. Basis

The initial motivation for the establishment of the new method was raised by a request from a construction company in order to experimentally support decisions on the velocity to imprint in slip-forming operations of a vertical pipeline on a hydroelectric power station. In this type of concrete construction technique, the form is moving at a constant rate and the velocity of the movement is controlled by the height of the form and by the concrete setting time. Therefore, it is of paramount importance to accurately define the setting time and even to potentially track the stiffness behaviour before such event.

Firstly, it was decided to try to use the EMM-ARM to do the job. However, the accuracy of the method prior to the setting is low, and the final setting time only can be accurately determined after the estimation of the whole E-modulus evolution curve. Furthermore, the actual applicability of E-modulus predictive formulae through EMM-ARM can be quite debatable before the setting time. Therefore, a new method based on the accumulated experience in the use vibration based techniques, was suggested and called SMEA (Stiffness Monitoring at very Early Age).

The basis of this new method was the inversion of the concept behind the EMM-ARM. Instead of having a composite beam, with the hardening material inside, supported over rigid supports, the new method uses a steel cantilever beam partially embedded into the material under test (Figure 6.20). As the material starts to harden, the support condition of the cantilever starts to change, and consequently the resonance frequency of the beam changes also. To identify the resonance frequency of the steel bar, an accelerometer is attached to its free end to measure the ambient induced vibrations. In similarity to the original implementation of EMM-ARM, a fan is placed in the vicinity of the specimen to amplify the ambient induced vibrations.

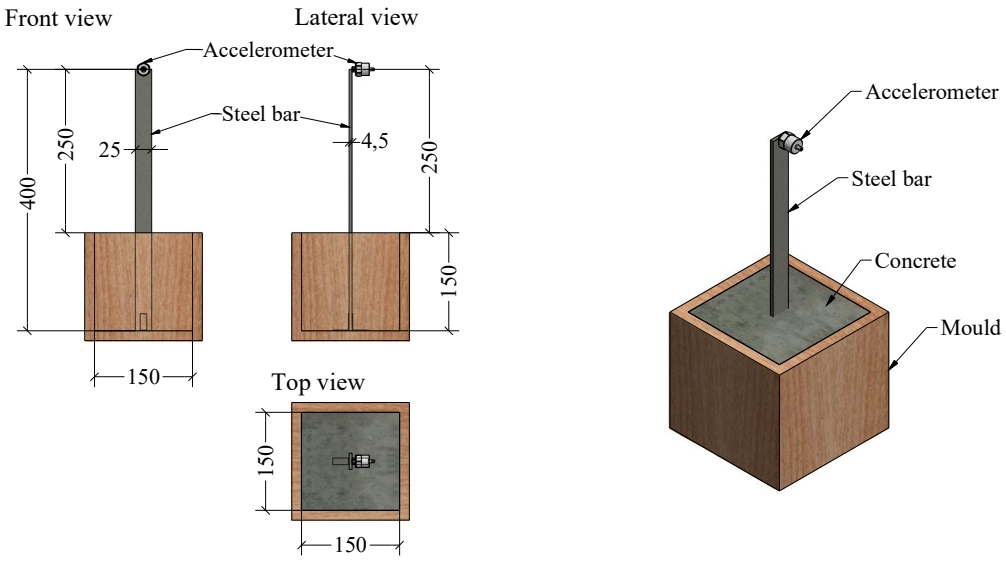

a) b)

Figure 6.20. New method to study very early age cementitious materials (SMEA): a) Scheme; b) 3D view [units: mm].

The scheme of the initial version of the test apparatus is shown in Figure 6.20, with the testing steel plate having 400 mm length, with a cross-section of 4.5×25 mm^2. The steel plate is vertically fixed to the bottom of a wood form with internal dimensions of 150×150×150 mm^3.

6.4.2. Pilot experimental program

A pilot experimental program was made to investigate the applicability of the new suggested method. The experimental program was composed of two identical test programs, T1 and T2, where 3 different geometries of the steel plate were selected: (*i*) cross-section of 25×4.5 mm^2 and 300 mm length (150 mm of free span): (*ii*) cross-section of 25×4.5 mm^2 and 400mm length (200 mm of free span); (*iii*) cross-section of 25×2.0 mm^2 and 400 mm length (200 mm of free span). The physical characteristics of the different specimens are presented in Table 6.10. Furthermore, to assess the repeatability of the method, two identical specimens (SM4.5-25-1 and SM4.5-25-2) where tested. The accelerations at the free end of the stripe were measured through an accelerometer PCB 352C04 (sensitivity: 1 V/g; range: ±5 g) connected to a dynamic acquisition system NI 9234 with 24-bit resolution. The accelerations were recorded at an acquisition frequency of 500 Hz in packages of 60 seconds each 10 minutes.

Table 6.10. Characteristics of the different test configurations used in the two pilot experiments.

Specimen	*Length (mm)*	*Thickness (mm)*	*Steel bar Width (mm)*	*Density (kg/m³)*	*Free span (mm)*	*Test*	*Average temperature (°C)*
SM2-25-T1	400.0	2.04	24.87	7741.7	255.0	T1	19.8
SM4.5-25-1-T1	400.0	4.48	25.47	7689.4	250.0	T1	19.8
SM4.5-25-2-T1	400.0	4.42	25.42	7732.0	250.0	T1	19.8
SM4.5-15-T1	300.0	4.45	25.41	7724.3	152.0	T1	19.8
SM2-25-T2	400.0	2.01	24.84	7839.4	250.0	T2	21.7
SM4.5-25-1-T2	400.0	4.42	25.53	7732.9	250.0	T2	21.7
SM4.5-25-2-T2	400.0	4.43	25.49	7684.9	250.0	T2	21.7
SM4.5-15-T2	300.0	4.46	25.41	7686.2	150.0	T2	21.7

The E-modulus of the concrete was accessed through one companion EMM-ARM specimen in each test program. The EMM-ARM specimens were 1.0 m PVC tubes with geometry similar to the one presented in Figure 3.15 (page 70). The characteristics of the specimens and testing technique are shown in Table 6.11. The protocol used in the EMM-ARM tests was similar the one presented in section 3.2.1.2.

Table 6.11. Physical and mechanical characteristics of the EMM-ARM beams.

Reference	*EMM-T1*	*EMM-T2*
Geometry		
$\varnothing_i$	86.50 mm	85.56 mm
$\varnothing_e$	90.60 mm	90.88 mm
Span	1000.0 mm	1000.0 mm
Connectors	Yes	Yes
(spacing)	(250)	(250)
Supports	$Ø_{TR}$=5 mm Concrete cubes	$Ø_{TR}$=5 mm Concrete cubes
Mould		
Material	PVC	PVC
Density	1461.5 kg/m³	1475.7 kg/m³
E-modulus	3.00 GPa	3.00 GPa
Concrete density	2388.0 kg/m³	2386.6 kg/m³
Type of test	OMA	OMA

Additionally P-wave velocity propagated trough the concrete was measured using PunditLab (see section 5.2.1.2 for more details) and the initial setting time was accessed through penetration resistance tests according to the ASTM C403 (2008) standard. One should remark that due to technical problems, since the experiments were performed in a concrete in-situ laboratory during a hydroelectric power plant construction, the protocol of the ASTM C403 standard was adapted. The adaptation comprised the use of the actual concrete instead of a

sieved one. This adaptation had a well-known drawback since the presence of the large aggregates increases the possibility of errors in the assessment of the penetration resistance (Carette, 2015). To attempt to counteract this potential problem, measurement comprised three valid penetrometer tests at the same instant, which were then averaged. Each penetration test was only considered valid if no coarse aggregate had been hit. A photo of the first test of the pilot experimental program is shown in Figure 6.21. The temperature of all specimens was acquired through K-type thermocouples (placed at the geometric centre of each specimen) connected to a PicoLog data acquisition system with 20-bit resolution.

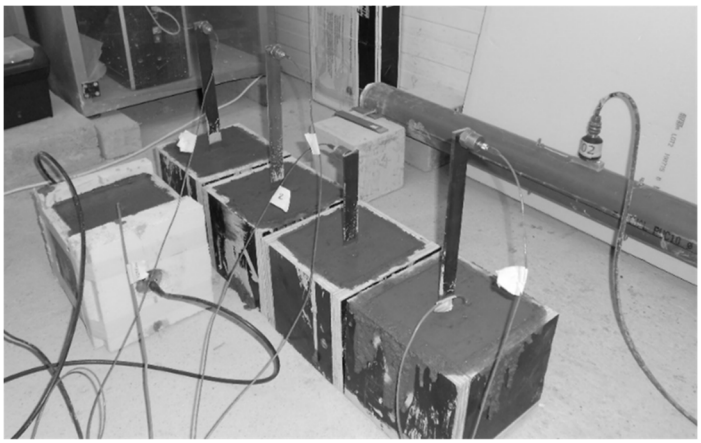

Figure 6.21. Photo of the pilot experimental program test 1.

For the pilot experiments a normal concrete mix was tested with the mix proportions provided in Table 6.12. It is word mention that the time '0' in the results was defined as the time when the water contacts with cement during the mixing process.

Table 6.12. Concrete mix composition.

Component	*Mix (kg/m^3)*
Sand	715 (0/4) natural
	257 (0/4) crushed
Gravel	793 (8/20)
Cement	240
	(CEM I 42.5R)
Fly ash	200
Water	152 l/m^3
Plasticiser	2.7
	(Glenium Sky 617)

6.4.3. Results and discussion

The room temperature histories observed during the two pilot test programs are shown in Figure 6.22. As can be seen during the first 5 hours the temperature of both test programs was similar with average temperatures of 20.1 and 22.4°C for the test 1 and 2, respectively. After this period the temperature of test program 1 was higher than that of test program 2 with maximum difference of ~7°C.

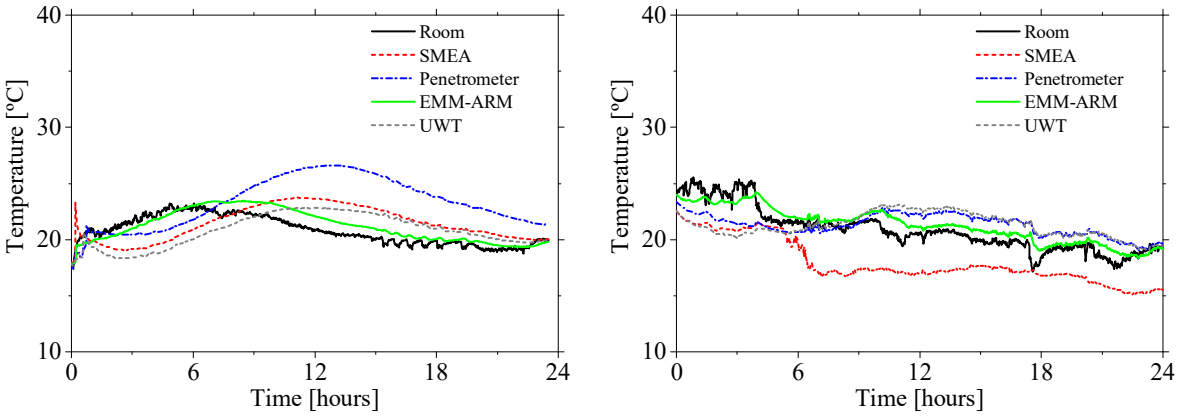

Figure 6.22. Temperature history: a) Test 1; b) Test 2.

The evolution of the penetration resistance obtained in the two test programs is given in Figure 6.23 where it is possible to see that the penetration resistance was null during the first 3 hours of curing. After this point the resistance started to increase, with a small difference between the two tests. The resistance evolution in test program 1 was slower and the identified initial setting time (time when the penetration resistance reach 3.5 MPa) was 4.00 hours, as opposed to the faster initial setting time of 3.68 hours observed in test program 2. This difference in the results is probably related to a small difference in the curing temperature during this period. In fact, the average temperatures observed in the specimens was 20.5 and 22.6°C in the tests 1 and 2, respectively.

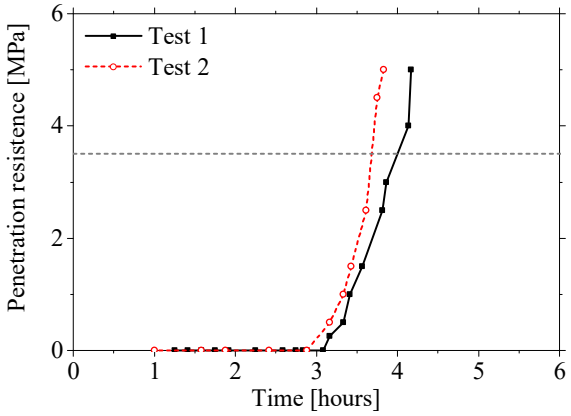

Figure 6.23. Penetration resistance evolution.

The elastic modulus evolutions during the first 24 hours of curing obtained with EMM-ARM are presented in Figures 6.24a and 6.24b for the test 1 and 2, respectively. The two evolutions have small differences between them since the E-modulus of 15 GPa is archived at 12.4 hours in the test 1 in opposite to the 14.9 hours observed in the test 2. The small difference in the rate of evolution is probably related to the slightly different temperature history of the specimens and to a slight different mixing procedure.

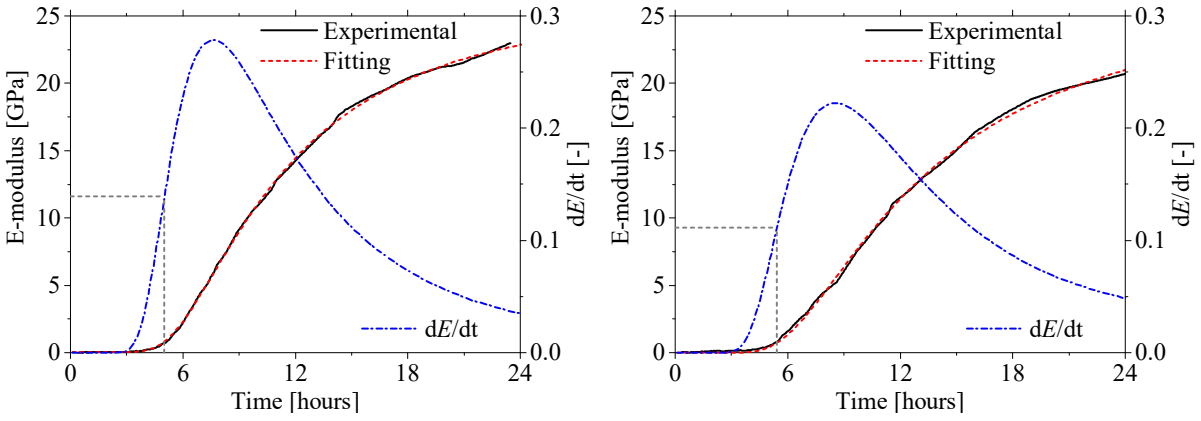

Figure 6.24. Final setting time estimation based on the EMM-ARM results: a) Test 1; b) Test 2.

Based on the E-modulus evolutions the final setting time was estimated by using the same protocol presented in section 5.2.1.3. To reduce numerical errors in final setting time estimations due to noise (variance) in the E-modulus evolutions each experimental curve was

fitted with an equation similar to (5.2) (page 150) as shown in Figure 6.24. The parameters obtained from the fitting are presented in Table 6.13. For the test programs 1 and 2, the following final setting times were estimated: 5.02 and 5.43 hours, respectively. These values have the opposite trend of the initial setting detect by the penetration tests, i.e. the fastest test to reach the initial setting is the one that has the later final setting. This fact could be related to some errors in the initial setting detection due to the use of non-sieved concrete.

Table 6.13. Parameters of the fitting models.

Parameter	*EMM-T1*	*EMM-T2*
α_1	26.568	26.503
α_2	0.131	2.427
β_1	2.004	1.825
β_2	0.0003	2.281
τ_1	0.392	0.455
τ_2	9.862	1.681
R^2	0.9997	0.9996

The identified evolutions of the first resonance frequency of the different strips of SMEA specimens are shown in Figure 6.25. A good coherence is observed between the results of the specimens with the same geometry, with maximum difference of 3.0 Hz, indicating that SMEA has a good repeatability. Furthermore, as can be seen in the figure, the resonance frequency identified in all specimens evolves significantly during the first 6 hours after casting. After this point the evolution is very small demonstrating that the method is only sensitive during the period when the material has very low stiffness, less than 1 GPa (as observed in the EMM-ARM results). By comparing the different curves, it is also evident that the frequency range during testing increases with the increase of the stripe's inertia (SM2-25 to SM4.5-25-1 and SM4.5-25-2) and with reduction of the stripe's slenderness (SM4.5-25-1, SM4.5-25-2 to SM4.5-15). Therefore, it becomes clear that the geometry of the specimen SM4.5-15 is the one that has more frequency range despite the lower amplitude of the vibrations observed during the tests. It is noted that a higher frequency range is desirable in view of better allowing to identify variations during the testing period: higher resolution of evaluation.

At the initial setting time, the identified frequency with specimens SM4.5-15 was 98.4 and 93.75 Hz in the test programs 1 and 2, respectively. Additionally, the frequency variation between the initial and final settings was of 3.2 and 5.7 Hz in the tests 1 and 2, respectively.

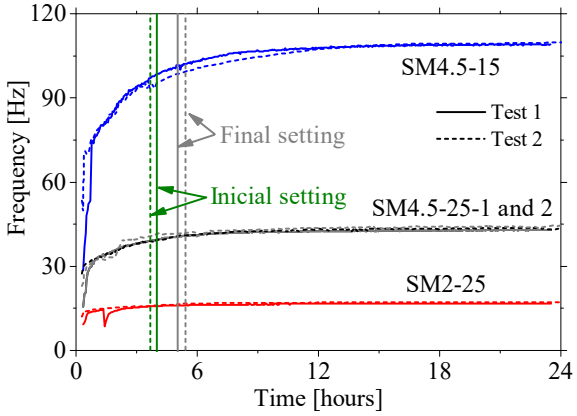

Figure 6.25. Resonance frequency evolution of the different steel bars.

By comparing the evolutions of the two specimens SMEA4 with the EMM-ARM E-modulus evolution, as shown in Figure 6.26a, it is possible to observe that even when the E-modulus is still negligible (first 3 hours) and EMM-ARM does not have enough resolution to identify/resolve relevant changes, the frequency identified with SMEA clearly shows that the material is getting stiffer. However, the computation of the material stiffness during this phase is not straightforward since the material cannot be considered as a solid and therefore the material needs to be modelled as a solid suspension fluid. Due to this added complexity the conversion of the frequency into viscoelastic properties of the material was not yet addressed (in the context of this thesis).

The SMEA results were also compared with the evolution of transmitted P-waves velocity as shown in Figure 6.26b. Even when capered with the UWT method it is possible to observe that the sensitivity of SMEA is much higher at the very beginning of the hydration process (until 3 hours of curing). In fact, it is well known that the ultrasonic waves transmitted through the material are attenuated by the presence of air bubbles in concrete (Zhu *et al.*, 2011a), which does not happen in SMEA method as only the viscoelastic properties of the material will influence the results.

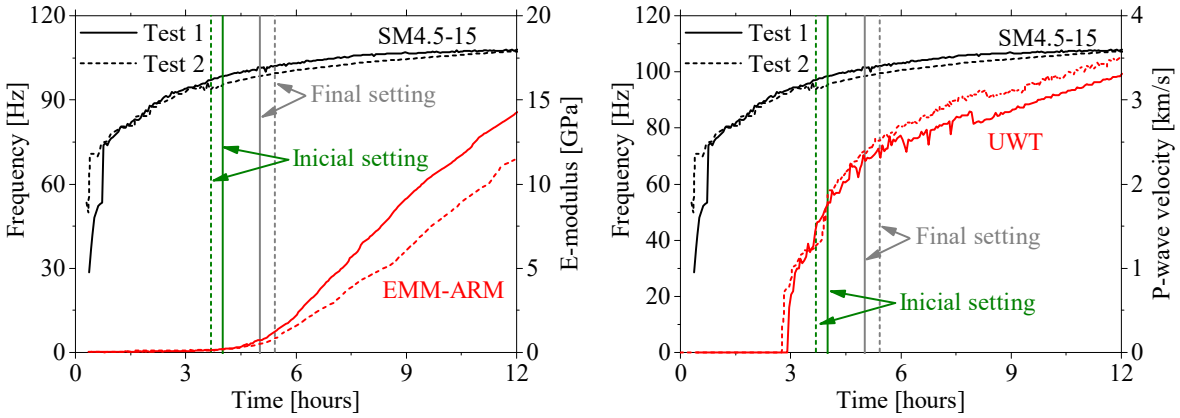

Figure 6.26. Comparison of the SMEA results with: a) EMM-ARM; b) UWT.

6.4.4. Influence of curing temperature

After the proof of concept of the SMEA method presented before, the new technique was used to study the temperature dependency of the viscoelastic properties of concrete during the beginning of cement hydration. In this new test, 5 specimens were tested at 3 different temperature histories: 13, 20 and 36°C. Regarding the geometry of embedded steel stripes and specimens, 300 mm long stripes with cross-section of 25×4.5 mm^2 were used, to get better results in accordance to the conclusions of the pilot experiments, partially embedded in concrete 150 mm edge cubes. The characteristics of the 5 specimens as well as the average temperature observed during the first 10 hours are presented in Table 6.13. The accelerations were acquired with the same type of accelerometer used in the pilot experiment connected to the same data acquisition equipment. The accelerations were acquired at 500 Hz in pack of 60 seconds each 10 minutes.

Table 6.14. Characteristics of the different test configurations used.

Specimen	*Length (mm)*	*Thickness (mm)*	*Steel bar Width (mm)*	*Density (kg/m^3)*	*Free span (mm)*	*Average temperature (°C)*
SMEA-T13-1	292.5	4.07	25.08	7745.4	142.5	13.69
SMEA-T13-2	293.5	4.32	25.25	7739.5	142.5	13.65
SMEA-T20-1	292.5	4.26	25.09	7710.5	142.5	20.63
SMEA-T20-2	290.5	4.22	25.13	7720.9	142.5	20.56
SMEA-T36-1	290.0	4.27	25.34	7738.2	139.5	35.57

As these experiments intended to study the early stages of the concrete hydration, the initial temperature of the raw materials was controlled. The control was made by placing all the raw materials needed create the concrete mix in a temperature controlled chamber at the target temperature of each test, for at least 12 hours prior to the mixing process. Then, the temperature of all specimens was acquired through K-type thermocouples connected to a PicoLog data acquisition system with 20-bit of resolution and the results are shown in Figure 6.27. Regarding the initial temperature of the concrete, despite the fact that prior to mixing all the components were placed in a temperature controlled chamber at the target temperature for 6 hours, after the mixing process the temperature of the concrete changed from the target due to the temperature of the mixing room and mixer.

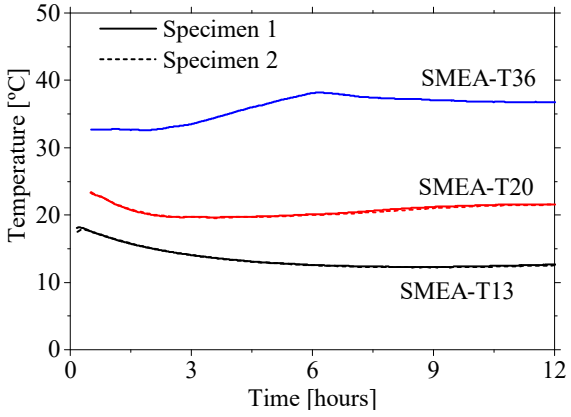

Figure 6.27. Temperature history.

The identified first resonance frequency evolutions from all the specimens tested are shown in Figure 6.28a. First one should highlight that results have a similar evolution kinetics to those observed in the pilot experiments. The frequency starts to evolve at a very fast rate with a progressive deceleration along time. Additionally, the different curing temperatures changed considerably the frequency evolutions: the 100 Hz frequency is reached at 0.9 hours in the specimen cured at 36°C as opposed to the 5.3 hours needed to reach the same frequency in the test at 13°C. There was also a very good coherence between the repeatability tests (specimens with the same geometry tested at the same curing conditions).

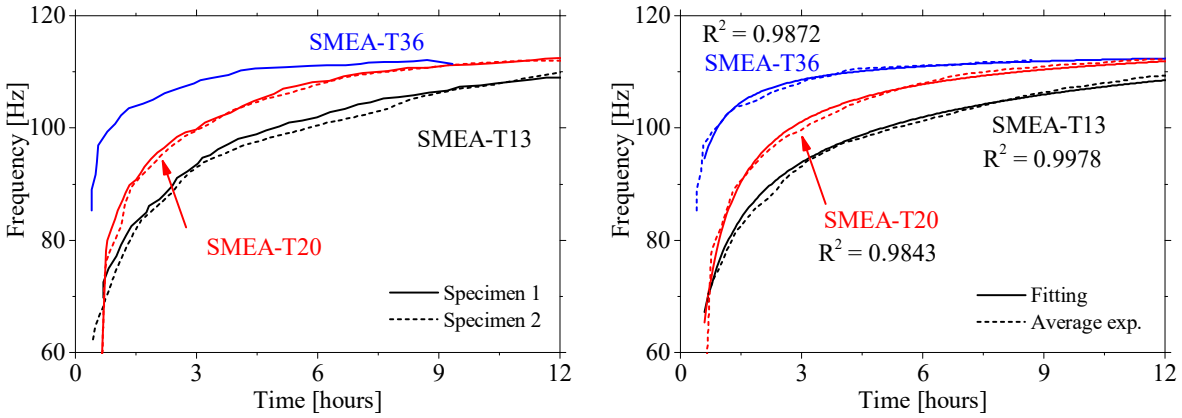

Figure 6.28. Frequency evolution along hydration: a) Experimental data; b) Fitting.

A further step in the analysis of gathered data, pertained to the evaluation of the apparent activation energy of concrete at these very early stages. Again, similarly to what was done in section 6.2.1, to reduce numerical errors in the apparent activation energy estimations due to noise (variance) in the frequency (*fr*) evolutions, the mean evolution curve was computed and fitted with the equation (6.7) as shown in Figure 6.28b.

$$fr(t) = d - \frac{e}{t^f} \tag{6.7}$$

The parameters obtained from the fitting are presented in Table 6.15.

Table 6.15. SMEA results fitting parameters.

Parameter	*SEMA-T13*	*SEMA-T20*	*SEMA-T36*
d	137.1	118.5	114.4
e	60.07	37.29	13.45
f	0.2984	0.6955	0.7578
R^2	0.9978	0.9843	0.9872

To compute the activation energy an adapted version of the so-called 'speed method' (see section 6.2.2.1) was used. In this version, the apparent activation energy (E_{act}), instead of being computed in steps of the hydration degree, is computed in steps each the normalized frequency (η) according to the following equation:

$$E_{act}(\eta) = -\frac{R}{\frac{1}{T_1(\eta)} - \frac{1}{T_2(\eta)}} \cdot \ln \frac{\left(\frac{d\eta}{dt}\right)_1(\eta)}{\left(\frac{d\eta}{dt}\right)_2(\eta)} \tag{6.8}$$

where T_1 and T_2 is the temperature of the material in the tests performed at two different temperatures 1 and 2, respectively. Here, the frequencies were normalized at 24 hours after casting as presented in Figure 6.29a. The obtained evolution of the apparent activation energy is shown in Figure 6.29b. The evolutions of E_{act} are difficult to interpret since no information exists about the relation between the parameter η (that has been established in this research work) and the degree of reaction or the stiffness of the material.

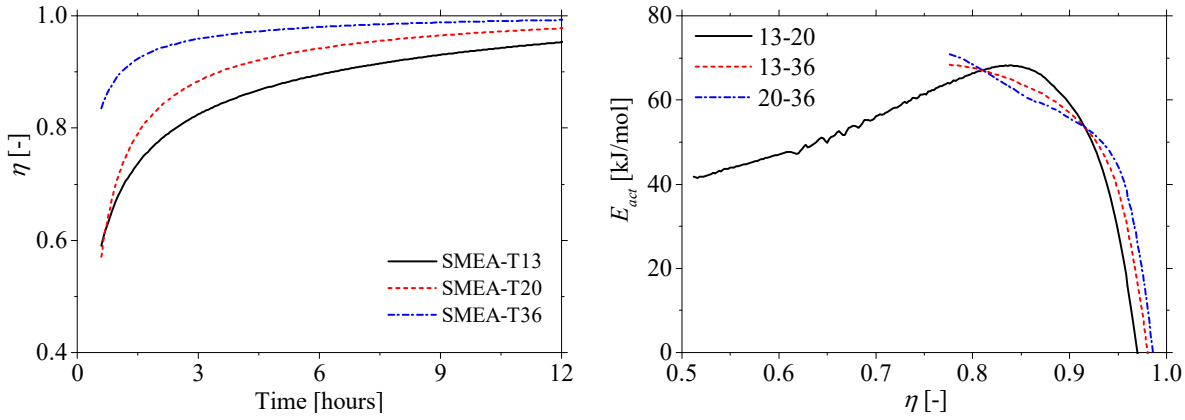

a) b)

Figure 6.29. a) Evolution of the normalized frequency at 24 hours (η); b) Evolution of the apparent activation energy with the normalized frequency (η).

Yet, by using the relation between apparent activation energy and the normalized frequency it is possible to obtain a perfect superposition of the frequency evolutions at different curing temperatures as shown in Figure 6.30.

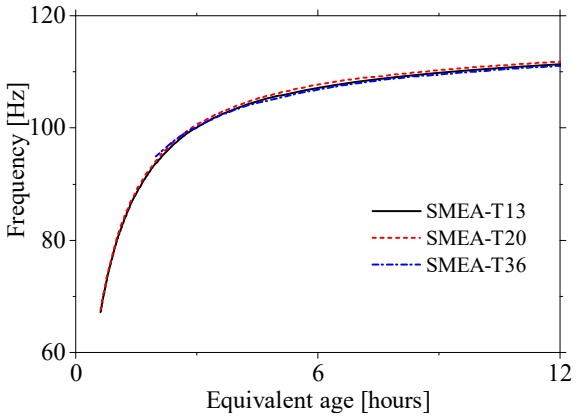

Figure 6.30. Evolution of the first resonance frequency over the equivalent age at 20°C.

Despite the difficulties, that can be superseded by performing parallel experiments to estimate the curing degree over time or converting the measured frequency to a viscoelastic property of the material, the results have shown that SMEA is sensitive enough to perform the quantification of the activation energy during the fresh state.

6.5. EMM-ARM applied to structural epoxy adhesives

Until now the EMM-ARM technique was only used to monitor the E-modulus evolution of cement-based materials and stabilized soils (Azenha, 2009, Azenha *et al.*, 2012a, Azenha *et al.*, 2010a, Silva *et al.*, 2013a, Silva *et al.*, 2014). However due to the good results obtained in all the implementations one have decided to expand EMM-ARM to test different hardening materials.

In recent years, the application of thermosetting resins in civil engineering applications has largely increased, mainly for their use in structural strengthening systems such as Fibre-Reinforced Polymer (FRP) reinforcements (Dunn, 2004). In FRP installations, the mechanical behaviour of the strengthening system is strongly influenced by the epoxy adhesive, particularly at early ages, while the mechanical properties of the adhesive are still enduring significant evolution. Therefore, the final performance of the whole application strongly depends on adequate preparation, application and curing of the epoxy resin itself. During the curing period, the fluid resin transforms into a rubber (gelation) and then in a solid glass (vitrification), developing a progressively denser polymeric network (Gillham, 1986). Additionally, it has

been shown that the necessary curing time to reach the targeted bond strength of a given resin significantly depends on environmental conditions, such as temperature and moisture (Czaderski *et al.*, 2012, Matsui, 1990). However, despite the known issue no methods were found in literature capable of measuring the mechanical properties of epoxy adhesives along the entire curing process that could be implemented during application in construction sites.

Thus this section aimed to validate the application of EMM-ARM to study the early-age evolution of E-modulus of epoxy materials used for FRP applications, and better understand the relationship between distinct approaches for its assessment. For this purpose, a simultaneous study of E-modulus of the same adhesive mixture was carried out through EMM-ARM, together with tensile testing at several ages. The work presented in this section was already published in (Granja *et al.*, 2015, Fernandes *et al.*, 2014, Granja *et al.*, 2014b). Additionally, these work have led to the following publications (Benedetti *et al.*, 2016, Fernandes *et al.*, 2015, Benedetti *et al.*, 2015)

6.5.1. Experimental Program

The experimental program consisted in the execution of an epoxy resin mixture and the characterization of the corresponding stiffness evolution along the curing time by EMM-ARM tests and monotonic tensile tests (MTT). The two-component epoxy resin-based adhesive used in the experimental work, produced by S&P® Clever Reinforcement, had the trademark 'S&P Resin 220 epoxy adhesive'. This adhesive is typically employed for bonding FRP laminates to concrete and steel, and therefore may be seen as representative. According to the manufacturer (S&P, 2011), the component A (resin) contains 20-25% (by weight) Bisphenol A-Epoxy Resin and 5-10% Neopentyl glycol diglycidyl ether and, the component B (hardener) includes 20-25% poly (oxypropylene) diamine, 1-2.5% piperazine and 20-25% 3,6-diazaoctanethylenediamin; triethylenetetramine. All the specimens tested in the scope of this research were originated from a single batch that involved a total volume of epoxy resin of ~1.2 litres. The individual components were separately stirred and then component B was added to component A at a ratio of 1:4 by weight of the respective constituents. To minimise air inclusions, the compound was thoroughly and slowly manually mixed until the colour was uniformly grey and free of any streaks. The whole mixing procedure lasted approximately 4 minutes.

All experimental procedures (mixing and testing) took place under controlled environmental conditions (in climatic chamber), with temperature of 20±1°C and relative humidity of 55±5%. The following sections detail the program of tests, methods and the procedures of test series, including sample geometries, test configurations and preparation of specimens.

6.5.1.1. EMM-ARM tests

In order to adapt the EMM-ARM technique to the study of epoxy adhesive used in FRP applications, some further adaptations were necessary. Since the grain size of the filler of the epoxy (maximum grain size usually ranging between 0.2 and 0.5 mm (Moussa *et al.*, 2012)) is comparable to that of cement paste, it was decided to adopt a similar mould/strategy to the one used in EMM-ARM version applied to cement pastes, which is described in section 3.3. Herein, focus will be addressed to essential aspects concerning the modified experimental setup and testing procedure.

Taking into account the extensive experience of the author with this testing technique and bearing in mind the trade-off that exists between the decrease in specimen size and the corresponding increase in resonant frequencies (thus less excitable structures), regarding the beam span, since the adhesive upon full hardening have a stiffness around 8 GPa (much lower than what is expected in a current cement paste) it was decided to use the EMM-ARM beams with the smaller spans (250 mm – see Figure 3.22 (page 78)). It is stressed that the adopted geometry simultaneously allows the test to endure a significant variation range of resonant frequency of 50-80 Hz for a stiffening of the testing material from 0 to ~8 GPa. This wide range of frequency variation allows E-modulus evolution to be identified with a good resolution. The same clamping device, as the one used in the cement paste tests, was used to assure complete fixation of the cantilever beam. The EMM-ARM experimental setup adopted for testing epoxy resin is similar to the one reproduced in Figure 3.22 (page 78). The mould consists of a 330 mm long acrylic tube, with internal and external diameters equal to 16 and 20 mm, respectively. This cross-sectional size respects the principle that the diameter of the beam should be at least 3 to 5 times larger than the nominal size of the particles of the tested material, in accordance to the criteria given by ASTM C192 / C192M (2015a).

In the EMM-ARM application for the study of cement pastes, the acrylic tube was already prepared with an extremity cap before the tube filling. However due to the higher viscosity of the epoxy adhesive after mixing, this was injected into the tube by using a 100 ml syringe, as shown in Figure 6.31. This method of injection had already been successfully verified in preliminary tests, checking the possible formation of air bubbles inside the tested material due to a potentially inefficient injection of epoxy inside the mould.

Figure 6.31. Photo of the epoxy injection into the acrylic tube.

When the tube was completely filled with the epoxy, two propylene lids were placed at both mould extremities. Finally, after putting the specimen in the final horizontal position, a ceramic shear piezoelectric accelerometer (PCB® Piezotronics 352C34, with mass of 5.8 grams, sensitivity 100 mV/g; frequency range: 0.5 to 10000 Hz) was placed at the free end of the cantilever, in order to monitor the accelerations of the extremity of the beam in the vertical direction. The tests were performed in OMA conditions, and the ambient vibrations were amplified by placing a domestic fan in the vicinity of the EMM-ARM specimens to increase the air movement. The measured accelerations are acquired in a 24-bit data logger (NI-USB-9233) at a frequency (f_{acq}) of 500 Hz, and divided in sets of 300 seconds each 10 minutes.

In order to check the method's ability to obtain results with good repeatability, two tests were performed simultaneously, using the same epoxy adhesive mixture employed for tensile tests. Table 6.16 shows the geometric characteristics of the used moulds, as well as the density of acrylic and epoxy adhesive.

Table 6.16. Characteristics of EMM-ARM specimens.

Reference	*EMM1*	*EMM2*
Geometry		
$\varnothing_i$	15.99 mm	15.94 mm
$\varnothing_e$	20.15 mm	20.14 mm
Span	250.0 mm	250.0 mm
Mould		
Material	Acrylic	Acrylic
Density	1202.5 kg/m^3	1198.9 kg/m^3
E-modulus	4.15 GPa	4.15 GPa
Epoxy density	1742.9 kg/m^3	1763.9 kg/m^3
Type of test	OMA	OMA

6.5.1.2. Tensile tests – MTT

An extensive set of thirty tensile tests were performed in order to determine the epoxy E-modulus at several ages. The specimens for testing were manufactured according to "type 1A" defined in EN ISO 527-2 (2012b). This specimen's geometry is characterized by having a dog bone shape at both extremities, with a thickness of 4 mm and overall geometry defined as shown in Figure 6.32. Teflon moulds were devised for fabrication of the specimens. After mixing the two resin components, the homogenized compound was cast into the referred Teflon moulds. Afterwards an acetate sheet was placed on the top surface and pressed with a steel roller. The specimens were kept sealed in the curing environment and were removed from the moulds just before being tested. For all specimens, width and thickness were measured at the three sections (S1, S2 and S3) identified in Figure 6.32, using a digital calliper with a precision of ±0.01 mm, to check tolerances and for longitudinal stress calculation.

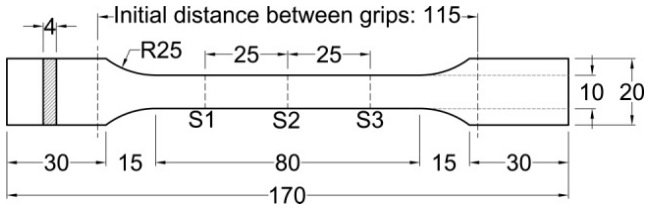

Figure 6.32. Specimen dimensions according to ISO 527-2 [units: mm].

The experimental program comprised the testing ages of 12, 18, 36 and 84 hours. For each age of testing, three monotonic tensile tests (MTT) were carried out. A specific nomenclature was devised for the test specimens, each one being labelled as MTT_X_Y, where X is the testing

time in hours (12, 18, 36 and 84) and Y is the specimen number within the series. The summary of all tensile tests performed is shown in Table 6.17.

Table 6.17. Experimental program of tensile tests.

Age	*Series*	*Number of specimens*
12h	MTT_12h	3
18h	MTT_18h	3
36h	MTT_36h	3
84h	MTT_84h	6

The tensile tests (MTT) were carried out in a universal testing machine (AG-X Shimadzu) with 50 kN capacity load cell and test force measurement precision of 1/1000 ±0.5%. A TML strain gauge (type: BFLA-5-3-3L; measuring length: 5 mm; gauge factor: 2.08 ±1%) was installed on the top surface of each specimen (i.e. the surface that was bounded by the acetate sheet), at mid-length, to measure its longitudinal strain (see Figure 6.33).

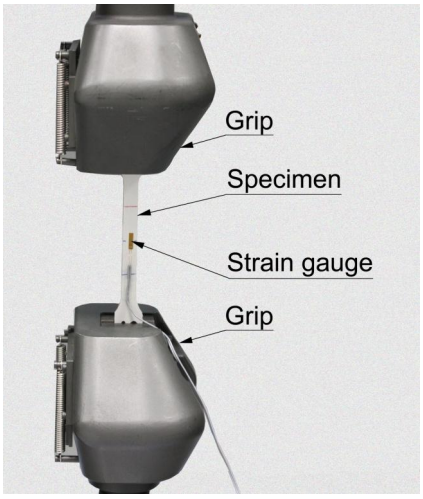

Figure 6.33. Layout configuration of tensile tests.

The tests were conducted under displacement control, at a rate of 1 mm/min, according to EN ISO 527-1 (2012a).

6.5.2. Results and discussion

6.5.2.1. EMM-ARM tests results

The resonant frequencies evolution obtained for the two specimens are shown in Figure 6.34. It is remarked that the two frequency curves are very coherent, providing an indication of good repeatability of the experimental setup and procedures. Moreover, a wide range of frequencies was covered throughout the curing process of the epoxy adhesive, ranging from 51.3 to 79.6 Hz within the testing period; E-modulus evolution can thus be identified with a good resolution (0.034 GPa for 51.3 Hz and 0.052 GPa for 79.6 Hz). The frequency evolution curves appear to be plausible, showing an initial period of approximately 6.4 hours in which the frequency remains almost constant. After this threshold, the frequencies evolved significantly for both tested specimens until approximately 36 hours of curing. After such period, the slope of variation exhibits a significant decrease.

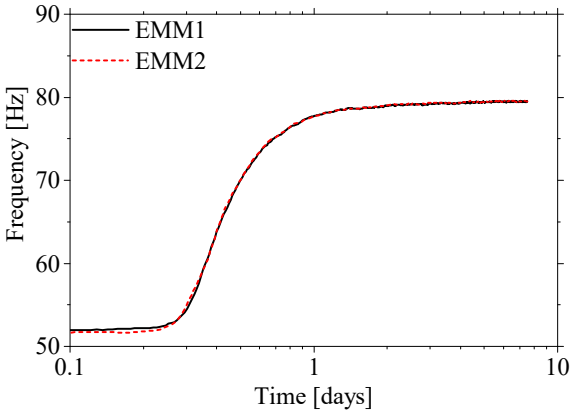

Figure 6.34. Resonant frequency evolution of the EMM-ARM beams.

The elasticity modulus of the tested epoxy adhesive mixture was estimated by applying equations (2.14) and (2.12) (page 35). The stiffness evolution for both EMM-ARM specimens is shown in Figure 6.35. The agreement between the results of the two specimens is very good, with absolute stiffness differences under 2.5% (0.22 GPa at the age of 168 hours), demonstrating adequate repeatability of EMM-ARM. In the initial period (during the first ~6.4 hours) the epoxy adhesive stiffness was nearly null for both specimens, which is consistent with its fluid-like behaviour. The kinetics of evolution of E-modulus was consistent with the one

already described and discussed for the frequency evolution, and the final reached value at the end of testing was 9.3/9.5 GPa for EMM1/EMM2.

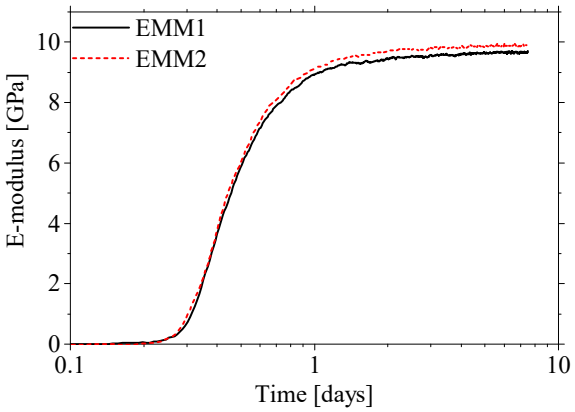

Figure 6.35. E-modulus evolution obtained by EMM-ARM.

6.5.2.2. Tensile tests results

Figure 6.36 presents the stress-strain curves obtained at various ages by monotonic tensile tests. Stress was evaluated by dividing the applied load by the cross-sectional area of the specimen's mid-height section (where the strain gauge was placed). From this figure, it is possible to observe the increase on stiffness along the curing process of epoxy adhesive. At the age of 12 hours, since the curing reactions had just begun, high values of strains were obtained. In fact, the monotonic tensile tests carried out at 12 hours were stopped at about 5% strain (limit of the used strain gauges). From 12 to 36 hours, the epoxy stiffness had a significant increase, shown by the strong slope difference of the curves obtained at 12, 18 and 36 hours. From 36 to 84 hours, the stress-strain curves did not exhibit any significant variation: in that period the average maximum tensile strength increased only of 0.2 MPa (1%). On the contrary, a decrease of 18% (0.0006 m/m) in ultimate strain was observed, confirming that curing reactions were still in progress between 36 and 84 hours.

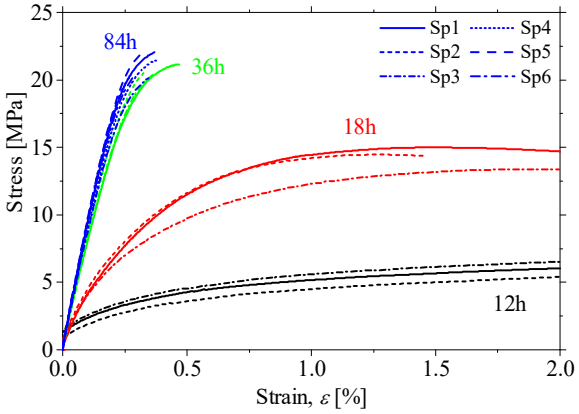

Figure 6.36. Stress-strain curves obtained from monotonic tensile tests.

The Young's modulus of epoxy adhesive was obtained by through the slope of the linear trend line of the experimental values gathered until 1/3 of the ultimate strength, in accordance with the American Standard ASTM D638M-93 (1993). In order to avoid the error caused by the possible starting misalignment of the grips and the presence of microscopic structural flaws, the initial region of positive second derivative of each experimental curve was not considered for the calculation of the E-modulus. The average Young's modulus values obtained are depicted in Figure 6.37.

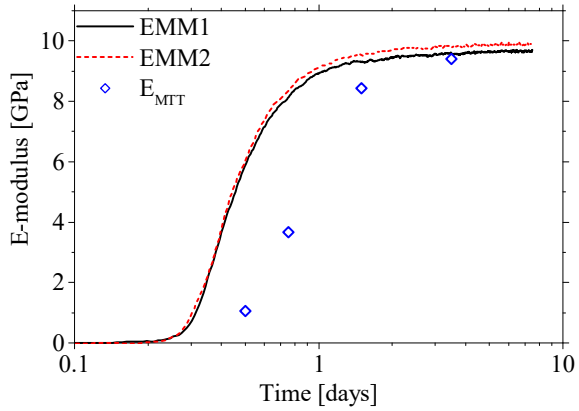

Figure 6.37. Epoxy E-moduli evolution obtained by EMM-ARM and tensile tests (MTT).

Figure 6.37 also shows the comparison between the elastic modulus results obtained by EMM-ARM and by monotonic tensile test. At the age of 84 hours, there is a good agreement between the values obtained through the EMM-ARM (EMM1 and EMM2), those collected in MTT. However, the results show relevant differences at the earlier ages of 12, 18 and 36 hours. At such ages, all the E-modulus values obtained from tensile tests are significantly lower than the

ones acquired from EMM-ARM, particularly at 12 and 18 hours. This deviation may be explained by different time-scales and strain-rates of the experimental tests. However, the strain-rate of the different methods, ranging between 10 and 50 με/s for EMM-ARM (computed through numerical integration of the accelerograms) and between 100 and 110 με/s for the monotonic tensile tests (computed directly from the strain measurements) are within the same order of magnitude and therefore are not different enough to justify the gap between the estimated E values. Nevertheless, the EMM-ARM has a much lower period of loading (within a range of 0.016 and 0.02 seconds) than the monotonic tensile tests (within a range of 10 and 20 seconds). This lower time-scale makes the method less sensitive to the viscoelasticity of the material. The full justification for this difference can be found in (Granja *et al.*, 2015).

This page intentionally left blank

Chapter 7

Simulation of stiffness evolution – cement pastes

7.1. Introduction

Throughout the history of science, simulation models have played an important role. Since the emergence of the first simple models, there has been a continuing effort to improve and increase in sophistication. However, for the case of cement-based materials, even the most advanced existing models for behaviour simulation still correspond to crude simplifications of reality (Bishnoi and Scrivener, 2009, Thomas *et al.*, 2011). Despite the notion that the models and the reality are always different, we have seen an increase in demand for simulation models, both in science and engineering (Dolado and van Breugel, 2011). This happens because of the need for tools that help the understanding and description of the physical and chemical properties of such materials, both to support the process of decision-making (which can lead to time savings in the construction process) or to the development of new materials (Pape *et al.*, 2008).

In the last decades several researchers have been proposing microstructural simulation models capable of estimating the mechanical properties of cement base materials (Bishnoi, 2008, van

Breugel, 1991, Maekawa *et al.*, 1999, Bentz, 1997b). These methods have been under constant evolution through the comparison/validation of the results with SEM and classical mechanical tests (cyclic compression and strength). However, these comparisons/validations are often made only for high degrees of hydration due to the characteristics of the experimental methods used (as presented in Chapter 2) (Haecker *et al.*, 2005, Do, 2013). Furthermore, to estimate the mechanical properties these models require the knowledge at the micro-scale of the mechanical properties of each individual component of the material during the hydration of the cement. The characterization of these properties is been made using nanoindentation tests (Manzano *et al.*, 2009). However, the type of tests is not feasible to characterize the components of the cement-based materials along the hydration process.

Taking into account the unprecedented information about the continuous evolution of the cement-based materials right since the instant of casting provided by the EMM-ARM a foray in the microstructural simulation of the cement-based materials will be made in this Chapter. An analysis was made in collaboration with EPFL to evaluate the possibility of using the EMM-ARM results to validate and estimate the evolving properties of the components of the cement pastes. But first it is appropriate to review the state of knowledge concerning micromechanical modelling of hardening of cementitious materials.

7.2. Estimation of mechanical properties

The estimation of the stiffness evolution of cement-based materials with the advance of the hydration reaction is the subject of a large number of studies (Bernard *et al.*, 2003, Do, 2013, Sanahuja *et al.*, 2007a). From a macroscopic point of view, the evolution of the mechanical properties of cementitious materials can be associated with the degree of hydration through empirical relationships (Bernard *et al.*, 2003, De Schutter and Taerwe, 1996). However, as is demonstrated in the work Krauß and Hariri (2006), at very early ages, after the initial setting, the existing simulation models failed to adequately correlate the stiffness and the degree of hydration. Hattel and Thorborg (2003) present a distinct macroscopic approach based on the concept of maturity. In this approach the evolution of the elastic modulus over time is defined as a function of the final modulus equivalent value related to age, through an Arrhenius equation.

Several authors have suggested relations between elastic modulus and percolation (ratio of volume of solids connected together and the total volume solids) (Torquato, 2001). In their work, Ye *et al.* (2004b) found that the relation between the static modulus of elasticity and the volume fraction of the solid phase (p) appears to follow a power law (as shown in equation (7.1)), which is a function of the volume fraction of the solid phase at which the solid starts to become interconnected (p_c) and a structural parameter (k_p).

$$E \approx (p - p_c)^{k_p} \tag{7.1}$$

However, these empirical relationships do not take into account the fundamental physical processes and microstructure, ignoring the physical and chemical properties, temperature, air content and, in the case of compression strength, cracking (Chamrová, 2010). These simplifications make the obtained estimations for the mechanical properties diverge considerably, particularly if the material has a high porosity. Thus more sophisticated models are needed for accurate prediction of the effective elastic properties of cementitious materials.

These problems can be solved by using homogenization theories of heterogeneous materials, such as concrete, with periodic distribution components. In these models, originally developed by Sanchez-Palencia (1980), the material is simulated as an infinite series of unit cells thus allowing the material properties to be obtained by separate analysis of each component. Under this theory, the analysis of a heterogeneous material is reduced to a simpler problem of a representative element in which the elastic properties can be calculated by analytical or numerical methods. Several authors have proposed a homogenization analytical approach for cementitious materials (Bernard *et al.*, 2003, Constantinides and Ulm, 2004, Pichler *et al.*, 2007, Sanahuja *et al.*, 2007a, Tian and Bian, 2013, Zhao *et al.*, 2013). The authors consider the microstructure of cementitious material at different levels (multi-level) as shown in Figure 7.1. The mechanical characteristics are obtained for the lowest level, homogenized and introduced into the next level model.

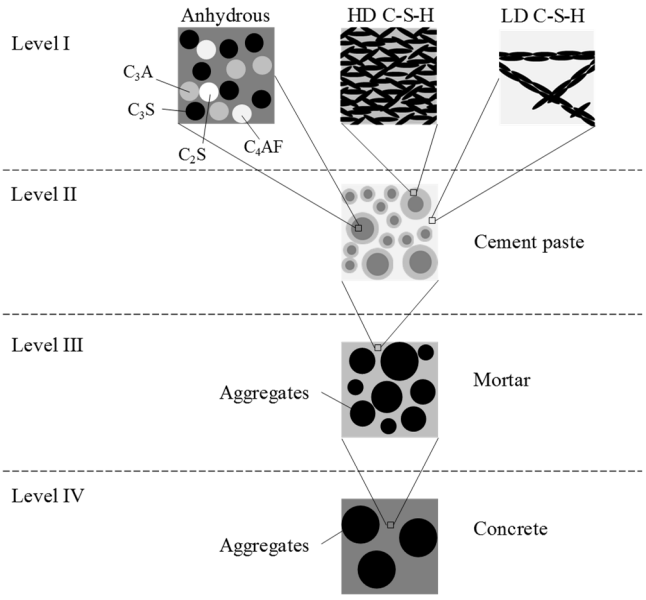

Figure 7.1. Four microstructural levels of cement-based composite materials. Adapted from (Pichler *et al.*, 2007) and (Sanahuja *et al.*, 2007a).

These approaches enable a large reduction in the complexity of simulation models. However, even considering only the lowest level of the homogenization models, the actual microstructure of a material it is frequently complex and not uniform, making the prediction of their mechanical properties in a non-trivial problem even in the case of microstructures with linear elastic properties of their phases.

Therefore several authors have started to create numerical discretized models (see Figure 7.2) of the complex microstructure of the materials in an attempt to estimate the mechanical properties (Chamrová, 2010, Do, 2013, Haecker *et al.*, 2005, Bernard and Kamali-Bernard, 2012, Kamali-Bernard and Bernard, 2009). Several numerical models have been proposed for modelling of heterogeneous materials microstructure such as the finite element method, methods based on fast Fourier transform, method based on network model and method of the extended finite element (XFEM) (Chamrová, 2010). It should be noted that, whichever simulation method is chosen, the computational cost associated with the simulation of the elastic properties of a 3D microstructure can be very high. These models normally simulate cement paste through cubic microstructure models, like the one presented in Figure 7.2. However, due to the high geometric complexity of the nanostructure of cementitious materials, these models are usually generated by considering the microscopic structures of the major components as homogeneous materials. This simplification implies knowledge of the

homogenized mechanical characteristics of various components involved, which are usually obtained by homogenization theories. However, these procedures still require extended experimental validation. This may represent an interesting opportunity due the amount of information that one can get from EMM-ARM experiments, thus supporting the possibility of improvements to existing simulation models.

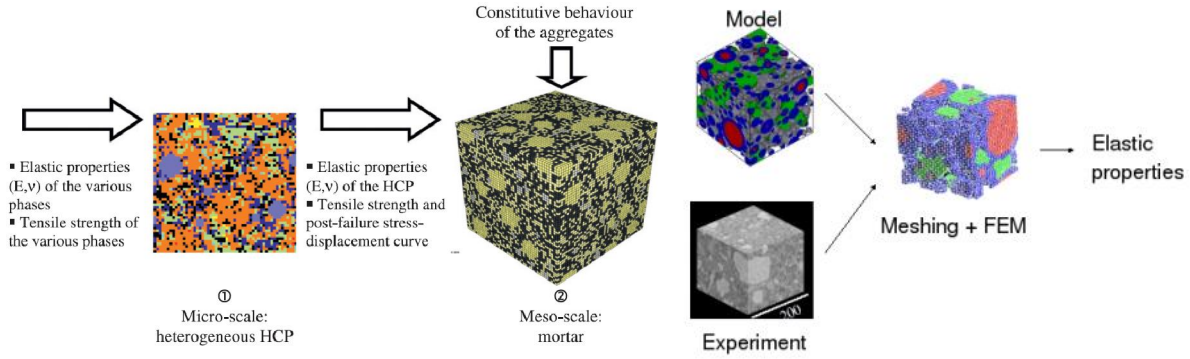

a) b)

Figure 7.2. Simulation strategies to obtain the mechanical properties of cement-based materials from: a) Kamali-Bernard and Bernard (2009); b) Chamrová (2010).

It should also be noted that the complexity of the microstructure and the associated computational cost require deep thinking on approaches and simplifications (Chamrová, 2010). The replacement of 3D microstructure by 2D slices is tempting. However, Hain and Wriggers (2008) demonstrated, by tomography, that the plane stress and plane strain in 2D are 30% smaller than in a 3D microstructure. The results suggest that connectivity to 3D is quite different and can not be easily established through 2D microstructure. It should also be noted that the models that have just been presented assume prior knowledge of the microstructure evolution along the hydration of cement and the behaviour of the fundamental components of the cement paste. Therefore, in the scope of this thesis, it is considered necessary to deepen the literature review on simulation models specifically dedicated to the cement paste hydration presented in the following section.

7.2.1. Numerical Models for Cement Microstructure

Throughout the years, several cement hydration models have been proposed (Thomas *et al.*, 2011). The first models were based on the hydration of a single cement particle (see Figure 7.3) (Pommersheim and Clifton, 1979) – These models have two basic limitations: they do not take into account the interaction between adjacent cement particles and they fail to faithfully reproduce the overall kinetics of a moisturizing series of particles with different sizes.

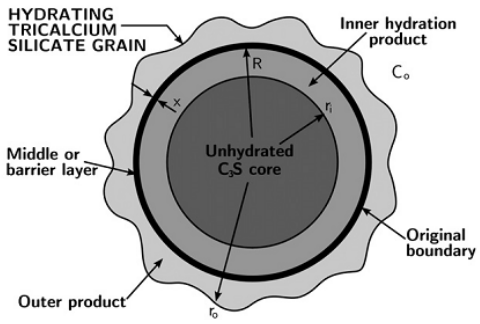

Figure 7.3. Schematic representation of the hydration of the C_3S particle model from Pommersheim and Clifton (1979).

Then, based on experimental observations, new series of models were developed with basis on the nucleation and growth phenomena (Scherer *et al.*, 2012). These models are based on observations that the hydration process is controlled by the formation of the C-S-H compounds (Avrami, 1939, Garrault-Gauffinet and Nonat, 1999, Garrault-Gauffinet and Nonat, 2001). However, although more sophisticated models are being implemented increasingly, they should be used with caution. In fact, in many cases, even though these models provide estimates that reproduce reasonably the experimental data, there is a large gap between the assumptions and the real physical process (Thomas *et al.*, 2011). These simple approaches to the complex problem of cement hydration have the ability, at best, to simulate the hydration of the cement paste during a limited period of time when the temperature is constant. To be able to simulate the complex hydration process of cement pastes a more comprehensive approach is needed that simultaneously encompasses multiple physical and chemical phenomena.

The first model with this level of complexity was proposed by Jennings and Johnson (1986). This model tries to reflect the complex nature of a cement particle system with the aim of

producing a virtual reactor without predetermined and artificial assumptions that were underlying the previous models. The cement particles are represented as spheres, placed inside a cubic computational volume, and hydration is simulated as reducing the radius of the anhydrous phases and concentric growth CSH layers on the surface of these particles, similar to the hydration models of a single cement particle (see Figure 7.4). However, due to lack of computational power at the time, this model had several simplifications to ensure its viability. These simplifications have limited the use of the model. Yet this model has given way to a new kind of much more complex simulation models.

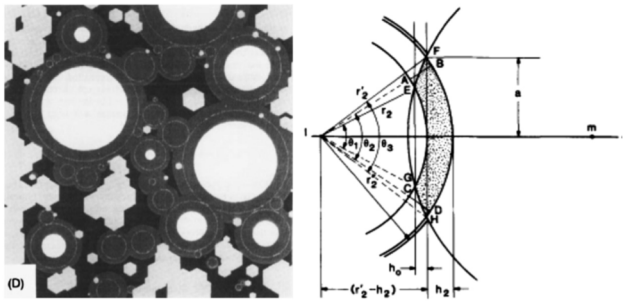

Figure 7.4. Microstructure generated with the model of Jennings and Johnson (1986).

Using a similar approach to that adopted by Jennings and Johnson (1986), van Breugel (1991, 1995), developed a similar microstructural simulation model, called HYMOSTRUC (HYdration, MOrphology and STRUCtural development). In this model a virtual 3D microstructure composed of randomly distributed spherical cement particles is considered. As the particles react, hydrates are formed in concentric layers around the cement particles. With the increasing volume, the particles start to overlap with the adjacent neighbour (see Figure 7.5). The model treats the entire microstructure through statistical method, instead of attempting to explicitly consider all individual particles enduring hydration. Additionally, the degree of hydration is reproduced as a function of the particle size distribution and of the chemical composition of the cement, the w/c ratio and the reaction temperature (Ye *et al.*, 2004a). This approach allows the models to be computationally feasible, but it is impossible to obtain localized information, such as the porous network and the connectivity between the particles.

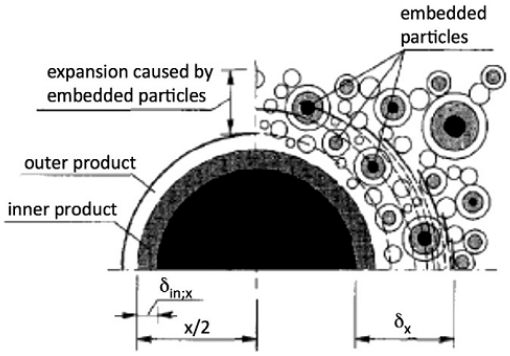

Figure 7.5. Hydration scheme in HYMOSTRUC model (van Breugel, 1991).

The multiscale model DuCOM, capable of simulating cement hydration, was created in the University of Tokyo by Maekawa *et al.* (1999, 2003). This model has been developed as a package with finite element prediction capabilities of the material of the reinforced concrete behaviour, including effects related to the durability (carbonation, alkali leaching, rebar's corrosion, etc.). The model simulates the cement pore size based on the hydration of representative unitary particles. Although this model may not be classified as a truly microstructural model, its development has been supported by extensive experimental and analytical programs. However, this model depends almost entirely on empirical relationships which have been calibrated by experimental results. Furthermore, the hydration is simulated using a single cement particle simulated as being an average particle size of the heterogeneous distribution of particles in the cement (Bishnoi, 2008).

An even more sophisticated model has been developed by Bentz and Garboczi (Garboczi and Bentz, 1992, Bentz, 1997b, Bentz, 1997a, Bentz, 2006) is the CEMHYD3D model. In contrast to the models described above, this one uses an approach based on the structure obtained from digital images. The 3D microstructure of cement paste is obtained by processing an actual image of a paste within a uniform cubic grid, wherein for each volume element (or voxel) of the network is assigned a material (water, alite, etc.). The changes in microstructure are simulated by means of a large number of rules that are evaluated locally and depend on the materials involved in the interaction of the temperature and, in some cases, global parameters that define the microstructure, as the water to cement ratio or a phase volume. These rules are used to mimic the dissolution, diffusion and nucleation and growth of hydration products. Hydration in CEMHYD3D progresses in different repeated cycles of dissolution, diffusion and reaction. This approach leads to a development of the 3D microstructure for ordinary Portland

cement pastes, which have a realistic appearance and a quantitative reasonable spatial distribution of anhydrous cement particles, hydration products and capillary porosity, as shown in example of Figure 7.6.

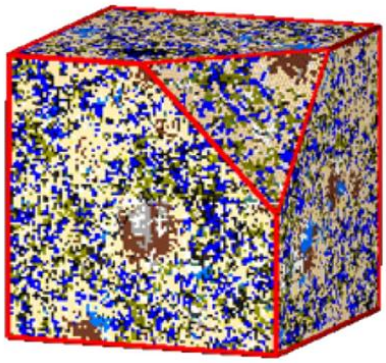

Figure 7.6. Simulated microstructure through CEMHYD3D model of an ordinary Portland cement paste type I with 14 days of hydration (Bentz, 1997b).

Despite the many success stories in the application of this model, this also presents a number of limitations, as the authors refer (Garboczi and Bentz, 2001). As an example it is stated that the time scale for the development of the microstructure must be calibrated with experimental data for each new cement mixture. In addition, the rules used in the model do not describe the whole of the hydration process, with several shortcomings identified. Finally, it should be noted that the model rules were calibrated for given a pixel size, and convergence problems have been reported to occur when the pixel size is reduced.

In response to the limitations of CEMHYD3D model Bullard (2007a, 2007b) developed a new stochastic simulation model called HydratiCA, based on more fundamental principles of the kinetics of cement hydration of each particle. This model simulates explicitly dissolution and growth of mineral phases, the diffusion of mobile particles in the solution, the reactions between the particles in solution or on solid surfaces, and nucleation of new phases. Thus, this model allows to make better predictions of the evolution kinetics of the hydration and the microstructural development depending on the chemical composition and temperature of mixing than other existing models. However, this level of detail and precision makes this approach computationally heavy. (Thomas *et al.*, 2011).

Recently a new model was created, based on the model originally developed by Jennings and Johnson (1986) called μic (Bishnoi and Scrivener, 2009, Bishnoi, 2008). This model is based on the growth of multiple layers of spherical particles and the interconnections between the different particles to represent the evolution of the microstructure of the cement paste. This model provides a new implementation of the vector approach of Jennings and Johnson (1986) model by overcoming some of the limitations. As the calculation of the distance or overlap between the particles can be computationally intensive, in previous implementations, made by Jennings and Johnson (1986), these interactions were not taken into account, which severely affected the performance of the models. However, the new libraries developed for μic model allow it to simulate the hydration of millions of cement particles needed to realistically represent the particle size distributions found in ordinary cements, taking into account the neighbourhood of each particle (Thomas *et al.*, 2011). A typical example of the microstructure of the aspect μic model is presented in Figure 7.7.

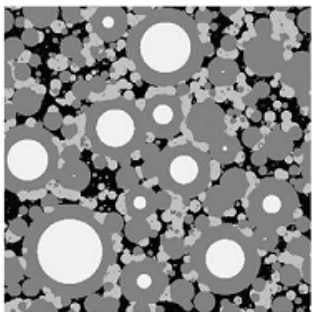

Figure 7.7. Cut of a microstructure of μic model of a cement paste 80% hydrated with C_3S grayscale, followed by CH and CSH and pores in black (Bishnoi and Scrivener, 2009).

However, it is important to note that the μic model presented some limitations, such as: represents the C-S-H product as a homogeneous layer over the cement particles (Do, 2013); no direct consideration of the chemical solution that provides the driving thermodynamic force; and no direct consideration of the transport phenomena such as diffusion (Thomas *et al.*, 2011). These limitations have direct influence on the distribution of the hydration products and thus on the microstructure evolution. Despite these limitations, and because of its high speed of calculation and flexibility, μic allows the simulation of systems with a large range of cement particles sizes, including non-reactive fines and considering very specific hydration mechanisms, such as a nucleation phase in particles of another (Dolado and van Breugel, 2011).

7.3. Validation of cement paste simulation model with EMM-ARM results

As mentioned in the introduction of these Chapter, due to the lack of experimental data of the mechanical properties during the whole hydration process the results estimated by the existing microstructural models capable of simulating the stiffness of cement-based materials are still lacking validation. Therefore, in this subsection the unprecedented information obtained with EMM-ARM results will be explored to validate the results obtained with a microstructural simulation model.

From the literature review presented before the modelling platform μic was chosen to simulate the cement paste microstructure evolution along the cement hydration since was identified as one of the most advance models. Additionally, these model is under constant evolution and the author had the opportunity to work in the research centre that has developed this model (Laboratory of Construction Materials (LMC) at EPFL). However, μic platform is not able to directly estimate the stiffness of the cement pastes. To perform this task, the microstructure needs to be modelled in a finite elements software and the correct mechanical properties of each individual phase present in the microstructure of the cement paste needs to be provided. Thus, this subchapter was divided in into two parts: (*i*) simulation of cement hydration to generate the microstructure of cement paste; (*ii*) numerical modelling of the microstructure to estimate the cement paste stiffness. In the end the simulations are compared with the EMM-ARM results.

7.3.1. Cement microstructure simulation

The modelling platform μic was used to simulate the hydration and the resulting three-dimensional microstructure of a cement paste. The advantage of using microstructures generated by μic is that it simulates the processes that lead to the development of the solid skeleton and is capable of generating quite realistic representations of microstructures (Bishnoi and Scrivener, 2009). Additionally, as μic uses a vector approach, the generated microstructures do not suffer from a resolution limit.

In order to simplify the complex problem of cement hydration, a cement with high content of alite (C_3S) was chosen. The chosen cement was a white cement with composition shown in

Table 7.1. Due to the high percentage of alite (C_3S) and belite (C_2S) (86.89% of the total weigh), and to the fact that the other components have a low impact on the final microstructure of the cement paste, this cement was model as an equivalent cement with composition shown in Table 7.1.

Table 7.1. Composition of the white cement selected to model.

Component	*White cement*	*Equivalent white cement*
C_3S [%]	66.89	76.98
C_2S [%]	20.00	23.02
C_3A [%]	3.51	0
C_4AF [%]	1.00	0
Free lime [%]	0.31	0

The cement paste had a water to cement ratio of 0.40 (named as W0.40). In the simulation, spherical particles of cement grains were placed in a cubic computational volume (CV) with 100 μm side having periodic boundaries, using random parking. The particle size distribution used for cement is shown in Figure 7.8.

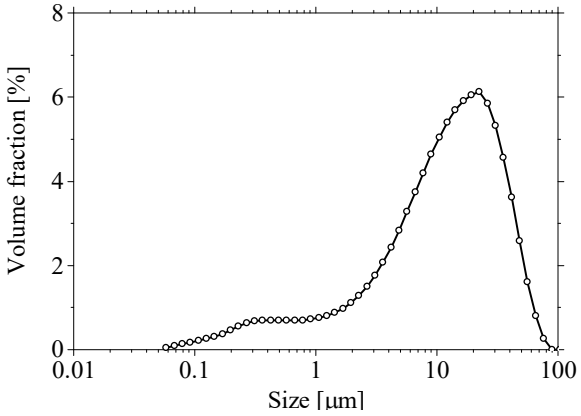

Figure 7.8. Particle size distribution used for cement grains.

In order to obtain a representative volume element (Do, 2013) both for hydration and mechanical simulations, the largest unhydrated cement particle was chosen to be 1.5 times smaller than the CV. The diameter of the smallest particle was 0.4 μm. The modelling strategy used was similar to the one used in the work of Do (2013). All the reactions (equations (7.2) and (7.3)) of the cement hydration were controlled using Avrami equation (7.4).

$$C_3S + 5.3H_2O \rightarrow 1.0\ HD\,CSH + 0.57\ LD\,CSH + 0.593\,CH \quad (7.2)$$

$$C_2S + 4.3H_2O \rightarrow 2.166\ HD\,CSH + 0.189\,CH \quad (7.3)$$

$$f = 1 - e^{-k_1 \cdot t^n} \quad (7.4)$$

where k_1 is a rate constant, f is the fraction of material reacted as a function of time, t and n is the Avrami exponent that depends upon the nucleation and growth mechanism.

Two models of particles were used, one for the cement particles and other of the Portlandite crystals (CH) as shown in Figure 7.9. The cement particle model was a three-layer model with at its centre the anhydrous cement. The two layers of the two different types of calcium silicate hydrate (C-S-H) (high density or inner and low density or outer) growth from its surface. The high density C-S-H (HD CSH) was assumed to grow inwards filling the space left by the anhydrous cement. As opposite the low density C-S-H (LD CSH) grew outwards from the surface of the particle. However, assuming the LD CSH as a homogeneous layer grown on the cement particles is unrealistic since the product is a heterogeneous material composed of layers. Additionally, the LD CSH may grow unevenly into the pore-space and build a fine pore network even at quite young ages (Do, 2013). Therefore, the packing density of the LD CSH was assumed to increase with hydration to simulate the effect of the increase on the number of C-S-H needles that start to pack (Do, 2013, Bishnoi and Scrivener, 2009). The CH particle was assumed to precipitate on the available space in the cement paste.

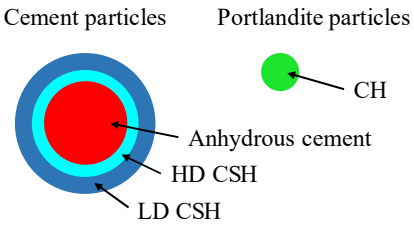

Figure 7.9. Particles model used in the simulations.

The parameters on Avrami equation and on the densification rate of the LD CSH were changed to fit the degree of reaction obtained to experimental results from calorimetry and ^{1}H NMR obtained in the work of Muller (2014). The hydration simulation was performed in steps of 1

hour until 100 hours of hydration and then in steps of 10 hours for more 560 hours. The final comparison obtained with the parameters of Table 7.2 can be observed in Figure 7.10.

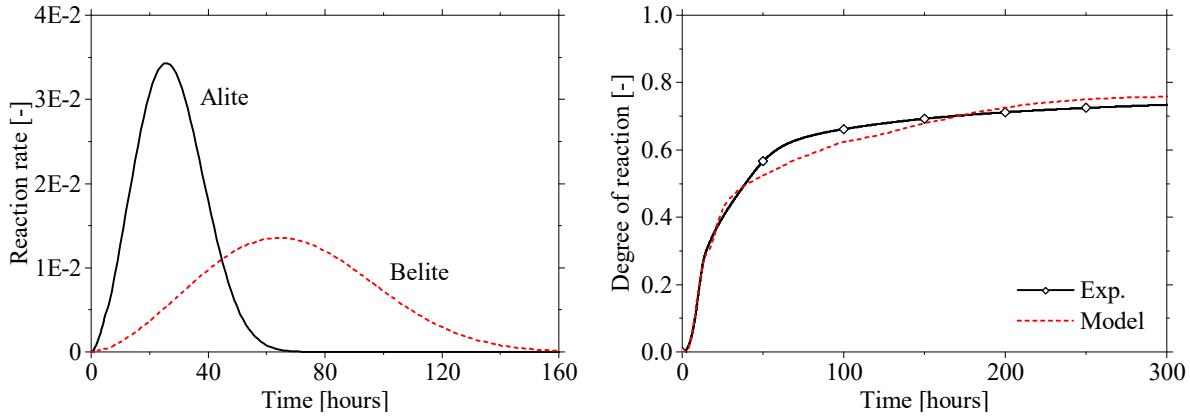

a) b)

Figure 7.10. a) Reaction rates of each hydration reaction; b) Comparison between the degree of reaction of the model and the one obtained through calorimetry and ^{1}H NMR.

Table 7.2. Parameters obtained from the overall cement hydration degree of reaction.

Parameter	C_3S	C_2S
k_1 (h^{-n})	1.40×10^{-4}	1.25×10^{-5}
n	2.6	2.6
t_0 (h)	0	0
α_0	0	0
$t_{1/2}$ (h)	6	-
$k_{den\ outer\ C\text{-}S\text{-}H}$ ($g/cm^3/h$)	1.0×10^{-4}	-
$\rho_{min\ outer\ C\text{-}S\text{-}H}$ (g/cm^3)	0.56	-
$\rho_{max\ outer\ C\text{-}S\text{-}H}$ (g/cm^3)	1.70	-
Vertical grow rate (μm/h)	0.085	-

As can be observed the overall reaction degree model fitted quite well the experimental measurements, despite some differences obtained in the post peak stage, as seen in Figure 7.10b. These differences could be related mainly to the use of the equivalent cement (with only the alite and belite components) and to the fact that the mechanism of cement hydration during this phase is not properly modeled in μic due to the use of an inadequate model for the LD CSH.

The resulting microstructure was generated with a resolution of 0.666 μm and is presented in Figures 7.11 and 7.12.

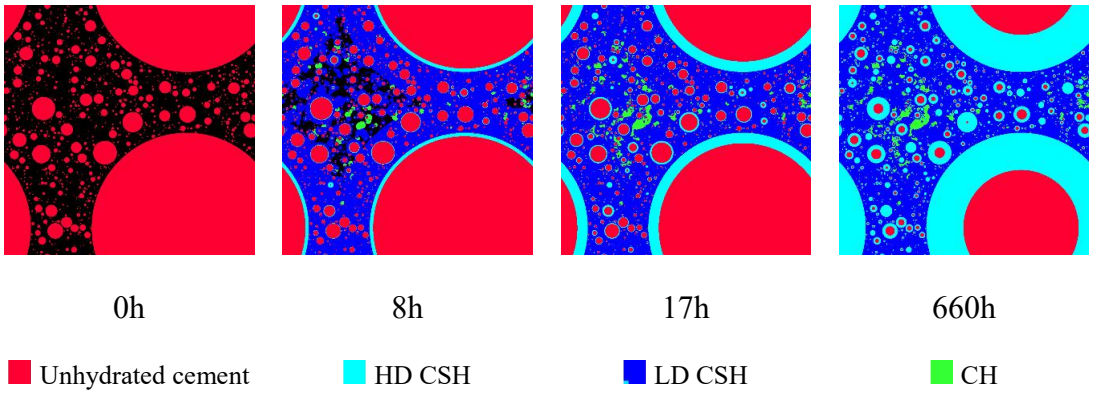

Figure 7.11. Evolution of the microstructure during the cement hydration.

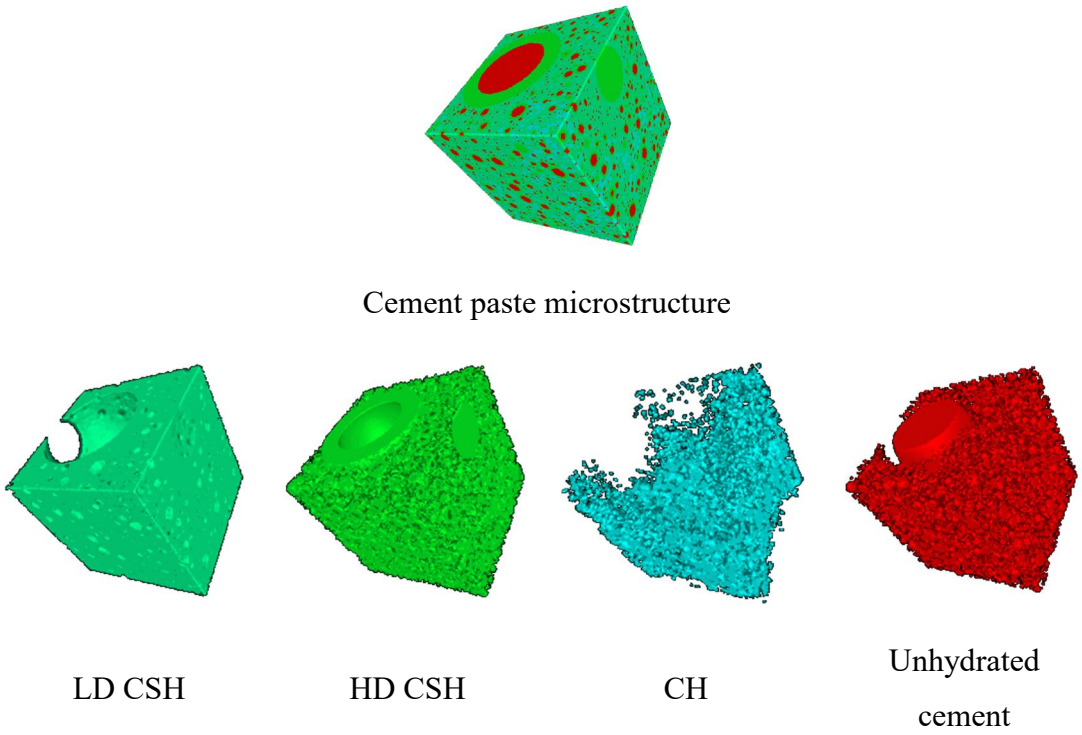

Figure 7.12. Cement paste microstructure after 100 hours of cement hydration.

From the evolution of the microstructure one can state that, despite small differences in the overall degree of reaction the microstructure of the cement paste seams feasible.

7.3.1. Stiffness modelling of the cement paste

After obtaining the cement microstructure along hydration, the elastic properties of the composite material can be estimated. There are several methods to perform this estimation that

can be separated in two main groups: analytical homogenization methods; and numerical modelling of the microstructure (e.g. through the finite element method – FEM) (Chamrová, 2010). The first approach is the most commonly used since the majority of the cement hydration models only give information about abundance of each phase in the system (Pichler *et al.*, 2007, Sanahuja *et al.*, 2007a). However, μic platform is capable of simulating the evolution of the microstructure of cement paste. Therefore, based on the richness of availability of data within this thesis, the second approach was used.

To perform the numerical modelling of the microstructure of cement paste, a new platform called AMIE (Automated Mechanics for Integrated Experiments) was used (Bordas *et al.*, 2007, Dunant *et al.*, 2007, Dunant and Scrivener, 2010, Dunant *et al.*, 2013). This platform, developed by Cyrille Dunant at LMC, is capable of automatically generating a finite element mesh of the cement microstructure based on the results provided by μic platform. The intrinsic elastic properties of the individual phases used in these simulations were taken from the literature and are listed in Table 7.3. From such table, it is possible to infer that almost all the individual phases of the cement paste have well defined stiffness values, except for the case of the LD CSH, for which a large range of variation can be observed. Furthermore, the LD CSH is simulated μic as an equivalent homogeneous material that densifies along the cement hydration. These issues make it necessary to characterize the evolution of the stiffness of the homogeneous LD CSH along the cement hydration.

Table 7.3. Intrinsic elastic properties of the individual phases of the cement paste (Manzano *et al.*, 2009).

Phase	*Young's modulus (GPa)*	*Poisson ratio (ν)*
Anhydrous cement	138.0	0.300
Portlandite	35.4	0.300
HD C-S-H	32.0	0.250
LD C-S-H	19 to 45	0.250
Water-filled porosity	0.0001	0.499

Aware of this information-gap a back analysis was made to fit the simulated stiffness of the cement paste to the experimental data from EMM-ARM (obtained previously in section 5.3.2), and get the evolution of the stiffness of the equivalent homogeneous LD CSH along the cement hydration. The back-analysis was made through trial-and-error in only 15 points at the ages of 1×10^{-7}, 5, 10, 15, 20, 30, 40, 50, 60, 70, 80, 90, 100, 110 and 120 hours due to the high

computational cost involved in the cement paste stiffness simulation. The analysis was started with a constant value to the LD CSH stiffness of 32 GPa (similar to the HD CSH) and each point was individually fitted to the experimental value. Figure 7.13 shows the results of the simulated stiffness and the LD C-S-H stiffness evolution.

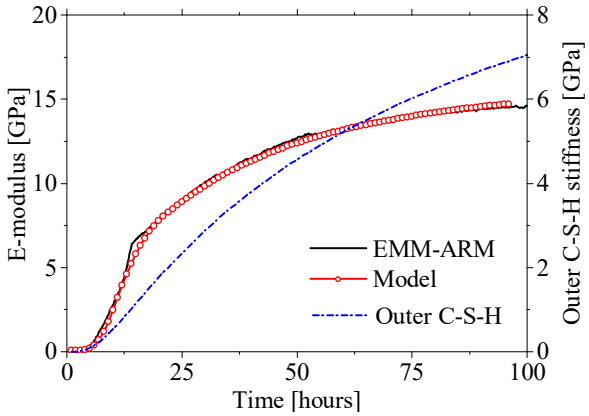

Figure 7.13. Evolution of the outer C-S-H stiffness.

After the quantification of the LD CSH stiffness through the back-fitting process, this evolution was correlated with the LD CSH porosity evolution. However, since the LD CSH porosity is not modelled in μic, to perform the correlation the porosity was obtained from ^{1}H NMR results (Muller, 2014) (Figure 7.14a). Figure 7.14b shows the relation between the porosity and the stiffness of the LD CSH obtained. Additionally, results from homogenization of the LD CSH are shown in the figure. The homogenization of the LD CSH was performed by Cyrille Dunant using by using a self-consistent scheme (SCS) (Sanahuja *et al.*, 2007b, Pichler *et al.*, 2009, Dunant and Granja, 2015) and considering three different scenarios: (*i*) undrained conditions (U-SCS), (*ii*) drained conditions and considering needle-like inclusions (D-SCS needles) and (*iii*) drained conditions and considering sphere-like inclusions (D-SCS spheres) (see Pichler *et al.* (2009) for more details). The inclusions were assumed to have E = 54 GPa and υ = 0.3. The obtained results indicate that the LD CSD behaves similarly to the estimation based on drained conditions (regardless of the shape considered for the inclusions) as can be observed in the figure. Furthermore, for porosities higher than 0.6, the observed behaviour seems to be between the estimations based sphere-like and needle-like inclusions. The percolation threshold of the LD CSH was observed to be at ~0.70 of porosity.

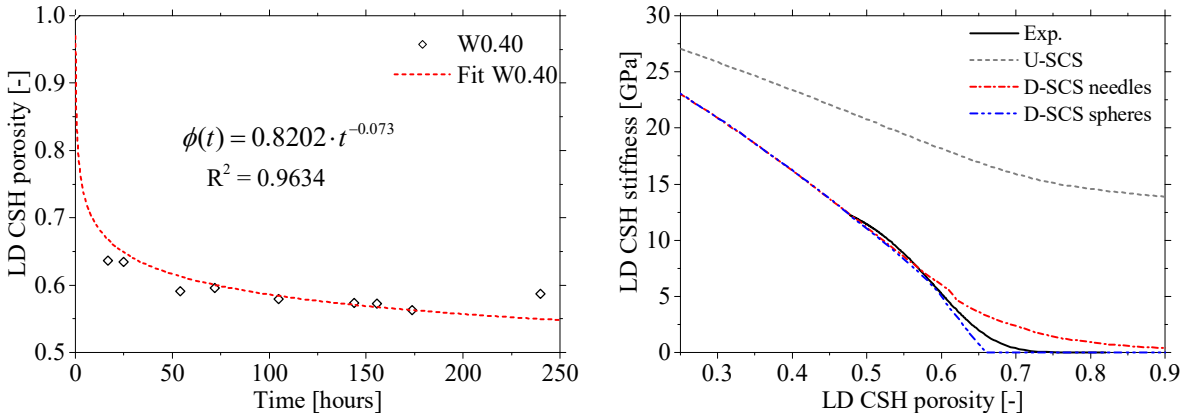

a) b)

Figure 7.14. a) Evolution of the LD C-S-H porosity; b) Correlation between LD C-S-H porosity and stiffness.

7.4. Blind simulations of the E-modulus of cement pastes

To confirm that the above assumption of correlation between LD CSH porosity and stiffness (obtained through back-analysis) is valid, two additional cement pastes were simulated (W0.32 and W0.48). These two cement pastes were composed by the same cement but with two different water to cement ratios: 0.32 and 0.48 (termed as W0.32 and W0.48, respectively). All the parameters used to simulate the microstructure of the cement paste were kept. The comparisons of the overall degree of reaction along the curing time obtained from the model, together with the information obtained experimentally, are shown in Figure 7.17a. As can be observed the evolutions obtained by the model have differences when compared to the experimental values mainly between the ages of 25 to 150 hours. These differences, as already discussed above for the W0.40 cement paste, could be related to the simplifications made, mainly in the cement composition and in the nature of the LD CSH. However, despite these simplifications the simulated microstructure seems feasible as can be observed in Figures 7.15 and 7.16.

a) b)

Figure 7.15. 3D microstructure 100 hours of cement hydration: a) W0.32 b) W0.48.

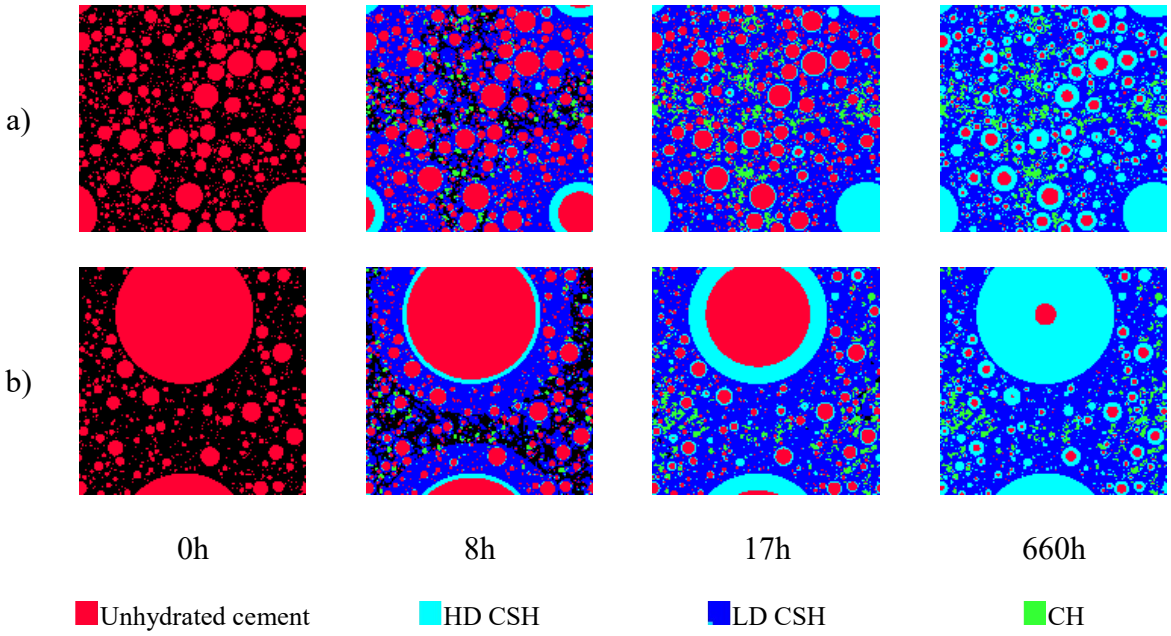

Figure 7.16. Evolution of the microstructure during the cement hydration: a) W0.32; b) W0.48.

In order to make the simulation of the cement paste E-modulus evolution along the cement hydration the same mechanical properties for the different phases as the ones presented in Table 7.3. For the LD CSH the relation between the porosity and stiffness presented in Figure 7.14b was used. However, from the results obtained by Muller (2014) it appears that the porosity evolution of the LD CSH for the different cement pastes changed as shown in Figure 7.17b. As can be observed the LD CSH porosity evolution for the different cement pastes is quite similar with only small differences in the cement paste W0.48 where the porosity is slightly lower. Thus, to estimate the LD CSH stiffness evolution the porosity obtained from ^{1}H NMR results

was used. The porosity evolutions were fitted by an analytical equation shown in the figure and the parameters obtained are given in Table 7.4.

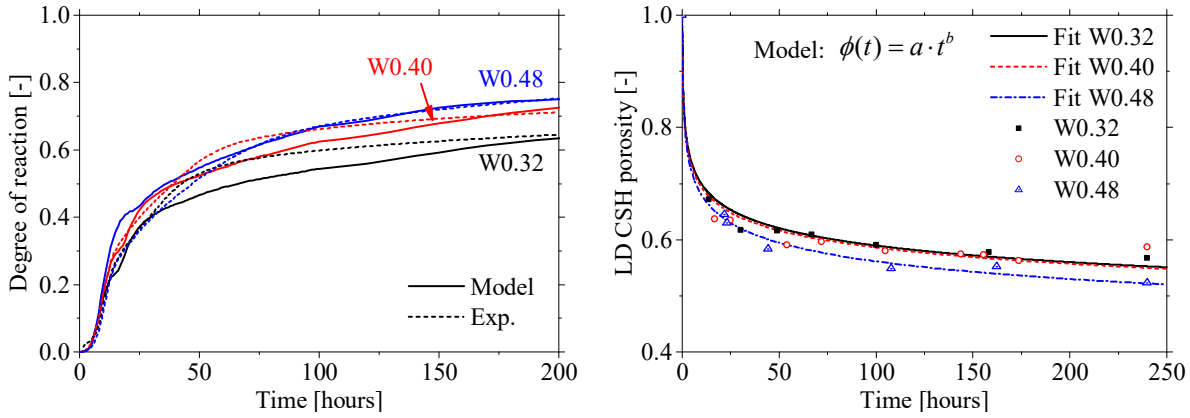

Figure 7.17. a) Comparison between the degree of reaction of the model and the one obtained through calorimetry and ^{1}H NMR; b) Evolution of the LD CSH porosity.

Table 7.4. LD CSH porosity fitting parameters.

Parameter	*W0.32*	*W0.40*	*W0.48*
a	0.8289	0.8202	0.8227
b	-0.074	-0.074	-0.083
R^2	0.9861	0.9634	0.9940

With the microstructure obtained from μic and the mechanical properties of all the components the stiffness of the two cement pastes (W0.32 and W0.48) where computed in AMIE without using any fitting parameter. The results of these new simulations are shown in Figure 7.18 together with the average evolution curve obtained from EMM-ARM tests in section 5.3.2. Firstly, one should note that the estimated E-modulus evolutions are in very good agreement with the experimental values. However, for the cement paste W0.32 the model estimated a significant stiffness value during the dormant period (t < 4 hours), well above the negligible stiffness that would be expectable at such stage. This problem may be related to the lack of resolution of the control volume under study (it was of 0.666 μm in this case), since the W0.32 is densest cement paste tested. In fact, the decrease in the distance between particles can lead to artificial connections between the anhydrous cement particles when the microstructure of the cement paste is not generated with enough resolution. Therefore, this problem can be solved by performing simulations with higher resolution than the 0.666 μm used in the current

simulations. However due to lack of computation power the it was not feasible to perform the simulation with higher resolution. Nevertheless, the results seem to indicate that the back-analysis procedure has brought a very reasonable set of values for LD CSH stiffness to be used in the prediction of the overall stiffness of cement paste.

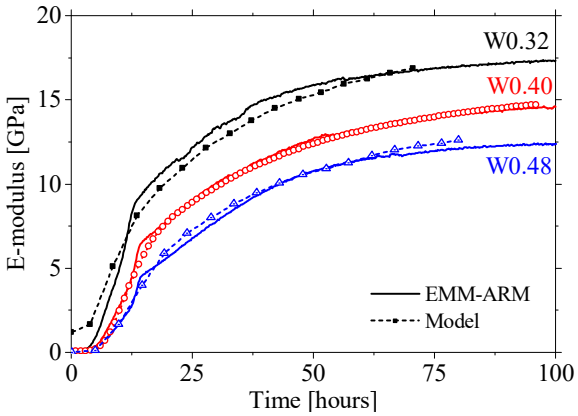

Figure 7.18. Comparison between the experimental results and numerical simulation of the cement pastes E-modulus.

Chapter 8

Conclusions

8.1. Overview

The aim of this thesis has been centred in providing the technical and scientific communities with a tool based on EMM-ARM capable to provide real-time information along the whole cement hydration process about the elastic modulus of cement-based materials. In particular, it has sought to explore five research questions: (*i*) Is EMM-ARM metrologically robust? (*ii*) What are the limitations of EMM-ARM? (*iii*) Can the quality of EMM-ARM results be improved by the application of new geometries/mould materials, as well as different modal identification techniques? (*iv*) Can EMM-ARM be implemented and applied in the construction industry as a quality control and decision support tool (with specific standards)? (*v*) How can EMM-ARM be used to validate/improve the microstructural simulation models of the cement-based materials mechanical properties?

This Chapter addresses the five research questions raised previously by synthesizing the main findings derived from the analysis of the experimental and numerical results, which were

thoroughly reported in Chapters from 3 to 7. This final Chapter proceeds as follows. First, the main findings related to each of the five research questions are outlined. Then, additional developments that transcend the research questions are described. Finally, the limitations of the study and suggestions for future research are presented.

8.2. Discussion of findings

(i) Is EMM-ARM metrologically robust?

From all the research questions raised in this thesis the most important conclusion to be found is probably the answer to this rather broad research question. Prior to this thesis, the EMM-ARM was in its infancy with only a pilot experiment performed in concrete and a few of them applied to cement paste. Therefore, a comprehensive validation of experimental technique was needed to prove the robustness and validity of the results. This issue is addressed mainly in Chapter 5, with also contributions for these subject in Chapters 3, 4 and 6.

The initial approach consisted in comparing EMM-ARM results with the results from other competing experimental methods. The inter-validation of the different experimental techniques, including the EMM-ARM, was initially made in the scope of concrete testing. For a more robust comparison, the study was made within a scope of an international collaboration with two research centres: the *Institut Français des Sciences et Technologies des Transports, de l'Aménagement et des Réseaux* (IFSTTAR) and the *Université libre de Bruxelles* (ULB). Additionally to the EMM-ARM technique, eight different techniques have been implemented in the three laboratories: four techniques of quasi-static loadings: (*i*) classical cyclic compression (CC) (all three labs), (*ii*) automated CC tests with BTJASPE (IFSTTAR), (*iii*) automated classical CC (ACC) (IFSTTAR), (*iv*) automated CC tests with a TSTM (ULB); and four techniques of high frequency loadings: three classical UPV measurements with PunditLab (UM), FreshCon (ULB), and BTPULS (IFSTTAR); and Smart Aggregates SMAGs (ULB). All the quasi-static methods yielded results that can be considered as similar to the classical CC measurements. Additionally, the EMM-ARM E-modulus estimations were within the range of the quasi-static methods, confirming its ability to quantify the quasi-static properties of concrete. The small differences that were observed were mostly attributed to the use of different mixing and casting protocols among the involved laboratories. From the EMM-ARM results, it

was also possible to infer that the method is able to estimate the E-modulus of concrete with good accuracy (with an average relation between the classical CC of 0.952) and high precision (with a standard deviation of the average relation between the classical CC of 0.0618), even when compared with the most advanced competing methods. These results enable the validation of the E-modulus estimations obtained with EMM-ARM, which has further proved to be simpler to implement and to be almost independent of operator-induced errors.

Besides the above-mentioned comparisons of EMM-ARM with other experimental techniques in the scope of concrete testing, further comparisons were made in the scope of cement paste testing. An extensive comparison was made between several experimental methodologies capable of quantifying the stiffness of cement pastes, such as: classical cyclic compression (CC), EMM-ARM, ultrasonic pulse velocity (UPV) bender-extender elements (BE) and penetration resistance (Vicat needle). The stiffness evolution results obtained by all the methods exhibited a considerably good agreement, which points to the mutual validation of the utilized methodologies. It is also worth mentioning that EMM-ARM and BE were able to detect the setting time with very good consistency in comparison with the Vicat test. The EMM-ARM was the method that proved to be the most advantageous by allowing continuous automatic monitoring of the E-modulus of the tested cement pastes, with collected data providing quantitative estimates of the elastic modulus.

During the inter-comparison study, it was found that there is a very good agreement of the final setting time obtained with Vicat with a final setting time computed by selecting the first point with 50% of the peak value of the first derivative of the E-modulus evolution obtained with EMM-ARM in both concrete and cement paste. Additionally, a good correlation was also found between these values and the final setting time computed from ultrasonic methods. Despite the limited number of experiments, the good coherence between the results seems to indicate that this relation is valid.

The experiments carried out with the EMM-ARM in different periods with the same concretes and cement pastes allowed to prove the good repeatability of the method. However, these tests were performed by the same operator. Therefore, an additional experimental program was carried out by a different operator, with no prior experience with EMM-ARM. The results obtained allowed to prove the good reproducibility of experimental method.

In the end of Chapter 5 the accuracy and sensitivity of the EMM-ARM E-modulus estimations are shown. It was observed that the EMM-ARM estimations are statistically very close to the values estimated by the classical CC method with differences lower than 1.9% and 4.5% in the versions for testing concrete and cement paste, respectively. Furthermore, a good precision of the EMM-ARM results was observed when compared to the CC method, with a 90% possibility of the EMM-ARM E-modulus estimations to be between 0.899 and 1.062 and between 0.769 and 1.137 of the CC results for the concrete and cement paste, respectively. From the sensitivity analyses to the input parameters, it was found that the most influential parameter in the accuracy of E-modulus estimations through EMM-ARM is the free span of the beams. It was also evident that the stiffness of supports has a relevant role in the estimations of E-modulus, particularly when smaller testing spans are selected. However, the use of the enhanced supports suggested in this thesis allows overcoming this support sensitivity issue.

(ii) What are the limitations of EMM-ARM?

The limitations of the EMM-ARM were raised in the Chapters 2, 3, 4 and 5 and overcome by evolving the experimental technique. To be able to perform the experiment correctly with the original prototype of the method the user needs to be aware of all the techniques used during the whole experimental procedure, as opposed to several commercial systems that frequently almost allow a 'one-button' operation framework (Brouwers *et al.*, 2011). Furthermore, the size, material and geometry of the original EMM-ARM testing beam (version to test concrete), posed practical limitations related to casting, handling and even disposing that made the practical application somewhat difficult as compared to traditionally shaped specimens (such as cubes or cylinders).

In addition to the aforementioned limitations, the method presented another potential problem related to the process of modal identification of the resonance frequency. The original implementations of EMM-ARM were conducted in laboratorial conditions, dully preceded by a careful selection of the location of the experiment itself. Preliminary experiments were made to ensure that the environmental vibrations behaved in average as a 'white noise' within 10 minute periods. If this premise were not valid, i.e if the vibrations of the beam were contaminated by noises with well-defined frequencies within the range of evolution of first natural frequency of the EMM-ARM test, the test frequency spectra would be affected by such

noises with significant potential to induce problems and errors in the frequency identification (Azenha *et al.*, 2010a). These contaminations bring additional challenges to the process of modal identification to such an extent that they might even disable the possibility of using of simple automatic identification algorithms. This is a major drawback when a generalized dissemination of EMM-ARM within the scientific and practising communities is considered. The process should preferably be fully automated and its proneness to environmental noise contamination should be negligible.

(iii) Can the quality of EMM-ARM results be improved by the application of new geometries/mould materials, as well as different modal identification techniques?

As mentioned previously, the original implementation of EMM-ARM had several weaknesses with high potential to decrease the quality and accuracy of the E-modulus estimations. Along Chapters 3 and 4, several changes to the EMM-ARM test apparatus and signal processing were studied with a remarkable success. Firstly, issues related to the testing mould used in the experiments were addressed. The most relevant changes to the testing mould involved the reduction of the beam's span and, in the case of the concrete testing, the change of the mould material from acrylic to PVC. These adaptations have increased the robustness of the method and made the casting, handling and disposal operations simpler. Additionally, a new support system was developed for the EMM-ARM beams, as to reduce dependence of results on the operator's skills/meticulousness, and facilitate the permanent assumption of infinitely rigid supports in the E-modulus estimation procedures.

Regarding the concrete testing version of EMM-ARM, the new supports allow to compensate misalignments between the horizontal supporting rods and limit to the gap between the supports and the beam to negligible values (i.e. with negligible effects on E-modulus estimates). A reusable mould for concrete testing was designed to enable easier systematic use of EMM-ARM, reducing uncertainties between tests related to the use of newly fabricated moulds, which inherently have slight variations in geometrical and mechanical characteristics. The possibility of omitting vertical connectors from the experimental setup was also studied, and no loss of composite behaviour was observed. Thus it became physically possible to introduce a vibratory needle in the EMM-ARM beam, during the casting operations to vibrate the concrete. This possibility was also assisted by the shift from a brittle mould material such as acrylic to the

more robust PVC that can endure direct contact with the vibrating needle without becoming damaged.

After the improvements of the testing mould, further developments were made towards the use of a more robust modal identification technique by introducing a very small forced vibration in the test beam. To perform the excitation, a custom low-cost electromagnetic actuator was developed, which is able to apply a small dynamic force (±6 mg) to the beam without any physical contact. This study concluded that the use of modal identification techniques with forced excitation improves the quality of the results when compared with those obtained using stochastic methods, without any evidence of damage to the bonds that are formed in the concrete microstructure.

Despite the several modifications to the test setup and data processing introduced during this research work, the method still has some potential limitations, such as:

- The assumption of perfect bond between the tested material and the surrounding mould in the E-modulus estimation framework demands that such condition is met during the entire testing period. In fact, some specific concretes with high autogeneous shrinkage (or expansion) potential may cause difficulties in EMM-ARM testing. It is however noted that this problem was only felt once throughout more than 50 EMM-ARM experiments during the entire research work, particularly when the long 'U-shaped' mould without connectors was used. Moreover, the newly proposed mould of reduced span clearly reduces the proneness to deboning problems in concrete testing. In cement paste testing, the proposed setup has never exhibited any debonding problems regardless of the tested material. Anyhow, when testing new mixes, or even other materials (e.g. not cement-based), prospect users of EMM-ARM should be aware of this potential issue. It should be easily detectable by a strong discontinuity in the identified resonance frequency at the instant of debonding.
- Additionally, the debonding between the mould and the material can also occur due to temperature variations during the EMM-ARM tests, since the thermal expansion coefficients of the mould and the cement-based materials. In fact, the thermal expansion coefficient of cement-based materials is usually around one fifth of the polymeric materials (Sellevold and Bjøntegaard, 2006, Nishi *et al.*, 1975). Nevertheless, even

though some EMM-ARM experiments have been carried out under non-isothermal conditions, relevant loss of the composite behaviour on the beam's cross-section was never observed.

- Additionally to the debonding problem, the restraint that the mould may pose to shrinkage/expansion or thermally induced volumetric changes can also lead to cracking of the materials inside the mould. However, in all the experiments performed with EMM-ARM this phenomenon was never observed.
- The reusability of the mould is still limited due to the material that is made (PVC). In fact, the PVC is a polymeric material that tends to suffer wear during a systematic use. However, after 8 experiments with the same reusable mould no relevant damages in the mould were observed. Nevertheless, this limitation can be overcome though the use of a more durable material such as Aluminium.

These potential limitations are no more than just implementations precautions. In fact, none of the limitations raised previously had impact in the laboratory and in-situ experiments performed during the research work conducted in this thesis.

(iv) Can EMM-ARM be implemented and applied in the construction industry as a quality control and decision support tool (with specific standards)?

As stated in the introduction of this thesis, there is a high demand for new advanced methods for monitoring the mechanical properties of concrete since early ages, as to support decision making (prestress application and framework removal) and quality control during construction of infrastructures. Due to the versatility, accuracy, ease of use, and quantitative nature of the EMM-ARM results proved along this thesis, two in-situ pilot tests were made in two different construction sites: a concrete prefabrication plant and a segmental prestressed concrete bridge. These tests allowed validating both the original and enhanced reusable versions of EMM-ARM in the context of in-situ environments. During these implementations, a fully automatic and user-friendly program was developed that allows the use of EMM-ARM by non-experienced operators. In view of the intent to match the temperature of EMM-ARM to the temperature of concrete in the vicinity of the prestressing heads of the segmental bridge, a temperature matched curing system has been developed and successfully demonstrated. It was finally possible to show the potential of EMM-ARM to serve as a support tool to decision-making in construction

sites by providing real-time information on the mechanical characteristics of the concrete. However, more tests need to be done to further validate this statement.

In addition to the in-situ application, the use of EMM-ARM to compute the apparent activation energy was investigated. Firstly, it was proved that with EMM-ARM permits testing at different isothermal curing temperatures within the range 10-40ºC, and the obtained results have shown the effect of the curing temperature on the kinetics of E-modulus evolution. Since the EMM-ARM is able to measure continuously the quasi-static E-modulus of the cementitious materials it gives unprecedentedly detailed information to compute the apparent activation energy of a mechanical property of the cementitious materials.

Still within Chapter 6, a new variant to EMM-ARM targeted for the measurement of viscoelastic properties of cement-based materials during the fresh state was proposed. Such variant is based on the measurement of the frequency of vibration of a cantilever steel bar partially embedded in the material under testing. During a pilot experiment in concrete it was demonstrated that this new method is capable of assessing significant behavioural evolutions during the dormant period with quite reasonable resolution. Additionally, the new method was used to measure the temperature dependency of the mechanical behaviour during the dormant period will significant success. However, the development of an analytical relationship between the resonance frequency of the steel bar and a specific concrete property (e.g. viscosity) has not yet been achieved.

Finally, Chapter 6 ends with an application of EMM-ARM to the study of structural epoxy adhesives used in FRP strengthening applications. The EMM-ARM technique revealed its capability in clearly identifying the hardening kinetics of epoxy adhesives, measuring the material setting time and the stiffness growth since very early ages. The results obtained by EMM-ARM were compared with the outcome of tensile tests. Quasi-static tests provided values of Young's modulus that were lower than the values collected by EMM-ARM at early ages. This difference can be explained by the significant visco-elastic behaviour that epoxy resin exhibits especially at very early ages. In fact, this difference significantly decreased as the epoxy adhesive hardened, becoming negligible at the age of 84 hours. With this application it was proved the EMM-ARM can be used to characterize a wide range of materials that

undergoes chemical hardening. Therefore, the method has potential in many industries beyond the construction.

(v) How can EMM-ARM be used to validate/improve the microstructural simulation models of the cement-based materials mechanical properties?

After the enhancement and validation of EMM-ARM, Chapter 7 extends this thesis to the use of the results of the quasi-static E-modulus evolution obtained by the EMM-ARM (with unprecedented richness of information) to validate and improve a microstructural simulation model of the cement-based materials mechanical properties. The selected modelling strategy was composed of two subtasks: (*i*) simulation of cement hydration to generate the microstructure of the cement paste; (*ii*) extraction of the E-modulus of the cement paste based on the microstructure generated and on the intrinsic stiffness of each component. The modelling platform μic was used to simulate the hydration of cement pastes and the resulting three-dimensional microstructure. After obtaining the cement microstructure along hydration, the elastic properties of the composite material were estimated by numerical modelling of the whole microstructure through the use of AMIE platform. This platform, developed by Cyrille Dunant at LMC, is capable of automatically generating a mesh of the cement microstructure based on the results provided by μic platform.

The properties of the Low Density CSH, specially their evolution along the hydration, are still unknown. Therefore, based on fitting the AMIE predictions with EMM-ARM results through back analysis, the relation between the bulk stiffness and porosity of the homogeneous LD CSH was obtained. This allowed to improve the modelling strategy by using a variable bulk stiffness of the LD CSH along the cement hydration. The relation between the bulk stiffness and porosity of the homogeneous LD CSH was validated through two blind simulations of two different cement pastes.

8.3. Additional developments

In addition to the findings that answer the research questions raised in the introduction of this thesis, the following conclusions were also found during the work conducted:

- During the international inter-laboratorial evaluation of experimental methods aimed to monitor the concrete stiffness, three classical techniques (PunditLab, FreshCon, BTPULS) were compared to a newly developed technique (SMAGs). The results have shown that the ultrasonic measurements are also automatic methods and they are good candidates for the monitoring of the stiffness of the concrete at very early age. However, they provided values of E-modulus that are higher than the values provided by the quasi-static or low-frequency tests at the time of the concrete setting. This difference decreases as the concrete hardens. Their results show a clear effect of the loading rate on the E-modulus calculation compared to values obtained with quasi-static tests.

- Regarding the study to compare different experimental methods aimed to monitor the cement paste stiffness, it was found that the UPV method did not allow to monitor the cement paste since the earliest ages (i.e. since right after mixing), with probable causes associated with to the presence of air bubbles in the samples and to the high stiffness impedance between the transducers and the paste (Zhu *et al.*, 2011a).

- In addition to the use of EMM-ARM, this study also presented stiffness evaluation through bender-extender elements, which had already been applied to cement paste by Zhu *et al.* (2011a). The results obtained in this research work were consistent with such previous approach, confirming that BE sensors have a high level of performance in a wide frequency range, which enables the stiffness monitoring of cementitious materials from very early ages (often not possible with UPV). This is achieved given the possibility of adjusting the input frequency to optimize the amplitude of the received signal. The results obtained with BE also demonstrate a higher suitability of the use of S-waves in detriment to P-waves to monitor the setting process, due to their sensitivity towards structure changes, since the propagation of shear waves only occurs in the solid skeleton of the specimens.

8.4. Prospects for future developments

The work conducted within this thesis presented the enhancement of the EMM-ARM technique in pursuit of increased robustness. The present is devoted to the discussion of some of the remaining limitations, and indication of future prospects for further developments.

The newly proposed reusable mould for EMM-ARM experiments is made of a material (PVC) that is prone to damage and wear upon repeated use. Further research should be considered to improve mould reusability through the use of more durable materials such as aluminium. It should be pointed however that problems can arise due to the increased rigidity of the system.

The scope of this thesis was to improve the EMM-ARM in its ability to measure the cement-based materials E-modulus. Nevertheless, the work development led to the identification of an interesting property that also evolves during EMM-ARM tests: the damping. It is well known that the damping of a structure is directly related to the viscoelastic properties of the corresponding building material (concrete, in this case). This achievement opens a new research opportunity to use the EMM-ARM to monitor the evolution of the viscoelastic properties of cement-based materials. However due to the composite nature of the section and to the viscoelastic properties of the mould itself (either PVC or acrylic), the separation of each component of the final structural damping was impossible to archive in the scope of this thesis. Therefore, more work is needed in order to ensure the capacity to correctly perform this separation, which may be possibly assisted by the use of other mould materials that have less influential viscoelastic properties (e.g. steel). Additionally, it must be taken into account that the relationship between the structural damping and viscoelastic properties is still a controversial issue in the cement-based materials science. Hence future work should be definitely considered in such concern.

The effect of the stress or strain rate on the elastic modulus of the cement-based materials was observed in this thesis by performing experimental tests at low and high frequency rates. However, the effective strain or stress rate of each experimental technique was not accessed due to the high complexity of such task. Therefore, further experimentations are also needed to quantify accurately these effects on the evolution of the elastic modulus, especially in what concerns the EMM-ARM technique.

This research work has proposed a methodology for estimation of the final setting time of cement-based materials based on the identification of the instant at which the derivate of the EMM-ARM E-modulus reaches 50% of its peak. It was found that the estimated final setting time was quite similar to the one obtained through penetration testing with the Vicat needle. Nonetheless, the number of experiments that pointed the validity of this methodology is

considered insufficient to consider it full validated. Therefore, it is considered that further experimental study for validation should be carried out.

The EMM-ARM was originally devised for study cement-based materials. The work of this thesis allowed to prove the validity of extending EMM-ARM to study structural epoxy adhesives. The results obtained proved the versatility and robustness of EMM-ARM to measure continuously the quasi-static elastic modulus of such materials since the fresh state with no human interaction and very low operator decency on the results. These facts have opened a window to use the method for measure different hardening materials, even outside the scope of construction materials. The breath of new testing possibilities is quite large, indeed.

Even though some efforts have been made in this thesis to disseminate the EMM-ARM among the scientific and practical communities the method is still fairly unknown. Thus a further international dissemination of the method is needed through its use in international benchmarking where various experimental techniques are used by several qualified international organizations (scientific or practical). These disseminations will allow additionally to validate even more the results obtained with the EMM-ARM technique. In this concern, efforts are being made in the context of the international Round Robin Test series (RRT^{+}) promoted by COST Action TU1404. Furthermore, a proposal for a standard for the elastic modulus measurement with the EMM-ARM needs to be written to allow the practical community to use the technique.

Finally, this thesis has demonstrated how the EMM-ARM results can be used to help the development/validation of microstructural simulation models of cement-based materials. In this study, a relationship between the porosity and bulk stiffness of the LD CSH was obtained. However, the relationship still needs further validation by simulating the elastic modulus of other cement paste mixtures. Additional research is also needed to investigate the identified problem of the lack of resolution of the microstructural numerical model of dense cement pastes. As a final prospect for future development, the possibility validating/development of the homogenization theories or meso-structural simulation models to estimate the concrete properties based on the equivalent cement paste with the EMM-ARM results for concrete and cement pastes should be considered.

This page intentionally left blank

References

Abo-Qudais, S. A. (2005). Effect of concrete mixing parameters on propagation of ultrasonic waves. *Construction and Building Materials,* 19 (4)**,** 257-263.

Aguilar, R., Ramírez, E., Haach, V. G. and Pando, M. A. (2016). Vibration-based nondestructive testing as a practical tool for rapid concrete quality control. *Construction and Building Materials,* 104 181-190.

Amziane, S. (2006). Setting time determination of cementitious materials based on measurements of the hydraulic pressure variations. *Cement and Concrete Research,* 36 (2)**,** 295-304.

ASTM (1991). Standard Test Method for Pulse Velocity Through Concrete. *C597.* Annual Book of ASTM Standards, Volume: 04.02: American Society for Testing and Materials.

ASTM (1993). Standard Test Method for Tensile Properties of Plastics. *D638M-93.* Annual Book of ASTM Standards: American Society for Testing and Materials.

ASTM (2002). Standard Test Method for Fundamental Transverse, Longitudinal, and Torsional Resonant Frequencies of Concrete Specimens. *C215.* Annual Book of ASTM Standards, Volume: 04.02: American Society for Testing and Materials.

ASTM (2004). Standard Specification for Portland Cement. *C150.* Annual Book of ASTM Standards, Volume: 04.01: American Society for Testing and Materials.

ASTM (2006). Standard Test Method for Static Modulus of Elasticity and Poisson's Ratio of Concrete in Compression. *C469.* Annual Book of ASTM Standards, Volume: 04.02: American Society for Testing and Materials.

ASTM (2008). Standard Test Method for Time of Setting of Concrete Mixtures by Penetration Resistance. *C403.* Annual Book of ASTM Standards: American Society for Testing and Materials.

ASTM (2011). Standard Practice for Estimating Concrete Strength by the Maturity Method. *C1074 - 11.* Annual Book of ASTM Standards, Volume: 04.02: American Society for Testing and Materials.

ASTM (2015a). Standard Practice for Making and Curing Concrete Test Specimens in the Laboratory. *C192 / C192M.* Annual Book of ASTM Standards, Volume: 04.02: American Society for Testing and Materials.

ASTM (2015b). Standard Test Method for Measuring the P-Wave Speed and the Thickness of Concrete Plates Using the Impact-Echo Method. *C1383 - 15.* Book of Standards Volume: 04.02: American Society for Testing and Materials.

Avrami, M. (1939). Kinetics of Phase Change. I General Theory. *The Journal of Chemical Physics,* 7 (12)**,** 1103-1112.

Azenha, M. (2009). Numerical Simulation of The Structural Behaviour of Concrete Since its Early Ages. PhD Thesis, Faculty of Engineering of the University of Porto.

Azenha, M., Faria, R., Magalhães, F., Ramos, L. and Cunha, Á. (2012a). Measurement of the E-modulus of cement pastes and mortars since casting, using a vibration based technique. *Materials and Structures,* 45 (1-2)**,** 81-92.

Azenha, M., Ferreira, C., Silva, J., Correia, A. G., Aguilar, R. and Ramos, L. F. (2011). Continuous stiffness monitoring of cemented sand through resonant frequency. *In: Dar-Hao Chen, Jia-Ruey Chang and Musharraf Zaman*, eds. Emerging Technologies for Material, Design, Rehabilitation, and Inspection of Roadway Pavements, 2011 Hunan, China. 174-183.

Azenha, M., Magalhães, F., Faria, R. and Cunha, Á. (2010a). Measurement of concrete E-modulus evolution since casting: A novel method based on ambient vibration. *Cement and Concrete Research,* 40 (7)**,** 1096-1105.

Azenha, M., Magalhães, F., Faria, R., Cunha, Á. and Ramos, L. (2010b). Um novo método para medição contínua do módulo de elasticidade de materiais cimentícios desde a betonagem. *BE2010 – Encontro Nacional Betão Estrutural.* Lisboa.

Azenha, M., Ramos, L. F., Aguilar, R. and Granja, J. L. (2012b). Continuous monitoring of concrete E-modulus since casting based on modal identification: A case study for in situ application. *Cement and Concrete Composites,* 34 (7)**,** 881-890.

Banfill, P. (2006). Rheology of fresh cement and concrete. *Rheology reviews,* 2006 61.

Basu, A. and Aydin, A. (2004). A method for normalization of Schmidt hammer rebound values. *International Journal of Rock Mechanics and Mining Sciences,* 41 (7)**,** 1211-1214.

Bayard, D. S. (1994). An algorithm for state-space frequency domain identification without windowing distortions. *Automatic Control, IEEE Transactions on,* 39 (9)**,** 1880-1885.

Beek, A. v. (2000). Dielectric properties of young concrete: non-destructive dielectric sensor for monitoring the strength development of young concrete. PhD Thesis, Delft University.

Beek, A. v., Breugel, K. V. and Hilhorst, M. A. (1999). Monitoring system for hardening concrete based on dielectric properties. *In:* Ravindra K. Dhir and Mukesh C. Limbachiya (eds.) *Creating with Concrete - Utilizing ready-mixed concrete and mortar.* Dundee, Scotland, United Kingdom.

Beek, A. v. and Hilhorst, M. A. (1999). Dielectric measurements to characterize the microstructural changes of young concrete. *Heron,* 44 (1)**,** 3-17.

Benedetti, A., Fernandes, P., Granja, J., Azenha, M. and Sena-Cruz, J. (2015). Effects of curing temperature on pull-out behavior and stiffness evolution of epoxy adhesives for NSM-FRP applications. *In: Caglar Goksu and Robert Widmann*, eds. SMAR2015 The Third Conference on Smart Monitoring, Assessment and Rehabilitation of Structures, 2015 Antalya, Turkey. 8.

Benedetti, A., Fernandes, P., Granja, J. L., Sena-Cruz, J. and Azenha, M. (2016). Influence of temperature on the curing of an epoxy adhesive and its influence on bond behaviour of NSM-CFRP systems. *Composites Part B: Engineering,* 89 219-229.

Benmeddour, F., Villain, G., Abraham, O. and Choinska, M. (2012). Development of an ultrasonic experimental device to characterise concrete for structural repair. *Construction and Building Materials,* 37 (0)**,** 934-942.

Bentur, A. (2003). Early Age Cracking in Cementitious Systems - Report of RILEM Technical Committee 181-EAS - Early age shrinkage induced stresses and cracking in cementitious systems.

Bentz, D. P. (1997a). Guide to using CEMHYD3D: a Three-Dimensional Cement Hydration and Microstructure Development Modeling Package. *In:* Technology Administration National Technical Information Service (NTIS), U.S. Department of Commerce (ed.).

Bentz, D. P. (1997b). Three-dimensional computer simulation of portland cement hydration and microstructure development. *Journal of the American Ceramic Society,* 80 (1)**,** 3-21.

Bentz, D. P. (2006). Modeling the influence of limestone filler on cement hydration using CEMHYD3D. *Cement & Concrete Composites,* 28 124–129.

Bentz, D. P. (2008). A review of early-age properties of cement-based materials. *Cement and Concrete Research,* 38 (2)**,** 196-204.

Bentz, D. P., Sato, T., de la Varga, I. and Weiss, W. J. (2012). Fine limestone additions to regulate setting in high volume fly ash mixtures. *Cement and Concrete Composites,* 34 (1)**,** 11-17.

Bentz, D. P. and Stutzman, P. E. (2006). Curing, Hydration, and Microstructure of Cement Paste. *ACI Materials Journal,* 103 (5)**,** 348-356.

Bernard, F. and Kamali-Bernard, S. (2012). Predicting the evolution of mechanical and diffusivity properties of cement pastes and mortars for various hydration degrees – A numerical simulation investigation. *Computational Materials Science,* 61 106-115.

Bernard, O., Ulm, F.-J. and Lemarchand, E. (2003). A multiscale micromechanics-hydration model for the early-age elastic properties of cement-based materials. *Cement and Concrete Research,* 33 (9)**,** 1293-1309.

Bischoff, P. and Perry, S. (1991). Compressive behaviour of concrete at high strain rates. *Materials and Structures,* 24 (6)**,** 425-450.

Bishnoi, S. (2008). Vector modelling of hydrating cement microstructure and kinetics. PhD Thesis, École Polytechnique Fédérale de Lausanne.

Bishnoi, S. and Scrivener, K. L. (2009). µic: A new platform for modelling the hydration of cements. *Cement and Concrete Research,* 39 (4)**,** 266-274.

Bordas, S., Nguyen, P. V., Dunant, C., Guidoum, A. and Nguyen-Dang, H. (2007). An extended finite element library. *International Journal for Numerical Methods in Engineering,* 71 (6)**,** 703-732.

Boulay, C. and Colson, A. (1979). Un extensomètre à béton éliminant l'influence des déformations transversales sur la mesure des déformations longitudinales. *Materials and Structures,* 14 (79)**,** 35-38.

Boulay, C., CRESPINI, M., CARETTE, J. and Staquet, S. (2012). Elastic properties of concrete at early age : monitoring of the e-modulus and the poisson's ratio with cyclic loadings and ultrasonic measurements. *In:* Structural Faults and Repair - 2012, 2012-07-03 2012 France. 11p.

Boulay, C., Merliot, E., Staquet, S. and Marzouk, O. (2010). Monitoring of the concrete setting with an automatic method. *In:* M. C. Forde (ed.) *Structural Faults & Repair.* Edinburgh: Engineering Technics press.

Boulay, C., Staquet, S., Azenha, M., Deraemaeker, A., Crespini, M., Carette, J., Granja, J., Delsaute, B., Dumoulin, C. and Karaiskos, G. (2013a). Monitoring Elastic Properties of Concrete since Very Early Age by means of Cyclic Loadings, Ultrasonic Measurements, Natural Resonant Frequency of Composite Beam (EMM-ARM) and with Smart Aggregates. *In:* J.G.M. Van Mier, G. Ruiz, C. Andrade, R.C. Yu and X.X. Zhang (eds.) *VIII International Conference on Fracture Mechanics of Concrete and Concrete Structures. FraMCoS-8.* Toledo, Spain.

Boulay, C., Staquet, S., Delsaute, B., Carette, J., Crespini, M., Yazoghli-Marzouk, O., Merliot, É. and Ramanich, S. (2013b). How to monitor the modulus of elasticity of concrete, automatically since the earliest age? *Materials and Structures,* 47 (1-2)**,** 141-155.

Boumiz, A., Vernet, C. and Tenoudji, F. C. (1996). Mechanical properties of cement pastes and mortars at early ages : Evolution with time and degree of hydration. *Advanced Cement Based Materials,* 3 (3-4)**,** 94-106.

Brignoli, E. G. M., Gotti, M. and Stokoe, K. H. (1996). Measurement of Shear Waves in Laboratory Specimens by Means of Piezoelectric Transducers. *Geotechnical Testing Journal (GTJ),* 19 (4)**,** 384–397.

Brinker, R., Ventura, C. E. and Andersen, P. (2001). Damping Estimation by Frequency Domain Decomposition. *The International Modal Analysis Conference.* Kissimmee, Florida: Society for Experimental Mechanics.

Brouwers, J., Schipper, R., Mijnsbergen, J., Lammers, M., Schaijk, R. v. and Wolf, M. v. d. (2011). ConSensor 2.0 Slimmer bouwen met beton. *Gelegenheid van de Betonvakdagen*

BSI (1997). Testing concrete - Recommendations for measurement of velocity of ultrasonic pulses in concrete. *BS 1881:203.* British Standards Institute.

Bullard, J. W. (2007a). Approximate Rate Constants for Nonideal Diffusion and Their Application in a Stochastic Model. *Journal of Physical Chemistry A,* 111 (11)**,** 2084-2092.

Bullard, J. W. (2007b). A three-dimensional microstructural model of reactions and transport in aqueous mineral systems. *Modelling and Simulation in Materials Science and Engineering,* 15 (7)**,** 711.

Bullard, J. W., D'Ambrosia, M., Grasley, Z., Hansen, W., Kidner, N., Lange, D., Lura, P., Mason, T. O., Moon, J., Rajabipour, F. and Sant, G. (2006). A Comparison of test methods for early-age behavior of cementitious materials. *In: J. Marchand, B. Bissonnette, R. Gagné, M. Jolin and F. Paradis*, eds. RILEM 2nd Symposium on Advances in Concrete through Science and Engineering, 2006 Quebec City, Canada. RILEM Publications SARL.

Caetano, E. (1992). Identificação experimental de parâmetros dinâmicos em sistemas estruturais. MSc, Faculdade de Engenharia da Universidade do Porto.

Cano-Barrita, P. d. J., Castellanos, F., Ramírez-Arellanes, S., Cosmes-López, M., Reyes-Estevez, L., Hernández-Arrazola, S. and Ramírez-Ortíz, A. (2015). Monitoring Compressive Strength of Concrete by Nuclear Magnetic Resonance, Ultrasound, and Rebound Hammer. *ACI Materials Journal,* 112 (1).

Carette, J. (2015). For a Better Understanding of Eco-Concrete Containing Blast-Furnace Slag and Limestone Filler: Mix Design Considerations, Early Age Characterisation, and Durability Issues. PhD Thesis, Université Libre de Bruxelles.

Carette, J., Dumoulin, C., Karaiskos, G., Staquet, S. and Deraemaeker, A. (2012). Monitoring of the E-modulus in early age concrete since setting time with embedded piezoelectric transducers. *In:* Conference: Structural Faults & Repair, 14th International Conference and Exhibition, 2012 Edinburgh, Scotland, UK. 1-7.

Carette, J. and Staquet, S. (2015). Monitoring the setting process of mortars by ultrasonic P and S-wave transmission velocity measurement. *Construction and Building Materials,* 94 196-208.

Carino, N. J. (2004a). Pullout Test. *In: V. M. Malhotra, Carino N. J.* (ed.) *Handbook on Nondestructive Testing of Concrete: Second Edition.* London: CRC Press.

Carino, N. J. (2004b). Stress Wave Propagation Methods. *In: V. M. Malhotra, Carino N. J.* (ed.) *Handbook on Nondestructive Testing of Concrete: Second Edition.* London: CRC Press.

Cauberghe, B. (2004). Applied frequency-domain system identification in the field of experimental and operational modal analysis. PhD Thesis, Vrije Universiteit Brussel.

CC (2016). Arduino Uno. Creative Commons.

CEB-FIP (2010). fib Model Code for Concrete Structures 2010 Lausanne, Switzerland, Ernst & Sohn.

CEN (2000). Testing hardened concrete - Part 1: Shape, dimensions and other requirements for specimens and moulds. *EN 12390-1.* Brussels, Belgium: European Committee for Standardization.

CEN (2004). Testing concrete. Determination of ultrasonic pulse velocity. *EN 12504-4.* Brussels, Belgium: European Committee for Standardization.

CEN (2005a). Methods of testing cement - Part 1: Determination of strength. *EN 196-1.* Brussels, Belgium: European Committee for Standardization.

CEN (2005b). Methods of testing cement - Part 3: Determination of setting times and soundness. *EN 196-3.* Brussels, Belgium: European Committee for Standardization.

CEN (2009). Testing hardened concrete - Part 3: Compressive strength of test specimens. *EN 12390-3.* Brussels, Belgium: European Committee for Standardization.

CEN (2010). Eurocode 2: Design of concrete structures - Part 1-1: General rules and rules for buildings. *EN 1992-1-1.* Brussels, Belgium: European Committee for Standardization.

CEN (2013). Testing hardened concrete - Part 13: Determination of secant modulus of elasticity in compression. *EN 12390-13.* Brussels, Belgium: European Committee for Standardization.

Chamrová, R. (2010). Modelling and Measurement of Elastic Properties of Hydrating Cement Paste. PhD Thesis, École Polytechnique Fédérale de Lausanne.

Chanvillard, G. and D'aloia, L. (1997). Concrete Strength Estimation at Early Ages: Modification of the Method of Equivalent Age. *Materials Journal,* 94 (6).

Chen, C.-W., Je-Nan, J. and Lee, G. (1993). Frequency Domain State-Space System Identification. *In:* American Control Conference, 1993, 2-4 June 1993 1993. 3057-3061.

Chengju, G. (1989). Maturity of Concrete: Method for Predicting Early-Stage Strength. *ACI Materials Journal,* 86 (4), 341-353.

Chopra, A. K. (1995). Dynamics of Structures: Theory and Application to Earthquake Engeneering, New Jersey, Electronic Publishing Services, Inc.

Chotard, T., Gimet-Breart, N., Smith, A., Fargeot, D., Bonnet, J. P. and Gault, C. (2001). Application of ultrasonic testing to describe the hydration of calcium aluminate cement at the early age. *Cement and Concrete Research,* 31 (3)**,** 405-412.

Christensen, B. J., Coverdale, T., Olson, R. A., Ford, S. J., Garboczi, E. J., Jennings, H. M. and Mason, T. O. (1994). Impedance Spectroscopy of Hydrating Cement-Based Materials: Measurement, Interpretation, and Application. *Journal of the American Ceramic Society,* 77 (11)**,** 2789-2804.

Christensen, B. J., Mason, T. O. and Jennings, H. M. (1992). Influence of Silica Fume on the Early Hydration of Portland Cements Using Impedance Spectroscopy. *Journal of the American Ceramic Society,* 75 (4)**,** 939-945.

Chung, C.-W., Suraneni, P., Popovics, J., Struble, L. and Weiss, W. J. (2013). Application of ultrasonic P-wave reflection to measure development of early-age cement-paste properties. *Materials and Structures,* 46 (6)**,** 987-997.

Chung, C.-W., Suraneni, P., Popovics, J. S. and Struble, L. J. (2012). Setting Time Measurement Using Ultrasonic Wave Reflection. *ACI Materials Journal,* 109 (1)**,** 109-118.

Clough, R. W. and Penzien, J. (1995). Dynamics of structures*,* Berkeley, USA, Computers & Structures, Inc.

Constantinides, G. and Ulm, F.-J. (2004). The effect of two types of C-S-H on the elasticity of cement-based materials: Results from nanoindentation and micromechanical modeling. *Cement and Concrete Research,* 34 (1)**,** 67-80.

Controls (2015). Ultrasonic pulse analyzer. *In:* Controls Group (ed.).

Cunha, A., Caetano, E. and Delgado, R. (2001). Dynamic Tests on Large Cable-Stayed Bridge. *Journal of Bridge Engineering,* 6 (1)**,** 54-62.

Czaderski, C., Martinelli, E., Michels, J. and Motavalli, M. (2012). Effect of curing conditions on strength development in an epoxy resin for structural strengthening. *Composites Part B: Engineering,* 43 (2)**,** 398-410.

D'Aloia, L. (2003). Early age kinetics: Activation energy, maturity and equivalent age. *In: A. Bentur* (ed.) *Early Age Cracking in Cementitious Systems - Report of RILEM Technical Committee 181-EAS - Early age shrinkage induced stresses and cracking in cementitious systems.* RILEM Publications SARL.

D'Aloia, L. and Chanvillard, G. (2002). Determining the “apparent” activation energy of concrete: Ea—numerical simulations of the heat of hydration of cement. *Cement and Concrete Research,* 32 (8)**,** 1277-1289.

D'Aloïa, L., Kada, H. L. B. and Lecrux, S. (2001). Resistance of the concrete in the work: the maturometry (in french) - CALIBE project. *In:* Paris Laboratoire central des ponts et chaussées, FRANCE (Revue) (ed.). Paris: Laboratoire central des ponts et chaussées, Paris, FRANCE.

Darquennes, A., Staquet, S., Delplancke-Ogletree, M.-P. and Espion, B. (2011). Effect of autogenous deformation on the cracking risk of slag cement concretes. *Cement and Concrete Composites,* 33 (3)**,** 368-379.

De Larrard, F., Hu, C., Sedran, T., Szitkar, J. C., Joly, M., Claux, F. and Derkx, F. (1997). A new rheometer for soft-to-fluid fresh concrete. *ACI Materials Journal,* 94 (3)**,** 234-243.

De Schutter, G. and Taerwe, L. (1995). General hydration model for portland cement and blast furnace slag cement. *Cement and Concrete Research,* 25 (3)**,** 593-604.

De Schutter, G. and Taerwe, L. (1996). Degree of hydration-based description of mechanical properties of early age concrete. *Materials and Structures,* 29 (6)**,** 335-344.

Dejian, S. and Xilin, L. (2008). Experimental study on dynamic compressive properties of microconcrete under different strain rate. *In: Hui Liangyu*, ed. The 14th World Conference on Earthquake Engineering 2008 Beijing, China.

Delsaute, B., Boulay, C., Granja, J., Carette, J., Azenha, M., Dumoulin, C., Karaiskos, G., Deraemaeker, A. and Staquet, S. (2016). Testing concrete E-modulus at very early ages through several techniques: an inter-laboratory comparison. *Strain,* January (2016)**,** 19.

Delsaute, B., Staquet, S. and Boulay, C. (2012). Monitoring of the creep and the relaxation behaviour of concrete since setting time. *SSCS 2012 (Numerical Modeling – Strategies for Sustainable Concrete Structures).*

Deniz, S. and Erdoğan, S. (2015). Prediction of Elastic Moduli Development of Cement Mortars Using Early Age Measurements. *Journal of Materials in Civil Engineering,* 27 (1)**,** 04014102.

Deraemaeker, A., Reynders, E., De Roeck, G. and Kullaa, J. (2008). Vibration-based structural health monitoring using output-only measurements under changing environment. *Mechanical Systems and Signal Processing,* 22 (1)**,** 34-56.

Diamond, S. (2004). The microstructure of cement paste and concrete—a visual primer. *Cement and Concrete Composites,* 26 (8)**,** 919-933.

Dishan, H. (1995). Phase error in fast Fourier transform analysis. *Mechanical Systems and Signal Processing,* 9 (2)**,** 113-118.

Do, Q. H. (2013). Modelling Properties of Cement Paste from Microstructure: Porosity, Mechanical Properties, Creep and Shrinkage. PhD Thesis, École Polytechnique Fédérale de Lausanne, Switzerland.

Dolado, J. S. and van Breugel, K. (2011). Recent advances in modeling for cementitious materials. *Cement and Concrete Research,* 41 (7)**,** 711-726.

Dotson, C. (2015). Fundamentals of dimensional metrology*,* Boston, USA, Cengage Learning.

Dumoulin, C., Karaiskos, G., Carette, J., Staquet, S. and Deraemaeker, A. (2012). Monitoring of the ultrasonic P-wave velocity in early-age concrete with embedded piezoelectric transducers. *Smart Materials and Structures,* 21 (4)**,** 047001.

Dunant, C. and Granja, J. (2015). Experimental C-S-H homogenization scheme. *In:* M. Wyrzykowski, F. Benboudjema, M. Azenha, S. Staquet and D. Schlicke (eds.) *TU1404 - 2nd workshop focus on Modeling of Cement Based Materials and Structures - Presentations ebook.*

Dunant, C., Vinh, P. N., Belgasmia, M., Bordas, S. and Guidoum, A. (2007). Architecture tradeoffs of integrating a mesh generator to partition of unity enriched object-oriented finite element software. *European Journal of Computational Mechanics,* 16 (2)**,** 237-258.

Dunant, C. F., Bary, B., Giorla, A. B., Péniguel, C., Sanahuja, J., Toulemonde, C., Tran, A.-B., Willot, F. and Yvonnet, J. (2013). A critical comparison of several numerical methods for computing effective properties of highly heterogeneous materials. *Advances in Engineering Software,* 58 1-12.

Dunant, C. F. and Scrivener, K. L. (2010). Micro-mechanical modelling of alkali–silica-reaction-induced degradation using the AMIE framework. *Cement and Concrete Research,* 40 (4)**,** 517-525.

Dunham, M. R., Rush, A. S. and Hanson, J. H. (2007). Effects of Induced Vibrations on Early Age Concrete. *Journal of Performance of Constructed Facilities,* 21 (3)**,** 179-184.

Dunn, D. J. (2004). Engineering and Structural Adhesives, iSmithers Rapra Publishing.

Ewins, D. J. (2000). Modal testing: theory, practice, and application, Research Studies Press.

Felber, A. J. (1993). Development of a hybrid bridge evaluation system. PhD Thesis, University of British Columbia.

Fernandes, J. F., Bittencourt, T. N. and Helene, P. (2011). Concrete subjected to vibrations in early-ages *Ibracon structures and materials,* 4 (4)**,** 592-609.

Fernandes, P., Granja, J., Sena-Cruz, J., Azenha, M. and Benedetti, A. (2014). A new methodology for assisting quality control of NSM-CFRP systems since very early ages. *In: Raafat El-Hacha, Ahmad Rteil, Amir Fam, Donna Chen, Fadi Oudah, Jian-Fei Chen, Kent Harris, Khaled Abdelrahman and Thomas Tannert*, eds. The 7th International Conference on FRP Composites in Civil Engineering, 2014 Vancouver, Canada. 6.

Fernandes, P., Granja, J. L., Benedetti, A., Sena-Cruz, J. and Azenha, M. (2015). Quality control and monitoring of NSM CFRP systems: E-modulus evolution of epoxy adhesive and its relation to the pull-out force. *Composites Part B: Engineering,* 75 (0)**,** 95-103.

Ferreira, C. M. (2008). The Use of Seismic Wave Velocities in the Measurement of Stiffness of a Residual Soil. Doctor in Civil Engineering, University of Porto.

Ferreira, C. M. (2009). The Use of Seismic Wave Velocities in the Measurement of Stiffness of a Residual Soil. PhD Thesis, Faculty of Engineering of the University of Porto.

Fischer, I., Pichler, B., Lach, E., Terner, C., Barraud, E. and Britz, F. (2014). Compressive strength of cement paste as a function of loading rate: Experiments and engineering mechanics analysis. *Cement and Concrete Research,* 58 186-200.

Fonseca, A. V. d., Ferreira, C. and Fahey, M. (2008). A Framework Interpreting Bender Element Tests, Combining Time-Domain and Frequency-Domain Methods. *Geotechnical Testing Journal,* 32 (2)**,** 1-17.

Gaede, K. (1941). Die Prüfung der Betonfestigkeit im Bauwerk (Testing of concrete strength in structures). *Der Bauingenieur.* in German.

Garboczi, E. J. and Bentz, D. P. (1992). Computer simulation of the diffusivity of cement-based materials. *Journal of Materials Science,* 27 2083-2092.

Garboczi, E. J. and Bentz, D. P. (2001). The effect of statistical fluctuation, finite size error, and digital resolution on the phase percolation and transport properties of the NIST cement hydration model. *Cement and Concrete Research,* 31 (10)**,** 1501-1514.

Garrault-Gauffinet, S. and Nonat, A. (1999). Experimental investigation of calcium silicate hydrate (C-S-H) nucleation. *Journal of Crystal Growth,* 200 (3–4)**,** 565-574.

Garrault-Gauffinet, S. and Nonat, A. (2001). Hydrated Layer Formation on Tricalcium and Dicalcium Silicate Surfaces: Experimental Study and Numerical Simulations. *Langmuir,* 17 (26)**,** 8131–8138.

Gigatec (2015). SMART BOX - Wireless sensor for concrete resistividade and temperature. *In:* Inc. Gigatec Scientific (ed.) *V15-01.* Ottawa, Ontario, Canada.

Gillham, J. K. (1986). Formation and properties of thermosetting and high Tg polymeric materials. *Polymer Engineering & Science,* 26 (20)**,** 1429-1433.

Giner, V. T., Ivorra, S., Baeza, F. J., Zornoza, E. and Ferrer, B. (2011). Silica fume admixture effect on the dynamic properties of concrete. *Construction and Building Materials,* 25 (8)**,** 3272-3277.

Goodwin, G. C. and Payne, R. L. (1977). Dynamic system identification : experiment design and data analysis*,* New York, USA, Elsevier Science.

Granja, J. and Azenha, M. (2015). Continuous monitoring of concrete mechanical properties since early age to support construction phasing. *In:* Mechanics and Physics of Creep, Shrinkage, and Durability of Concrete and Concrete Structures, 2015 Vienna, Austria.

Granja, J., Azenha, M., Ramos, L. F. and Aguilar, R. (2012). Avaliação experimental do módulo de elasticidade de materiais cimentícios desde as primeiras idades : aplicação laboratorial e in situ. *Betão Estrutural 2012.* Porto, Portugal: FEUP.

Granja, J., Azenha, M., Sousa, C. d. and Ferreira, C. (2014a). Comparison Between Different Experimental Techniques for Stiffness Monitoring of Cement Pastes. *Journal of Advanced Concrete Technology,* 12 (2)**,** 46-61.

Granja, J., Fernandes, P., Benedetti, A., Azenha, M. and Sena-Cruz, J. (2014b). Nova metodologia para o controlo de qualidade de sistemas NSM-CFRP durante a cura do adesivo. *In:* 5as Jornadas Portuguesas de Engenharia de Estruturas, 2014b Lisbon, Portugal.

Granja, J. L. (2011). Experimental evaluation of the elastic modulus of cementitious materials at early ages (in Portuguese). MSc Thesis, University of Minho.

Granja, J. L. and Azenha, M. (2016). Towards a robust and versatile method for monitoring E-modulus of concrete since casting: enhancements and extensions of EMM-ARM. *Submitted to Cement and Concrete Composites*.

Granja, J. L., Fernandes, P., Benedetti, A., Azenha, M. and Sena-Cruz, J. (2015). Monitoring the early stiffness development in epoxy adhesives for structural strengthening. *International Journal of Adhesion and Adhesives,* 59 77–85.

Grant (2012). Concrete Maturity Meter - Squirrel Data Logger OQ610. *In:* Grant Instruments (ed.). Shepreth Cambridgeshire, United Kingdom.

Greening, P. D. and Nash, D. F. T. (2004). Frequency Domain Determination of G(0) Using Bender Elements. *Geotechnical Testing Journal,* 27 (3)**,** 288 - 294.

Greening, P. D., Nash, D. F. T., Benahmed, N., Ferreira, C. and Fonseca, A. V. d. (2003). Comparison of shear wave velocity measurements in different materials using time and frequency domain techniques. *3rd International Symposium on Deformation Characteristics of Geomaterials.* Lyon - França.

Gu, H., Song, G., Dhonde, H., Mo, Y. L. and Yan, S. (2006). Concrete early-age strength monitoring using embedded piezoelectric transducers. *Smart Materials and Structures,* 15 (6)**,** 1837-1845.

Guo, Z. G. and Sun, Z. (2012). Piezoelectric Impedance Based Elastic Modulus Monitoring for Concrete during Curing. *Applied Mechanics and Materials,* 166 969-973.

Haecker, C. J., Garboczi, E. J., Bullard, J. W., Bohn, R. B., Sun, Z., Shah, S. P. and Voigt, T. (2005). Modeling the linear elastic properties of Portland cement paste. *Cement and Concrete Research,* 35 (10)**,** 1948-1960.

Hain, M. and Wriggers, P. (2008). Numerical homogenization of hardened cement paste. *Computational Mechanics,* 42 (2)**,** 197-212.

Hanehara, S. and Yamada, K. (2008). Rheology and early age properties of cement systems. *Cement and Concrete Research,* 38 (2)**,** 175-195.

Hassan, A. M. T. and Jones, S. W. (2012). Non-destructive testing of ultra high performance fibre reinforced concrete (UHPFRC): A feasibility study for using ultrasonic and resonant frequency testing techniques. *Construction and Building Materials,* 35 361-367.

Hattel, J. H. and Thorborg, J. (2003). A numerical model for predicting the thermomechanical conditions during hydration of early-age concrete. *Applied Mathematical Modelling,* 27 (1)**,** 1-26.

He, J. and Fu, Z. F. (2001). Modal Analysis*,* Oxford, UK, Elsevier Science.

Hong, S. and Park, S.-K. (2015). Effect of vehicle-induced vibrations on early-age concrete during bridge widening. *Construction and Building Materials,* 77 179-186.

Hönig, A. (1991). Radiometry of compaction of fresh concrete in-situ. *In: H. W. Reinhardt* (ed.) *Proceedings of the International Workshop on Testing During Concrete Construction.* London: RILEM Proceedings PRO.

Hu, J. and Wang, K. (2011). Effect of coarse aggregate characteristics on concrete rheology. *Construction and Building Materials,* 25 (3)**,** 1196-1204.

Igarashi, S., Kawamura, M. and Watanabe, A. (2004). Analysis of cement pastes and mortars by a combination of backscatter-based SEM image analysis and calculations based on the Powers model. *Cement and Concrete Composites,* 26 (8)**,** 977-985.

ISO (2010). Testing of concrete - Part 10: Determination of static modulus of elasticity in compression. *1920-10.* Genève, Switzerland: International Organization for Standardization.

ISO (2012a). Plastics – Determination of tensile properties – Part 1: General principles. *527-1* Genève, Switzerland: International Organization for Standardization.

ISO (2012b). Plastics – Determination of tensile properties – Part 2: Test conditions for moulding and extrusion plastics. *527-2.* Genève, Switzerland: International Organization for Standardization.

ISO (2014). Testing of concrete – Part 7: Non-destructive tests on hardened concrete. *ISO 1920-7:2004.* Genève, Switzerland: International Organization for Standardization.

Jau, W.-C. and Yang, C.-T. (2010). Development of a modified concrete rheometer to measure the rheological behavior of conventional and self-consolidating concretes. *Cement and Concrete Composites,* 32 (6)**,** 450-460.

JCGM (2012). International Vocabulary of Metrology – Basic and General Concepts and Associated Terms (VIM 3rd edition). *JCGM,* 200.

Jennings, H. M. and Johnson, S. K. (1986). Simulation of Microstructure Development During the Hydration of a Cement Compound. *Journal of the American Ceramic Society,* 69 (11).

Jin, X. and Li, Z. (2001). Dynamic Property Determination for Early-Age Concrete. *ACI Materials Journal,* 98 (5)**,** 365-370.

Jones, R. (1949). A non-destructive method of testing concrete during hardening. *Concrete and Constructional Engineering,* 44 (4)**,** 127–128.

Juang, J.-N. (1994a). Applied System Identification*,* Englewood Cliffs, New Jersey, Prentice-Hall Inc.

Juang, J.-N. (1994b). Applied System Identification. Prentice Hall Englewood Cliffs*,* New Jersey, USA.

Juang, J. N. and Pappa, R. S. (1985). An eigensystem realization algorithm for modal parameter identification and model reduction. *Journal of Guidance, Control, and Dynamics,* 8 (5)**,** 620-627.

Juang, J. N. and Suzuki, H. (1988). An Eigensystem Realization Algorithm in Frequency Domain for Modal Parameter Identification. *Journal of Vibration, Acoustics, Stress, and Reliability in Design,* 110 (1)**,** 24-29.

Kamada, T., Uchida, S. and Rokugo, K. (2005). Nondestructive Evaluation of Setting and Hardening of Cement Paste Based on Ultrasonic Propagation Characteristics. *Journal of Advanced Concrete Technology,* 3 (3)**,** 343-353.

Kamali-Bernard, S. and Bernard, F. (2009). Effect of tensile cracking on diffusivity of mortar: 3D numerical modelling. *Computational Materials Science,* 47 (1)**,** 178-185.

Karaiskos, G., Deraemaeker, A., Aggelis, D. G. and Hemelrijck, D. V. (2015). Monitoring of concrete structures using the ultrasonic pulse velocity method. *Smart Materials and Structures,* 24 (11)**,** 113001.

Kim, J. H., Shah, S. P., Sun, Z. and Kwak, H.-G. (2009). Ultrasonic Wave Reflection and Resonant Frequency Measurements for Monitoring Early-Age Concrete. *Journal of Materials in Civil Engineering,* 21 (9)**,** 476-483.

Kim, S., Pakzad, S., Culler, D., Demmel, J., Fenves, G., Glaser, S. and Turon, M. (2007). Health Monitoring of Civil Infrastructures Using Wireless Sensor Networks. *Proceedings of the 6th International Conference on Information Processing in Sensor Networks (IPSN '07),* . Cambridge, MA: ACM Press.

Kishi, T., Lin, Z. and Lim, S. (2008). Early-age creep of fly ash, blast furnace slag, and expansive concretes. *Creep, Shrinkage and Durability Mechanics of Concrete and Concrete Structures, Two Volume Set.* Taylor & Francis.

Klausen, A. E., Kanstad, T. and Bjøntegaard, Ø. (2015). Updated Temperature-Stress Testing Machine (TSTM): Introductory Tests, Calculations, Verification, and Investigation of Variable Fly Ash Content. *In: Christian Hellmich, Bernhard Pichler and Johann Kollegger*, eds. 10th international conference on mechanics and physics of creep, shrinkage, and durability of concrete and concrete structures 2015 Vienna, Austria. ASCE, 724-732.

Kolluru, S. V., Popovics, J. S. and Shah, S. P. (2000). Determining elastic properties of concrete using vibrational resonance frequencies of standard test cylinders. *Cement Concrete and Aggregates,* 22 (2)**,** 81-89.

Kovler, K. (2006). Radon exhalation of hardening concrete: monitoring cement hydration and prediction of radon concentration in construction site. *Journal of Environmental Radioactivity,* 86 (3)**,** 354-366.

Kovler, K. and Roussel, N. (2011). Properties of fresh and hardened concrete. *Cement and Concrete Research,* 41 (7)**,** 775-792.

Krauß, M. and Hariri, K. (2006). Determination of initial degree of hydration for improvement of early-age properties of concrete using ultrasonic wave propagation. *Cement and Concrete Composites,* 28 (4)**,** 299-306.

Krüger, M., Grosse, C. U. and Lehmann, F. (2013). Automated Shear-Wave Techniques to Investigate the Setting and Hardening of Concrete in Through-Transmission. *In: Oğuz Güneş and Yılmaz Akkaya* (eds.) *Nondestructive Testing of Materials and Structures.* Springer Netherlands.

Kung, S. Y. (1978). A New Identification and Model Reduction Algorithm via Singular Value Decomposition. *12th Asilomar conference on circuits, systems and computers.* Pacific Grove, CA.

Larcher, N., Takarli, M., Angellier, N., Petit, C. and Sebbah, H. (2015). Towards a viscoelastic mechanical characterization of asphalt materials by ultrasonic measurements. *Materials and Structures,* 48 (5)**,** 1377-1388.

Lee, H. K., Lee, K. M., Kim, Y. H., Yim, H. and Bae, D. B. (2004). Ultrasonic in-situ monitoring of setting process of high-performance concrete. *Cement and Concrete Research,* 34 (4)**,** 631-640.

Lee, J.-S. and Santamarina, J. C. (2005). Bender Elements: Performance and Signal Interpretation. *Journal of Geotechnical and Geoenvironmental Engineering,* 131 (9)**,** 1063-1070.

Lee, K.-M., Kim, D.-S. and Kim, J.-S. (1997). Determination of dynamic Young's modulus of concrete at early ages by impact resonance test. *KSCE Journal of Civil Engineering,* 1 (1)**,** 11-18.

Li, H., Xiao, H.-g., Yuan, J. and Ou, J. (2004). Microstructure of cement mortar with nano-particles. *Composites Part B: Engineering,* 35 (2)**,** 185-189.

Li, Z., Qin, L. and Huang, S. (2009). Embedded Piezo-Transducer in Concrete for Property Diagnosis. *Journal of Materials in Civil Engineering,* 21 (11)**,** 643-647.

Liang, C., Sun, F. and Rogers, C. A. (1996). Electro-mechanical impedance modeling of active material systems. *Smart Materials and Structures,* 5 (2)**,** 171.

Liang, C., Sun, F. P. and Rogers, C. A. (1994). An Impedance Method for Dynamic Analysis of Active Material Systems. *Journal of Vibration and Acoustics,* 116 (1)**,** 120-128.

Liao, Y. and Wei, X. (2014). Penetration resistance and electrical resistivity of cement paste with superplasticizer. *Materials and Structures,* 47 (4)**,** 563-570.

Lim, Y. Y. and Soh, C. K. (2014). Towards more accurate numerical modeling of impedance based high frequency harmonic vibration. *Smart Materials and Structures,* 23 (3)**,** 035017.

Liu, S., Zhu, J., Seraj, S., Cano, R. and Juenger, M. (2014). Monitoring setting and hardening process of mortar and concrete using ultrasonic shear waves. *Construction and Building Materials,* 72 248-255.

LNEC (1993). Betões - Determinação do módulo de elasticidade em compressão. *E 397.* Lisbon, Portugal: Laboratório Nacional de Engenharia Civil.

Lootens, D., Jousset, P., Martinie, L., Roussel, N. and Flatt, R. J. (2009). Yield stress during setting of cement pastes from penetration tests. *Cement and Concrete Research,* 39 (5)**,** 401-408.

Lu, X., Sun, Q., Feng, W. and Tian, J. (2013). Evaluation of dynamic modulus of elasticity of concrete using impact-echo method. *Construction and Building Materials,* 47 231-239.

Lura, P. (2003). Autogenous Deformation and Internal Curing of Concrete*.* PhD Thesis, Delft University.

Ma, S., Li, W., Zhang, S., Hu, Y. and Shen, X. (2015). Study on the hydration and microstructure of Portland cement containing diethanol-isopropanolamine. *Cement and Concrete Research,* 67 122-130.

Maekawa, K., Chaube, R. and Kishi, T. (1999). Modelling of concrete performance : hydration, microstructure formation and mass transport*,* London [u.a.], E & FN Spon.

Maekawa, K., Ishida, T. and Kishi, T. (2003). Multi-scale modeling of concrete performance. *Journal of Advanced Concrete Technology,* 1 (2)**,** 91-126.

Magalhães, F., Caetano, E. and Cunha, Á. (2006). Operational Modal Analysis of the Braga Sports Stadium Suspended Roof. *IMAC-XXIV: Conference & Exposition on Structural Dynamics.* Orlando, Florida, USA.

Maia, L., Azenha, M., Faria, R. and Figueiras, J. (2011a). Influence of the cementitious paste composition on the E-modulus and heat of hydration evolutions. *Cement and Concrete Research,* 41 (8)**,** 799-807.

Maia, L., Azenha, M., Faria, R. and Figueiras, J. (2012a). Identification of the percolation threshold in cementitious pastes by monitoring the E-modulus evolution. *Cement and Concrete Composites,* 34 (6)**,** 739-745.

Maia, L., Azenha, M., Geiker, M. and Figueiras, J. (2011b). Describing paste E-modulus evolution of commercial cements and the relationship with volume solids formation.

Maia, L., Azenha, M., Geiker, M. and Figueiras, J. (2012b). E-modulus evolution and its relation to solids formation of pastes from commercial cements. *Cement and Concrete Research,* 42 (7)**,** 928-936.

Maia, L., Figueiras, H., Nunes, S., Azenha, M. and Figueiras, J. (2012c). Influence of shrinkage reducing admixtures on distinct SCC mix compositions. *Construction and Building Materials,* 35, 304-312.

Malhotra, V. M. and Carette, G. G. (2004). Penetration Resistance Methods. *In: V. M. Malhotra, Carino N. J.* (ed.) *Handbook on Nondestructive Testing of Concrete: Second Edition.* London: CRC Press.

Malhotra, V. M. and Sivasundaram, V. (2003). Resonant Frequency Methods. *In: V. M. Malhotra, Carino N. J.* (ed.) *Handbook on Nondestructive Testing of Concrete: Second Edition.* London: CRC Press.

Manzano, H., Dolado, J. S. and Ayuela, A. (2009). Elastic properties of the main species present in Portland cement pastes. *Acta Materialia,* 57 (5)**,** 1666-1674.

Matsui, K. (1990). Effects of curing conditions and test temperatures on the strength of adhesive-bonded joints. *International Journal of Adhesion and Adhesives,* 10 (4)**,** 277-284.

McKelvey, T., Akcay, H. and Ljung, L. (1996). Subspace-based multivariable system identification from frequency response data. *Automatic Control, IEEE Transactions on,* 41 (7)**,** 960-979.

Mendes, P. and Oliveira, S. (2008). Análise Dinâmica de Estruturas: utilização integrada de modelos de identificação modal e modelos de elementos finitos. Lisboa: LNEC.

Meyers, M. A. and Chawla, K. K. (2008). Mechanical Behavior of Materials*,* New York, USA, Cambridge University Press.

Mindess, S. (2004). Acoustic Emission Methods. *In: V. M. Malhotra, Carino N. J.* (ed.) *Handbook on Nondestructive Testing of Concrete: Second Edition.* London: CRC Press.

Mitchell, T. M. (2004). Radioactive/Nuclear Methods. *In: V. M. Malhotra, Carino N. J.* (ed.) *Handbook on Nondestructive Testing of Concrete: Second Edition.* London: CRC Press.

Moussa, O., Vassilopoulos, A. P., de Castro, J. and Keller, T. (2012). Early-age tensile properties of structural epoxy adhesives subjected to low-temperature curing. *International Journal of Adhesion and Adhesives,* 35 (0)**,** 9-16.

Muller, A. (2014). Characterization of porosity & C-S-H in cement pastes by ^{1}H NMR. PhD thesis, École Polytechnique Fédérale de Lausanne.

Muller, A. C. A., Scrivener, K. L., Gajewicz, A. M. and McDonald, P. J. (2013). Densification of C–S–H Measured by 1H NMR Relaxometry. *The Journal of Physical Chemistry C,* 117 (1)**,** 403-412.

Naik, T. R. (2004). The Break-Off Test Method. *Handbook on Nondestructive Testing of Concrete: Second Edition.* London: CRC Press.

Naik, T. R., Malhotra, V. M. and Popovics, J. S. (2004). The Ultrasonic Pulse Velocity Method. *In: V. M. Malhotra, Carino N. J.* (ed.) *Handbook on Nondestructive Testing of Concrete: Second Edition.* London: CRC Press.

Neithalath, N., Persun, J. and Manchiryal, R. (2010). Electrical conductivity based microstructure and strength prediction of plain and modified concretes. *International Journal of Advances in Engineering Sciences and Applied Mathematics,* 2 (3)**,** 83-94.

Neithalath, N., Weiss, J. and Olek, J. (2006). Characterizing Enhanced Porosity Concrete using electrical impedance to predict acoustic and hydraulic performance. *Cement and Concrete Research,* 36 (11)**,** 2074-2085.

Neville, A. (1995). Properties of Concrete*,* London, Longman Singapore Publishers Pte Ltd.

Nishi, T., Kwei, T. K. and Wang, T. T. (1975). Physical properties of poly(vinyl chloride) - copolyester thermoplastic elastomer mixtures. *Journal of Applied Physics,* 46 (10)**,** 4157-4165.

Oppenheim, A. V., Schafer, R. W. and Buck, J. R. (1989). Discrete-time signal processing*,* New Jersey, USA, Prentice-hall Englewood Cliffs.

Overschee, P. V. and Moor, B. D. (1996). Subspace Identification for Linear Systems: Theory, Implementation, Applications*,* London, Kluwer Academic Publishers.

Ozturk, T., Rapoport, J. R., Popovics, J. S. and Shah, S. P. (1999). Monitoring the setting and hardening of cement-based materials with ultrasound. *Concrete Science and Engineering,* 1 83–91.

Pape, Y. L., Toulemonde, C., Masson, R. and Gharib, J. E. (2008). Benhur and Vi(CA)2T, two toolboxes to model concrete as an heterogeneous material combining analytical and numerical approaches. *In:* E. Schlangen and G. De Schutter (ed.) *International RILEM Symposium on Concrete Modelling - ConMod '08.* Delft, Netherlands: RILEM Publications SARL.

Park, G. and Inman, D. J. (2005). Impedance-based structural health monitoring. *Damage prognosis for aerospace, civil and mechanical systems,* 275-292.

Park, G., Sohn, H., Farrar, C. R. and Inman, D. J. (2003). Overview of piezoelectric impedance-based health monitoring and path forward. *Shock Vib. Digest,* 35 451–63.

Parrott, L. J. (1990). A review os methods to determine the moisture conditions in concrete. *British Cement Association Publication C/7.*

Pazdera, L., Topolář, L., Kořenská, M., Smutny, J., Kusák, I. and Luňák, M. (2014). Application Acoustic Emission Method and Impedance Spectroscopy for Monitoring Concrete During Hardening. *Advanced Materials Research,* 1000 257-260.

Peeters, B. (2000). System Identification and Damage Detection in Civil Engineering*.* PhD Thesis, Catholic University of Leuven.

Peeters, B. and De Roeck, G. (1999). Reference-based stochastic subspace identification for output-only modal analysis. *Mechanical Systems and Signal Processing,* 13 (6)**,** 855-878.

Peeters, B. and De Roeck, G. (2001). Stochastic System Identification for Operational Modal Analysis: A Review. *Journal of Dynamic Systems, Measurement, and Control,* 123 (4)**,** 659-667.

Pessik, S. P. and Carino, N. J. (1988). Setting time of concrete using the impact-echo method. *ACI Materials Journal,* 85 389-399.

Philleo, R. E. (1955). Comparison of results of three methods for determing Young's modulus of elasticity of concrete. *Journal of the American Concrete Institute,* 51 (25)**,** 461-469.

Pichler, B., Fischer, I., Lach, E., Ch, T., Barraud, E. and Britz, F. (2014a). The influence of loading rate on the compressive strength of cementitious materials. *Computational Modelling of Concrete Structures.* CRC Press.

Pichler, B., Fischer, I., Lach, E., Ch, T., Barraud, E. and Britz, F. (2014b). The influence of loading rate on the compressive strength of cementitious materials: Experiments and "separation of time scales"-based analysis. *In: Nenad Bićanić, Herbert Mang, Günther Meschke and René de Borst* (eds.) *Computational Modelling of Concrete Structures.* Arlberg, Austria: CRC Press.

Pichler, B., Hellmich, C. and Eberhardsteiner, J. (2009). Spherical and acicular representation of hydrates in a micromechanical model for cement paste: prediction of early-age elasticity and strength. *Acta Mech,* 203 137–162.

Pichler, C., Lackner, R. and Mang, H. A. (2007). A multiscale micromechanics model for the autogenous-shrinkage deformation of early-age cement-based materials. *Engineering Fracture Mechanics,* 74 (1–2)**,** 34-58.

Pintelon, R., Guillaume, P., Rolain, Y., Schoukens, J. and Van Hamme, H. (1994). Parametric identification of transfer functions in the frequency domain-a survey. *Automatic Control, IEEE Transactions on,* 39 (11)**,** 2245-2260.

Pommersheim, J. M. and Clifton, J. R. (1979). Mathematical modeling of tricalcium silicate hydration. *Cement and Concrete Research,* 9 (6)**,** 765-770.

Poole, J. L., Riding, K. A., Folliard, K. J., Juenger, M. C. G. and Schindler, A. K. (2007). Methods for Calculating Activation Energy for Portland Cement. *Materials Journal,* 104 (1).

Poon, C. S. and Groves, G. W. (1988). TEM observations of a high alumina cement paste. *Journal of Materials Science Letters,* 7 (3)**,** 243-244.

Popovics, J. and Subramaniam, K. L. (2014). Review of Ultrasonic Wave Reflection Applied to Early-Age Concrete and Cementitious Materials. *Journal of Nondestructive Evaluation,* 34 (1)**,** 1-12.

Popovics, J. S., Zemajtis, J. and Shkolnik, I. (2008). ACI-CRC final report – a study of static and dynamic modulus of elasticity of concrete. *American Concrete Institute.* University of Illinois, Urbana, Illinois, USA.

Powers, T. C. (1938). Measuring Young's modulus of elasticity by means of sonic vibrations. *ASTM Proceedings,* 38 460–467.

Proceq (2014). Pundit Lab Ultrasonic Instrument. *In:* Proceq SA (ed.). Schwerzenbach, Switzerland.

Provis, J. L., Myers, R. J., White, C. E., Rose, V. and van Deventer, J. S. J. (2012). X-ray microtomography shows pore structure and tortuosity in alkali-activated binders. *Cement and Concrete Research,* 42 (6)**,** 855-864.

Qin, L. and Li, Z. (2008). Monitoring of cement hydration using embedded piezoelectric transducers. *Smart Materials and Structures,* 17 (5)**,** 055005.

Qualitest (2015). Ultrasonic Concrete Testing. *In:* Worldoftest (ed.).

Rainieri, C. and Fabbrocino, G. (2014). Operational Modal Analysis of Civil Engineering Structures: An Introduction and Guide for Applications, Springer New York.

Rapoport, J. R., Popovics, J. S., Kolluru, S. V. and Shah, S. P. (2000). Using Ultrasound to Monitor Stiffening Process of Concrete with Admixtures. *Materials Journal,* 97 (6)**,** 675-683.

Reinhardt, H. W. and Grosse, C. U. (2004). Continuous monitoring of setting and hardening of mortar and concrete. *Construction and Building Materials,* 18 (3)**,** 145-154.

Ren, W.-X. and Zong, Z.-H. (2004). Output-only modal parameter identification of civil engineering structures. *Structural Engineering and Mechanics,* 17 (3-4)**,** 1-16.

Reynders, E. (2012). System Identification Methods for (Operational) Modal Analysis: Review and Comparison. *Archives of Computational Methods in Engineering,* 19 (1)**,** 51-124.

RILEM (1972). RILEM Recommendations for the Testing and Use of Constructions Materials. *NDT 1 Testing of concrete by the ultrasonic pulse method.* E & FN SPON.

RILEM (1975). Modulus of elasticity of concrete in compression. *CPC 8.* RILEM TC14-CPC.

Robeyst, N., Gruyaert, E., Grosse, C. U. and De Belie, N. (2008). Monitoring the setting of concrete containing blast-furnace slag by measuring the ultrasonic p-wave velocity. *Cement and Concrete Research,* 38 (10)**,** 1169-1176.

Rodrigues, J. (2004). Stochastic Modal Identification, Analysis Methods and Applications in Civil Engineering Structures (in Portuguese). PhD Thesis, Engineering Faculty of University of Porto.

Rojas-Henao, L., Fernandez-Gomez, J., Carlos, J. and Lopez-Aguí (2012). Rebound Hammer, Pulse Velocity, and Core Tests in Self-Consolidating Concrete. *Materials Journal,* 109 (2)**,** 235-243.

Roussel, N. (2007). Rheology of fresh concrete: from measurements to predictions of casting processes. *Materials and Structures,* 40 (10)**,** 1001-1012.

S&P (2011). S&P Resin 220 epoxy adhesive, Saftey Data Sheet.

Sanahuja, J., Dormieux, L. and Chanvillard, G. (2007a). Modelling elasticity of a hydrating cement paste. *Cement and Concrete Research,* 37 (10)**,** 1427-1439.

Sanahuja, J., Dormieux, L. and Chanvillard, G. (2007b). Modelling elasticity of a hydrating cement paste. *Cement and Concrete Research,* 37 1427–1439.

Sanchez-Palencia, E. (1980). Non-Homogeneous Media and Vibration Theory, Springer Berlin Heidelberg.

Sanchez, F. and Sobolev, K. (2010). Nanotechnology in concrete – A review. *Construction and Building Materials,* 24 (11)**,** 2060-2071.

Sanish, K. B., Neithalath, N. and Santhanam, M. (2013). Monitoring the evolution of material structure in cement pastes and concretes using electrical property measurements. *Construction and Building Materials,* 49 288-297.

Sant, G., Dehadrai, M., Bentz, D., Lura, P., Ferraris, C. F., Bullard, J. W. and Weiss, J. (2009). Detecting the Fluid-to-Solid Transition in Cement Pastes: comparing experimental and numerical techniques. *Concrete international,* 31 (6)**,** 53-58.

Santamarina, J., Klein, A. and Fam, M. (2001). Soils and waves:Particulate materials behavior, characterization and process monitoring. *Journal of Soils and Sediments,* 1 (2)**,** 130.

Saul, A. G. A. (1951). Principles underlying the steam curing of concrete at atmospheric pressure. *Magazine of Concrete Research,* 2 (6)**,** 127-140.

Scherer, G. W., Zhang, J. and Thomas, J. J. (2012). Nucleation and growth models for hydration of cement. *Cement and Concrete Research,* 42 (7)**,** 982-993.

Schirrer, R. and Goett, C. (1982). The Young's modulus of the craze in PMMA. *Journal of Materials Science Letters,* 1 (8)**,** 355-357.

Schoppel, K., Plannerer, M. and Springenschmid, R. (1994). Determination of restraint stresses and of material properties during hydration of concrete with the temperature-stress testing machine. *In: R Springenschmid*, ed. Thermal Cracking in Concrete at Early Ages: Proceedings of the International RILEM Symposium, 1994 Munich, Germany. CRC Press, 153.

Scrivener, K. L. (2004). Backscattered electron imaging of cementitious microstructures: understanding and quantification. *Cement and Concrete Composites,* 26 (8)**,** 935-945.

Segre, N. and Joekes, I. (2000). Use of tire rubber particles as addition to cement paste. *Cement and Concrete Research,* 30 (9)**,** 1421-1425.

Sellevold, E. J. and Bjøntegaard, Ø. (2006). Coefficient of thermal expansion of cement paste and concrete: Mechanisms of moisture interaction. *Materials and Structures,* 39 (9)**,** 809-815.

Shin, S., Qureshi, A. R., Lee, J.-Y. and Yun, C. B. (2008). Piezoelectric sensor based nondestructive active monitoring of strength gain in concrete. *Smart Materials and Structures,* 17 8.

Shirley, D. J. and Hampton, L. D. (1978). Shear Wave Measurements in Laboratory Sediments. *Journal of the Acoustical Society of America,* 63 (2)**,** 607–613.

Shkolnik, I. E. (2008). Influence of high strain rates on stress–strain relationship, strength and elastic modulus of concrete. *Cement and Concrete Composites,* 30 (10)**,** 1000-1012.

Silva, J. (2010). Contribuição para o estudo do tratamento de solos:Avaliação da Deformabilidade. Dissertação de mestrado, Universidade do Minho.

Silva, J., Azenha, M., Correia, A. G. and Ferreira, C. (2013a). Continuous stiffness assessment of cement-stabilised soils from early age. *Géotechnique,* 63 (16)**,** 1419-1432.

Silva, J., Azenha, M., Correia, A. G. and Ferreira, C. (2013b). Continuous stiffness assessment of cement-stabilised soils from early age. *Géotechnique*.

Silva, J., Azenha, M., Correia, A. G. and Granja, J. (2014). Continuous monitoring of sand-cement stiffness since layer compaction with a resonant frequency based method: issues on mould geometry and sampling. *Soils and Foundations,* 54 (1)**,** 56–66.

Sleiman, H., Perrot, A. and Amziane, S. (2010). A new look at the measurement of cementitious paste setting by Vicat test. *Cement and Concrete Research,* 40 (5)**,** 681-686.

Smith, A., Chotard, T., Gimet-Breart, N. and Fargeot, D. (2002). Correlation between hydration mechanism and ultrasonic measurements in an aluminous cement: effect of setting time and temperature on the early hydration. *Journal of the European Ceramic Society,* 22 (12)**,** 1947-1958.

Song, G., Gu, H. and Mo, Y.-L. (2008). Smart aggregates: multi-functional sensors for concrete structures - a tutorial and a review. *Smart Materials and Structures,* 17 (3)**,** 033001.

Song, H., Lim, H. J. and Sohn, H. (2013). Electromechanical impedance measurement from large structures using a dual piezoelectric transducer. *Journal of Sound and Vibration,* 332 (25)**,** 6580-6595.

Staquet, S., Boulay, C., Robeyst, N. and De Belie, N. (2009). Ultrasonic monitoring of setting and autogenous shrinkage development of high performance concrete. *In*, 2009. 321-327.

Staquet, S., Delsaute, B., Darquennes, A. and Espion, B. (2012). Design of a revisited TSTM system for testing concrete since setting time under free and restraint conditions. *In:* F. Toutlemonde and J.-M. Torrenti (eds.) *Concrack3 – Rilem-JCI Int. Workshop on Crack Control of Mass Concrete and Related Issues Concerning Early-age of concrete structures.* Paris, France: RILEM Publications SARL.

Subramaniam, K. V. and Wang, X. (2010). An investigation of microstructure evolution in cement paste through setting using ultrasonic and rheological measurements. *Cement and Concrete Research,* 40 (1)**,** 33-44.

Sun, W.-b. and Wu, C.-q. (2009). Analytical Solutions to Strain Rates of Reinforced Concrete Simply Supported Slabs under Blast Loads. *Journal of Southwest Jiaotong University,* 17 (3)**,** 212-217.

Sun, X., Dai, Q. and Ng, K. (2014). Computational investigation of pore permeability and connectivity from transmission X-ray microscope images of a cement paste specimen. *Construction and Building Materials,* 68 240-251.

Sun, Z., Voigt, T. and Shah, S. P. (2006). Rheometric and ultrasonic investigations of viscoelastic properties of fresh Portland cement pastes. *Cement and Concrete Research,* 36 (2)**,** 278-287.

Suraneni, P., Struble, L., Popovics, J. and Chung, C. (2015). Set Time Measurements of Self-Compacting Pastes and Concretes Using Ultrasonic Wave Reflection. *Journal of Materials in Civil Engineering,* 27 (1)**,** 04014117.

Swamy, R. N. and Bandyopadhyay, A. K. (1975). The elastic properties of structural lightweight concrete. *ICE Proceedings,* 59 (3)**,** 381-394.

Tatsuoka, F. (2011). Laboratory stress-strain tests for developments in geotechnical engineering and pratice *In: C.-K. Chung, H.-K. Kim, J.-S. Lee and Y.-H. Jung*, eds. Fifth International Symposium on Deformation Characteristics of Geomaterials, 2011 Seoul, Korea. IOS Press, 3-52.

Thomann, T. and Hryciw, R. (1991). Laboratory measurement of small strain shear modulus under Ko conditions : Thomann, T G; Hryciw, R D Geotech Test JV13, N2, June 1990, P97-105. *International Journal of Rock Mechanics and Mining Sciences & Geomechanics Abstracts,* 28 (1)**,** A25-A25.

Thomas, J. J., Biernacki, J. J., Bullard, J. W., Bishnoi, S., Dolado, J. S., Scherer, G. W. and Luttge, A. (2011). Modeling and simulation of cement hydration kinetics and microstructure development. *Cement and Concrete Research,* 41 (12)**,** 1257-1278.

Thompson, J. K. and Tree, D. R. (1980). Leakage error in Fast Fourier analysis. *Journal of Sound and Vibration,* 71 (4)**,** 531-544.

Tian, Z. and Bian, C. (2013). Numerical modeling of elastic modulus for cement paste using homogenization method. *Journal of Wuhan University of Technology-Mater. Sci. Ed.,* 28 (4)**,** 751-760.

Torquato, S. (2001). Random heterogeneous materials: microstructure and macroscopic properties, Springer.

Torrenti, J. M., Dantec, P., Boulay, C. and Semblat, J. F. (1999). Projet de processus d'essai pour la détermination du module de déformation longitudinale du béton. *Bulletin de Liaison des Ponts et Chaussées,* 220 79-81.

Trtnik, G. and Gams, M. (2015). Ultrasonic assessment of initial compressive strength gain of cement based materials. *Cement and Concrete Research,* 67 148-155.

Tuleubekov, K. (2012). Micromechanical Modeling of Concrete at Early Age. PhD Thesis, University of Minnesota.

van Breugel, K. (1991). Simulation of hydration and formation of structure in hardening cement-based materials. PhD Thesis, Technical University of Delft.

van Breugel, K. (1995). Numerical simulation of hydration and microstructural development in hardening cement-based materials (I) theory. *Cement and Concrete Research,* 25 (2)**,** 319-331.

Van Den Abeele, K., Desadeleer, W., De Schutter, G. and Wevers, M. (2009). Active and passive monitoring of the early hydration process in concrete using linear and nonlinear acoustics. *Cement and Concrete Research,* 39 (5)**,** 426-432.

Viana da Fonseca, A., Ferreira, C. and Fahey, M. (2009). A Framework Interpreting Bender Element Tests, Combining Time-Domain and Frequency-Domain Methods. *Geotechnical Testing Journal,* 32 (2)**,** 1-17.

Voigt, T. (2005). The Aplication of an Ultrasonic Shear Wave Reflection Method for Nondestrutive Testing of Cement-Based Materials at Early Ages: An Experimental and Numerical Analysis. PhD thesis, University of Leipzig, Germany.

Voigt, T., Grosse, C. U., Sun, Z., Shah, S. P. and Reinhardt, H.-W. (2005). Comparison of ultrasonic wave transmission and reflection measurements with P- and S-waves on early age mortar and concrete. *Materials and Structures,* 38 (8)**,** 729-738.

Voigt, T., Sun, Z. and Shah, S. P. (2006). Comparison of ultrasonic wave reflection method and maturity method in evaluating early-age compressive strength of mortar. *Cement and Concrete Composites,* 28 (4)**,** 307-316.

Vyazovkin, S. (2011). Handbook of thermal analysis and calorimetry: Recent advances, techniques and applications, Amsterdam: Elsevier.

Wallevik, J. E. (2009). Rheological properties of cement paste: Thixotropic behavior and structural breakdown. *Cement and Concrete Research,* 39 (1)**,** 14-29.

Wang, B., Faure, P., Thiéry, M. and Baroghel-Bouny, V. (2013). 1H NMR relaxometry as an indicator of setting and water depletion during cement hydration. *Cement and Concrete Research,* 45 1-14.

Wang, D.-s., Yu, L.-p. and Zhu, H.-p. (2010a). Strength monitoring of concrete based on embedded PZT transducer and the resonant frequency. *In: Hang Guo, Yuan-tai Hu, Cun-fa Gao and Wei-qiu Chen*, eds. Symposium on Piezoelectricity, Acoustic Waves and Device Applications (SPAWDA), 2010a Xiamen, China. IEEE, 202-205.

Wang, D., Song, H. and Zhu, H. (2014). Embedded 3D electromechanical impedance model for strength monitoring of concrete using a PZT transducer. *Smart Materials and Structures,* 23 (11)**,** 115019.

Wang, D., Zhang, J. and Zhu, H. (2015). Embedded Electromechanical Impedance and Strain Sensors for Health Monitoring of a Concrete Bridge. *Shock and Vibration,* 2015 12.

Wang, D. and Zhu, H. (2011). Monitoring of the strength gain of concrete using embedded PZT impedance transducer. *Construction and Building Materials,* 25 (9)**,** 3703-3708.

Wang, X. and Subramaniam, K. V. (2011). Ultrasonic monitoring of capillary porosity and elastic properties in hydrating cement paste. *Cement and Concrete Composites,* 33 (3)**,** 389-401.

Wang, X., Subramaniam, K. V. and Lin, F. (2010b). Ultrasonic measurement of viscoelastic shear modulus development in hydrating cement paste. *Ultrasonics,* 50 (7)**,** 726-738.

Wei, X. and Li, Z. (2006). Early Hydration Process of Portland Cement Paste by Electrical Measurement. *Journal of Materials in Civil Engineering,* 18 (1)**,** 99-105.

Welch, P. D. (1967). The use of fast Fourier transforms for the estimation of power spectra: A method based on time averaging over short modified periodograms. *IEEE Transactions on Audio and Electroacoustics,* 15 70-73.

Williams, A. (1986). Temperature Matched Curing Systems. *ACI Special Publication,* 95.

Wu, S., Chen, X. and Zhou, J. (2012). Influence of strain rate and water content on mechanical behavior of dam concrete. *Construction and Building Materials,* 36 448-457.

Xian-yu, J., Nan-guo, J. and Zong-jin, L. (2002). Xian-yu (2002) Study on the electrical properties of young concrete.pdf. *Journal of Zhejiang University Sience,* 3 (2)**,** 174-180.

Yang, Y., Divsholi, B. S. and Soh, C. K. (2010). A Reusable PZT Transducer for Monitoring Initial Hydration and Structural Health of Concrete. *Sensors,* 10 5193-5208.

Ye, G., Lura, P., van Breugel, K. and Fraaij, A. L. A. (2004a). Study on the development of the microstructure in cement-based materials by means of numerical simulation and ultrasonic pulse velocity measurement. *Cement and Concrete Composites,* 26 (5)**,** 491-497.

Ye, G., Sun, Z. H., Voigt, T., Breugel, K. v. and Shah, S. P. (2004b). A micromechanical model for characterization of cement paste at early age validated with experiments. *In: K. Kovler J. Weiss, J. Marchand, and S. Mindess*, ed. International RILEM Symposium on Concrete Science and Engineering: A Tribute to Arnon Bentur, 2004b Evanston, Illinois, USA. RILEM Publications SARL, 11.

Yuan, D., Nazarian, S. and Zhang, D. (2004). Use of Stress Wave Technique to Monitor and Predict Concrete Strength Development. *Airfield Pavements,* 409-423.

Zeiger, H. and McEwen, A. (1974). Approximate linear realizations of given dimension via Ho's algorithm. *Automatic Control, IEEE Transactions on,* 19 (2)**,** 153-153.

Zhang, J., Fan, T., Ma, H. and Li, Z. (2015). Monitoring setting and hardening of concrete by active acoustic method: Effects of water-to-cement ratio and pozzolanic materials. *Construction and Building Materials,* 88 118-125.

Zhao, H., Huang, D., Wang, X. and Chen, X. (2014). Dynamic elastic modulus of cement paste at early age based on nondestructive test and multiscale prediction model. *Journal of Wuhan University of Technology-Mater. Sci. Ed.,* 29 (2)**,** 321-328.

Zhao, H., Wu, S., Huang, D., Chen, X. and Zhao, L. (2013). A multi-scale percolation-based approach for the prediction of elasticity of early-age cement paste. *European Journal of Environmental and Civil Engineering,* 17 (sup1)**,** s304-s320.

Zhu, J., Kee, S.-H., Han, D. and Tsai, Y.-T. (2011a). Effects of air voids on ultrasonic wave propagation in early age cement pastes. *Cement and Concrete Research,* 41 (8)**,** 872-881.

Zhu, J. and Kee, S. H. (2010). Monitoring early age microstructure development of cement paste using bender elements. *In: Peter J. Shull, Aaron A. Diaz and H. Felix Wu*, eds. Nondestructive Characterization for Composite Materials, Aerospace Engineering, Civil Infrastructure, and Homeland Security, 2010 San Diego, California, USA.

Zhu, J., Tsai, Y.-T. and Kee, S.-H. (2011b). Monitoring early age property of cement and concrete using piezoceramic bender elements. *Smart Materials and Structures,* 20 (11)**,** 115014.

Appendix A

EMM-ARM users guide

Minho University
School of Engineering
Civil Engineering Department

Elastic Modulus Measurement through Ambient Response Method

User's Guide

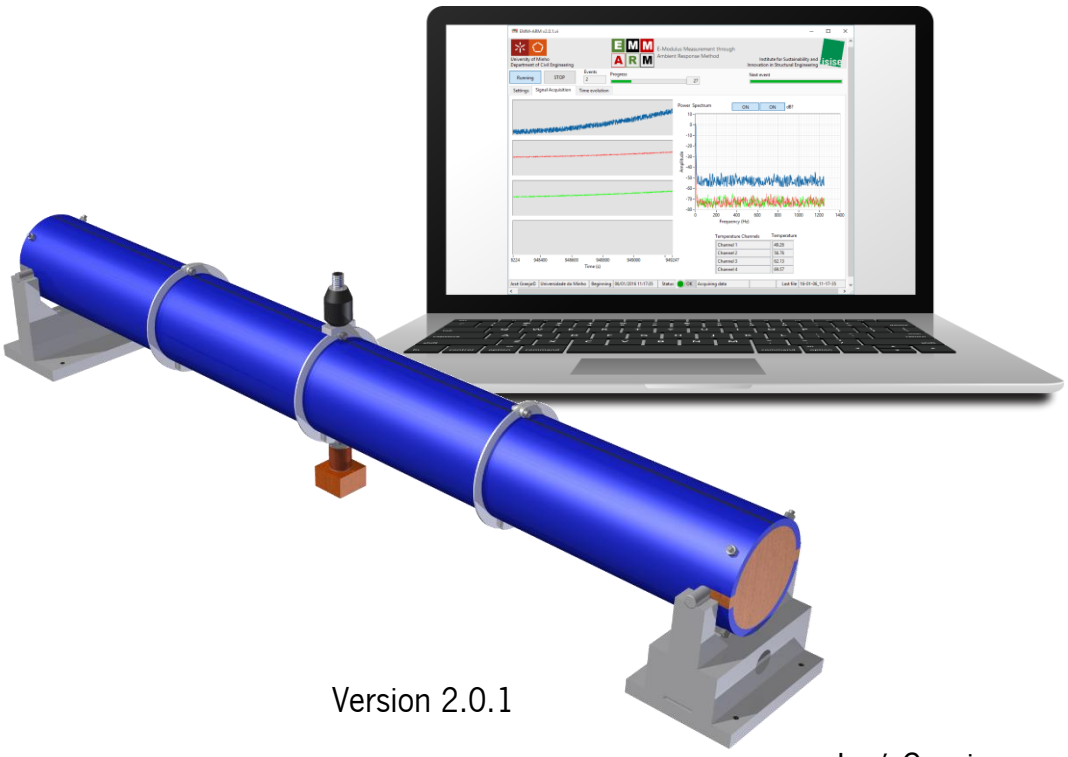

Version 2.0.1

José Granja
Miguel Azenha

isise Institute for Sustainability and Innovation in Structural Engineering

Table of contents

1 General Information

1.1 Warnings

- The manufacturer does not accept any responsibility for direct or indirect damage to people, things or animals and use of the appliance in different conditions from those foreseen.
- The manufacturer reserves the right to make changes to the documentary information or to the appliance without advance notice.
- All operations necessary for maintaining machine efficiency before and throughout use are the operator's responsibility.
- Carefully read the entire manual before operating the machine.
- It is vital to know the information and limitations contained in this manual for correct machine use by the operator.
- Interventions are only permitted if the operator is accordingly competent and trained.
- The operator must be knowledgeable about machine operations and mechanisms.
- The purchaser must ensure that operators are trained and aware of all the information and clarifications in the supplied documentation.
- Even with such certainty the operator or user must be informed and therefore aware of potential risks when operating the machine.
- Safety, reliability and optimum performance is guaranteed when using original parts.
- Any tampering or modifying of the appliance (electrical, mechanical or other) which has not been previously authorized in writing by the manufacturer is considered abusive and disclaims the constructor from any responsibility for any resulting damage.
- All necessary operations to maintain the efficiency of the machine before and throughout use are the responsibility of the user.

2 Introduction: What is the EMM-ARM?

The EMM-ARM is recently developed method that allows the automatic and continuous evaluation of the E-Modulus of cement based materials immediately after casting. This methodology is based on continuous modal identification of the first flexural resonant frequency of a composite beam. This beam is placed horizontally, with a well-known support conditions, that can be simply supported at both extremities or fixed as a cantilever, and vertical accelerations resulting from ambient or forced vibration are measured or at mid-span or at the free end, respectively.

By monitoring this accelerations, it is possible to perform modal identification and evaluate the first flexural resonance frequency of the beam (see Figure 1). The resonant frequency of the tested beam evolved as a result of the increasing stiffness of the cementitious material, and was correlated with the Young's modulus by applying the dynamic equation of motion. Therefore it was possible to obtain a real-time curve of E-Modulus against time.

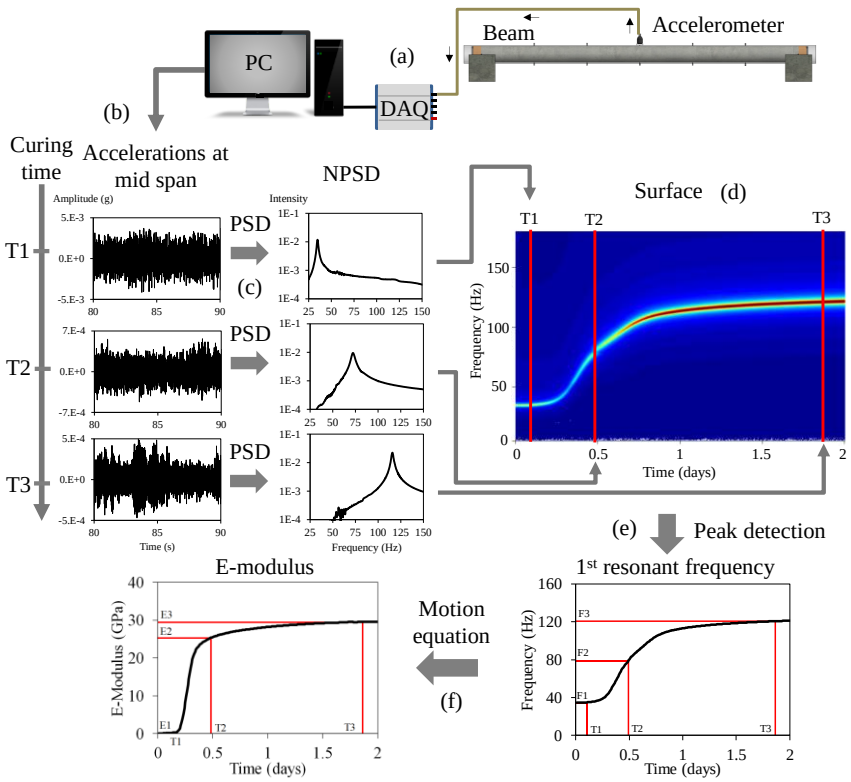

Figure 1. Data processing scheme.

3 General description of the EMM-ARM

3.1 Concrete version

The version of EMM-ARM devised for studying concrete was introduced by Azenha et al. (2010). The basic unit of the test specimen is the mould, which is a special designed PVC tube with inner/outer diameter of 96 mm/110 mm and with three aluminium rings to reinforce the tube presenting them to lose the geometry, as shown in Figure *2*. Before actually casting concrete inside the tube, some preparations are necessary. Firstly, two horizontal rods are placed through holes near the extremities of the beam, in order to materialise simple supports for a 1.0 m span beam. The mould also comprises two extremity lids, one of which is kept fixed, and the other one is removable for casting operations. Casting of the specimen is made with the mould in an inclined position, until complete filling is achieved (with the mould placed vertically) and the top lid is fixed in place. After casting is finished, the composite beam is placed horizontally and simply supported on its extremity rods over two steel rigid supports (see Figure *2*). An accelerometer is attached to the mid-span of the beam as well as a custom electromagnetic actuator, and acceleration measurements can start within a period of less than 20 min from the beginning of casting operations. Based on the measured accelerations and excitation, and assuming that environmental vibrations have very low influence on the measured accelerations, the resonance frequency of the first mode of vibration is identified.

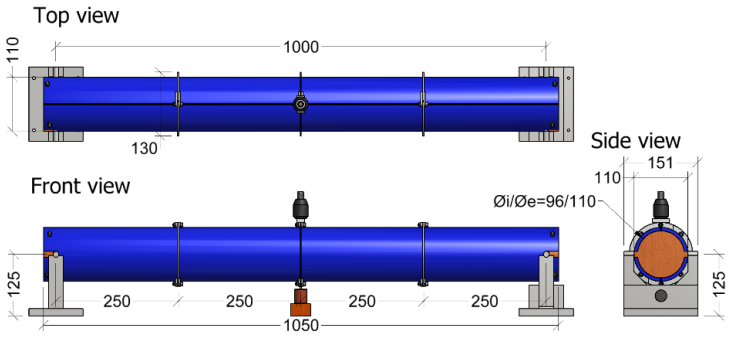

Figure 2. Experimental setup for EMM-ARM testing of concrete. Units [mm].

3.2 Cement paste version

The version of EMM-ARM devised for studying cement pastes was introduced by Azenha et al. (2012). The fundamental component of this method is a hollow tubular beam made of acrylic, with outside/inside diameters of 20/16 mm. The composite beam consists of a 550 mm long acrylic tube filled with fresh cement paste, with extremity caps made of polypropylene. The composite beam is then fixed in the horizontal position, operating as a cantilevered structural system with a span of 450 mm – see Figure *3*. The specimen is fixed using a metal clamping device with inner diameter matching the outer diameter of the beam. The metal clamping device is then rigidly connected to a rigid base to ensure complete fixation. A lightweight accelerometer is afterwards attached to the free end of the cantilevered beam. The cantilevered beam is then excited by ambient noise (e.g., wind, people walking nearby, vibrations originated by mechanical equipment, etc.) which can conceptually be assumed to have an average behaviour of white noise, i.e. a stochastic process with constant spectral intensity at all frequencies. It should be noted that, due to the slender-ness of the beam, the vibrations that are merely caused by the surrounding environment are high enough to be registered by the accelerometer, enabling modal identification without using any external or forced excitation. However, in order to intensify the ambient vibration associated to air movement, and thus facilitate the process of automatic modal identification, fans were placed in the vicinity of EMM-ARM specimens. The experiment starts as soon as all components are correctly placed.

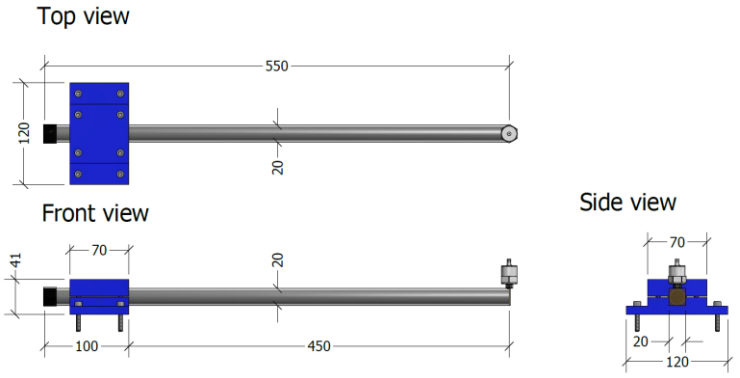

Figure 3. Experimental setup for EMM-ARM testing of cement paste. Units [mm].

4 Test assemble

4.1 Hardware

4.1.1 Acquisition system

In the EMM-ARM tests we use two types of equipments to perform the data acquisition: the NI USB 9234 or 9233 and the NI USB 4431.

4.1.1.1 NI USB 9234 or 9233

The NI 9233 or 9234 is a 4-channel dynamic signal acquisition module for making high-accuracy audio frequency measurements from integrated electronic piezoelectric (IEPE) and non-IEPE sensors. For more information please see : http://www.ni.com/datasheet/pdf/en/ds-316

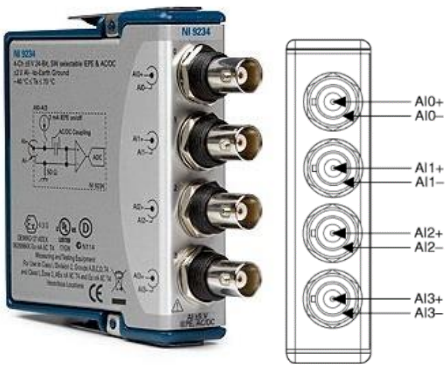

4.1.1.2 NI USB 4431 or NI 4432

The NI USB-4432 bus-powered dynamic signal analyzer (DSA) with 24-bit resolution. The first four measurement channels have selectable IEPE. The fifth channel is a generating signal and has 24-bit resolution. For more information please see: http://www.ni.com/pdf/products/us/cat_ni4432.pdf

4.1.2 Signal generation system

For signal generation it is possible to use the NI USB 4432 or any other signal generator from National Instruments. Additionally, when the tests has more than one beam with excitation it is required a signal multiplexer.

4.1.2.1 Signal multiplexer

The signal multiplexer is a custom made equipment based on a Arduino. It needs to be connected to the acquisition computer. The excitation signal is connected to the 'Input' and then each electromagnetic actuator is connected to one of the 'Outputs'.

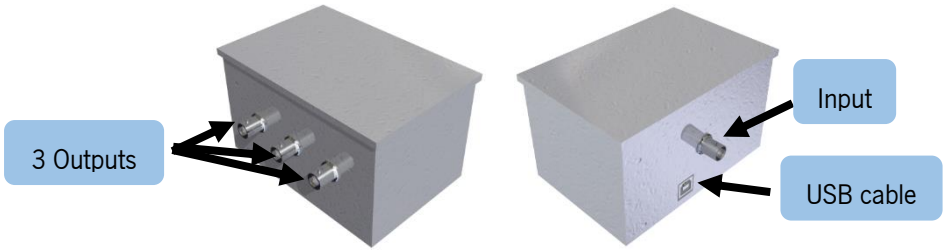

4.2 Accelerometers

4.2.1 Concrete testing

Requirements:

Sensitivity	>10 Volts/g
Measurement range	±0.1 to ±0.5 g
Frequency range	0.1 to 1000 Hz
Resonant Frequency	>10 kHz
Weight	<400 g
Type of sensing part	Piezoelectric

Note:

Usually the tests are performed with the accelerometers PCB 393B12. For more information see: http://www.pcb.com/contentstore/docs/PCB_Corporate/Vibration/Products/Specsheets/393B12_J.pdf

4.2.2 Cement paste testing

Requirements:

Sensitivity	>0.5 Volts/g
Measurement range	±0.5 to ±10 g
Frequency range	1 to 1000 Hz
Resonant Frequency	>10 kHz
Weight	<50 g
Type of sensing part	Piezoelectric

Note:

Usually the tests are performed with the accelerometers PCB 352B. For more information see: http://www.pcb.com/contentstore/docs/PCB_Corporate/Vibration/Products/Specsheets/352B_C.pdf

4.3 Cable connections

4.3.1 Without excitation

It is possible to use the NI 9234, 9233 or 4432 as data acquisition system. As example in the next figures are presented the cables needed to perform the tests without excitation on two beams. In the first figure a NI 9234 or 9233 is used and the accelerometers of the beams are connected to the channels ai0 and ai1.

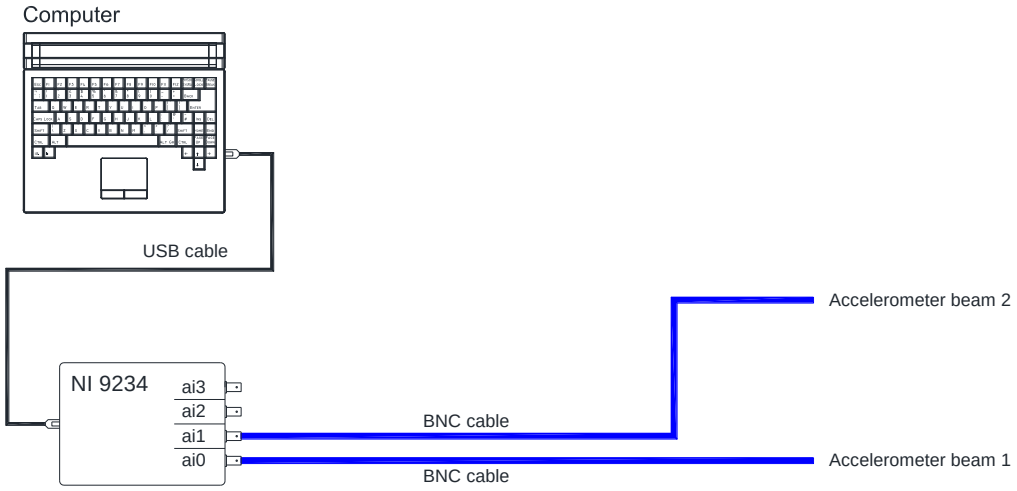

In the second figure the a NI 4431 or NI 4432 is used and the accelerometers of the beams are connected to the channels ai0 and ai1.

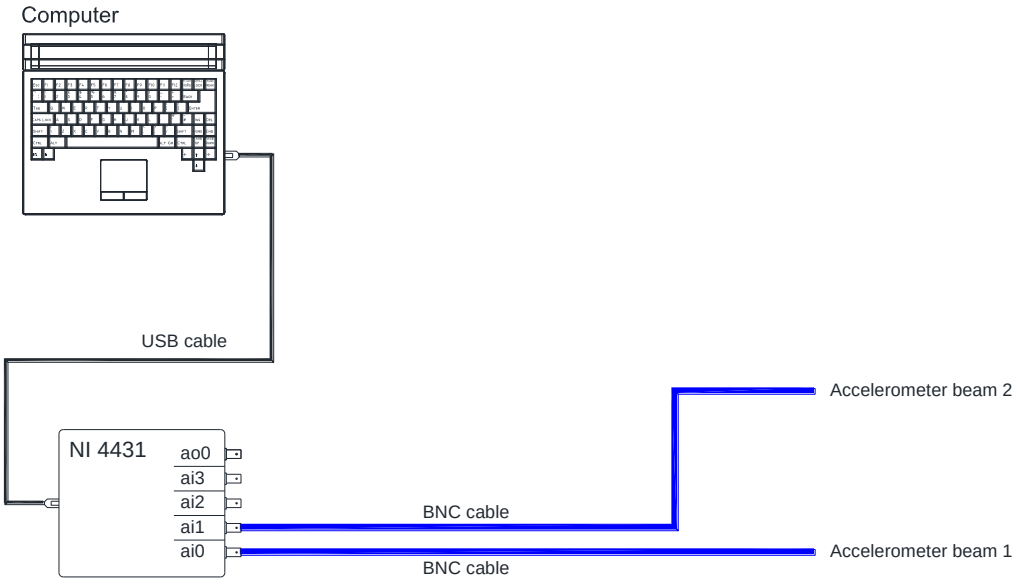

4.3.2 With excitation

When the tests are made with excitation it is need to use the NI 4432 or a combination of acquisition and generation devices. For propose of example, the following figures presents the cable connection needed for a teste with two beams with excitation on one of them and with excitation on all the beams, respectively. It should be noted that when more than one beam with excitation is used a signal multiplexer is needed. The excitation is generated in the channel ao0 and needs to be divided in two to allow the reading of the real excitation to the beams. After this division one cable is connected to electromagnetic actuator, in the case one, and to the 'Input' of the multiplexer, in the case two. The other cable needs to be connected to the input channel ai0 to read the real excitation.

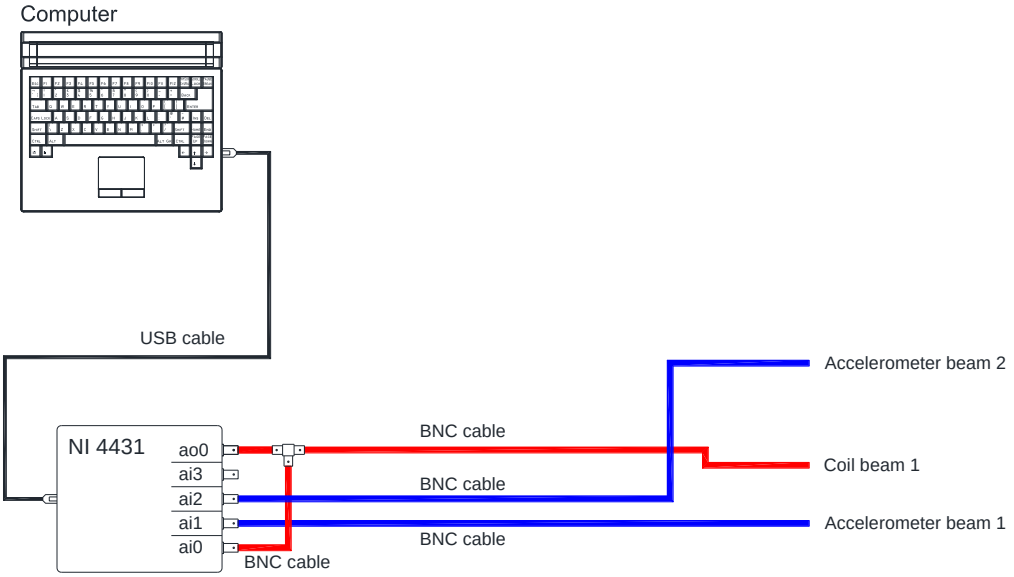

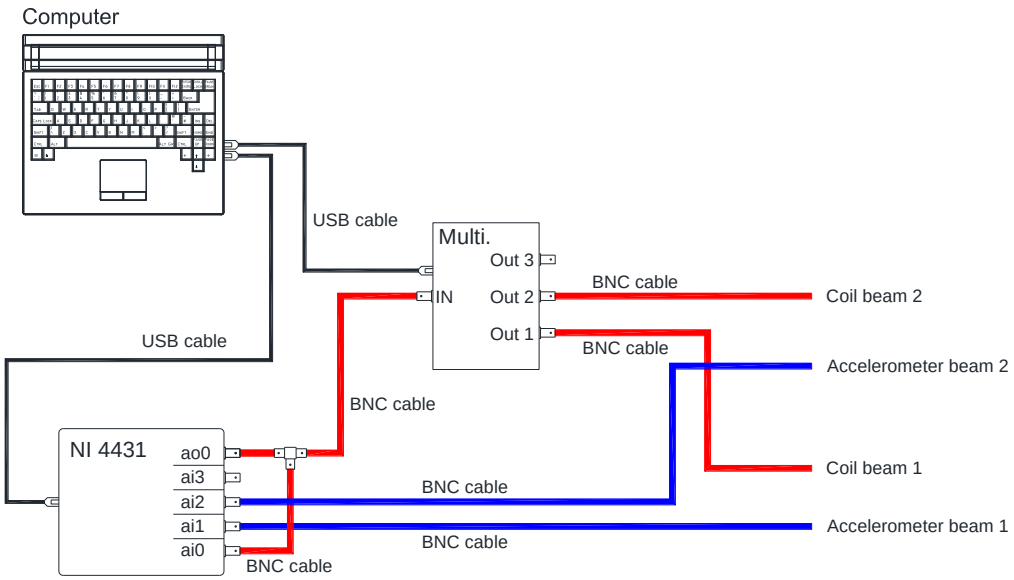

4.4 Concrete setup

4.4.1 Reusable beams components

Part	Number	Photo	Features
Half PVC tube	2	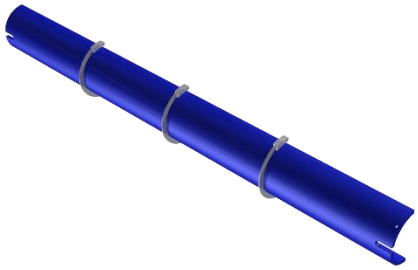	Total length – 1050mm External diameter – 110mm Internal diameter – 96mm Material – PVC and Aluminium
Sealing rubber	4	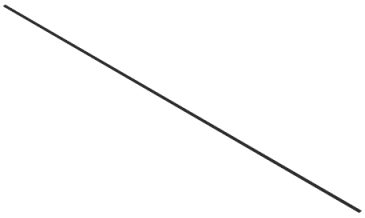	Withd – 3mm Height – 7mm Length – 1050mm Material – Rubber
Bolt	6		Diameter – 5mm Length – 16mm Material – Steel
Extremity lid	2		Material – Wood
Rod	2		Diameter – 12mm Length – 150mm Material – Steel
Fixed support	1	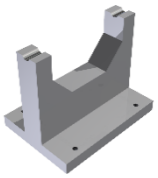	Support spacing – 111mm Material – Steel
Pivot support	1	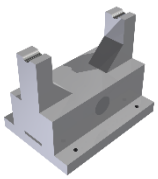	Support spacing – 111mm Material – Steel
Threaded rods	4		Diameter – 5mm Length – 125mm Material – Steel

Part	Number	Photo	Features
Accelerometer support	1	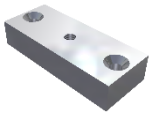	Material – Aluminum
Magnet support	1	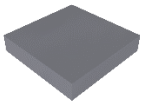	With – 10mm Length – 10mm Thikness – 1mm Material – Steel
Magnet	1		Diameter – 8mm Length – 15mm Material – Neodymium
Coil	1	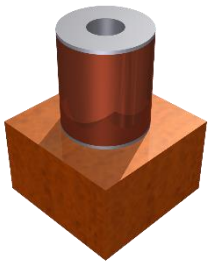	Custom
Accelerometer	1		Sensitivity – 10V/g Range – ±0.5g

4.4.2 Mould assembling for casting

[1] Glue the rubbers strips in the sides of the two half's of the PVC tube

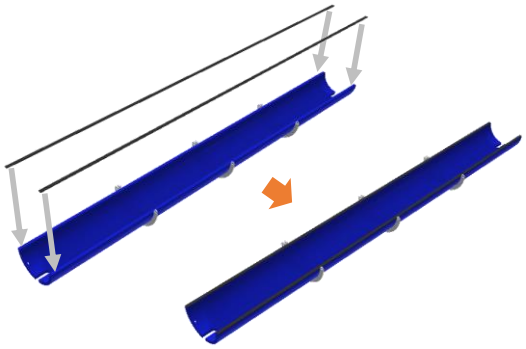

[2] Assemble the half's of the PVC tube

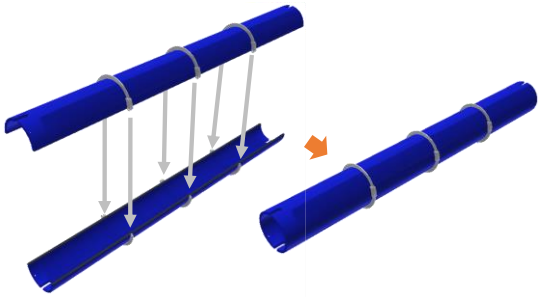

[3] Place the screws in the aluminium rings

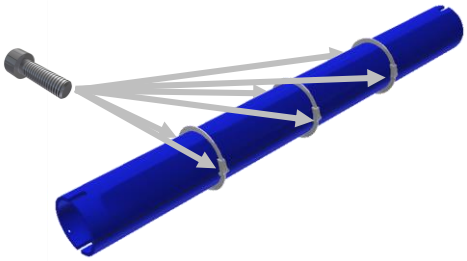

[4] Place the horizontal rod on one of the extremities of the tube

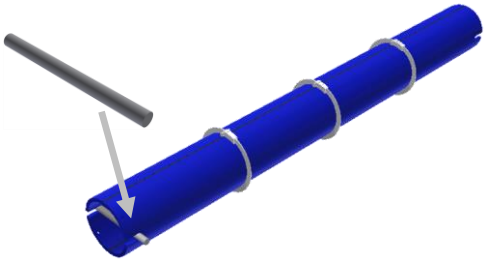

[5] Place one of the extremities lids

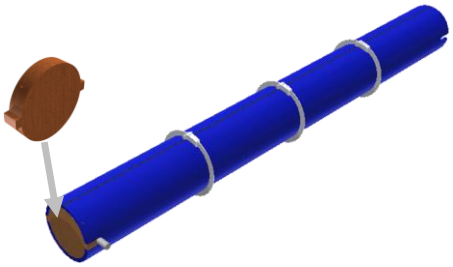

Note: don't change the position of the two lids because they have small differences between them.

[6] Place the threaded rods to fix the lid in place

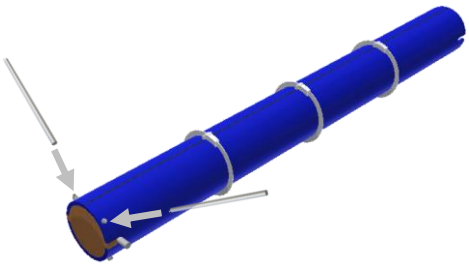

Note: tighten the nuts to ensure the geometry of the beam.

[7] The mould is ready for casting

Important: after assemble the mould wait at least 2 hours to cure the glue of the rubbers strips

4.4.3 Casting operations

[8] Put the concrete in a wheelbarrow.

[9] Cast the tube from the top (open extremity).

[10] Until 1/3 of the length of the tube.

[11] Vibrate the concrete with a vibrating needle with a diameter ≤25mm.

Note: be careful to avoid damaging the tube with the vibrating needle.

[12] Repeat the steps [9] to [11] until the tube is full.

[13] After the filling of the tube place the horizontal rod.

Important: vibrate manually the concrete on the top of the tube around the horizontal rod.

[14] Insert a thermocouple in the concrete and pass the wire through the groove of the horizontal rod.

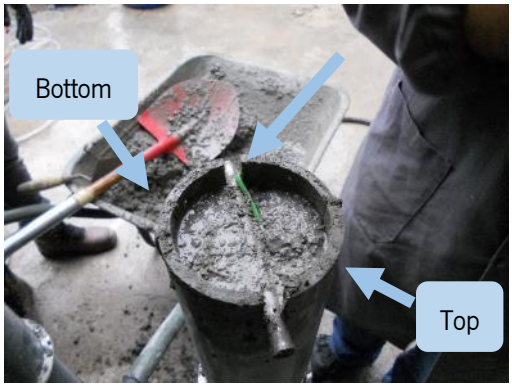

Important: the thermocouple wire must be at the top of the rod when the beam is in its final testing position.

[15] Place the lid on the open end of the tube and fix it with two threaded rods.

Note: tighten the nuts to ensure the geometry of the beam.

4.4.4 Test setup assemble

[16] After closing the tube.

[17] Place the beams in the supports.

Important: checking whether the beam is properly supported.

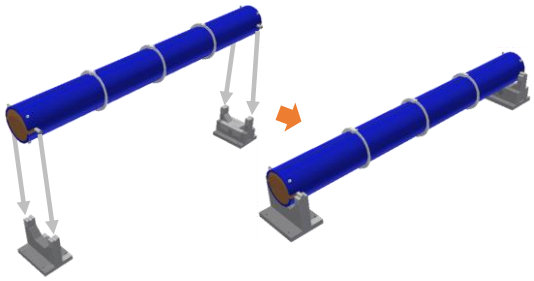

[18] Glue the accelerometer supports to the top of the mid span aluminium ring.

Note: to simplify the assembly process of the experimental setup after casting, this support can be glued prior to the casting.

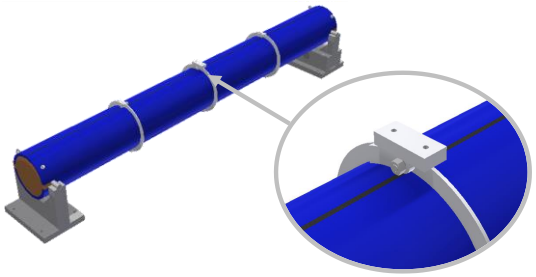

[19] Glue the magnet support to the bottom of the mid span aluminum ring.

Note: to simplify the assembly process of the experimental setup after casting, this support can be glued prior to the casting.

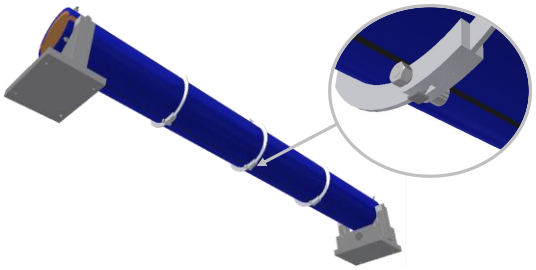

[20] Attach the accelerometer to the support.

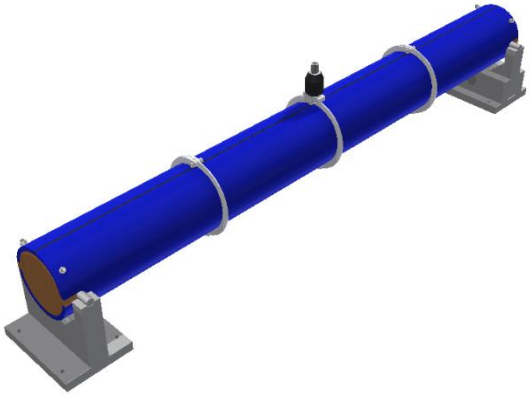

[21] Place the magnet in the support.

Note: the magnet does not need any type of glue to stay in position during the test once the support is ferromagnetic.

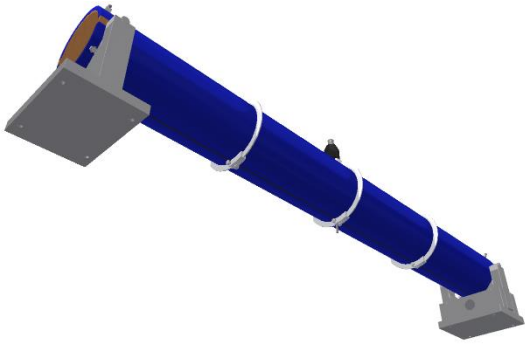

[22] Place the coil in position.

Important: ensure that the coil does not touch the magnet.

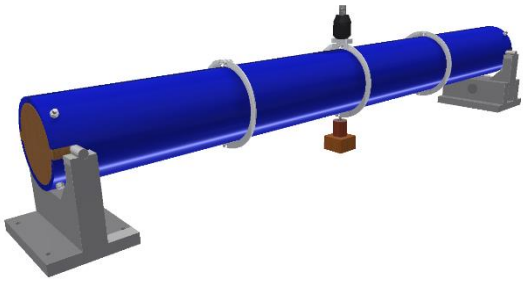

[23] Connect the cables to the accelerometer and to the coil and the test can start.

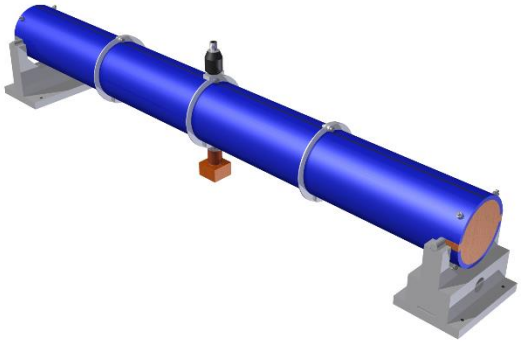

4.5 Cement paste setup

4.5.1 Specimen components

Part	Number	Photo	Features
Acrylic tube	1		Total length – 550mm External diameter – 20mm Internal diameter – 16mm Material – Acrylic
Clamping device	1	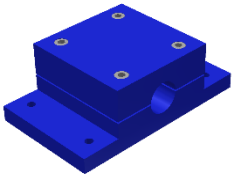	Internal diameter – 20mm Material – Steel
Extremity lid	1		Wigth – 20mm Length – 20mm Thikness – 0.2mm Material – Propylene
Accelerometer support	1		Material – steel
Plastic adhesive tape	1		Material – Plastic adhesive tape
Bolt	4		Diameter – 5mm Length – 50mm Material – Steel
Accelerometer	1		Sensitivity – 1 V/g Range – ±5g

4.5.2 Mould assembling for casting

[1] Glue the extremity lid to one of the extremities of the acrylic tube.

[2] Glue the accelerometer support to the same extremity in a way that the axis of the support became in the end of the beam.

[3] Place the clamping device on the other end of the acrylic tube in order to have a 450mm cantilever.

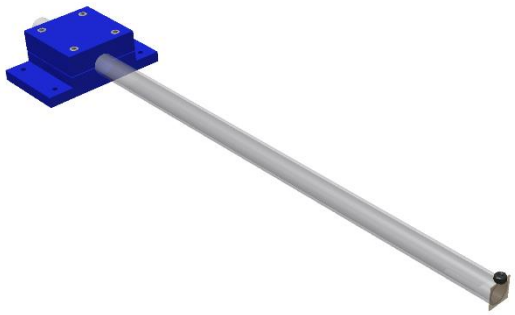

4.5.3 Casting operations

[1] Place the tube in the vertical position.

[2] Caste the cement paste inside the tube.

[3] Close the open end of the tube with the plastic adhesive tape.

4.5.4 Test setup assemble

[1] Place beam in the final testing position and connect the clamping device to a rigid support.

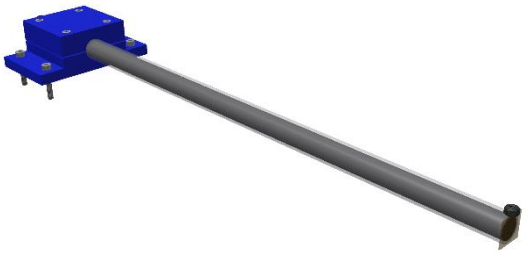

[2] Attach the accelerometer to the support and connect the cable of the accelerometer.

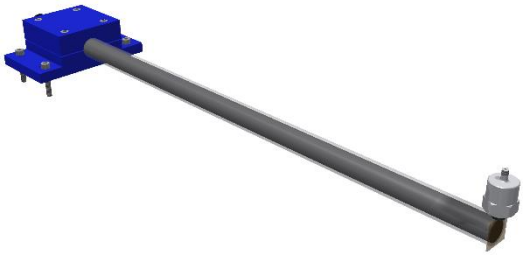

5 Software

5.1 Getting started

Launch the EMM-ARM v2.0.1 program

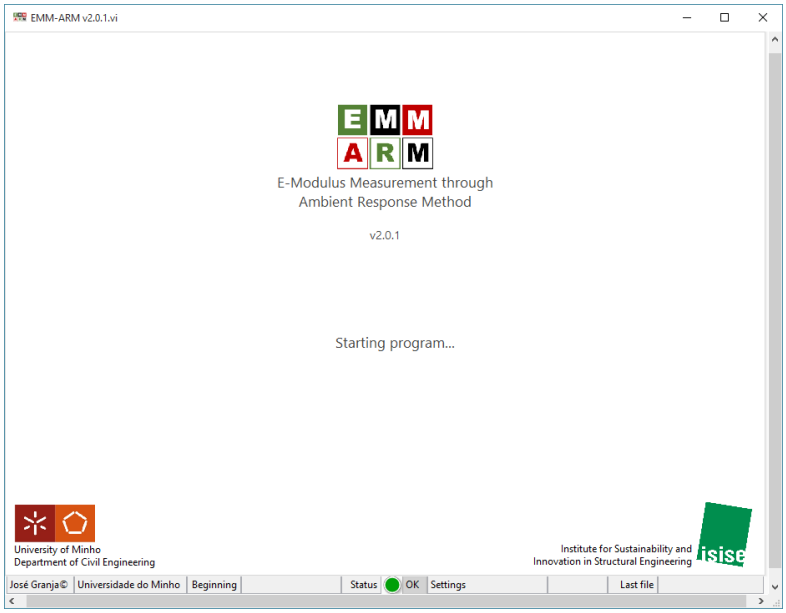

The main window will appear:

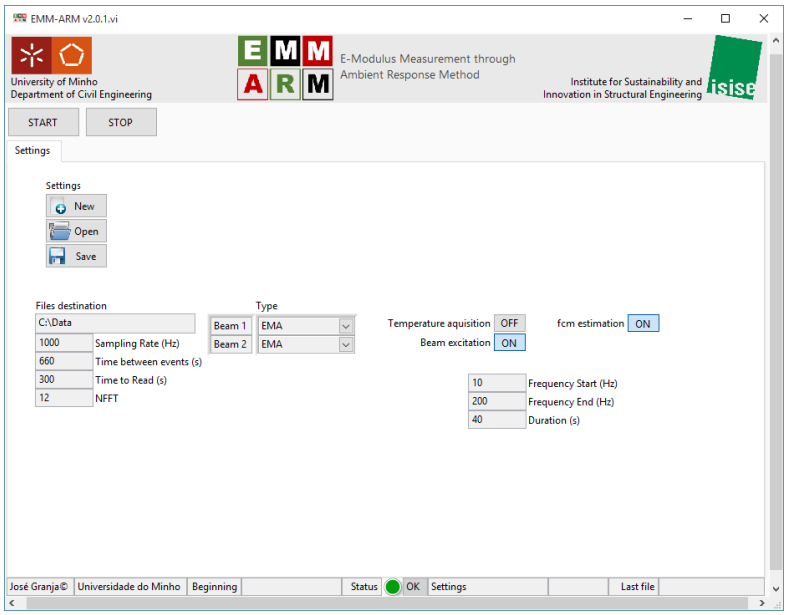

To load the configurations press the "Open" button.

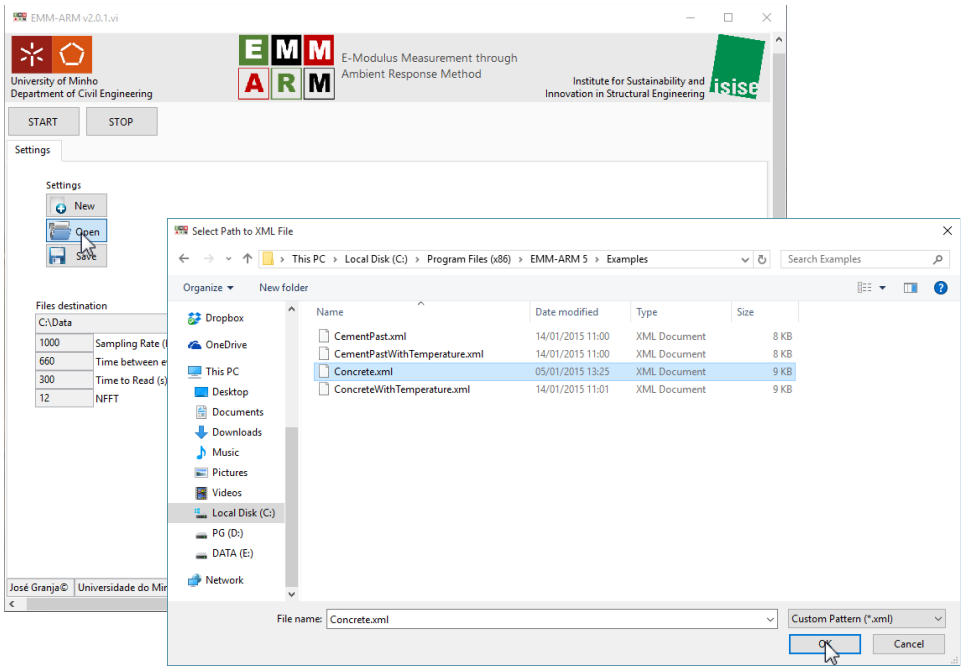

Then choose the name and the location of the xml file with the configurations. The program already have 4 configuration files for tests: in concrete with and without temperature acquisition and in cement paste with and without temperature acquisition.

After the loading of the configurations, press the "New" button to set the physical channels of the acquisition and generation devices.

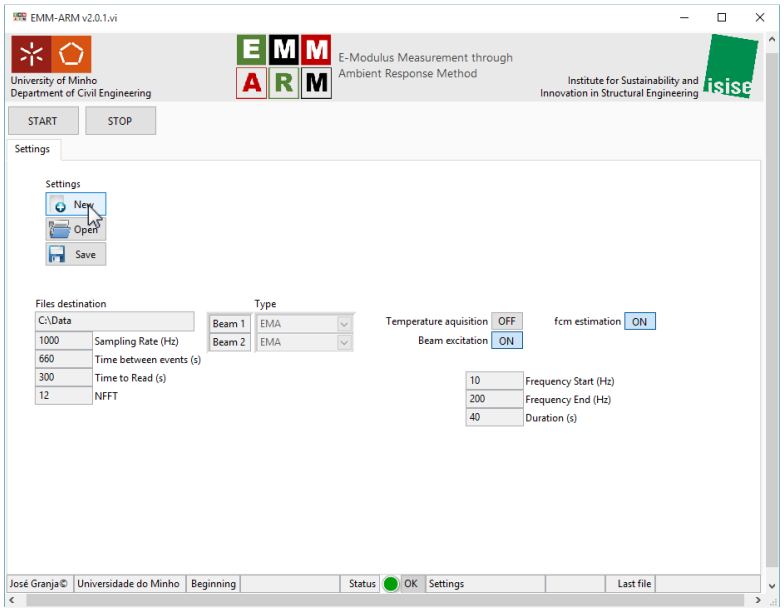

Press "Next" button

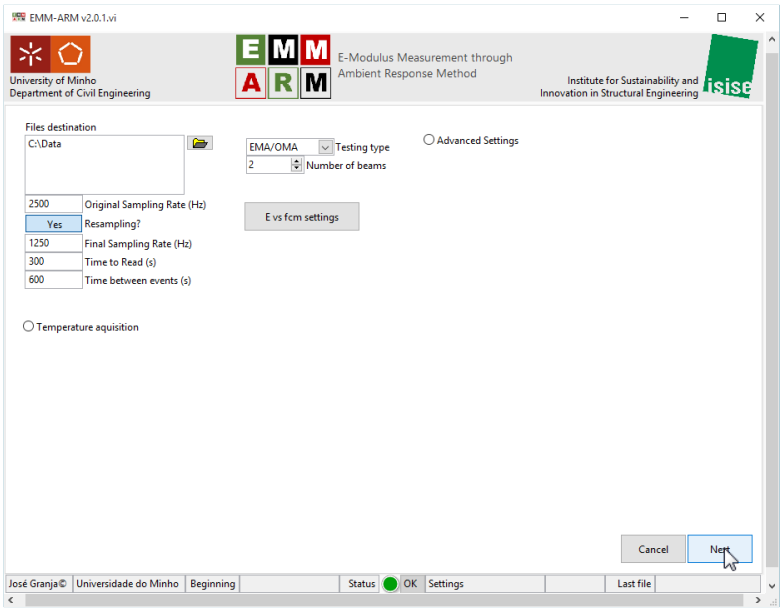

Press "Next" button

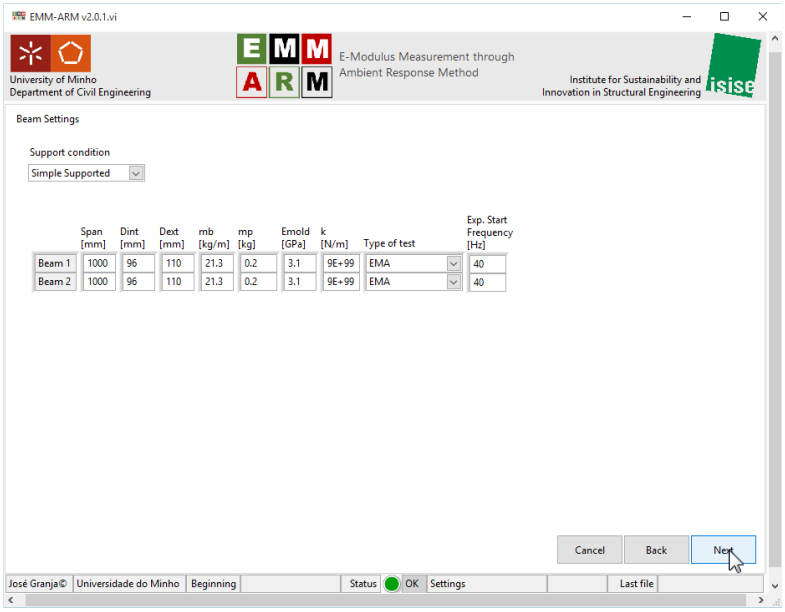

An accelerometer configuration page will appear:

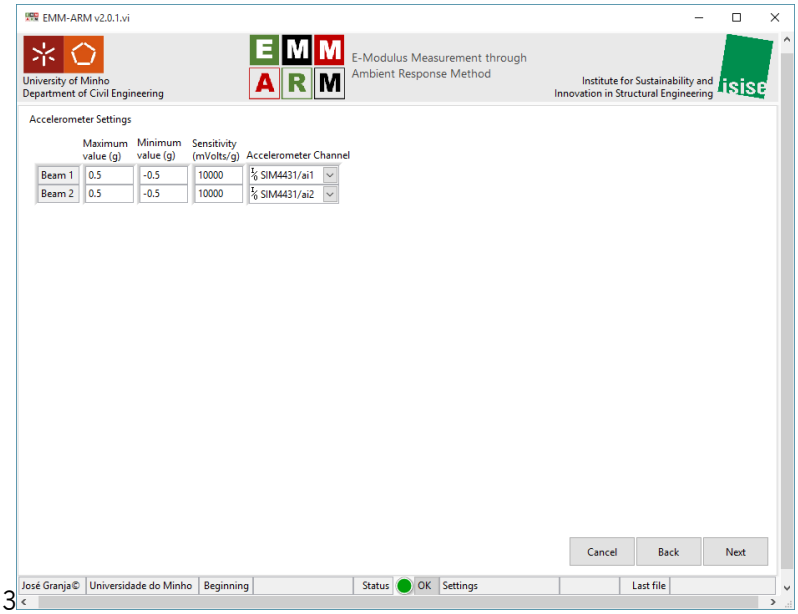

3

In this page set:

[3] The physical channel for the accelerometers (Accelerometer Channel)

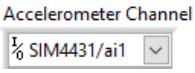

- The physical channel of the accelerometers have the device ID, that needs to be a NI DAQ signal acquisition, and the number of the channel in the signal acquisition devise.

Press "Next" button

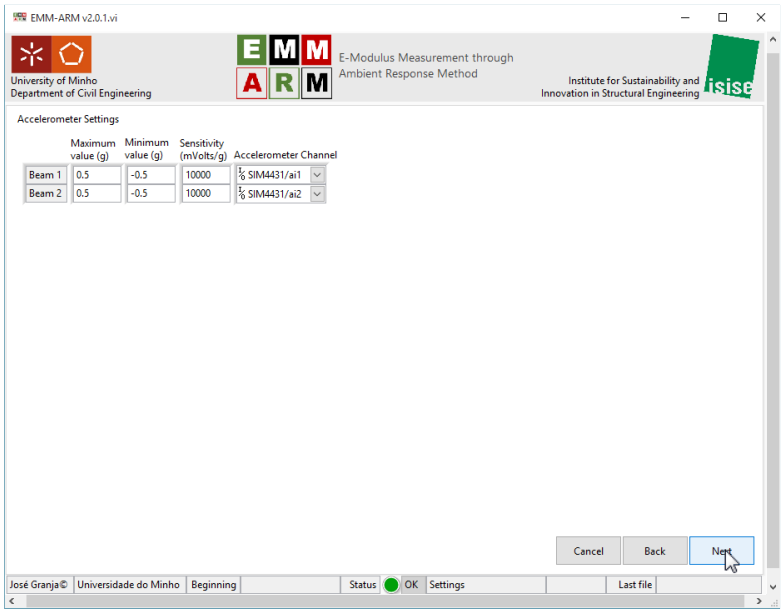

A generation configuration page will appear:

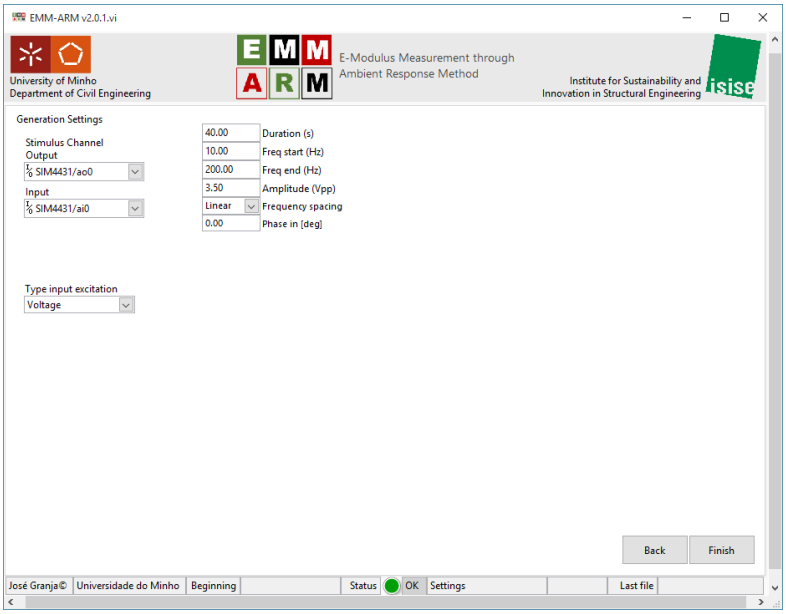

In this page set:

[4] The output physical channel of the stimulus

- The output physical channel of the stimulus have the device ID, that needs to be a NI DAQ signal generation, and the number of the channel in the signal generation devise.

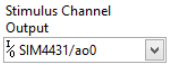

[5] The input physical channel of the stimulus

- The input physical channel of the stimulus have the device ID, that needs to be a NI DAQ signal acquisition, and the number of the channel in the signal acquisition devise.

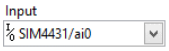

Press "Finish" button

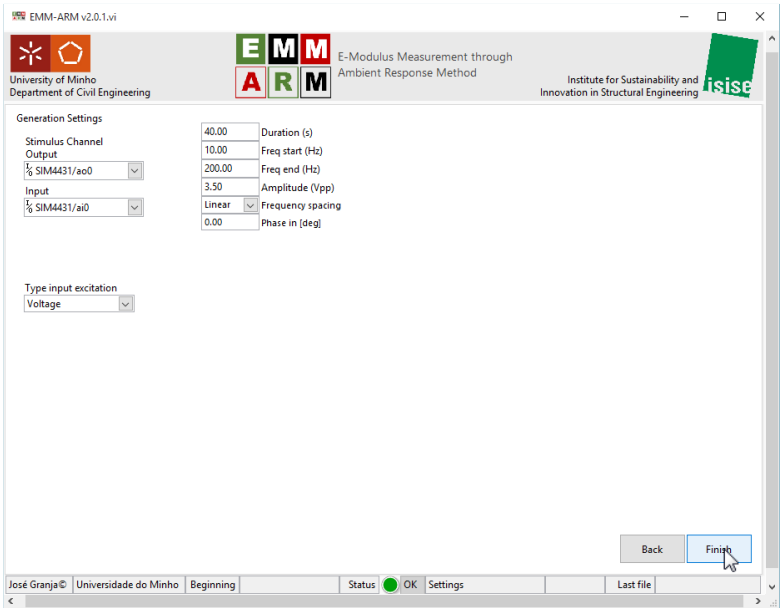

To start the acquisition press "START" button

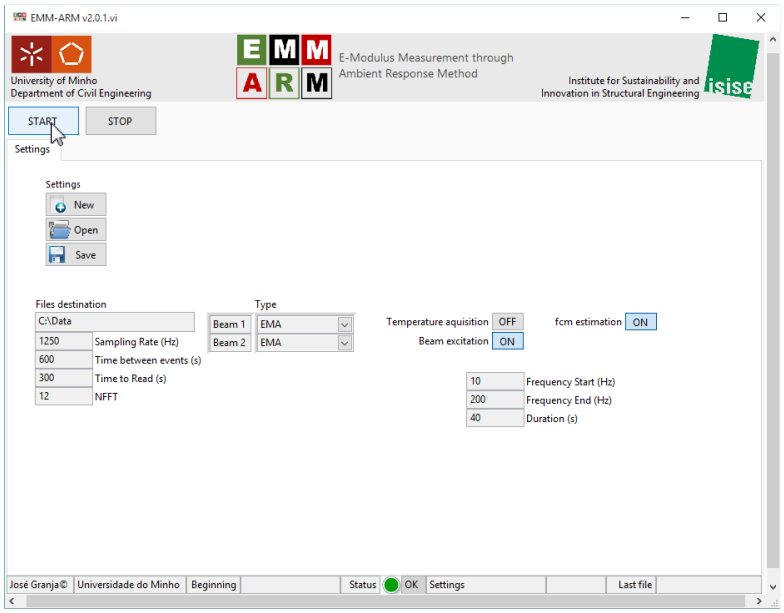

To know more details about the program see the next section.

5.2 Overview

Launch the EMM-ARM v2.0.1 program

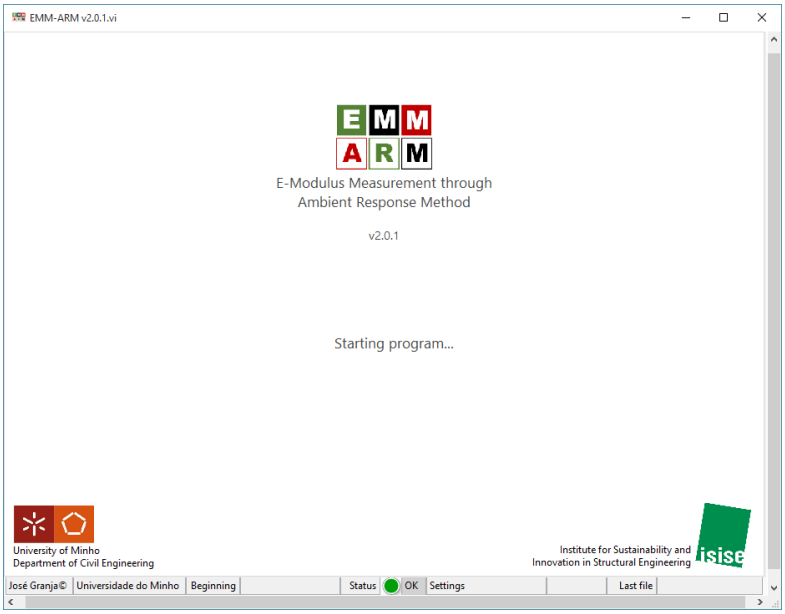

The main window will appear:

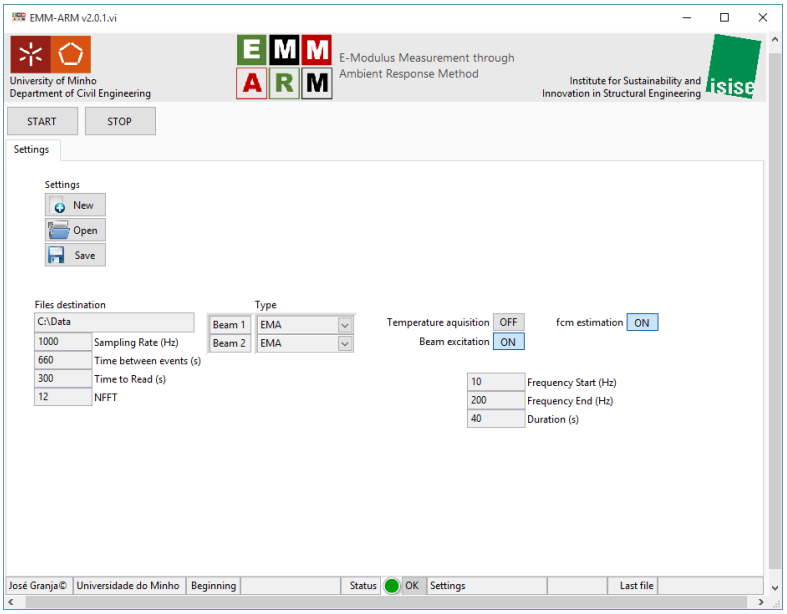

5.2.1 Configurations

5.2.1.1 Create new configuration

To create a custom configuration for the test press "New" button

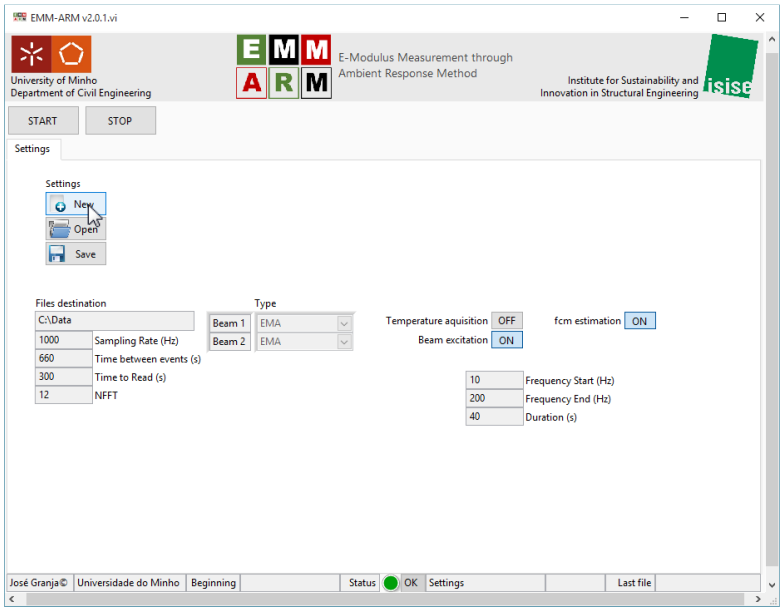

A configuration window will appear:

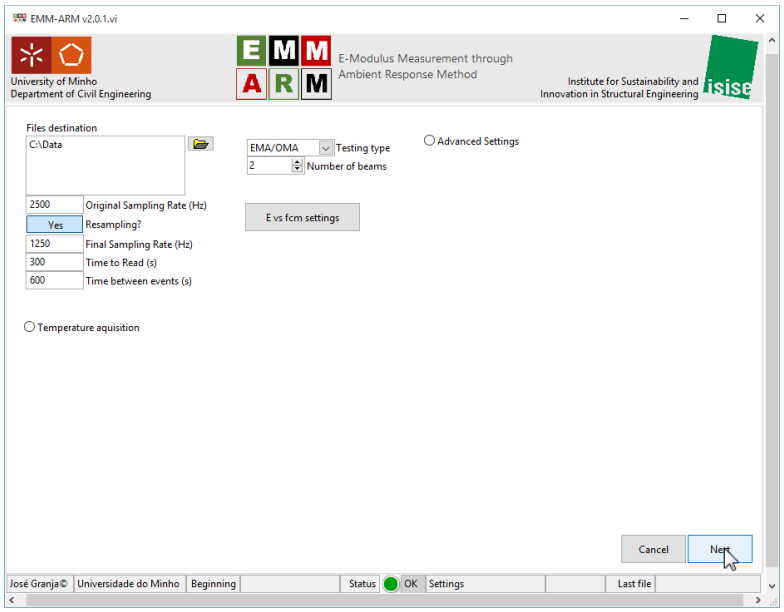

In this window it is possible to set:

[1] The path to save the data:

- Folder where all the data will be saved.

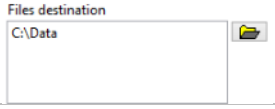

[2] The generation and acquisition sampling rate (Hz)

- Needs to be at least 10 times larger than the higher excitation frequency or in case of output-only tests 4 times larger than the higher resonance frequency of the beam.

2500 Original Sampling Rate (Hz)

[3] Turn ON or OFF the data resampling

- This feature was added to the program to reduce the data processing time and output data size. If the data resampling is ON it becomes necessary to set the final sampling rate.

Yes Resampling?

[4] The acquisition sampling rate (Hz)

- Needs to be at least 4 times larger than the higher expected resonance frequency of the beams.

1000 Final Sampling Rate (Hz)

[5] The acquisition time (s)

- Testing time of each beam. It is recommended to use 300 seconds.

300 Time to Read (s)

[6] The time between events (s)

- Time between each reading in each beam.

660 Time between events (s)

[7] The type of the test:

- EMA/OMA – if the test will be performed with an imposed excitation with an electromagnetic actuator;
- OMA – if the test will be performed with ambient excitation only.

EMA/OMA Testing type

[8] The number of beams

- Number of samples to be tested. This number is limited by the capacity of the data acquisition system. For reliability of the system do not use at the same time more than: 4 beams in output-only tests and 3 beams in input-output tests.

2 Number of beams

In this window it is also possible turn ON or OFF the temperature acquisition by pressing "Temperature acquisition" button.

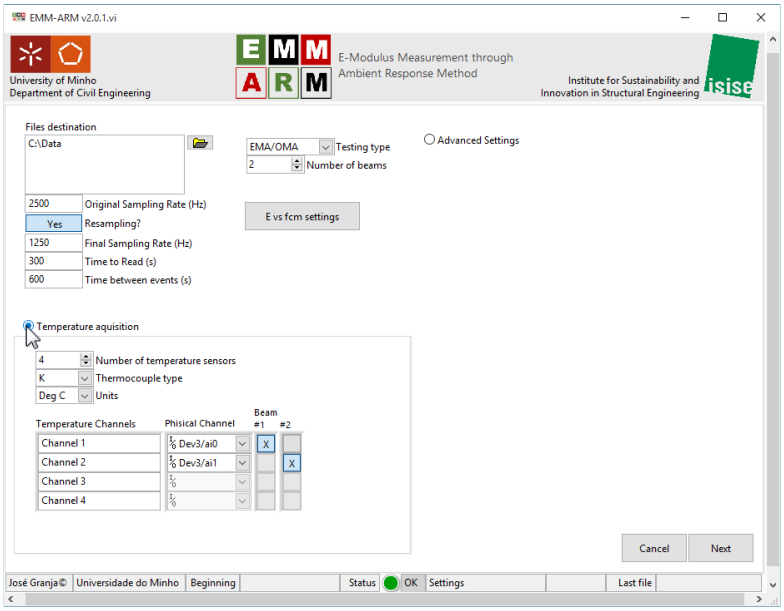

If the temperature acquisition is ON a new window will appear were it is possible to set:

[9] The number of temperature sensors

- It is possible to set a maximum of 6 temperature sensors.

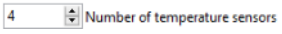

[10] The type of thermocouple

- The type of alloys combination. The default type is K.

[11] The temperature units

- It is possible to choose between: Celsius, Kelvin, Fahrenheit, Rankine and a costume scale.

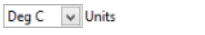

[12] The name of the temperature channels

- List of names to assign to the temperature channels.

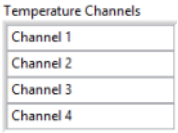

[13] The physical channel

- The physical channel of each sensor have the device ID, that needs to be a NI DAQ temperature acquisition, and the number of the channel in tbe acquisition devise.

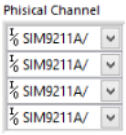

[14] The correspondence between the temperature sensors and the beams

In the same window it is also possible to go to the advanced settings by pressing "Advanced Settings" button.

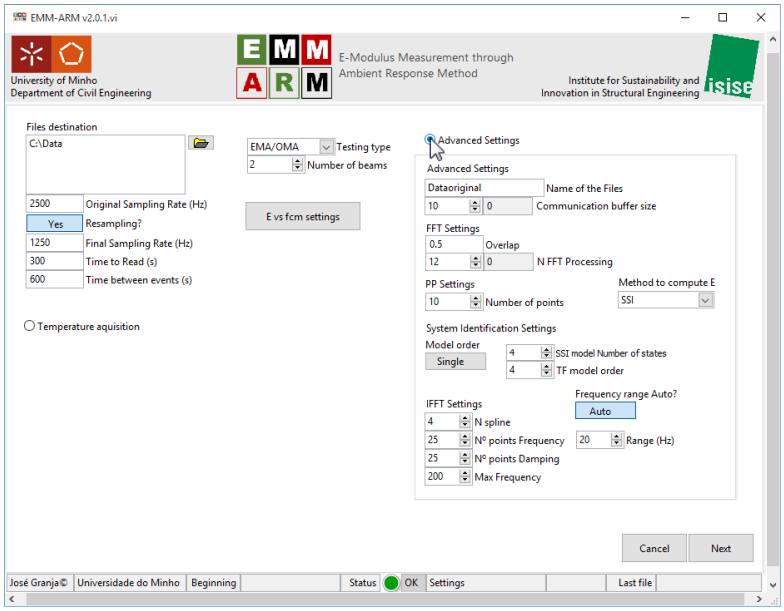

A new window will appear were it is possible to set:

[15] The name of the files

- Prefix to the files with the measured accelerograms. Then the final name of the files will be "Prefix"_YYYY-MM-DD_HH-MM-SS.txt

[16] The communication buffer size to each channel

- 2^x is number of points per channel to buffer in the data acquisition system.It is recommended to use a buffer size to each channel close to half of the acquisition frequency.

FFT Settings

[17] The window overlap on the welch procedure for the data processing

- It is recommended to use 50% overlap to prevent lost of data, once in the data processing it is applied a Hanning window on the signals

[18] The size of the FFT in the welch procedure for the data processing

- 2^x is number of points used in the FFT for the data processing.

PP Settings

- Peak picking modal identification settings

[19] The number of points to detect the frequency

- The number of points, around the detected peak on the power spectrum density of the response of each beam, used to detect the resonance frequency.

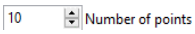

System identification Settings

- Peak picking modal identification settings

[20] Model order

- Single or multiple

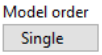

[21] SSI model Number of states

- If Model order = Single – SSI model number of states
- If Model order = Multiple – maximum SSI model number of states

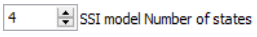

[22] TF model order

- If Model order = Single – TF model order
- If Model order = Multiple – maximum TF model order

IFFT Settings

- Inverse of Fast Fourier Transform settings

[23] N spline

- Increase factor of the number of points of the SDOF accelerogram resulting from the IFFT algorithm

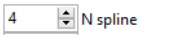

[24] Number of points Frequency

- Number of points to perform a linear regression to identify the resonance frequency

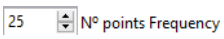

[25] Number of points Damping

- Number of points to perform a linear regression to identify the damping of the testing beam

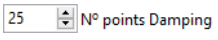

[26] Maximum Frequency

- Frequency upper limit to select the range to perform the IFFT of the frequency spectrum

Frequency range

- Range of frequencies to perform the resonance frequency identification

[27] Frequency range Auto

- Automatic frequency range or manual fix limits

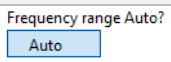

[28] The size of the window to select the resonance frequency

- Window width to detect the peak of higher intensity in power spectrum density of the response of each beam. The limits of the window are the resonance frequency of the last event +/- the width of the window.

[29] Method used in the frequency identification to compute the E-modulus of the material

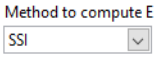

In the same window it is also possible to configure the relationship between the E-Modulus and the compressive strength of the material by pressing the "E vs fcm settings" button.

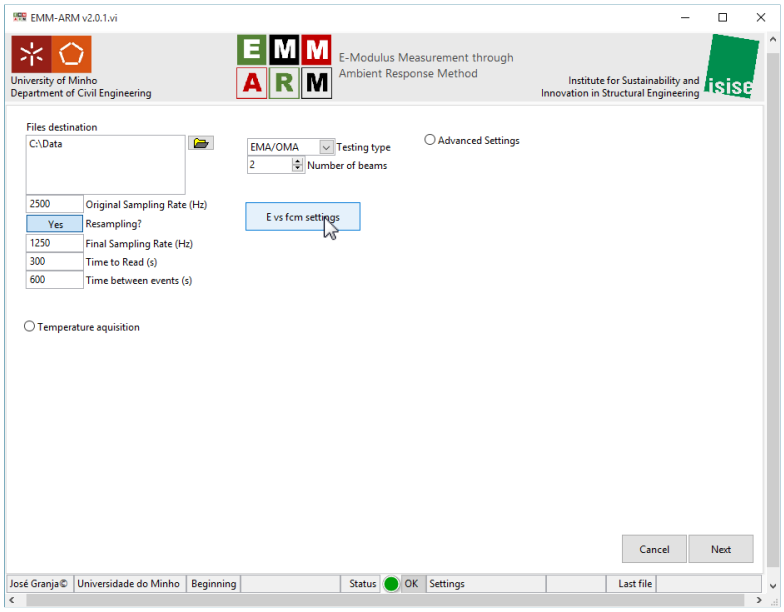

A new window will appear

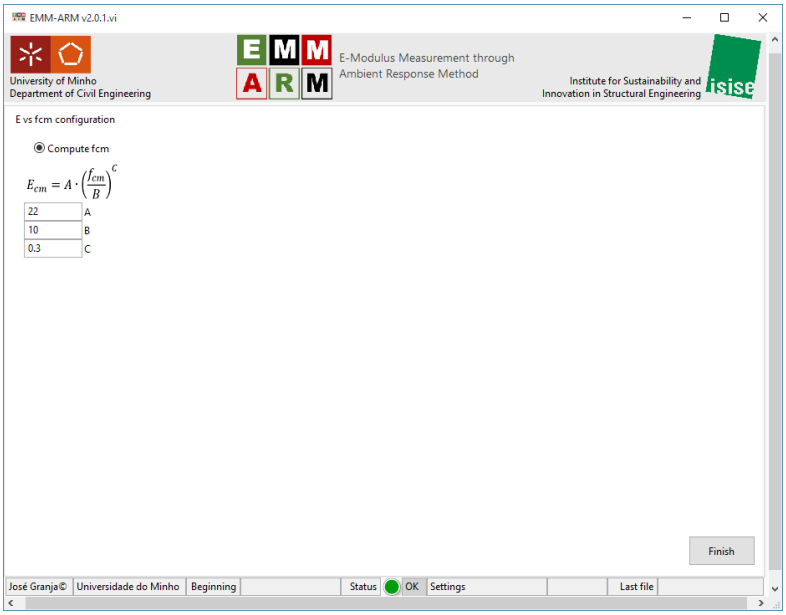

In this window it is possible to:

[30] Turn ON/OFF the compressive strength (fcm) estimation

- By default the program will compute the compressive strength of the material.

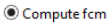

[31] Set the parameters of the relation between the E.Modulus and the compressive strength

- The correlation between Ecm and fcm is based on the eurocode 2 as well as the default values for the variables.

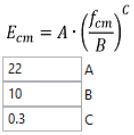

Press "Finish" button

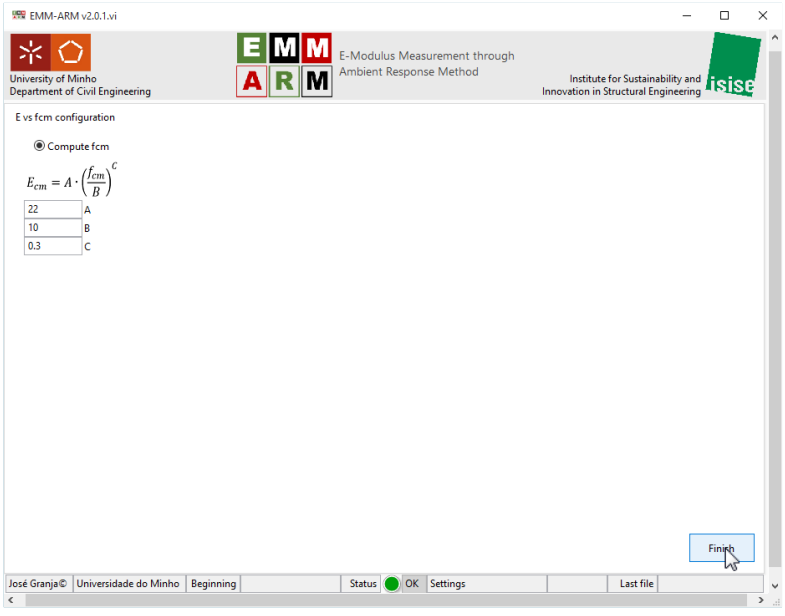

Press "Next" button

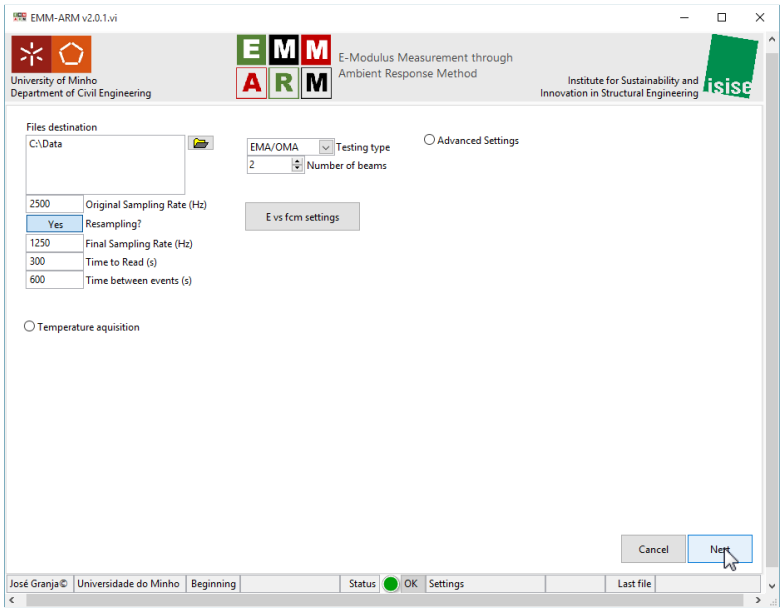

A beam configuration page will appear:

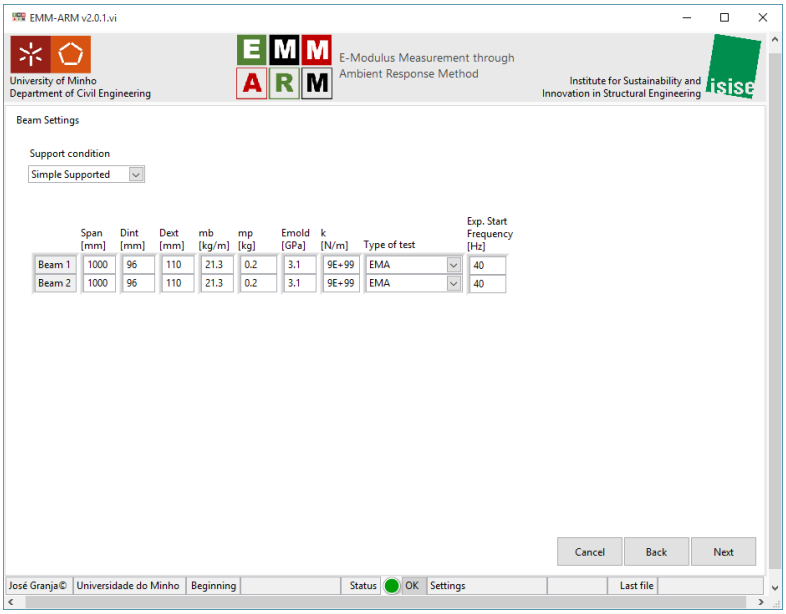

In this page it is possible to set:

[32] The support conditions

- It is possible to choose between a Simple Supported beam and a Cantilever beam.

Support condition: Simple Supported

[33] The beam geometrical and mechanical characteristics

- Span — Span [mm]: 1000
- Internal diameter (Dint) — Dint [mm]: 96
- External diameter (Dext) — Dext [mm]: 110
- Distributed mass (mb) — mb [kg/m]: 21.3
- Concentrated mass at mid span (mp) — mp [kg]: 0.2
- E-Modulus of the mould (Emold) — Emold [GPa]: 3.1
- Vertical Stiffness of the supports (k) — k [N/m]: 9E+99
- Type of data processing (Type of test) — Type of test: EMA
- Expected first resonance frequency (Exp. Start Frequency) — Exp. Start Frequency [Hz]: 40

Press "Next" button

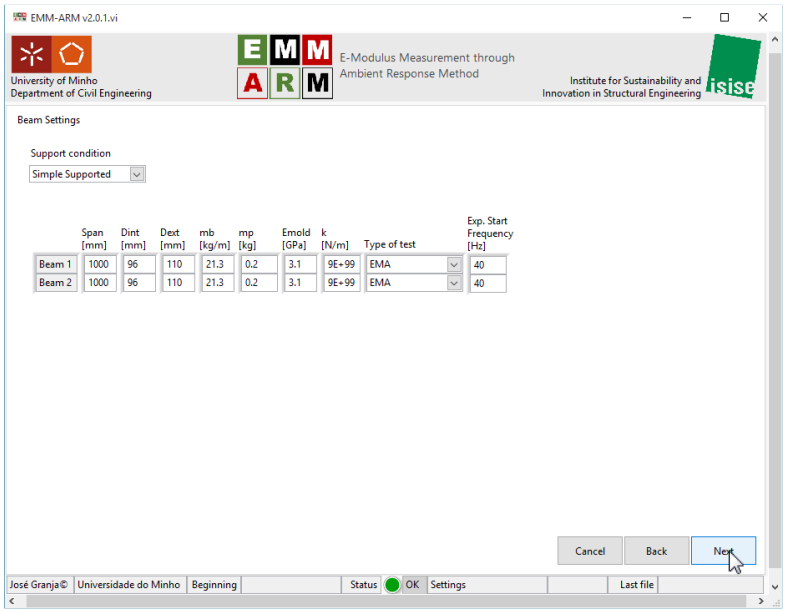

An accelerometer configuration page will appear:

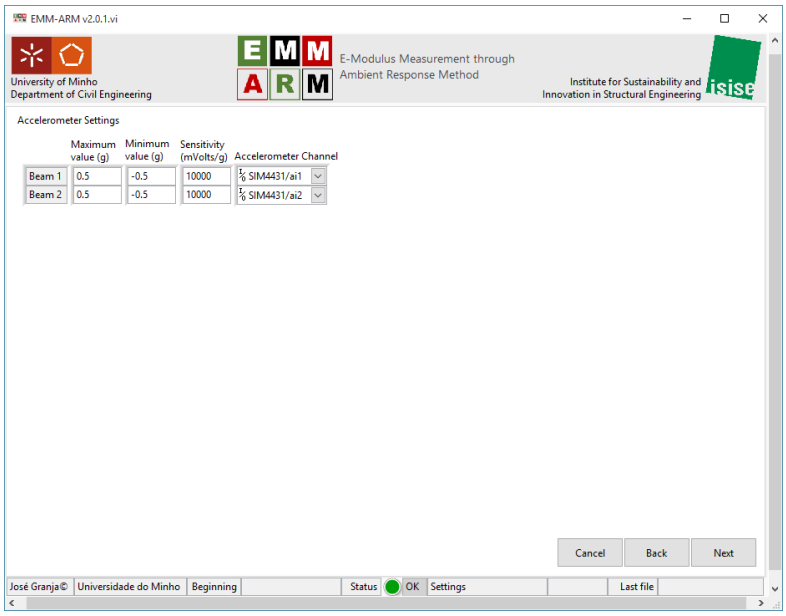

In this page it is possible to set:

[34] The characteristics of the accelerometers	
• Accelerometer maximum value	Maximum value (g) 0.5
• Accelerometer minimum value	Minimum value (g) -0.5
• Sensitivity	Sensitivity (mVolts/g) 10000

- Physical Channel (Accelerometer Channel)

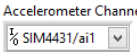

Press "Next" button

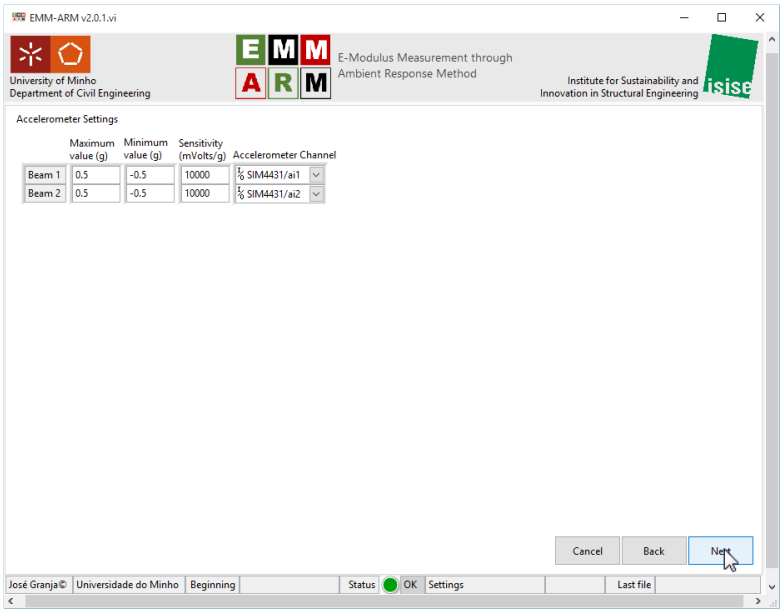

A generation configuration page will appear:

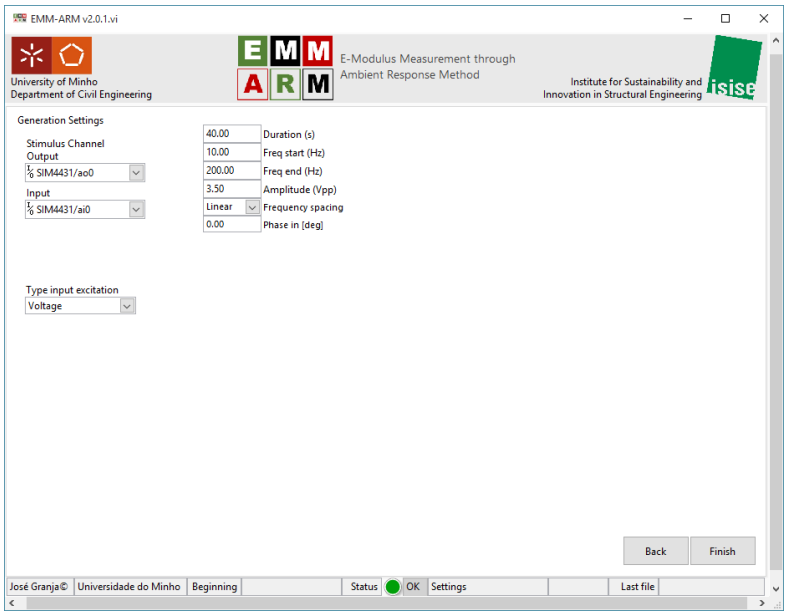

In this page it is possible to set the parameters needed to configure the sine sweep that will be send to the beams:

[35] The duration (s)

- Duration of each sweep. If the duration is less than the testing time of each event the sweep will be repeated until the end of the event.

[36] The start frequency (Hz)

- Lower bond of the frequency sweep. It is recommended to use not more than half of the first expected resonance frequency of the beams.

[37] The end frequency (Hz)

- Upper bond of the frequency sweep. It is recommended to use at least 30Hz more than the ultimate expected resonance frequency of the beams.

[38] The amplitude (Vpp)

- Amplitude of the excitation signal.

[39] Frequency spacing

- Type of variation of the frequency in the sweep. It is recommended to use linear variation.

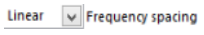

[40] The phase of the signal

- It is recommended to keep this value in zero.

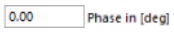

[41] The output physical channel of the stimulus

- The output physical channel of the stimulus have the device ID, that needs to be a NI DAQ signal generation, and the number of the channel in the signal generation devise.

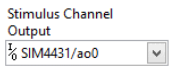

[42] The input physical channel of the stimulus

- The input physical channel of the stimulus have the device ID, that needs to be a NI DAQ signal acquisition, and the number of the channel in the signal acquisition devise.

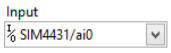

[43] The type of reading of the stimulus

- The excitation can be characterized in two ways: by measuring the generated signal or through a force sensor placed between the electromagnetic actuator and the beam.

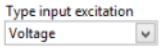

Press "Finish" button

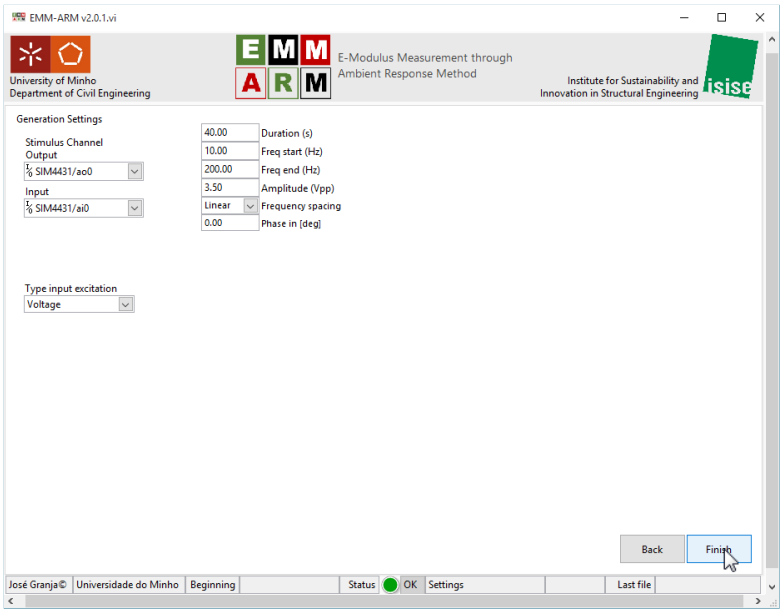

5.2.1.2 Save configurations to file

To save the configurations press the "Save" button.

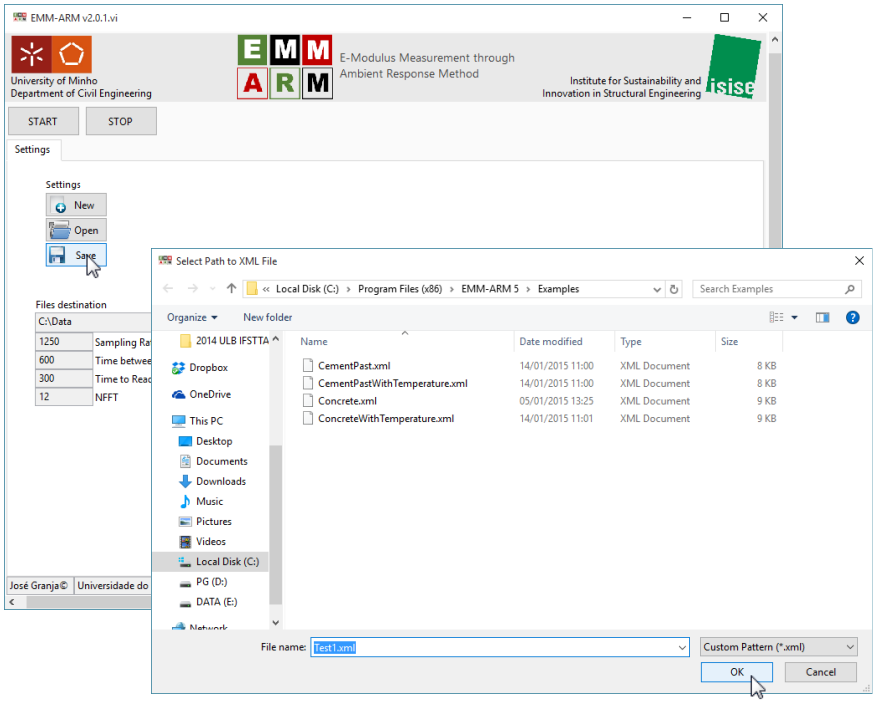

Then choose the name and the location of the xlm file.

5.2.1.3 Load configurations from file

To load the configurations press the "Open" button.

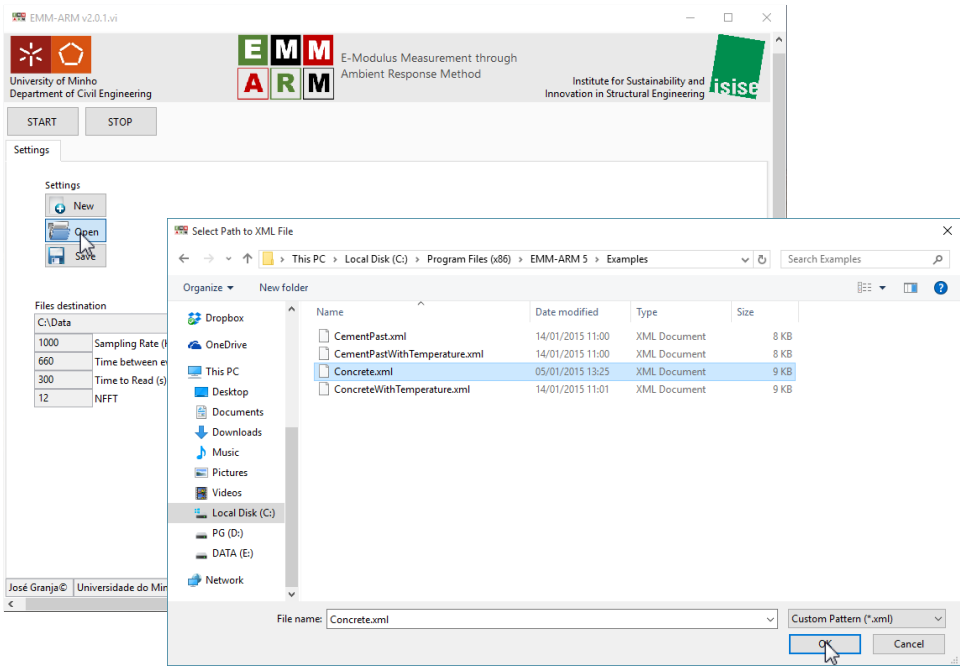

Then choose the name and the location of the xml file with the configurations.

5.2.2 Start

To start the acquisition press "START" button

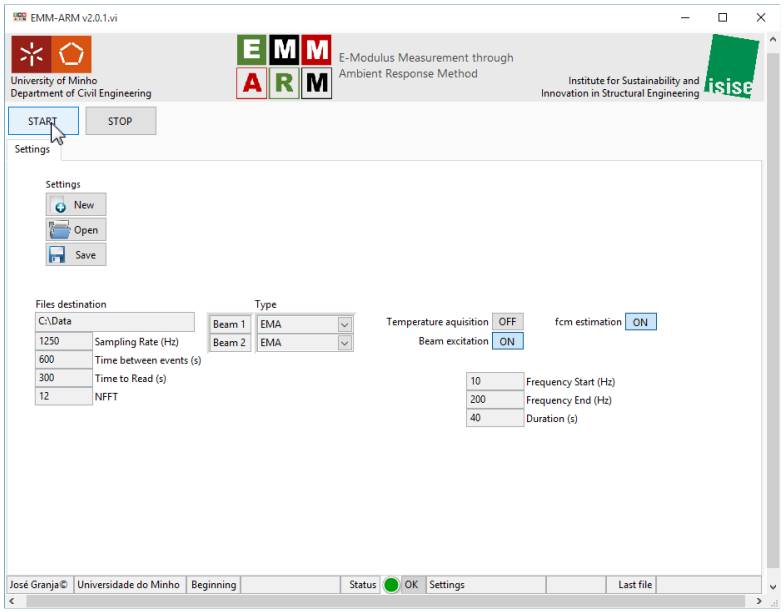

5.2.3 Running

5.2.3.1 Acquiring signals tab

In this tab it is possible to observe:

[1] The acquired accelerograms

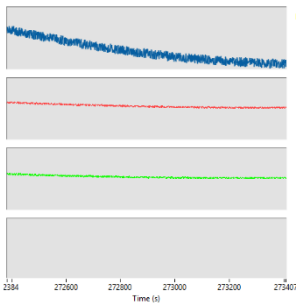

[2] The real-time Power Spectrum of the acquired accelerograms.

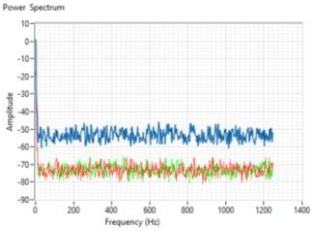

[3] It is also possible to turn ON/OFF the power spectrum and change the intensity to dB or linear scale

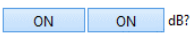

[4] The temperature acquired from the temperature sensors

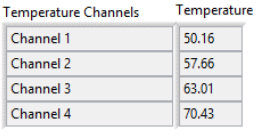

5.2.3.2 Processed signals tab

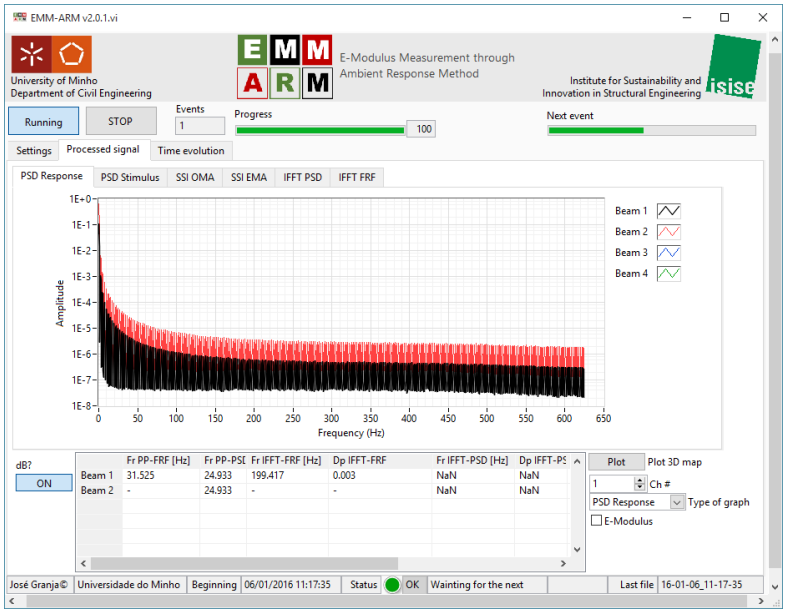

In this tab it is possible to observe:

[5] The processed data from the last event:

- The power spectrum density of the response (**PSD Response**)
- The power spectrum density of the stimulus (**PSD Stimulus**)
- The power spectrum density of the response with the SSI frequency identification technique stabilization diagram (**SSI OMA**)
- The frequency response function spectrum with the SSI frequency identification techniques stabilization diagrams and estimated FRF spectrums (**SSI EMA**)
- SDOF accelerogram obtained through the IFFT technique from the power spectrum density of the response (**IFFT PSD**)
- SDOF accelerogram obtained through the IFFT technique from the frequency response function (**IFFT FRF**)

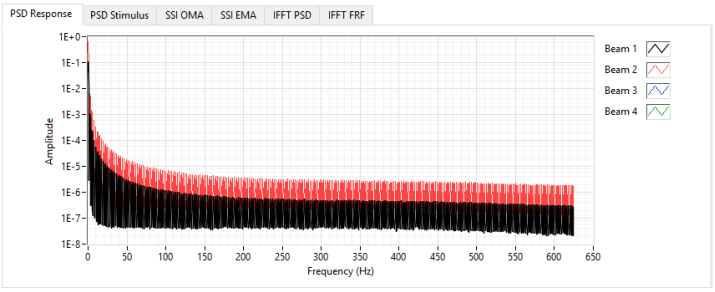

[6] A table with the identified parameters:

- Resonance frequency obtained through the identification of the peak of higher intensity in the frequency response function (**Fr PP-FRF [Hz]**)
- Resonance frequency obtained through the identification of the peak of higher intensity in the power spectrum density of the response accelerogram (**Fr PP-PSD [Hz]**)
- Resonance frequency identified through the inverse of fast Fourier transform technique of the frequency response function (**Fr IFFT-FRF [Hz]**)
- Damping of the testing specimen identified through the inverse of fast Fourier transform technique of the frequency response function (**Dp IFFT-FRF**)
- Resonance frequency identified through the inverse of fast Fourier transform technique of the power spectrum density of the response accelerogram (**Fr IFFT-PSD [Hz]**)

- Damping of the testing specimen identified through the inverse of fast Fourier transform technique of the power spectrum density of the response accelerogram (**Dp IFFT-PSD**)
- Resonance frequency identified through the transfer function model identification technique (**Fr TF-FRF [Hz]**)
- Damping of the testing specimen identified through the transfer function model identification technique (**Dp TF-FRF**)
- Resonance frequency identified through the subspace system identification technique (**Fr SSI-FRF [Hz]**)
- Damping of the testing specimen identified through the subspace system identification technique (**Dp SSI-FRF**)
- Estimated E-modulus of the material based on the selected resonance frequency (**E-Modulus [GPa]**)
- Compressive strength estimation based on the estimation of the E-Modulus of the material (**fcm [MPa]**)

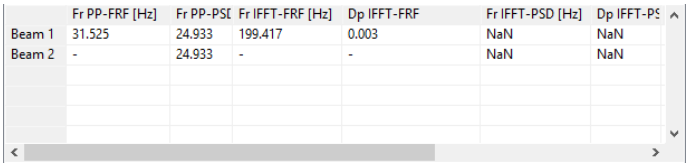

[7] It is possible to change the intensity of the spectrums to dB or linear scale

Additionally it is possible to plot a 3D map of the evolution of the spectrums by pressing the "Plot" button.

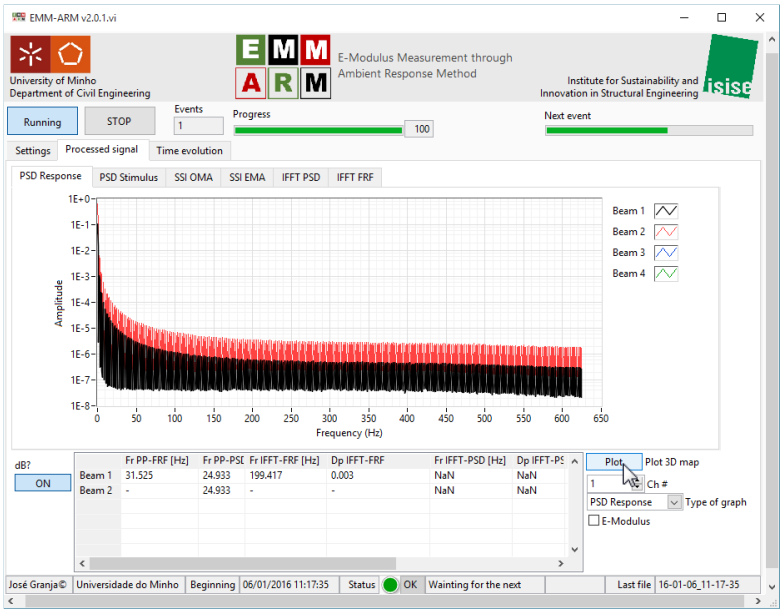

Must be selected:

- The channel number 

- The type of spectrum that can be: PSD Response, PSD Stimulus or FRF Amplitude 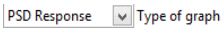

- Turn ON/OFF the conversion of the frequency to E-Modulus 

A new window will appear

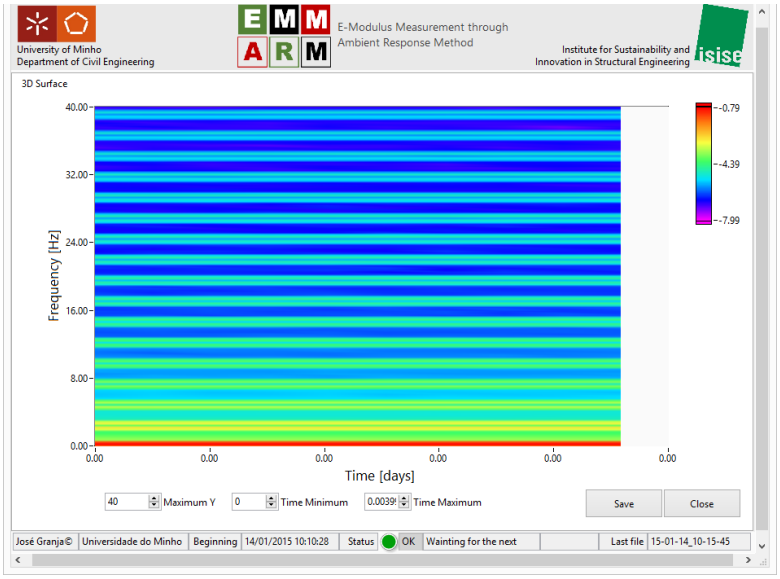

In this page it is possible to set:

[8] The maximum value of the Y-axis

- It can be Frequency or E-Modulus depending on the option chosen before

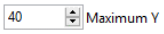

[9] The minimum of the X-axis

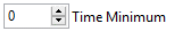

[10] The maximum of the X-axis

[11] Save the color map

- The file will be saved in the same folder as the results files and will have the following name: "Type_of_spectrum"_"Ch#".bmp. For example: PSD_Response_Ch1.bmp. If the save button were pressed the window will be closed too.

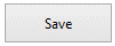

Press "Close" button to exit

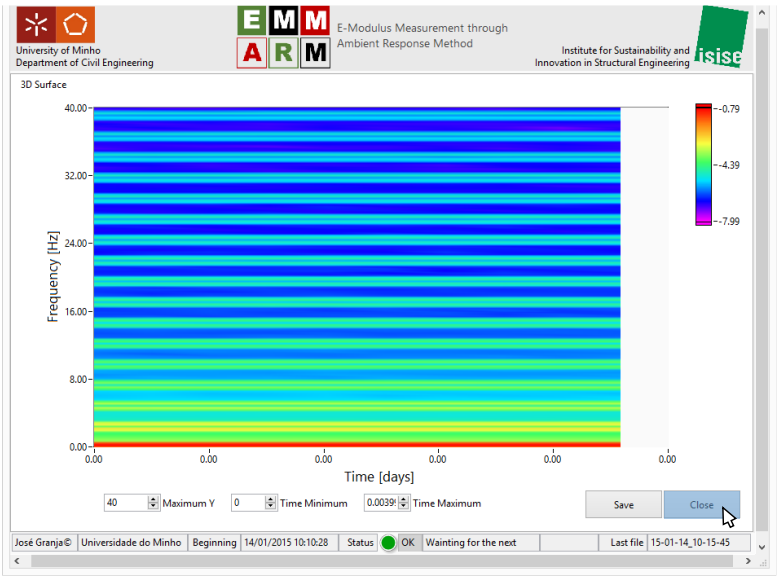

5.2.3.3 Time evolution tab

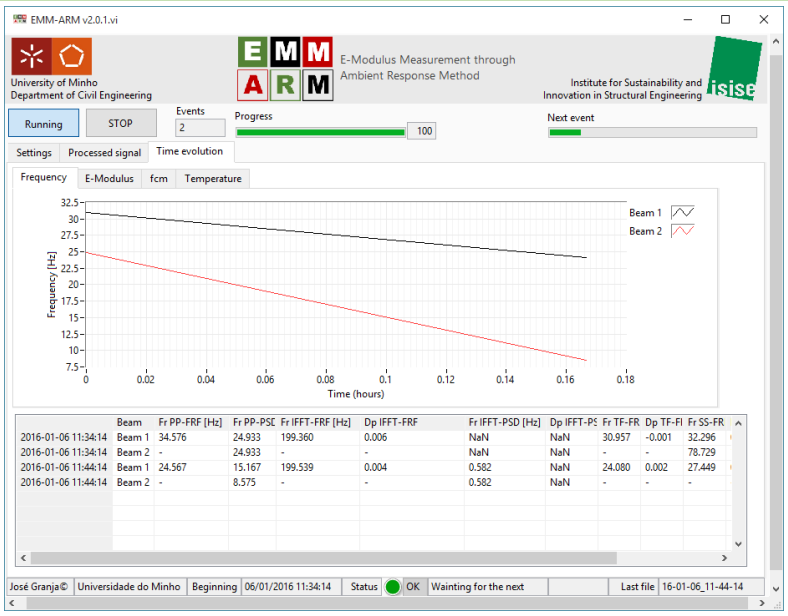

In this tab it is possible to observe:

[12] The time evolution of the:

- Resonance frequency of the beams obtained through the identification of the peaks of higher intensity in the power spectrums densities of the responses accelerograms (**Frequency**)
- Estimated E-modulus of the materials of the beams based on the previous resonance frequency (**E-Modulus**)
- Compressive strength estimation based on the estimation of the E-Modulus of the material (**fcm**)
- Temperature sensors (**Temperature**)

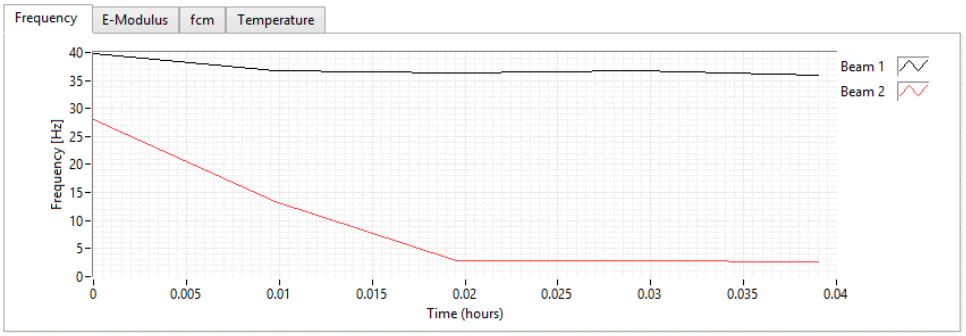

[13] A table with the history of the identified parameters:

- Date of the measurement
- Number of the beam (**Beam**)
- Resonance frequency obtained through the identification of the peak of higher intensity in the frequency response function (**Fr PP-FRF [Hz]**)
- Resonance frequency obtained through the identification of the peak of higher intensity in the power spectrum density of the response accelerogram (**Fr PP-PSD [Hz]**)
- Resonance frequency identified through the inverse of fast Fourier transform technique of the frequency response function (**Fr IFFT-FRF [Hz]**)
- Damping of the testing specimen identified through the inverse of fast Fourier transform technique of the frequency response function (**Dp IFFT-FRF**)
- Resonance frequency identified through the inverse of fast Fourier transform technique of the power spectrum density of the response accelerogram (**Fr IFFT-PSD [Hz]**)
- Damping of the testing specimen identified through the inverse of fast Fourier transform technique of the power spectrum density of the response accelerogram (**Dp IFFT-PSD**)

- Resonance frequency identified through the transfer function model identification technique (**Fr TF-FRF [Hz]**)
- Damping of the testing specimen identified through the transfer function model identification technique (**Dp TF-FRF**)
- Resonance frequency identified through the subspace system identification technique (**Fr SSI-FRF [Hz]**)
- Damping of the testing specimen identified through the subspace system identification technique (**Dp SSI-FRF**)
- Estimated E-modulus of the material based on the selected resonance frequency (**E-Modulus [GPa]**)
- Compressive strength estimation based on the estimation of the E-Modulus of the material (**fcm [MPa]**)

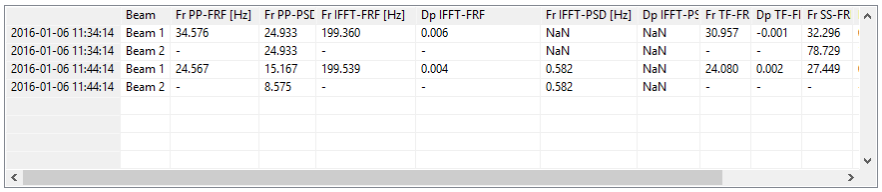

	Beam	Fr PP-FRF [Hz]	Fr PP-PSD	Fr IFFT-FRF [Hz]	Dp IFFT-FRF	Fr IFFT-PSD [Hz]	Dp IFFT-PS	Fr TF-FR	Dp TF-FI	Fr SS-FR
2016-01-06 11:34:14	Beam 1	34.576	24.933	199.360	0.006	NaN	NaN	30.957	-0.001	32.296
2016-01-06 11:34:14	Beam 2	-	24.933	-	-	NaN	NaN	-	-	78.729
2016-01-06 11:44:14	Beam 1	24.567	15.167	199.539	0.004	0.582	NaN	24.080	0.002	27.449
2016-01-06 11:44:14	Beam 2	-	8.575	-	-	0.582	NaN	-	-	-

5.2.4 Stop

To stop the program press "STOP" button.

When the program is stopped a menu bar will appear.

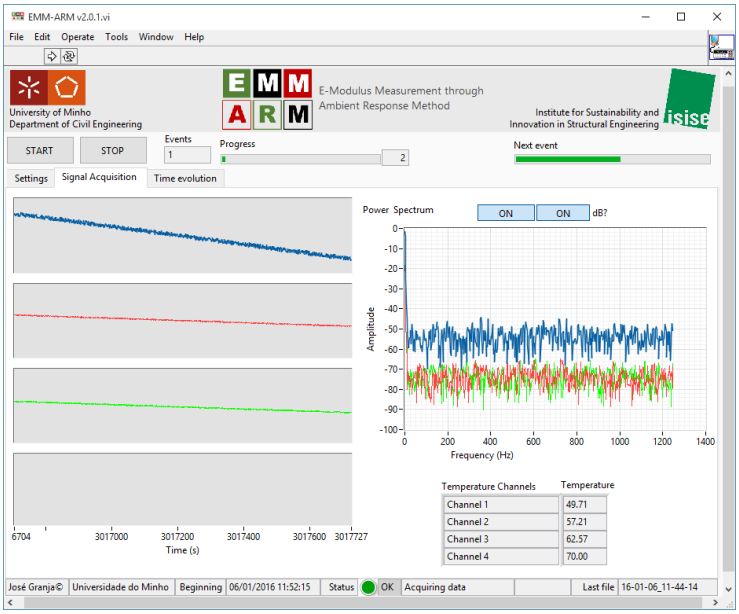

5.2.5 Restart

To restart the program press the arrow button in the top menu bar.

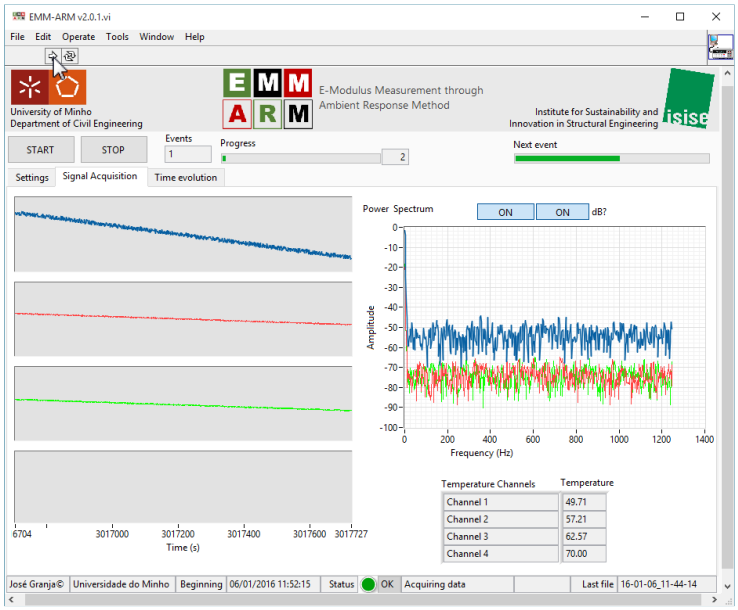

Then go to the section 5.2.1 of the manual.

5.3 Output results files

During a test the program will create several results files. All this files has a suffix to his name that represents the date of creation: YY-MM-DD_hh:mm:ss. In the flowing examples the files were created on 3 of February of 2015 at 10:18:05.

- **Dataoriginal_15-02-03_10-18-05.zip**

All data acquired during the tests. Each column represents one input channel starting in the channel 1 until the last channel. Note that when there is excitation to the beams there will be a column that represents the real excitation readings.

- **Tempdata.dat**

Temporary binary data file that will be deleted after the data processing is finished.

- **Results_2015-01-14_11-07-25.txt**

This file contains all the important configurations of the program and the final processed results:

Fr PP-FRF [Hz] – Resonance frequency obtained through the identification of the peak of higher intensity in the frequency response function;
Fr PP-PSD [Hz] – Resonance frequency obtained through the identification of the peak of higher intensity in the power spectrum density of the response accelerogram;
Fr IFFT-FRF [Hz] – Resonance frequency identified through the inverse of fast Fourier transform technique of the frequency response function;
Dp IFFT-FRF – Damping of the testing specimen identified through the inverse of fast Fourier transform technique of the frequency response function;
Fr IFFT-PSD [Hz] – Resonance frequency identified through the inverse of fast Fourier transform technique of the power spectrum density of the response accelerogram;
Dp IFFT-PSD – Damping of the testing specimen identified through the inverse of fast Fourier transform technique of the power spectrum density of the response accelerogram;
Fr TF-FRF [Hz] – Resonance frequency identified through the transfer function model identification technique;
Dp TF-FRF – Damping of the testing specimen identified through the transfer function model identification technique;
Fr SSI-FRF [Hz] – Resonance frequency identified through the subspace system identification technique;
Dp SSI-FRF – Damping of the testing specimen identified through the subspace system identification technique;
E-Modulus [GPa] – Estimated E-modulus of the material based on the selected resonance frequency;
fcm [MPa] – Compressive strength estimation based on the estimation of the E-Modulus of the material.

- **Temprature_2015-01-14_11-07-25.txt**

This file contains the acquired temperature evolution along the test for the configured channels.

Version 2.0.1

isise Institute for Sustainability and Innovation in Structural Engineering